A Lithostratigraphic and Microfossil Investigation into Late Holocene Coseismic Land Level Change and Tsunami Inundation on Nagai Island, Shumagin Islands, Alaska.

EMMA CATHERINE BRAMLEY

A Lithostratigraphic and Microfossil Investigation into Late Holocene Coseismic Land Level Change and Tsunami Inundation on Nagai Island, Shumagin Islands, Alaska.

Emma Bramley

Abstract

Cycles of earthquakes and tsunamis are complex, occurring over timescales greater than the instrumental data, therefore, palaeoseismic reconstructions best constrain seismic and tsunami hazards. This research investigates late Holocene great earthquakes (M_w >8.0) and high tsunami inundation (>present-day intertidal zone) on Nagai Island in the Shumagin section of the Alaska-Aleutian subduction zone (AASZ) through palaeoseismic reconstruction of sediment cores from four sites across Nagai Island. DV.19.03 and 19.DV.17 are selected for detailed lithostratigraphic, diatom, grain size, and chronological analysis. Nagai Island does not exhibit identifiable land level change or sand beds conclusively demonstrating high tsunamis over the last ~2900 years, supporting the geological evidence from nearby Simeonof Island where no land level change >0.3 m or tsunami inundation exceeding the present-day intertidal zone are identified. Thus, it appears that the Shumagin section of the AASZ has accommodated plate convergence throughout the late Holocene through long term persistent creep, neither generating a great earthquake nor coseismically weakening from the propagation of a great earthquake from adjacent Semidi or Unimak sections. Further, absence of geological evidence for high tsunami inundation on Nagai Island alongside Simeonof Island suggests that the Shumagin section of AASZ has neither generated a high tsunami nor exhibited deposition of high tsunamis sourced from teletsunamis generated elsewhere along the AASZ or other subduction zones throughout the late Holocene. The geological evidence from Nagai Island combined with Simeonof Island implies low hazard for great earthquakes and high tsunamis generating or propagating into the Shumagin section. This suggests a low hazard for Shumagin sourced tsunamis to far field communities in the Pacific. However, great earthquakes and high tsunamis cannot be ruled out because the geological evidence may not extend to the Shumagin section recurrence intervals of great earthquakes, potential future changes in the locking of the plate interface, and possible missing geological evidence.

A Lithostratigraphic and Microfossil Investigation into Late Holocene Coseismic Land Level Change and Tsunami Inundation on Nagai Island, Shumagin Islands, Alaska.

Emma Bramley

Master of Research in Science

Durham University Geography Department

31st December 2022

Word Count: 46,206

Table of Contents

List of Tables

List of Figures

Acknowledgments

I would like to thank my supervisor, Dr. Simon Engelhart, for the continued support, advice and expertise throughout this project, your knowledge and passion for palaeoseismology is an inspiration. Thank you also to my secondary supervisor Dr. Matthew Brain for all the encouragement and advice on navigating the ups and downs of a Master of Research.

Thank you to all the geography lab technicians at Durham University, especially Neil Tunstall and Sion Kennaway for guiding me through new techniques.

I am incredibly lucky to have had the support and funding from the Alaskan Sea Level Research team and the USGS including Rich Briggs, Tina Dura, Simon Engelhart, Peter Haeussler, Richard Koehler and Rob Witter, I will be forever grateful for the opportunities it has enabled.

And finally thank you to my family and friends for the constant encouragement and belief in my abilities, especially in times of doubt.

1.0 Introduction

1.1 The Importance of Palaeoseismic Reconstructions

Cycles of earthquakes and tsunamis are complex and occur over timescales greater than instrumental and observational data (Cohen and Freymeuller, 2004; Shennan and Barlow, 2008). Therefore, to capture multiple cycles of earthquakes and tsunamis to best understand their characteristics and recurrence intervals, and to subsequently produce the most accurate hazard maps, the decadal to centennial instrumental and observational records need to be extended to centennial and millennial timescales (Jankaew *et al.,* 2008; Simmons *et al.,* 2011). Palaeoseismic reconstructions using sediment and microfossil archives enable the extension of short-term instrumental data to geological data on timescales of centuries to millennia (Atwater and Hemphill-Haley, 1997; Dura, 2014). Long term palaeoseismic data is especially important for capturing the rarer largest magnitude earthquakes and tsunamis which pose the greatest hazard to populations (Pilarczyk *et al.,* 2014). In addition to paleoseismic reconstructions extending the instrumental and observational records to better understand long-term seismicity, paleoseismic reconstructions are critical to determine the reliability of interpretating observational seismic records. For example, in the Shumagin section of the Alaska-Aleutian subduction zone, where this research focuses, Davies *et al.* (1981) interpreted reports of strong ground shaking and high tsunami (greater than present-day intertidal zone) waves in 1788 from Russian outpost documents as evidence for the Shumagin section to be a likely site for a near future great earthquake. Thus, geological evidence from paleoseismic reconstruction is essential to reinforce the non-definitive interpretations of observational records.

The Alaska-Aleutian subduction zone is one the world's most active subduction zones with six great earthquakes (M_w > 8.0) since 1937, rupturing almost the entirety of the approximately 4000 km long subduction zone (Figure 1.1a) (Sykes, 1971; von Huene *et al.,* 2012). The largest historical earthquake was a 9.2 M_w in 1964 which ruptured roughly 950 km of fault from Prince William Sound to Sitkinak Island (Figure 1.1a) (Zweck *et al.,* 2002; Calver and Plafker, 2008). Other historical great earthquakes along the Alaska-Aleutian subduction zone include 1938 (8.2 M_w), 1946 (8.6 M_w), 1957 (8.6 M_w), 1964 (9.2 M_w), 1965 (8.7 M_w), and 2021 (8.2 M_w) (Figure 1.1a) (von Huene *et al.,* 2012; Freymueller *et al.,* 2021; Wood *et al.,* 2021). Since the Alaska-Aleutian subduction zone has been relatively active during the instrumental and observational

period, it is critical to understand the long-term behaviour of the subduction zone through Alaskan palaeoseismic reconstructions to best constrain the hazard of future great earthquakes and high tsunamis and to produce the most effective mitigation strategy to reduce their impacts (Dura, 2014).

Further, great earthquakes and subsequent high tsunamis generated along the Alaska-Aleutian subduction zone do not only produce local hazards that need to be analysed and mitigated against but also the tsunamis can impact far field locations including the Pacific coast of the United States and Canada, Hawaii, Japan, Mexico and the Marquesas Islands (House *et al.,* 1981; Goff *et al.,* 2006; Becel *et al.,* 2017; Witter *et al.,* 2019). For example, the 1964 9.2 M_w Alaskan earthquake killed four people in Oregon and caused up to one million US dollars (equivalent of approximately six million US dollars in 2011) of damage along the US Pacific coastline (Witter *et al.,* 2011; Ryan *et al.,* 2012). Teletsunamis increase the area and the number of people vulnerable to the great earthquakes generated along the Alaska-Aleutian subduction zone hence, the importance of understanding the long-term characteristics of earthquakes and tsunamis generated along the Alaska-Aleutian subduction zone through palaeoseismic reconstruction (Witter *et al.,* 2011; Givens *et al.,* 2013). The importance of understanding long term earthquake and tsunami behaviour through palaeoseismic reconstructions is further exacerbated by the projected rise of relative sea level along coastlines vulnerable to Alaska-Aleutian sourced tsunamis because teletsunamis generated by the more frequent relatively lower magnitude earthquakes will pose higher destruction potential due to producing greater maximum wave heights (Ryan *et al.,* 2012; Ross *et al.,* 2013; Butler *et al.,* 2014; Dura *et al.,* 2021).

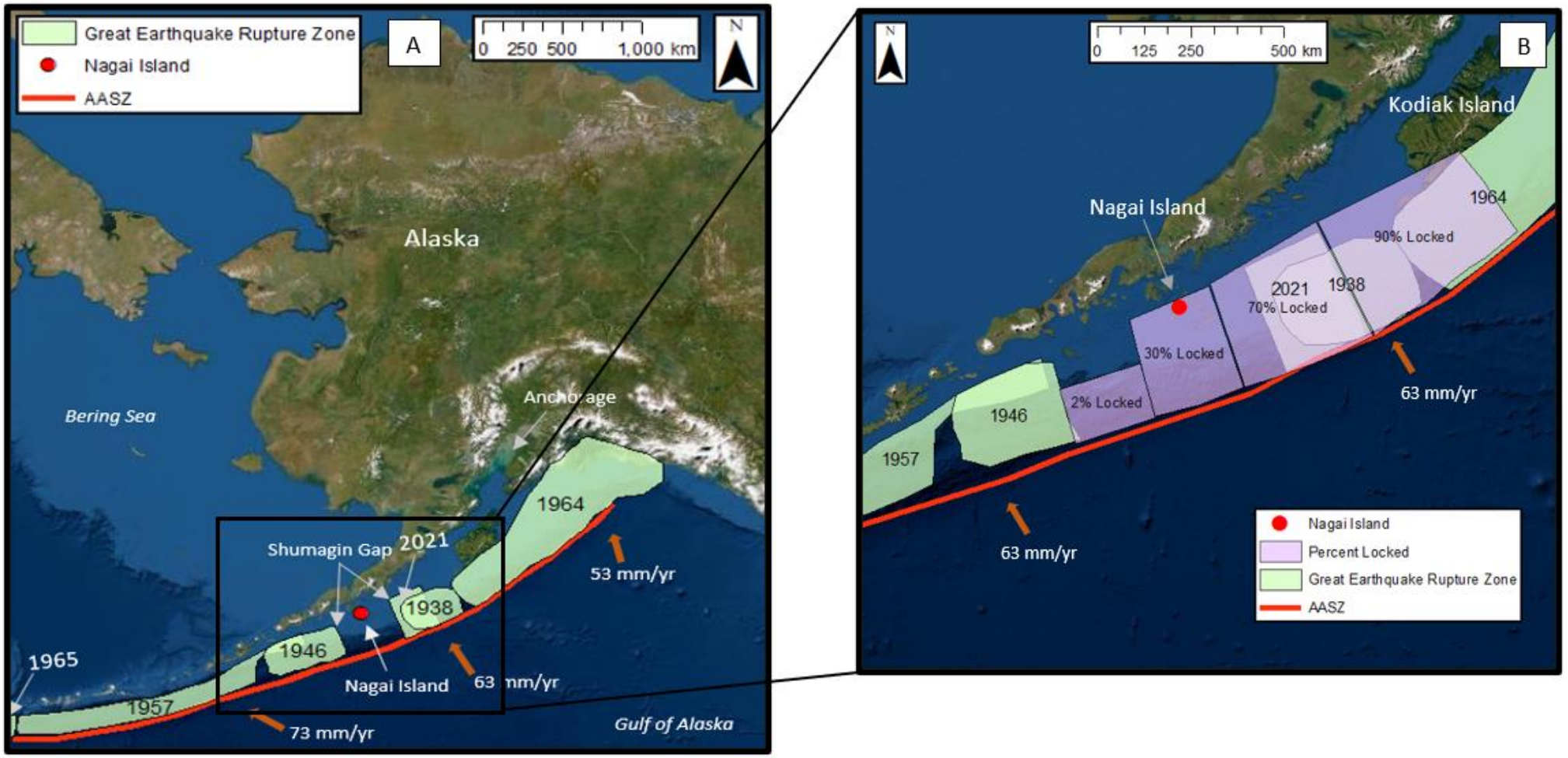

Figure 1.1 A. Location of historic great earthquakes (>8.0 Mw) along the Alaska-Aleutian subduction zone outlined in green (Jordon et al., 1965; Witter et al., 2014; Nicolsky et al., 2016; Wood et al., 2021). B. Locking of the Alaska-Aleutian megathrust including the percentage of plate coupling (adapted from Fournier and Freymueller, 2007; von Huene et al., 2019).

1.2 Aims and Research Questions

This research aims to extend the instrumental and observational seismic and tsunami record of the Shumagin section of the Alaska-Aleutian subduction zone to better constrain the seismic hazard that the Shumagin section poses both locally and to far field communities vulnerable to teletsunamis generated from the Shumagin section of the Alaska-Aleutian subduction zone. The instrumental and observational record will be extended through a sediment and microfossil reconstruction.

To achieve the research aim, the following research questions are addressed:

1) Is there sediment and microfossil evidence for coseismic land level changes and or tsunami inundation on Nagai Island throughout the Late Holocene?
2) Does the Late Holocene sediment and microfossil data from Nagai Island support Davies' *et al.* (1981) interpretation of the Russian outpost documents for a great earthquake in the Shumagin section of the Alaska-Aleutian subduction zone in 1788?
3) What are the implications of the Nagai Island palaeoseismic reconstruction for the seismic and tsunamigenic potential of the Shumagin section of the Alaska-Aleutian subduction zone?

2.0 Literature Review

2.1 Introduction to Literature Review

Palaeoseismic reconstructions aim to understand long term patterns of great earthquakes (M_w >8.0) and high tsunamis (greater than the present-day intertidal zone) to produce the most accurate hazard maps possible to minimise the impact associated with great earthquakes and high tsunamis (Grant, 2002). Relying on short term instrumental and observational data limits the understanding of great earthquakes and associated tsunamis because the cycles of great earthquakes and high tsunamis occur on timescales that exceed the instrumental and observational data (Sawai *et al.,* 2008; Shennan *et al.,* 2014c). Hence, the instrumental and the observational data does not well represent long term seismic and tsunami histories (Sawai *et al.,* 2008).

Palaeoseismic reconstructions have proven to be effective in understanding the long term earthquake and tsunami histories over multiple earthquake deformation cycles at subduction zones around the world, including the Cascadia subduction zone (e.g. Engelhart *et al*., 2013), the Chilean subduction zone (e.g., Dura, *et al.,* 2015), the Sumatra subduction zone (e.g., Fujino *et al*., 2006), the Kuril-Kamchatka subduction zone (e.g., Sawai *et al*., 2002), and the Hikurangi subduction zone (e.g. Cochran *et al*., 2006), as well as along the Alaska-Aleutian subduction zone (Figure 2.1) (e.g. Shennan *et al*., 1999).

This literature review first explains what palaeoseismic reconstructions are followed by important palaeoseismic reconstructions along subduction zones globally, palaeoseismic reconstructions along the Alaska-Aleutian subduction zone, the instrumental and observational research conducted in the Shumagin section of the Alaska-Aleutian subduction zone and finally, the palaeoseismic data from the Shumagin section.

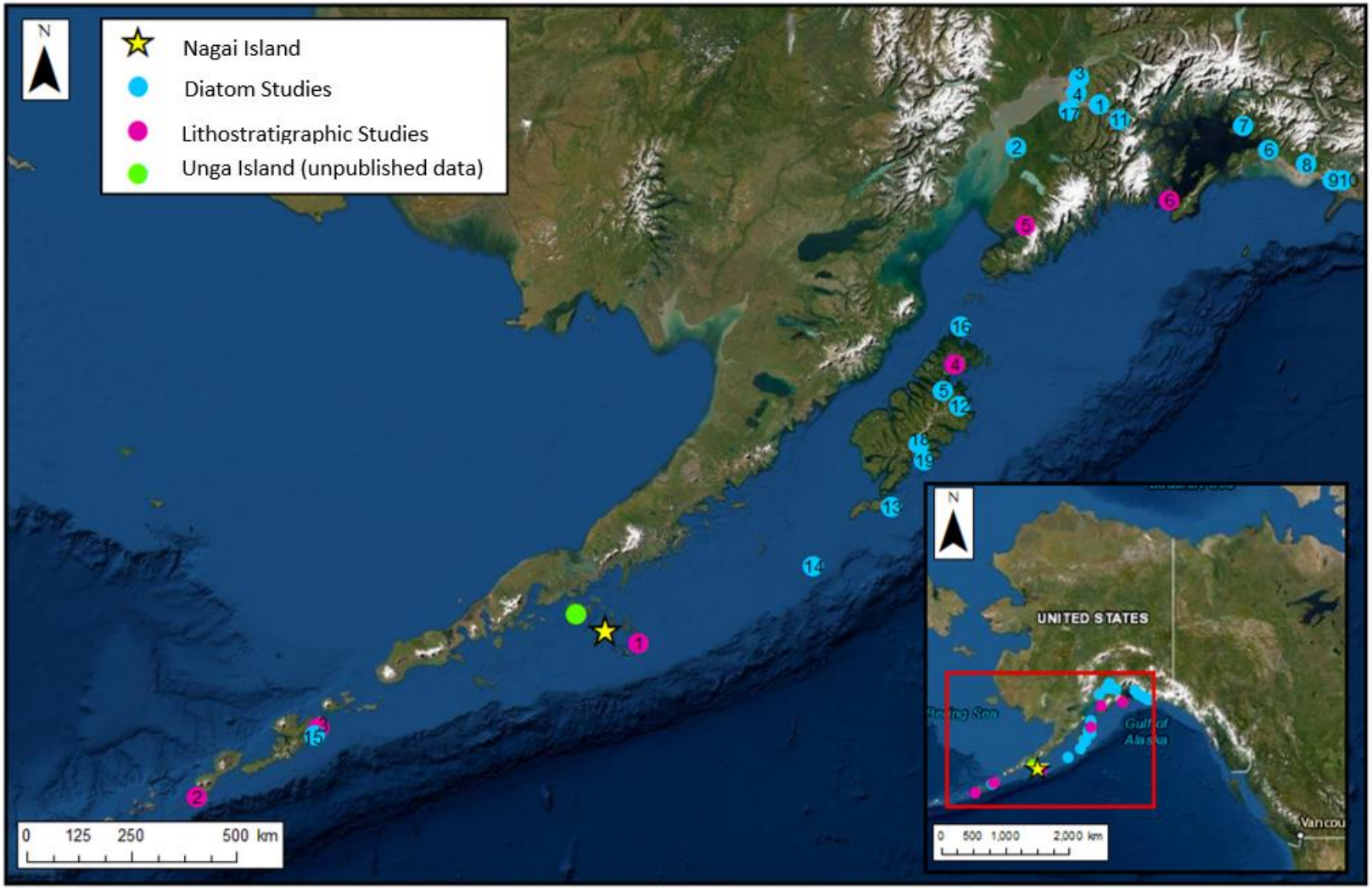

Figure 2.1. Map showing the palaeoseismic reconstructions along the Alaska-Aleutian subduction zone. Blue circles represent palaeoseismic reconstructions including both lithostratigraphic and diatom analysis, pink circles represent palaeoseismic reconstructions using lithostratigraphic evidence only. The numbers within the circles refer to the studies which are detailed in Table 2.1.

Table 2.1. Location and reference for the palaeoseismic reconstructions along the Alaska-Aleutian subduction zone displayed in Figure 2.1. N.B. Diatom studies refers to the blue circles in Figure 2.1 and lithostratigraphy refers to the pink circles in Figure 2.1.

Figure label	**Location**	**References**
Diatom studies 1	Girdwood Flats, Cook Inlet	Shennan *et al.* (1999) ; Zong *et al.* (2003); Hawkes *et al.* (2005); Hamilton and Shennan (2005a); Shennan and Hamilton (2006); Shennan and Barlow (2008); Shennan *et al.* (2016).
Diatoms studies 2	Kenai, Cook Inlet	Zong *et al.* (2003); Hamilton and Shennan (2005b); Hamilton and Shennan (2006)
Diatoms studies 3	Anchorage	Hamilton *et al.,* 2005
Diatoms studies 4	Ocean Bay, Cook Inlet	Hamilton and Shennan (2005a)
Diatoms studies 5	Hartney and Middle Bay, Kodiak	Watcham *et al.* (2013)
Diatoms studies 6	Cordova	Watcham *et al.* (2013)
Diatoms studies 7	Yakutat	Shennan *et al.* (2009)
Diatoms studies 8	Copper River Delta	Shennan *et al.* (2014a)
Diatoms studies 9	Lower Katalla River	Shennan *et al.* (2014a)
Diatoms studies 10	Pluffy Slough	Shennan *et al.* (2014a)
Diatoms studies 11	Portage	Shennan *et al.* (2014b)
Diatoms studies 12	Kaisin Bay, Kodiak Island	Shennan *et al.* (2014c); Shennan *et al.* (2016)
Diatoms studies 13	Sitkinak Island	Briggs *et al.* (2014)
Diatoms studies 14	Chirikof Island	Nelson *et al.* (2015)
Diatoms studies 15	Sedanka Island	Witter *et al.* (2016)
Diatoms studies 16	Shuyak Island	Shennan *et al.* (2018)
Diatoms studies 17	Turnagain Arm, Cook Inlet	Shennan *et al.* (2016)
Diatoms studies 18	Old Harbour, Kodiak Island	Janigian (2018)
Diatom studies 19	Sitkadilik Island	Prater (2021)
Lithostratigraphy 1	Simeonof Island	Witter *et al.* (2014)
Lithostratigraphy 2	Umnak Island	Witter *et al.* (2019)
Lithostratigraphy 3	Sedanka Island	Witter *et al.* (2016, 2019)
Lithostratigraphy 4	Kodiak Section	Hutchinson and Crowell (2007)
Lithostratigraphic 5	Kenai Section	Hutchinson and Crowell (2007)
Lithostratigraphic 6	Prince William Sound Section	Hutchinson and Crowell (2007)

2.2 What are Palaeoseismic Reconstructions?

Palaeoseismic reconstructions expand the instrumental and observational record through analysing geological evidence including sediment and microfossil evidence on scales from centuries to millennia to capture multiple earthquake deformation cycles (Jankaew *et al*., 2008; McCalpin, 2009; Simmons *et al*., 2011). Palaeoseismicity based upon relative sea- level changes links different stages of the earthquake deformation cycle to associated changes in relative sea level which are recorded in the sediment and microfossil evidence (Nelson *et al.,* 1996; Dura and Hemphill-Haley, 2020). Low energy depositional environments, such as marshes, best record and preserve relative sea-level changes, thus are critical to palaeoseismic reconstructions based upon relative sea-level changes (Pilarczyk *et al.,* 2014; Kelsey *et al.,* 2015).

There are three phases to the earthquake deformation cycle; interseismic (between earthquakes), coseismic (during an earthquake) and postseismic deformation (after an earthquake), which produce different geological imprints associated with changes in relative sea level (Long *et al.,* 1999; Nelson *et al.,* 1996). The geological imprint of the three earthquake deformation phases is dependent on if the study site exhibits coseismic uplift or coseismic subsidence based upon the proximity to the trench and the characteristics of the rupture (Figure 2.2) (Atwater, 1987; Briggs *et al.* 2014). Shennan *et al.* (1999) suggested a preseismic signal as a possible additional fourth stage of the earthquake deformation cycle, where the period of long term interseismic land level uplift is interrupted by a period of preseismic relative sea-level rise. Though the suggestion of a preseismic signal is controversial as it is not a spatially and temporally consistent signal, and non-seismic related processes such as sediment mixing from spring thaw, El Nino, or the build-up of sea ice disturbing tidal flat sediments could be responsible for the preseismic signal (Shennan *et al.,* 1996; Shennan *et al.,* 1998; Hamilton *et al.,* 2005b). The preseismic signal is discussed in more detail in section 2.4.

The interseismic phase is characterised by gradual subsidence and relative sea-level rise close to the trench and gradual uplift and relative sea-level fall landward of the trench (Figure 2.2) (Nelson *et al.,* 1996). Lithostratigraphically, the interseismic phase is characterised by non-abrupt lithostratigraphy contacts and gradual changes in diatom assemblages in terms of a gradual decrease in freshwater diatoms and a gradual increase in brackish and marine diatoms in areas of gradual interseismic subsidence, and a gradual increase in freshwater diatoms and

a gradual decrease in brackish and marine species in areas of gradual interseismic uplift (Dura, 2014; Prater, 2021).

The coseismic phase of the earthquake deformation cycle is characterised by abrupt coseismic uplift close to the trench and abrupt coseismic subsidence landward of the trench (Figure 2.2) (Nelson *et al.,* 1996; Dura, 2014). In coastal marshes, coseismic uplift and relative sea-level fall is represented by a sharp lithostratigraphic change from mud deposits to peat and an abrupt increase in freshwater diatom species, whereas coseismic subsidence and relative sea-level rise is represented by a sharp lithostratigraphic change from peat to mud deposits and an abrupt increase in brackish and marine diatom species (Long *et al.,* 1999; Dura *et al.,* 2015). A sand deposit between the sharp lithostratigraphic and biostratigraphic changes suggests a coinciding tsunami inundation associated with the coseismic land level change (Atwater, 1987; Witter *et al.,* 2016; Prater, 2021) (Figure 2.2).

The postseismic phase of the earthquake deformation cycle includes the short period immediately after coseismic land level change where normal sedimentation in the new environmental conditions commences and the diatom assemblage will respond to the sudden changes associated with either the coseismic uplift or subsidence in terms of an increase in freshwater diatom species or an increase in brackish and marine species respectively (Figure 2.2). Following the postseismic phase of the earthquake deformation cycle, the long term coseismic phase resumes (Dura and Hemphill-Haley*.,* 2020). However, coseismic vertical motion is not consistent through time, and a location can change between coseismic subsidence and uplift between different earthquake deformation cycles depending on the proximity to the rupture area, hence, the geological imprint of the earthquake deformation cycle is not persistent through time and space (Briggs *et al.,* 2014).

Palaeoseismic reconstructions can also identify teletsunamis sourced from earthquakes that are too far away to record coseismic land level changes in the geological evidence (Nelson *et al.,* 2015). Identifying palaeo teletsunamis is more complex in absence of coseismic land level changes because non tsunami local processes such as storm surges, wind deposition, the melt out of aeolian sand covering snow in winter, channel deposits, and debris flows appear as tsunami like deposits in the geological record, hence it cannot be assumed that all sand deposits in the geological record represent tsunami deposits (Engel and Brückner, 2011; Nelson *et al.,* 2015). Therefore, a multi- proxy approach including lithostratigraphic and biostratigraphic analysis is critical for most accurately identifying palaeo teletsunamis (Dura and

Hemphill-Haley, 2020). Palaeotsunamis are characterised by sharp upper and lower contacts, upward fining, considerable lateral extent, laterally uniformed thickness, and landward thinning (Atwater and Hemphill-Haley, 1996; Switzer, 2010; Witter *et al*., 2016). In terms of microfossil evidence, palaeotsunamis are often dominated by planktonic marine diatoms accompanied by beach and inland diatom species and exhibit a high percentage of fractured valves (>75%) (Dominey-Howes *et al.,* 2006; Kortekaas and Dawson, 2007; Pilarczyk *et al.,* 2014) (Figure 2.2).

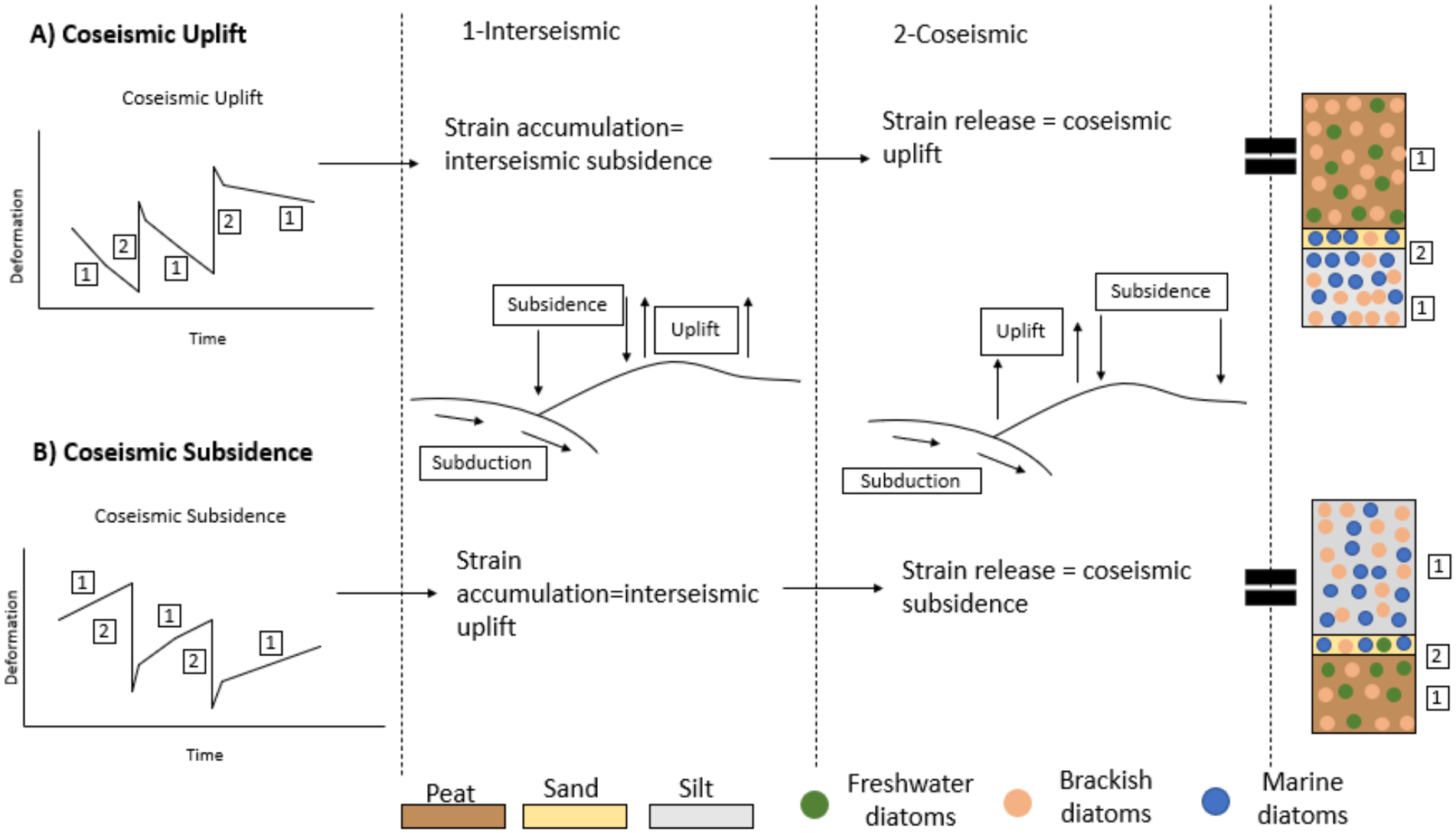

Figure 2.2. Earthquake deformation cycle adapted from Nelson et al. (1996), Dura (2014), and Prater, 2021.

2.3 Palaeoseismic Reconstructions Along Subduction Zones Globally

Globally, palaeoseismic reconstructions have improved the understanding of long-term seismicity and challenged assumptions produced from short term instrumental and observational data to best constrain seismic and tsunami potential and their recurrence intervals (e.g., Atwater, 1987; Hemphill-Haley, 1996b; Nelson *et al.,* 1996; Jankaew *et al.,* 2008; Engel and Brückner, 2011; Sawai *et al.,* 2012; Noda and Lapustra, 2013; Dura *et al.,* 2015).

Firstly, palaeoseismic reconstructions highlight the danger of using instrumental and observational data to infer seismic hazard, as the instrumental and observational data is unlikely to represent the true seismic history (Dura*,* 2014). For example, historical data from the central Chile coast identifies M_w 8.0- 8.5 earthquakes and subsequent low tsunamis (<4m) every 80 years with an additional M_w 9.0- 9.5 earthquake and 10m tsunami in AD 1730 (Dura *et al.,* 2015). However, a 2600-year geological record between 6200 and 3600 cal years BP identifies six probable coseismic land level changes and associated high tsunami inundations on the central Chile coast suggesting that prehistorically, larger earthquakes and associated tsunamis occurred (Dura *et al.,* 2015). Hence basing hazard maps for central Chile on the historical smaller earthquakes and tsunamis in 1822,1906 and 1985 could underestimate the seismic potential of the central Chile coast and lead to poorly prepared and shocked communities (Dura *et al.,* 2015).

Further, palaeoseismic reconstructions in both Japan and Thailand, following the seemingly unusually large 2011 9.0 M_W Tohoku-Oki and the 2004 9.2 M_W Sumatra-Andaman earthquakes, reveal that geological evidence for earthquakes and tsunamis, could have better prepared the devastated coastlines through identifying probable precedents to the modern earthquakes and tsunamis to better constrain seismic hazards along the vulnerable coastlines (Jankaew *et al.,* 2008; Sawai *et al.,* 2012). Therefore, it is critical to conduct palaeoseismic reconstructions along potentially destructive subduction zones to best constrain seismic history and thus, seismic hazard to produce the most accurate hazard maps possible (Jankaew *et al.,* 2008; Sawai *et al.,* 2012).

Identifying coseismic land level changes in the geological record is complex because local non-seismic processes can produce similar geological imprints to coseismic land level change, especially since only the largest subduction zone earthquakes produce changes in relative sea-level rise that exceed nontectonic local and regional processes (Nelson *et al.,* 1996). Example

non-tectonic local and regional processes that produce changes in relative sea level in the geological record include changes in the level of the ocean due to winds, currents or gravity, changes in tidal regimes, isostatic rebound, subsidence from fluvial withdrawal, and seawater loading on continental shelves (Nelson *et al.,* 1996; Shennan *et al.,* 2016). Therefore, to ensure the correct identification of coseismic land level changes in the geological record to most accurately reconstruct seismic histories, Nelson *et al.* (1996) suggested four key criteria for sediment and microfossil evidence for identifying coseismic land level changes based on research along the Cascadia subduction zone and was later updated by Shennan *et al.* (2016). Coseismic land level changes must exhibit considerable lateral extent, abrupt sediment and microfossil changes, relatively large magnitude of subsidence or uplift, and correlation between widely spaced sites (Nelson *et al.,* 1996). A tsunami deposit is additional noncritical evidence to support coseismic land level changes in geological records (Nelson *et al.,* 1996). The identified criteria for identifying coseismic land level changes have improved the accuracy of palaeoseismic reconstructions as it ensures that local and regional processes are considered to reduce the potential for misinterpreting non-tectonic sources for changes in relative sea level recorded in the geology (Nelson *et al.,* 1996).

Identifying palaeotsunamis is more complex than identifying palaeoseismic land level changes in the geological record, especially for identifying teletsunamis that do not have coinciding land level changes (Dura, 2014). Sediment criteria for tsunami deposits include anomalous deposits with sharp upper and lower contacts, upward fining from medium sand to very fine sand, considerable lateral extent of the deposit, uniformed thickness between different sites with similar inland distances, and landward thinning of the deposit (Switzer, 2010). However, the microfossil criteria for identifying palaeotsunamis is not well defined due to the high spatial variance in identified palaeotsunamis both in terms of the diatom assembles and the preservation of diatoms as well as the difficulty in distinguishing between non tsunami processes, especially storms which produce very similar geological imprints (Dawson *et al.,* 1996; Dura *et al.,* 2015).

Distinguishing between palaeotsunamis and palaeostorms remains a key challenge limiting the reconstructions of palaeotsunamis and producing effective tsunami hazard maps (Engel and Brückner, 2011). Atwater (1987) followed by Dawson *et al.* (1988) pioneered analysis of coastal lithostratigraphy to produce criteria for identifying palaeotsunamis which led to the production of tsunami facies models which provide criteria for distinguishing between palaeotsunamis and

palaeostorms (e.g., Dominey-Howes *et al.,* 2006; Mamo *et al*., 2009). However, the criteria for identifying palaeotsunamis such as sharp lower and upper contacts, normally graded deposits, and landward fining are synonymous to palaeostorm deposits (Engel and Brückner, 2011). Therefore, Engel and Brückner (2011) conclude that to identify palaeotsunami deposits, researchers must consider a range of factors as there is not a defined uniformed signature or a single proxy which can distinguish between palaeotsunamis and palaeostorms. Further, analysing local modern or known historical tsunamis and extreme storm deposits can better produce localised criteria for distinguishing between palaeotsunami and extreme palaeostorm deposits compared to the previous attempts of producing a global tsunami facies model that sets defined characteristics for global palaeotsunami deposits (Engel and Brückner, 2011).

Hemphill-Haley (1995b) made a key advancement in reconstructing palaeotsunami magnitudes because it was previously assumed that the tsunami run up height for palaeotsunamis could be calculated by the distance of the sand deposit. However, diatom analysis of tsunami deposits from the AD1700 earthquake from the Niawaikum River in Washington in the United States determined that the tsunami extended four kilometers inland, whereas the sand deposit only extended three kilometers inland, thus, the sand deposit vastly underestimates the magnitude of the tsunami (Hemphill-Haley, 1995b).

Prior to the 2011 9.0 M_W Tōhoku-Oki earthquake, it was assumed that creeping sections of a subduction zone posed lower seismic and tsunami hazards compared to locked sections of a subduction zone (Noda and Lapustra, 2013). However, the largest slip in the 2011 Tōhoku-Oki earthquake occurred in an area determined as creeping and thus, the assumption that this area posed limited seismic hazard, vastly underprepared vulnerable communities (Tsura *et al.,* 2000; Loveless *et al.,* 2010). Noda and Lapustra (2013) propose a model where creeping sections of a subduction zone can become coseismically weakened and unstable due to the rapid shear heating of pore fluids enabling unstable slip to propagate into sections identified as creeping. Therefore, creeping sections of a subduction zone do not always act as barriers to rupture and can in fact produce the greatest slip during an earthquake, as evident in the 9.0 M_W Tōhoku-Oki earthquake (Noda and Lapustra, 2013). The identification of coseismic weakening, challenging the assumption of creeping sections of a subduction zone acting as barriers to rupture, highlights the need of palaeoseismic reconstructions to determine if a creeping section of a subduction zone can become coseismically unstable in seismic events and thus, pose a considerable seismic hazard that needs to be addressed in seismic hazard mapping (Wei *et*

al., 2012; Noda and Lapustra, 2013). The 2011 9.0 M_W Tōhoku-Oki earthquake clearly identifies the urgency of palaeoseismic reconstructions in currently creeping sections of subduction zones globally to best constrain their seismic potential and to prevent inaccurate seismic hazard assumptions (Noda and Lapustra, 2013).

Despite the progress that palaeoseismic reconstructions have enabled in terms of understanding long term seismicity and to challenge assumptions based on short term instrumental and observational data, there are limitations of palaeoseismic reconstructions (Dura, 2014; Dura and Hemphill-Haley, 2020). For example, not all earthquakes and tsunamis leave a large enough geological imprint to be identifiable in the geological evidence (Hamilton and Shennan, 2005; Nelson *et al.,* 2008). Thus, not all palaeoearthquakes and palaeotsunamis can be reconstructed (Hamilton and Shennan, 2005; Nelson *et al.,* 2008). Generally, vertical displacement of more than 0.3m should be identifiable in the geological evidence (Witter *et al.,* 2014). Therefore, palaeoseismic reconstructions are limited to reconstructing earthquakes that are greater than 0.3m of vertical displacement which tends to be limited to great earthquakes (M_w >8.0) (Witter *et al.,* 2014).

The amount of vertical displacement associated with coseismic land level change is dependent upon the location of the hingeline, for example, Witter *et al.* (2014) use an elastic model to simulate earthquake scenarios which produce less than 0.3m of vertical displacement and hence, are unlikely to be identifiable in the geological evidence. A scenario where a large earthquake with 15 m of slip would produce too little vertical displacement due to the proximity of the hingeline suggests that under certain conditions even great earthquakes may not be recorded in the geological evidence (Witter *et al.,* 2014). Therefore, even though palaeoseismic reconstructions have enabled the extension of seismic and tsunami histories, it does not represent the entire seismic record as it is unlikely that vertical displacements less than 0.3 m will leave a lasting geological imprint that would be identified in a palaeoseismic reconstruction (Witter *et al.,* 2014). Further, the continued uncertainty in reconstructing palaeotsunamis especially palaeo teletsunamis which do not coincide with coseismic land level changes, is a key limitation of palaeoseismic reconstructions (Engel and Brückner, 2011). Finally, although palaeoseismic reconstructions expand the historical and observational record of earthquakes and tsunami, they still do not cover the entire seismic history of a subduction zone and thus, it cannot be assumed that the entire seismic history of a subduction zone is represented in a palaeoseismic reconstruction (Dura, 2014; Shennan *et al.,* 2016).

2.4 Palaeoseismic Reconstructions Along the Alaska-Aleutian Subduction Zone

Despite an abundance of palaeoseismic reconstructions along the Alaska-Aleutian subduction zone, they are mostly clustered in the area that ruptured in the AD1964 9.2 M_w earthquake (Figure 2.1). Recently palaeoseismic reconstructions have expanded to west of the AD1964 earthquake rupture area, though they are still sparse with only five palaeoseismic reconstructions and only two which include both sediment and microfossil analysis (Figure 2.1) (Hutchinson and Crowell, 2007; Briggs *et al.,* 2014*;* Witter *et al.,* 2014; Nelson *et al.,* 2015; Witter *et al.,* 2019). Palaeoseismic reconstructions that only conduct stratigraphical analysis (e.g. Hutchinson and Crowell, 2007; Witter *et al.,* 2014; Witter *et al.,* 2019) are useful for a rapid initial understanding of a study area and to compare to known palaeoearthquakes and palaeotsunamis that used a multi-proxy approach to identify them from other areas, but they are limited to qualitative analysis as without microfossil analysis, the magnitude of earthquakes identified in the geological record cannot be accurately estimated (Engelhart *et al.,* 2013; Watcham *et al.,* 2013). Further, research relying on only sediment evidence is more prone to uncertainty due to the single proxy approach limiting the understanding of complex geological seismic imprints, especially when analysed independently of known palaeoearthquakes and palaeotsunamis (Judd *et al.,* 2017). To best constrain seismic hazards along a subduction zone a holistic approach is required in terms of understanding the history and dynamics of the entire subduction zone rather than limited to sections of it, thus, the lack of palaeoseismic research west of the AD1964 Alaskan earthquake rupture zone limits the understanding of the Alaska-Aleutian subduction zone and poses opportunity for improved understanding of earthquake and tsunami histories (Briggs *et al.,* 2014).

Despite the large spatial gap in palaeoseismic research along the Alaska-Aleutian subduction zone west of the AD1964 Alaskan earthquake rupture area, palaeoseismic research along the Alaska-Aleutian subduction zone has improved the understanding of palaeoearthquakes and palaeotsunamis in terms of identifying a potential preseismic signal, calculating earthquake and tsunami recurrence intervals, and a shift from a simplistic deterministic paradigm for the earthquake deformation cycle to one that acknowledges spatial and temporal variability between earthquake deformation cycles (e.g. Shennan *et al.,* 1999; Zong *et al.,* 2003; Hawkes *et al.,* 2005; Shennan and Hamilton, 2005a,b; Shennan and Barlow, 2008; Watcham *et al.,* 2013; Shennan *et al.,* 2014 a, b). Further, palaeoseismic reconstructions have challenged assumptions produced from the instrumental and observational records including identifying

non-persistent rupture boundaries and the potential seismic hazards of currently creeping areas of the Alaska-Aleutian subduction zone (e.g., Briggs *et al.,* 2014; Shennan *et al.,* 2016; Witter *et al.,* 2016; Shennan *et al.,* 2018; Witter *et al.,* 2019). Finally, palaeoseismic reconstructions along the Alaska-Aleutian subduction zone have advanced the understanding of palaeotsunamis in terms of calculating recurrence intervals, distinguishing between tsunami deposits and non-tsunami deposits, identifying similar tsunami hazards at both creeping and locked sections of the Alaska-Aleutian subduction zone and determining the importance of analysing multiple sites to best assess tsunami hazards (Nelson *et al.,* 2015; Witter *et al.,* 2016; Janigian, 2018; Witter *et al.,* 2019 ; Prater, 2021).

Overall, palaeoseismic reconstructions along the Alaska-Aleutian subduction zone have enabled a better constraint on seismic hazard mapping compared to relying on instrumental and observational data to identify areas of greatest seismic hazard, though work remains to be done to fill the large spatial gaps in palaeoseismic data west of the AD1964 Alaska earthquake rupture area to truly assess the seismic hazard for the entirety of the Alaska-Aleutian subduction zone (e.g. House *et al.,* 1981; Briggs *et al.,* 2014).

Early palaeoseismic reconstructions along the Alaska-Aleutian subduction zone focused on Shennan's *et al.* (1999) suggestion of a fourth stage of the earthquake deformation cycle. Microfossil analysis at Girdwood Flats, Alaska, of the AD1964 earthquake identified a potential preseismic signal, where the period of long term interseismic land level uplift was interrupted by a period of preseismic relative sea-level rise (Shennan *et al.,* 1999). The determination of a potential short term preseismic signal could better prepare vulnerable communities to seismic hazards (Shennan *et al.,* 1999). Research by Zong *et al.* (2003) identified the preseismic subsidence signal for the AD1964 earthquake at other study sites at Girdwood Flats as well as Kenai Flats in the Cook Inlet which all exhibited approximately 0.15m of preseismic subsidence. Shennan and Hamilton (2006) used microfossil and sediment evidence to expand the theory of a potential preseismic signal from the AD1964 earthquake to five previous earthquakes throughout the last 3330 years in the Cook Inlet. All four study sites in the Cook inlet exhibited the preseismic signal suggesting Shennan's *et al.* (1999) proposal of a preseismic signal could be valid (Shennan and Hamilton, 2006). However, the magnitude of the preseismic signal is smaller than the error and the tide gauge records from the AD1964 earthquake did not record a preseismic signal; both limiting the confidence of a consistent preseismic signal which could be used to predict future ruptures (Karlstrom, 1964; Shennan and Hamilton, 2006). Further,

Hawkes *et al.* (2005) tested the preseismic signal theory at Netarts Bay on the Cascadia subduction zone and found evidence to support an earthquake precursor phase, suggesting inter subduction zone mechanisms responsible for the preseismic signals. However, Shennan *et al.* (1996) only identified preseismic subsidence in two of the eight earthquakes identified over the last 5,000 years in the lower Johns River on the Cascadia subduction zone. Therefore, more evidence from more study sites is required to understand the mechanisms and distribution of the preseismic phase as non-seismic related processes such as sediment mixing from spring thaw, El Nino, or the build-up of sea ice disturbing tidal flat sediments could be responsible for a preseismic signal (Shennan *et al.,* 1996; Shennan *et al.,* 1998; Hamilton *et al.,* 2005b). Despite the uncertainty in the mechanisms and the distribution of the preseismic signal, the preseismic signal demonstrates the potential of palaeoseismic research to improve the understanding of the mechanisms of earthquakes and potential predictor events to better prepare vulnerable communities to the associated seismic hazards (Shennan *et al.,* 1999).

Palaeoseismic reconstructions along the Alaska-Aleutian subduction zone have improved the calculation of recurrence intervals for great earthquakes enabling more accurate assessments of seismic hazard compared to instrumental and observational data (e.g., Hamilton and Shennan, 2005a; Hamilton and Shennan, 2005b Hamilton *et al.,* 2005; Hutchinson and Crowell, 2007). For example, tidal marsh sequences in Anchorage identified five potential great earthquakes throughout the last 2,500 years similar to those observed on Cook Inlet, suggesting a widespread history of AD1964 like earthquakes (Hamilton and Shennan, 2005a; Hamilton *et al.,* 2005). Transfer function models produced from local modern diatom assemblages enabled the quantification of coseismic land level changes to compare the magnitudes of palaeoearthquakes identified in the geological record (e.g., Zong *et al.,* 2003; Hamilton *et al.,* 2005a; Hamilton *et al.,* 2005b). However, Watcham *et al.* (2013) determined that regional scale modern diatom data enhanced by site specific samples most accurately reconstructs changes in relative sea level in Alaska. Thus, the lack of regional modern diatom datasets and the reliance on local modern training data in transfer functions used along the Alaska-Aleutian subduction zone may limit the accuracy of changes in relative sea level which could over or underestimate the magnitude of palaeoearthquakes such as those calculated in Zong *et al.* (2003) and Hamilton *et al.* (2005a). Despite, the potential to improve the quantification of the magnitude of palaeoearthquakes by using regional modern training sets enhanced by site specific samples for research prior to Watcham *et al.* (2013), palaeoseismic

reconstructions using transfer functions along the Alaska-Aleutian subduction zone have clearly advanced the understanding of palaeoseismicity (e.g., Shennan *et al.,* 2014 a, b; Shennan *et al.,* 2016; Shennan *et al.,* 2018). Most notably, transfer functions have enabled the comparison of palaeoearthquake magnitudes and to subsequently calculate magnitude specific recurrence intervals, especially for the research since 2013 where regional datasets with local enhancements are used to produce more accurate transfer functions and hence more accurate estimates of earthquake magnitudes (e.g., Shennan *et al.,* 2014 a, b; Shennan *et al.,* 2016; Shennan *et al.,* 2018).

Another key advancement in the understanding of palaeoseismicity through palaeoseismic reconstructions along the Alaska-Aleutian subduction zone is the shift from a simplistic deterministic paradigm for the earthquake deformation cycle to identifying both spatial and temporal variability and similarities between earthquake cycles (Shennan and Barlow, 2008). Shennan and Barlow (2008) identified seven great earthquakes at Girdwood Flats, Alaska over the last 4000 years which exhibited spatial variability in the rupture area and no fixed recurrence intervals, despite similar subsidence for each identified earthquake. The results from Girdwood Flats challenges the assumption of a deterministic paradigm (Kagan and Jackson, 1991; Cohen and Freymeuller, 2004), where past earthquakes determine future earthquakes in terms of longer recurrence intervals equating to greater coseismic subsidence or uplift (Shennan and Barlow, 2008). Further, the patterns of spatial deformation are not uniformed across the seven great earthquakes identified at Girdwood Flats suggesting non-persistent dimensions, location or depth of ruptures between earthquake cycles (Shennan and Barlow, 2008). For example, Kasilof and Kenai exhibit ~0.3 to ~0.5 m subsidence in the AD1964 earthquake whereas between ~6500 and 1500 B.P and the penultimate earthquake between 910-780 B.P. there was no evidence of coseismic deformation, despite multiple earthquakes of similar magnitude recorded at Girdwood Flats (Shennan and Barlow, 2008).

There is extensive research on the spatial variability of prehistoric earthquakes within the rupture of the AD1964 Alaska earthquake to identify if the largest ruptures exhibit persistent boundaries or if larger than observed ruptures are possible, as this could have drastic implications on seismic and tsunami hazard assessment and hazard mapping (Hamilton and Shennan, 2005a; Hutchinson and Crowell, 2007; Shennan *et al.,* 2009; Shennan *et al.,* 2014a; Shennan *et al.,* 2014c; Shennan *et al.,* 2016; Shennan *et al.,* 2018). Key conclusions include that the Prince William Sound and Kenai sections consistently rupture together in great

earthquakes (Shennan *et al.,* 2014a). Contrastingly the Kodiak section only occasionally ruptures at the same time as the Prince William Sound and Kenai sections (two or possibly four of the last seven great earthquakes) (Hutchinson and Crowell, 2007; Shennan *et al.,* 2014a; Shennan *et al.,* 2016), and there is evidence for a rupture area approximately 15% greater than the AD1964 both in 900 B.P. and 1500 B.P., where the Yakutat microplate ruptured simultaneously with the adjacent sections of the Alaska-Aleutian subduction zone that ruptured in AD1964; suggesting that there is a greater hazard potential than the AD1964 earthquake (Figure 2.3) (Shennan *et al.,* 2009). However, due to the error of radiocarbon ages it is possible that independent earthquakes occurred in close temporal proximity rather than larger multi section earthquakes (Shennan *et al.,* 2009; Shennan *et al.,* 2018). Therefore, further research by Shennan *et al.* (2018) led to the conclusions that the AD1964 earthquake exhibited a unique rupture pattern as it was the only earthquake in the last 2000 years to rupture the Kodiak, Kenai and Prince William Sound sections of the Alaska-Aleutian subduction zone and in 850 B.P. and 1500 B.P. the Kodiak section ruptured independently as opposed to the combination of the Kodiak, Kenai, Prince William Sound and the Yakutat microplate as previously proposed by Shennan *et al.* (2009).

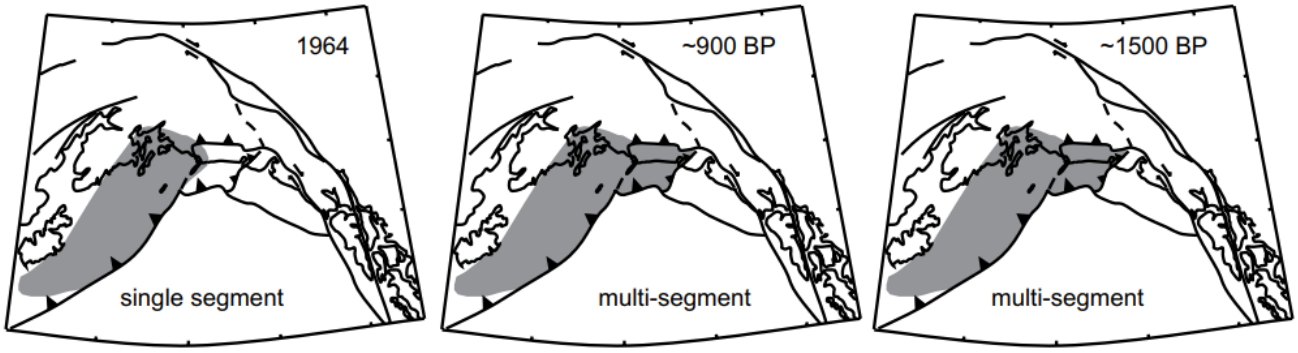

Figure 2.3 Inferred rupture areas of the great earthquakes analysed in the geological record in AD1964, ~900 B.P. and ~1500 B.P. (Shennan et al., 2009). Showing the suggestion of the multi section rupture and combination with Yakutat microplate in ~900 B.P. and ~1500 B.P. (Shennan et al., 2009).

Briggs *et al.* (2014) expanded the research on non-persistent rupture boundaries to Sitkinak Island which lies on the western edge of the AD1964 earthquake and the eastern edge of the AD1938 earthquake, which was assumed to represent a persistent barrier to ruptures from the east (Figure 2.1). Coseismic uplift in three and coseismic subsidence in two of the five great earthquakes recorded on Sitkinak Island demonstrates the non-persistent rupture boundary

near Sitkinak Island, thus, challenging the previous assumption of a persistent rupture boundary for the western boundary of the AD1964 earthquake (Briggs *et al.,* 2014). Palaeoseismic reconstructions along the Alaska-Aleutian subduction zone have challenged the assumption of persistent rupture boundaries which could have led to an underestimation of the seismic potential as witnessed in the 2004 Sumatra-Andaman and the 2011 Tohoku-Oki earthquakes and tsunamis (Shennan and Barlow, 2008; Shennan *et al.,* 2009; Briggs *et al.,* 2014). The identification of spatial and temporal variation between great earthquakes demonstrates the importance of analysing multiple earthquake deformation cycles to best understand the seismic hazard and to produce the most accurate hazard maps possible (Shennan *et al.,* 2014a; Shennan *et al.,* 2018).

Another assumption challenged by palaeoseismic reconstructions along the Alaska-Aleutian subduction zone is that creeping sections of a subduction zone pose a lower seismic hazard than locked sections of the subduction zone (Witter *et al.,* 2016). Witter *et al.* (2016) identify six large tsunamis from the past 1700 years at Stardust Bay, Sedanka Island where geodetic measurements suggest is creeping (Figure 2.1). An at least 18 m runup height of the 1957 Andreanof great earthquake conflicts with the 1957 earthquake slip model (Johnson *et al.,* 1994) suggesting an unrecognised source of tsunami in a creeping section of the Alaska-Aleutian subduction zone (Witter *et al.,* 2016). Further, Witter *et al.* (2019) challenge the assumption that creeping section of the Alaska-Aleutian subduction zone pose a lower seismic hazard compared to locked section by comparing the tsunami history of Driftwood Bay (presently locked) and Stardust Bay (presently creeping). Repeated large tsunami inundation at both Driftwood Bay and Stardust Bay identify similar tsunami hazards, hence, the determination of locking or creeping sections of a subduction zone does not provide insight into the tsunami hazard (Witter *et al.,* 2019). The use of palaeoseismic reconstructions to challenge the assumption of lower seismic hazard along creeping sections of the Alaska-Aleutian subduction zone has enhanced the constraint of seismic hazard along the Alaska-Aleutian subduction zone (Witter *et al.,* 2016; Witter *et al.,* 2019)

Early palaeoseismic reconstructions along the Alaska Aleutian subduction zone focused on reconstructing earthquakes and associated tsunamis in the AD1964 rupture area (e.g., Shennan *et al.,* 1999; Zong *et al.,* 2003; Shennan *et al.,* 2009). However, there has been a recent focus on palaeoseismic reconstructions to advance the understanding of tsunami hazard along other sections of the Alaska-Aleutian subduction zone (e.g., Nelson *et al.,* 2015; Witter

et al., 2016; Janigian, 2018; Witter *et al.,* 2019; Prater, 2021). Nelson *et al.* (2015) conducted the first reconstruction of Aleutian palaeotsunamis throughout the Holocene (over the last 3500 years) on Chirikof Island in the Semidi section of the Alaska-Aleutian subduction zone (Figure 2.1). Understanding palaeotsunami histories are more complex than coseismic land level change due to the inability to set specific criteria for distinguishing between palaeotsunami and palaeostorm deposits and that not all tsunamis coincide with coseismic land level changes as they can be sourced from far field earthquakes and other non-seismic processes such as submarine landslides (Engel and Brückner, 2011).

Nelson *et al.* (2015) determine that the Semidi section of the Alaska-Aleutian subduction zone has a recurrence interval of 180-270 years over the last 3500 years for high tsunamis posing a hazard to the Pacific basin. Witter *et al.* (2016) identify large tsunamis every 300-340 years over the past 1700 years at Stardust Bay, Sedanka Island, near the source of the 1946 and 1957 great earthquakes despite its currently low geodetic coupling (Cross and Freymeuller, 2008). Comparison of the palaeotsunami histories between Stardust Bay (currently creeping) and Driftwood Bay (currently locked) identify that both sites likely recorded five large tsunamis similar to the 1957 tsunamis, and at least twice in the last 1700 years a large tsunami inundated only one but not the other site resulting in the recurrence interval of large eastern Aleutian tsunamis to be reduced to 164-257 years (Witter *et al.,* 2019). Witter *et al.* (2019) determine that the currently creeping section of the Alaska-Aleutian subduction zone at Stardust Bay does not pose a lower tsunami hazard compared to the locked section at Driftwood Bay and demonstrates the importance of palaeoseismic reconstructions at multiple sites to best constrain tsunami hazards and most accurately calculate recurrence intervals of large tsunamis as one site may not encapsulate the entire palaeotsunami history.

A prevailing finding from the Palaeotsunami research along the Alaska-Aleutian subduction zone is that it cannot be assumed that all sand deposits in the geological record represent tsunami deposits (Nelson *et al.,* 2015; Janigian, 2018). For example, Janigian (2018) identified six sand deposits representing potential tsunami deposits from the last 300 years at Old Harbour, Kodiak Island, yet determined only two likely represented tsunami deposits. Diatom assemblages prove to be critical in determining likely tsunami deposits demonstrating that a multi-proxy approach to palaeoseismic reconstructions is essential to best interpret the tsunami deposits in the geological record (Prater, 2021). Despite the complexities of reconstructing palaeotsunamis, especially when they do not coincide with coseismic land level change,

palaeotsunami research along the Alaska-Aleutian subduction zone has enhanced the understanding of tsunami histories and enabled the calculation of palaeotsunami recurrence intervals which are crucial for assessing tsunami hazard and producing hazard maps. However, the spatially fragmented research west of the AD1964 earthquake rupture area limits the understanding of palaeotsunamis along the Alaska-Aleutian subduction zone and thus, needs to be resolved to best determine the tsunami hazard, not only to the local communities but also to the communities in the Pacific basin who are vulnerable to inundation from large tsunamis generated along the Alaska-Aleutian subduction zone (Witter *et al.,* 2019).

2.5 Instrumental and Observational Record of the Shumagin Section of the Alaska-Aleutian Subduction Zone

Understanding the seismic hazard of the Shumagin section of the Alaska-Aleutian subduction zone, which is bounded by the western end of the 1938 and the eastern end of the 1946 great earthquakes, is predominantly reliant upon the instrumental and observational data with only one palaeoseismic reconstruction by Witter *et al.* (2014). Therefore, there is an urgent need to understand the long-term seismicity of the Shumagin section to best constrain the seismic hazard, especially due to conflicting conclusions and uncertainties of the Shumagin section's seismic hazard identified in the current literature (e.g., Davies *et al.,* 1981; Fournier and Freymueller, 2007). Palaeoseismic reconstruction of the Shumagin section will not only enhance the understanding of the independent seismic hazard of the Shumagin section but will also enable a more holistic approach to understanding the seismic hazard from the Alaska-Aleutian subduction zone as a whole by infilling one of the large spatial gaps evident along the Alaska-Aleutian subduction zone (Figure 2.1) (Briggs *et al.,* 2014).

The observational record of earthquakes and tsunamis along the Alaska-Aleutian subduction zone extends to 1784 from written Russian outpost documents followed by records kept by the United States Coast Guard and the United States Geodetic Survey after Alaska was sold to the United States in 1867 (Lander, 1996; Engelhart *et al.,* 2018). However, the observational record has limited reliability as it is temporally and spatially fragmented, thus, it is unlikely to fully represent the seismic history of the Alaska-Aleutian subduction zone (Lander, 1996). There were nine Russian settlements across the Aleutian Islands, including Unga Island in the Shumagin section of the Alaska-Aleutian subduction zone which all kept handwritten first hand records (Lander, 1996).

The spatially fragmented observational records make reconstructing the history of earthquakes and tsunamis along the Alaska-Aleutian subduction zone complicated as the spatial extent of the earthquake ruptures, the earthquake magnitudes and the associated tsunamis cannot be inferred from the spatially distant Russian outpost records (Lander, 1996; Shennan *et al.,* 2014c). Therefore, despite the Russian outpost documents expanding the observational seismic records, their use is limited and reported earthquakes and tsunamis need to be reconciled with palaeoseismic evidence (Witter *et al.,* 2014). The reported 1788 earthquake and tsunami demonstrates the uncertainty associated with the Russian outpost documents (Lander, 1996). Strong ground shaking and high tsunami waves (10-50 m) were reported in Russian outpost documents in 1788 on Three Saints Bay on Kodiak Island, Unga Island and Sanak Island, suggesting a potential 700 km long rupture (Figure 2.4) (Soloviev, 1990; Lander, 1996). Palaeoseismic reconstructions confirm the presence of the 1788 earthquake on Kodiak and Sitkinak Islands identifying a great earthquake rupturing at least 300 km (Briggs *et al.,* 2014; Shennan *et al.,* 2018; Prater, 2021), though there is a lack of geological evidence for the 1788 earthquake in the Shumagin section suggesting that the great earthquake in the Kodiak section in 1788 did not rupture as far as the Shumagin section (Witter *et al.,* 2014; Engelhart *et al.,* 2018). Therefore, it is proposed that two earthquakes occurred sixteen days apart, the first was a great earthquake and a subsequent tsunami on July 22nd, 1788, which ruptured the Kodiak section of the Alaska-Aleutian subduction zone, followed by a second smaller earthquake and tsunami on the 7th of August 1788 between Unga and Sanak Island, though the magnitude and spatial extent is uncertain (Witter *et al.,* 2014; Shennan *et al.,* 2018). The initial belief that the Alaska-Aleutian subduction zone ruptured in a single great earthquake from Kodiak to Sanak Island demonstrates that the spatial scarcity of the Russian outpost documents limits the interpretation of the reported earthquakes and tsunamis highlighting the need for palaeoseismic reconstructions to best understand palaeoseismicity (Davies *et al.,* 1981; Lander, 1996).

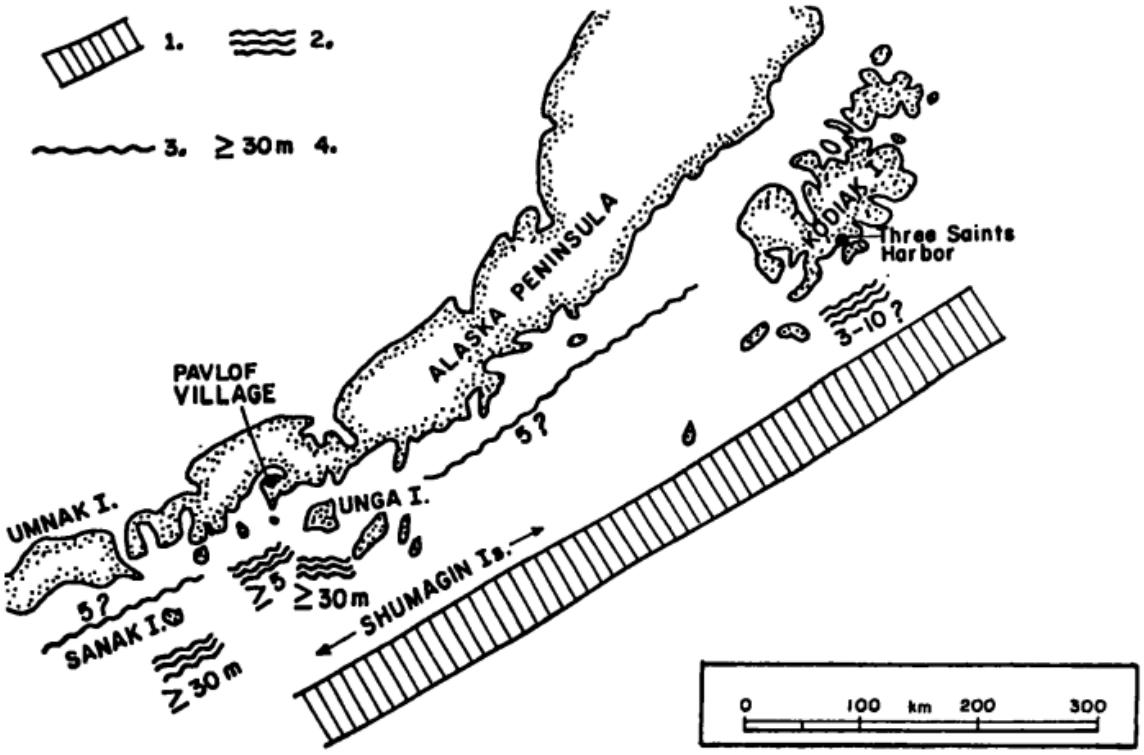

Figure 2.4 Initial interpretations of the 1788 earthquake rupture area and tsunami inundation inferred from Russian out post documents (Lander, 1996). (1) Earthquake ruputre area, (2) observed tsunamis, (3) possible tsunami inundation, (4) approximate tsunami height (m) (Lander, 1996).

Further, the Russian outpost documents are potentially limited due to the conflict between the Russian settlers and the Indigenous populations (Engelhart *et al.,* 2018). The Russian document from Unga Island, translated by Soloviev (1990), states that in 1788 “there was a terrible inundation on Unga Island in which many Aleuts perished but God spared the Russians”. It is possible that the 1788 earthquake was exaggerated to cover up the deaths of indigenous populations and thus, without geological evidence the magnitude of the 1788 earthquake and tsunami cannot be accurately identified from the Russian outpost documents (Engelhart *et al.,* 2018).

Based on the spatial and temporal distribution of the aftershocks of magnitude 7 or greater earthquakes along the Alaska-Aleutian subduction zone between 1920 and 1970, Sykes (1971) first proposed the Shumagin section as a potential site of a near future great

earthquake, speculating that the absence of rupture in the 1938 and 1946 great Alaska-Aleutian earthquakes in adjacent sections leads to a high probability for a great earthquake in the Shumagin section in the near future (McCann *et al.,* 1979). Davies *et al.* (1981) later supported Sykes' (1971) speculation that the Shumagin section is a likely site for a near future great earthquake through a combination of aftershock distribution analysis, historical records from Russian outpost documents, the interaction of plates, and the state of plate stress (Fedotov, 1965; Mogi, 1968). Davies *et al.* (1981) added a timeframe to Sykes' (1971) speculation, concluding that there is a high probability that a great earthquake will rupture the Shumagin section within the following two decades. Both Sykes (1971) and Davies *et al.* (1981) believe that seismicity as opposed to aseismic slip accommodates plate motion in the Shumagin section. The reports of earthquakes and tsunamis in the Russian outpost documents on Unga Island in 1788 and 1847 were interpreted as great earthquakes (M_W >8.0) by Davies *et al.* (1981), hence, the lack of ruptures in the great earthquakes in 1938 and 1946 suggests that there is high strain accumulation in the Shumagin section and the high probability of a great earthquake to accommodate the relatively long-term strain accumulation.

Skyes' (1971) proposal led to the installation of telemetered microearthquake array in 1973 to determine the subduction zone dynamics of the Shumagin section (Reyners and Cole, 1981). Reyners and Cole (1982) analysed 1.5 years of data from the telemetered microearthquake array to analyse the structure and tectonics of the subduction zone in the Shumagin section. The telemetered array suggested that the plate interface at shallower depths is locked, thus, slab pull is overprinting the unbending stresses, consistent with Sykes (1971) and Davies *et al.* (1981) proposal of a high seismic potential for the Shumagin section. However, Reyners and Cole (1982) acknowledge the need for longer term data as well as deep seismic sounding and velocity inversion experiments to fully understand the crustal structure and slab configuration in the Shumagin section to determine its seismic hazard.

Jacob (1984) calculated a 99-30% time dependant conditional probability for a great earthquake in the Shumagin section, equalling the highest of all assessed areas in the United States. The probability estimation was calculated using a list of large (M_W > 7.0) and great earthquakes (M_W > 8.0) since 1788 (Jacob, 1984). Though, like Reyners and Cole (1982), Jacob (1984) noted the potential limitations in their data; the earthquakes recorded prior to 1898 relied on historical intensity and tsunami run up heights, plate-kinetic moment rate and the 'time- predictable' model to estimate the magnitude and spatial distribution of the earthquakes resulting in

uncertainties and potential gaps in the data used to calculate the probability (Shimazaki and Nakata, 1980). Jacob (1984) concluded that longer term data is critical to better estimate the probability estimates for a great earthquake. A common fundamental limitation in the suggestion for a high probability of a great earthquake in the Shumagin section by Sykes (1971), Davies *et al.* (1981), Reyners and Cole (1982), and Jacob (1984) is the lack of long-term data and the reliance on fragmentary, subjective and non-quantifiable historical data from Russian outpost documents limiting the reliability of the conclusions.

Triangulation surveys from continuous line length (EDM) measurements conducted firstly in the eastern section of the Shumagin section (1980-1985) (Savage and Lisowski, 1986), followed by GPS measurements in the western Shumagin section (1993-1998) (Freymeuller and Beavan, 1999) established an absence of significant strain accumulation. The findings of Savage and Lisowski (1986) and Freymueller and Bevan (1999) suggest that the Shumagin section is creeping as opposed to accommodating strain accumulation through seismicity. Further, Freymueller and Beavan (1999) conclude that the Shumagin section independently cannot produce a great earthquake unless there is a temporal variation in the locking of the plate interface in the Shumagin section. The findings of Savage and Lisowski (1986) and Freymueller and Bevan (1999) contradict the earlier conclusions of a high probability for a great earthquake in the Shumagin section (Sykes, 1971; Davies *et al.,* 1981; Reyners and Cole, 1982; Jacob, 1984). Therefore, it is evident that a palaeoseismic reconstruction is critical to understand the long-term seismic history of the Shumagin section and identify if the Shumagin section has exhibited long term creep as the conclusions from of Savage and Lisowski (1986) and Freymueller and Bevan (1999) pose starkly different seismic hazards compared to those from Sykes (1971) and Davies *et al.* (1981).

Longer term GPS velocity surveys of the Shumagin section (1991-2005) identified the eastern Shumagin section as 30% locked and the western Shumagin section as 2% locked; meaning that 70% and 98% of plate movement is accommodated through aseismic slip respectively (Fournier and Freymueller, 2007). Therefore, still agreeing with Freymueller and Beavan (1999), that independently the Shumagin section cannot produce a great earthquake (Mw >8.0). Although Fournier and Freymueller (2007) conclude that the east of the Shumagin section could independently rupture in a large earthquake (Mw 7.0-7.9) due to it being 30% locked. Fournier and Freymeuller (2007) believe that any strain accumulation in the Shumagin section is accommodated through a high density of small to moderate earthquakes

accompanied by a few large earthquakes in the east of the Shumagin section. The longer-term GPS velocity surveys further contradict Sykes' (1971) and Davies' *et al.* (1981) suggestions that the Shumagin section is experiencing high strain accumulation and hence contradicts their suggestion for a high probability for a great earthquake in the following two decades (Fournier and Freymueller, 2007; Freymueller *et al.,* 2008).

The small strain accumulation identified from GPS velocity surveys questions the possibility of a great earthquake in the Shumagin section in 1788, documented by Russian outpost documents (Davies *et al.,* 1981). Fournier and Freymueller's (2007) conclusion that the east of the Shumagin section could rupture independently in a large earthquake could suggest that an independent large earthquake occurred in the east of the Shumagin section in 1788, in close temporal proximity to the great earthquake that ruptured in the Kodiak section, rather than the large multi-section great earthquake initially proposed (Lander, 1996; Shennan *et al.,* 2018). Alternatively, Fournier and Freymueller's (2007) suggestion that the east of the Shumagin section could rupture in a multi-section rupture, such as a Semidi-Shumagin or a Kodiak-Semidi-Shumagin rupture, due to the 30% locking with a rapid transition to 70% locking in the adjacent Semidi section, could support a second great earthquake in 1788 where a great earthquake generated in the Semidi section propagated into the Shumagin section or a single great multi section earthquake occurred in terms of a Kodiak-Semidi-Shumagin rupture. Multi-section ruptures including the Shumagin section pose a considerable seismic and tsunami hazard both locally and transpacifically for far field communities (Fournier and Freymueller, 2007). Therefore, palaeoseismic reconstructions in the east of the Shumagin section are critical to better constrain the 1788 reported earthquake and tsunami in the Shumagin section and to determine if multi-section ruptures have occurred in the past as they considerably increase the seismic hazard of the Shumagin section.

Von Huene *et al.* (2012) aimed to identify geological features of the Shumagin section responsible for the creeping behaviour of the Shumagin section. The geology of the Shumagin section does differ from the adjacent Unimak and Semidi section but a causal mechanism for the creeping behaviour could not be identified (von Huene *et al.,* 2012). Von Huene *et al.* (2012) concluded that there needs to be better palaeoseismic data for the Shumagin section and the adjacent sections of the Alaska-Aleutian subduction zone to understand if there are long term barriers to rupture in the Shumagin section or if the plate interface of the Shumagin section has transitioned between creeping and locking. Further analysis of the geological features of the

Shumagin section by Bécel *et al.* (2017) and von Huene *et al.* (2019) focused on the tsunami potential as there appears to be characteristic structural configurations for sections of subduction zones that are capable of producing tsunamigenic earthquakes. Using multichannel seismic reflection, wide angle reflection and refraction, and bathymetric data, Bécel *et al.* (2017) determined that the Shumagin section displays the characteristic structural features of a subduction zone capable of generating a tsunamigenic earthquake including heterogenous plate interfaces, a small wedge of deformed sediment in the frontal prism and splay faults, despite it creeping.

Von Huene *et al.* (2019) found evidence of a downward dipping crustal scale normal fault system that is similar to the rupture area of the 2011 Tohoku-Oki earthquake, supporting Bécel *et al.* (2017) and establishing that a shallow rupture producing a very large tsunami could be possible in the Shumagin section. Bécel *et al.* (2017) and von Huene *et al.* (2019) propose that the reported 1788 tsunamigenic earthquake in the Shumagin section may have resulted from the lateral propagation of an earthquake from the Semidi section and therefore, argue that the Shumagin section may pose a very large tsunami hazard that is currently underestimated (Bécel *et al.,* 2017). A potential mechanism for the propagation of a great earthquake into a creeping section of a subduction zone, as suggested for the 1788 earthquake and tsunami by Bécel *et al.* (2017) and von Huene *et al.* (2019), is coseismic weakening due to the rapid shear heating of pore fluids (Noda and Lapustra, 2013). The findings of Bécel *et al.* (2017) and von Huene *et al.* (2019) display the urgency of thorough palaeoseismic research in the Shumagin section of the Alaska-Aleutian subduction zone to determine the long-term history of earthquakes and tsunamis; specially to determine if in the past great earthquakes generated in the adjacent Semidi section have propagated into the creeping to weakly coupled Shumagin section as this has major implications for the seismic hazard of the Shumagin section.

Palaeoseismic reconstructions west of the Shumagin section in another area of the subduction zone that is currently creeping identified a history of large tsunamis at Stardust Bay (currently creeping) similar to that of the adjacent locked section at Driftwood Bay (currently locked) (Witter *et al.,* 2016, 2019). The evidence for the repeated propagation of great earthquakes from a locked section (Driftwood Bay) into a creeping section of the Alaska-Aleutian subduction zone (Stardust Bay) resulting in high tsunami inundation suggests that despite it creeping, the Shumagin section could also be prone to earthquake propagation from the adjacent locked Semidi and Unimak sections which would result in high tsunami inundation, especially with the

report of strong ground shaking and tsunamis inundation in 1788 (Davies *et al.,* 1981; Witter *et al.,* 2016, 2019). Therefore, Witter *et al.* (2016, 2019) findings highlight the urgency for detailed palaeoseismic reconstructions in the Shumagin section of the Alaska-Aleutian subduction zone to understand the long-term tsunami history because the tsunami hazard cannot be determined based of its strain accumulation.

2.6 Palaeoseismic Data from the Shumagin Section of the Alaska-Aleutian Subduction Zone

Witter *et al.* (2014) conducted the first palaeoseismic reconstruction in the Shumagin section on Simeonof Island (Figure 2.1) through marine terrace investigations, searching for tsunami deposits and identifying stratigraphic signs of coseismic land level changes. The lack of evidence for coseismic land level changes and tsunami inundation on Simeonof Island during the last ~3400 years suggests an absence of great earthquakes in the Shumagin section and the persistence of long-term creep throughout the late Holocene (Witter *et al.,* 2014). Further, elastic strain stored in the Shumagin section is likely to be sufficiently released through large earthquakes such as those witnessed since 1917 (Witter *et al.,* 2014). The palaeoseismic evidence from Simeonof Island implies that the Shumagin section has not coseismically weakened throughout the late Holocene (Noda and Lapustra, 2013) and thus, suggests an absence of Semidi-Shumagin or Kodiak-Semidi-Shumagin multi-section ruptures (Witter *et al.,* 2014).

The findings of Witter *et al.* (2014) conflict Davies *et al.* (1981) interpretation of the Russian outpost documents which reported strong ground shaking and high tsunami inundation on Unga Island in 1788 and potentially in 1847 as great earthquakes as there is no geological evidence for them on Simeonof Island. The discrepancy between the Russian outpost documents and the geological evidence for the 1788 and 1847 earthquakes and tsunamis could be due to the earthquakes being too small to leave a geological imprint (<0.3m of displacement), thus they were more likely single section large earthquakes (up to 7.9 M_w) rather than a great multi-section earthquake (M_w > 8.0) (Witter *et al.,* 2014). Witter *et al.* (2014) suggest that the evidence from Simeonof Island is consistent with two independent earthquakes in 1788, firstly on the 21st of July 1788 in the Kodiak section followed by an earthquake in the Shumagin section on August 6th 1788. Elastic modelling suggests less than 5m of slip on the megathrust beneath Simeonof Island resulting in vertical deformation less than 0.3m and hence insufficient to imprint the geological evidence (Witter *et al.,* 2014). Witter *et al.* (2014) predict an upper limit of the rupture

scenario to a 125km long M_w 7.7-8.1 rupture. The lack of evidence for coseismic land level change and tsunami inundation from known historical large earthquakes such as the 1993 M_w 6.9 earthquake in the Shumagin section supports the suggestion that the 1788 earthquake as well as other earthquakes in the Shumagin section more generally were at most large earthquakes (up to 7.9 M_w) as opposed to great earthquakes (M_w >8.0) (Beavan, 1994).

An alternative explanation to the discrepancy between the Russian outpost documents and the geological evidence from Simeonof Island is the possibility that the hingeline for the 1788 earthquake was located close to Simeonof Island, thus, a great earthquake would not produce enough deformation to be recorded in the geological evidence on Simeonof Island (Witter *et al.,* 2014). Witter *et al.* (2014) generated megathrust rupture scenarios that produced 0.3m of coseismic uplift or subsidence below Simeonof Island using an elastic model as these scenarios would lack a detectable geological imprint. A scenario where a larger earthquake (M_w > 9.0) with 15m of megathrust slip extending to 40km depth resulted in too little vertical deformation to be identified in the geological record and placed the hingeline near Simeonof Island, suggesting that certain criteria in the 1788 earthquake could have led to a lack of geological evidence on Simeonof Island (Murotani *et al.,* 2013; Witter *et al.,* 2014). Though, with an earthquake magnitude greater than nine, it is expected that there would be geological evidence for a high tsunami which Witter *et al.* (2014) did not find, limiting the argument for the giant Shumagin rupture scenario for the reported 1788 earthquake and tsunami.

Despite critical geological evidence from Witter *et al.* (2014), more palaeoseismic reconstructions from additional sites in the Shumagin section is essential to identify the presence or absence of considerable coseismic land level change that would be expected if the giant Shumagin rupture scenario discussed by Witter *et al.* (2014) occurred in 1788 and to confirm the suggestion of Witter *et al.* (2014) that long term creep has persisted in the Shumagin section of the Alaska-Aleutian subduction zone throughout the late Holocene. Determining long term creep and the lack of great earthquakes over the late Holocene in the Shumagin section has considerable implications for the assessment of seismic and tsunami hazard for the Shumagin section, thus, more study sites within the Shumagin section would better reconstruct its seismic history to best assess its seismic and tsunami hazard. Further, the lack of microfossil evidence from the Shumagin section needs to be resolved because relying on qualitative observations alone rather than robust quantitative reconstructions to assess the seismic hazard of the Shumagin section has the potential to oversee seismic evidence and limits the confidence

of the reconstruction of the seismic history of the Shumagin section and hence its seismic hazard (Hemphill-Haley, 1996; Dura and Hemphill-Haley, 2020).

2.7 Literature Review of Palaeoseismic Reconstruction Methods

2.7.1 Field Site Reconnaissance and Lithostratigraphy

Early palaeoseismic reconstructions focused on lithostratigraphic evidence for coseismic land level changes in terms of identifying distinct and abrupt changes in lithostratigraphy (e.g., Bartsch-Winkler and Schmoll, 1987; Combellick, 1991; Bartsch-Winkler and Schmoll, 1993). The later introduction of microfossil analysis improved palaeoseismic reconstructions as it enabled a multi-proxy approach in the identification of coseismic land level changes, and the transition from qualitative based reconstructions to quantitative based reconstructions (e.g., Atwater, 1992; Nelson, 1992; Hemphill-Haley, 1995). Pioneering microfossil palaeoseismic reconstructions produced errors greater than 0.5m limiting the comparison of magnitudes between different earthquakes (Atwater, 1987; Atwater and Hemphill- Haley, 1997). However, the introduction of transfer functions has reduced the error in land level change calculations enabling better quantification of the magnitude of palaeoseismic earthquakes and improved the comparison between different palaeoearthquakes (Hawkes *et al.,* 2011; Watcham *et al.,* 2013; Engelhart *et al.,* 2013). Transfer functions estimate the rate of coseismic land level change through quantifying the relationship between modern microfossil assemblages and their elevational distributions which is then applied to the assemblages in the geological record to estimate coseismic changes in relative sea level and hence, calculate the magnitude of coseismic land level change (Horton and Sawai, 2010; Dura, 2014).

In terms of lithostratigraphy, coseismic land level changes are identified through peat-mud or mud-peat couplets and tsunamis are identified as sand layers in low energy environments such as salt marshes (Nelson *et al.,* 1996a; Horton and Sawai, 2010). Field site reconnaissance is a critical aspect of palaeoseismic reconstructions because it enables a holistic understanding of the study area to better constrain the seismic history (Long *et al.,* 1999; Shennan *et al.,* 2014a). Further, field site reconnaissance aids the determination of the most appropriate sampling strategy for the detailed laboratory analysis as time and resource constraints limit the number of diatom, grain size and radiocarbon dating samples, hence, producing an effective sampling strategy is critical (Parnell and Gehrels, 2015; Switzer and Pile, 2015; Zong and Sawai, 2015).

X-ray images enable a better representation of the contact sharpness of lithostratigraphic units identified by visual inspection in the field and are better than using photographs which can be problematic due to varying light conditions (Johnson, 2015; Nelson *et al.,* 2015; Witter *et al.,* 2019). The improved visual representation of the lithostratigraphic units through X-ray imaging can further assist the production of an effective sampling strategy for palaeoseismic reconstruction (Parnell and Gehrels, 2015; Switzer and Pile, 2015; Zong and Sawai, 2015).

2.7.2 Diatom Analysis

The introduction of microfossil analysis enabled better understanding of sand beds deposited by tsunamis that accompanied coseismic land level changes in the geological record as well as improving the identification of teletsunami deposits, which do not coincide with coseismic land level changes in the geological record (Dura, 2014). The application of microfossils in the identification of palaeotsunamis focuses on diatom assemblages, in terms of species salinity and substrate preferences, and the preservation of diatoms (Kortekaas and Dawson, 2007; Dura and Hemphill-Haley. 2020). Early research on palaeotsunamis used the geological imprint of known historical tsunamis to identify palaeotsunamis in the geological evidence (e.g., Minoura and Nakeya, 1991; Dawson *et al.,* 1996). However, microfossil analysis of recent large tsunamis such as the 2004 Sumatra- Andaman and the 2011 Tohoku-Oki tsunamis have improved the characterisation of tsunami deposits to better identify palaeotsunamis (Sawai *et al.,* 2009; Sawai et al., 2012).

Lithostratigraphic analysis alone cannot identify coseismic land level changes and tsunami inundation (Dura, 2014). Diatoms are unicellular, photosynthetic algae which live in marine, brackish and freshwater environments (Jones, 2007). Diatom analysis compliments sediment analysis for palaeoseismic reconstructions because diatom species are dependent upon environmental conditions including salinity and substrate (Hemphill-Haley, 1993). Thus, the species abundances vary depending on the environmental conditions (Palmer and Abbott, 1986; van de Plassche, 1986; Hemphill-Haley, 1993). Over time diatoms become incorporated into sediments providing a fossil record of the palaeoenvironmental conditions of the local environment (Witter *et al*., 2003; Pilarczyk *et al.,* 2014). The silicious valves of diatoms are often well preserved due to their resistance to degradation from oxidation and depositional processes making them good proxies for palaeoenvironmental reconstructions (Charles *et al.,* 2002; Zong and Sawai, 2015). Salinity and elevation covary and since diatoms are strongly influenced by

salinity, diatom assemblages are used to infer their elevation during deposition (Patterson *et al.,* 2000; Watcham *et al.,* 2013).

Diatoms are a robust proxy for identifying coseismic land level changes as abrupt changes in diatom assemblages could represent a sudden change in relative sea level associated with coseismic subsidence (relative sea-level rise) or coseismic uplift (relative sea-level fall) (Long and Shennan, 1994; Zong and Sawai, 2015). However, the utility of diatoms for reconstructing palaeoseismicity is dependent upon having sufficient accommodation space to preserve the sediment and microfossil evidence as limited accommodation space can result in the erosion of evidence (Brill *et al.,* 2014; Kelsey *et al.,* 2015). Gradual long term relative sea-level rise promotes sediment preservation as it enables accommodation space for sediment aggradation and minimal erosion (Kirwan *et al.,* 2010; Kirwan and Megonigal, 2013; Dura *et al.,* 2016a).

In Alaska palaeoseismic reconstructions, diatom analyses are more appropriate than foraminifera and pollen analyses because diatoms are more prevalent and diverse compared to foraminifera which are limited in diversity, quantity, and preservation in high latitudes, and diatoms have a higher resolution than pollen data (Shennan *et al.,* 1999; Janigian, 2018).

There are four crucial criteria identified for sediment and microfossil evidence for identifying palaeo coseismic land level changes which distinguish between local processes which could produce a similar record in the sediment and microfossil evidence (Nelson *et al.,* 1996a). Sediment and microfossil evidence for coseismic land level changes exhibit a large lateral extent, abrupt changes, regional synchroneity and considerable vertical motion (Shennan *et al.,* 2014c; Shennan *et al.,* 2016). The presence of a tsunami deposit is additional evidence to support the four crucial criteria for identifying palaeo coseismic land level changes (Shennan and Barlow, 2008).

Using diatom abundances to infer a palaeotsunami deposit in absence of coseismic land level change is more complex than using diatoms to identify palaeo coseismic land level changes due to the high spatial variance in palaeotsunami diatom assemblages, spatial variance in the preservation of diatoms, and the similar sediment record produced from non-tsunami processes (Dawson *et al.,* 1996; Dura *et al.,* 2015). Hence, diatoms alone cannot identify a palaeotsunami deposit, instead they should be used as part of a multi-proxy analysis including sediment type and grain size evidence (Shennan *et al.,* 2014b).

Pilarczyk *et al.* (2014) identify palaeotsunamis as chaotic anomalous sand sheets often dominated by marine diatoms due to tsunamis transporting and depositing scoured marine sediments landward (Tanaka *et al.,* 2012). However, diatom compositions of tsunami deposits are not uniformed both spatially between tsunami deposits and within the tsunami deposit (Chagué-Goff *et al.,* 2011; Dura, 2014). Tsunami deposits often contain marine diatoms as well as brackish and freshwater diatoms due to the erosion, transport and deposition of coastal sediment and associated taxa as the tsunami moves inland (Goff *et al.,* 2001; Goff *et al.,* 2004; Grand Pre *et al.,* 2012). Though, Nelson *et al*. (2015) and Szszucinski *et al.* (2012) identified tsunamis that contained abundant freshwater diatoms with very few brackish diatoms and no marine diatoms due to the entrainment of freshwater diatoms as the tsunami travelled over low dunes and boggy lowlands. The diatom assemblages within a tsunami deposit often change throughout the deposit where the base of the tsunami deposit is usually dominated by beach diatoms, the middle is often dominated by marine diatoms and the surface of the tsunami deposit is usually a mix between freshwater, brackish and marine diatom species due to the reworking of terrestrial diatoms (Dura and Hemphill-Haley, 2020).

Further, poor preservation of diatom valves greater than 40 µm (usually >75%) or an abrupt increase in the percentage of fractured valves greater than 40 µm compared to the underlying and overlying lithostratigraphic units could be indicative of a tsunami deposit because the turbulent waves associated with tsunamis can break diatoms (Kortekaas and Dawson, 2007; Chagué-Goff *et al.,* 2011). For example, Dawson and Smith (2000) identified 90 % diatom fracturing in tsunami deposits. The percentage of fractured diatoms greater than 40µm often increases from the base of a tsunami deposit to the surface due to the longer entrainment in turbulent flows and hence, increases the fracturing of the diatoms deposited in the surface of the tsunami deposit (Gelfenbaum and Jaffe, 2003; Srisutam and Wagner, 2010; Engel and Brückner, 2011). However, some tsunami deposits exhibit low diatom valve breakage such as in palaeotsunamis identified along the Pacific coast in Washington state and the Puget Sound, and in modern diatom assemblages such as in the Phra Thong tsunami deposits because of the rapid entrainment, deposition and sedimentation of diatoms enabling high preservation (Hemphill-Haley, 1996; Dawson, 2007; Sawai *et al.,* 2009; Nelson *et al.,* 2015). Thus, again complicating the identification of palaeotsunami deposits through diatom preservation alone (Sawai *et al.,* 2015).

The substrate in which diatom species live is another analysis to aid the interpretation of a palaeotsunami deposit (Dura *et al.,* 2015). Tsunami deposits often contain anonymously large quantities of marine planktonic species compared to the host peat, thus, a large increase in marine planktonic species compared to the overlying and underlying lithostratigraphic layers alongside anomalous diatom assemblages and high fragmentation (>75 %) could indicate a tsunami deposit (Dominey-Howes *et al.,* 2006; Dura and Hemphill-Haley, 2020). Diatom substrate preferences is a useful analysis tool for reconstructing palaeoseismicity, though it is not as useful as diatom species salinity preferences because not all diatom species have a known substrate preference which limits its use (vos de Wolf, 1988; Dura *et al.,* 2015).

Storm surges, wind deposition, the melt out of aeolian sand covering snow in winter, channel deposits, and debris flows appear as tsunami like sand deposits in the sediment record and thus, to identify a palaeotsunami deposit the other potential processes need to be ruled out (Engel and Brückner, 2011; Nelson *et al.,* 2015). It is important not to assume that all sand deposits identified in the sediment record represent tsunamis (Dura and Hemphill-Haley, 2020). For example, Nelson *et al.* (2015) identified ten silty to sand deposits yet only determined four to be probable tsunamis. Tsunamis and storm deposits are the most difficult to distinguish between as many of the tsunami diatom identification criteria apply to storm deposits (Wise *et al.,* 1981; Switzer and Jones, 2008; Witter *et al.,* 2019). Therefore, diatoms alone cannot identify a palaeotsunami deposit and thus, diatom analysis needs to be complemented with sediment evidence in terms of sharp upper and lower contacts, considerable lateral extent of the sand deposit, uniformed thickness of the sand deposit between different sites, and the landward thinning of sand deposits (Switzer, 2010; Witter *et al.,* 2016). Grain size analysis, discussed below, further complements palaeotsunami identification in terms of upward fining within the sand bed deposits (Sawai *et al.,* 2015).

Stratigraphically constrained cluster analysis is a common technique in palaeoseismic reconstructions as it divides sequences of biostratigraphic data and identifies similarities between adjacent samples from different stratigraphic zones (e.g., Heyworth *et al.,* 1985; Zong *et al.,* 2003; Witter *et al.,* 2009; Dura, 2014). Detrended correspondence analysis is a further statistical method used in palaeoseismic reconstructions to identify diatom samples that exhibit similar and dissimilar assemblages (e.g., Dura, 2014; Janigian, 2018).

2.7.3 Grain Size Analysis

Alone, grain size analysis cannot identify palaeotsunami deposits, but grain size analysis is a useful tool to complement diatom analysis for identifying palaeotsunami deposits (Switzer, 2010). As discussed above, identifying palaeotsunami deposits is complex, especially with the absence of coseismic land level changes, thus, adding grain size analysis into a multi-proxy approach for identifying palaeotsunami is critical for a robust analysis (Nelson *et al.,* 2015). Grain size reflects the hydrodynamics during sediment deposition and since tsunamis exhibit high velocities initially with a decrease in velocities over time, tsunami deposits exhibit an upward fining of grain size reflecting the reduction in depositional energy over time (Dura, 2014). The base of a tsunami deposit contains medium sands compared to very fine sands at the surface of a tsunami deposit (Sawai *et al.,* 2015). Further, tsunami deposits are poorly sorted and often contain anomalously coarse grain sizes compared to the host peat (Van Hengstrum *et al.,* 2011; Janigian, 2018). Therefore, anomalously larger grain sizes which are poorly sorted and fine upwards could indicate a tsunami deposit (Sawai *et al.,* 2015).

2.7.4 Chronology

Core chronology is important in palaeoseismic reconstructions to correlate coseismic land level changes and tsunami inundations between local scale sediment cores from within the same study site, with adjacent study sites, and regionally between sediment cores from further afield study sites (Corbett and Walsh, 2015). Further core chronology enables the calculation of sedimentation rates and earthquake and tsunami recurrence intervals (Shennan, 2015).

AMS radiocarbon dating is a robust and a commonplace method for dating sediment up to 50,000 years old by measuring the abundance of the radioactive carbon isotope, ^{14}C, in plant macrofossils (Scott, 2003; Kemp *et al.,* 2013). Living plants absorb ^{14}C through photosynthesis and once they die, plants stop absorbing ^{14}C and the ^{14}C absorbed prior to death begins to decay (Törnqvist *et al.,* 2015). Since the half-life of ^{14}C is 5700 years (+/- 30 years), the age of a plant macrofossil can be identified and thus, used to infer the age of the surrounding deposited sediment (Coe, 2003). Reliable AMS radiocarbon dating has an upper limit of 50,000 years because the quantity of ^{14}C in plant macrofossils older than 50,000 years is too small to accurately calculate (Kemp *et al.,* 2013).

Further, shallow sediment cannot be accurately dated using AMS radiocarbon dating due to the anthropogenic production of ^{14}C from atomic bomb and nuclear weapons testing, which

results in one sample producing multiple calibrated ages (Briggs *et al.,* 2014). Therefore, caesium dating (^{137}Cs) is required to compliment AMS radiocarbon dating for dating shallow samples (Libby, 1958; Pennington *et al.,* 1973). ^{137}Cs is a radioactive isotope produced from the nuclear fission of uranium-235 and first appeared in the atmosphere in 1952 from anthropogenic nuclear fission reactions (Drexler *et al.,* 2018). Atmospheric^{137}Cs peaked in the atmosphere in 1963, thus, ^{137}Cs can be used as a single event chronomarker as the sedimentary peak in ^{137}Cs concentrations correlates to 1963 (Hardy, 1971).

Tephra deposits can complement AMS radiocarbon and caesium dating in areas that have had volcanic activity (Shennan *et al.,* 2018). Tephrachronology is a useful tool as tephra is deposited across a large area and thus, provide a temporal marker across multiple sediment cores (Alloway *et al.,* 2007). Tephra deposits can be used to correlate ages between sediment cores or in between dateable layers within cores both relatively or absolutely if dated. Since there is a limit on the number of radiocarbon dating samples from sediment cores, tephrochronology can complement radiocarbon dating and caesium dating to understand the chronology of a sediment core (Parnell and Gehrels, 2015; Alloway *et al.,* 2007).

AMS radiocarbon dating is sensitive to error; thus, it requires the careful selection of the most appropriate datable material in the sample that is representative of the depositional environment (Nilsson *et al.,* 2001; Kemp *et al.,* 2013). Terrestrial plant macrofossils are preferred for radiocarbon dating to avoid the added complication and error associated with the marine reservoir effect for dating marine sample (Törnqvist *et al.,* 1992; Dura, 2014). It is important that the selected terrestrial plant macrofossils are delicate, so it is known that they lived either shortly before or grew directly after the sediment deposition or that the plant macrofossils are in growth positions (Nelson, 1992; Dura *et al.,* 2017). The most accurate material for AMS radiocarbon dating in Alaska includes in situ plant macrofossils such as rhizomes, carex seeds, twigs, and woody debris (Kemp *et al.,* 2013; Dura *et al.,* 2017).

3.0 Study Location, Tectonic Setting and Seismic History of Nagai Island

3.1 Study Location

This research focuses on Nagai Island which is in the Shumagin section of the Alaska-Aleutian subduction zone (Figure 3.1). The Shumagin section is located in the eastern Aleutian arc and is approximately 200 km between Sanak Island to just east of the Shumagin Islands (Figure 3.1) (López and Okal, 2006; von Huene *et al.,* 2019).

The Shumagin section has not ruptured in a great earthquake throughout the instrumental and observational record (M_w >8.0), though non persistent rupture boundaries and Russian outpost documents reporting strong ground shaking and high tsunami inundation in the Shumagin Islands in 1788 suggests that a great earthquake in the Shumagin section cannot be ruled out (Sykes, 1971; Davies *et al.,* 1981; Witter *et al*., 2014; Briggs *et al*. 2014; Wood *et al*., 2021) (Figure 1.1). Further, Lui *et al.* (2021) argue that the 2021 great Chignik earthquake (M_w 8.2) ruptured into the eastern Shumagin section as opposed to just the Semidi section. Therefore, it is possible that a great earthquake ruptured into the Shumagin section in 2021 (Lui *et al.,* 2021).

The Shumagin section is the focus of this research because if the Shumagin section ruptured in a great earthquake (M_w >8.0), it has the potential to cause tsunamis that could make landfall on the Pacific west coast of Canada and the US, and in Hawaii (Cross and Freymueller, 2008; Ryan *et al.,* 2012; Witter *et al.,* 2016). Therefore, it is critical to assess the seismic and tsunamigenic hazard of the Shumagin section to produce effective mitigation strategies to the large populations vulnerable to Shumagin section sourced tsunamis (Butler *et al.,* 2014).

Nagai Island is one of the largest Shumagin Islands (50 km long) located in the east of the Shumagin section (Figure 3.1). The country rock of Nagai Island is composed of the Lower Cretaceous Shumagin Formation (Wilson *et al.,* 1995; Roe *et al.,* 2013). Nagai island is an uninhabited island and was selected to supplement the palaeoseismic data retrieved from Simeonof Island due to the proximity to the Alaska-Aleutian trench (Witter *et al.,* 2014). Further, Nagai Island is located within the 30 % locked area of the Shumagin section adjacent to the 70% locked Semidi section, thus, enabling an investigation into the potential of multi- section ruptures propagating into the Shumagin section (Figure 3.1) (Nada and Lapustra, 2013).

On Nagai Island, four study sites including Deranged Valley, Larsen Lake Marsh, Bog's Bog and Peter's Marsh were selected as low energy depositional environments that are likely to best preserve palaeoseismic evidence (Figure 3.1) (Shennan *et al.,* 2016). Deranged Valley is a tidal flat, Larsen Lake Marsh is a freshwater marsh forming within a lake, Bog's Bog is a freshwater marsh and Peter's Marsh is a saltwater marsh (Figure 3.1).

The research focuses on the Deranged Valley and Larsen Lake Marsh sites as these are trench facing so are likely to record tsunami inundation and had cores that contained relatively long section of peat, critical for identifying palaeoseismic evidence (Nelson *et al.,* 1996; Shennan *et al.,* 2016; Witter *et al.,* 2019). Bog's Bog and Peter's Marsh were used as secondary study sites as they are not trench facing so their palaeoseismic record may be incomplete (Witter *et al.,* 2019). Deranged Valley is a sand dominated environment, evident by the prevalence of sand in the exploratory cores.

On nearby Simeonof Island, Witter *et al.* (2014) identify evidence that suggests slow relative sea-level rise (<0.2 m/ka) over at least the last ~3400 years from the analysis of deposits in cores and bluff exposures. The slow relative sea-level rise over at least the last ~3400 years in the Shumagin section of the Alaska-Aleutian subduction zone is conducive to the preservation of palaeoseismic evidence due to the availability of accommodation space which promotes sediment preservation, critical for representative palaeoseismic reconstructions (Figure 2.1) (Kirwan *et al*., 2010; Kirwan and Megonigal, 2013; Kelsey *et al*., 2015 Dura *et al*., 2016a).

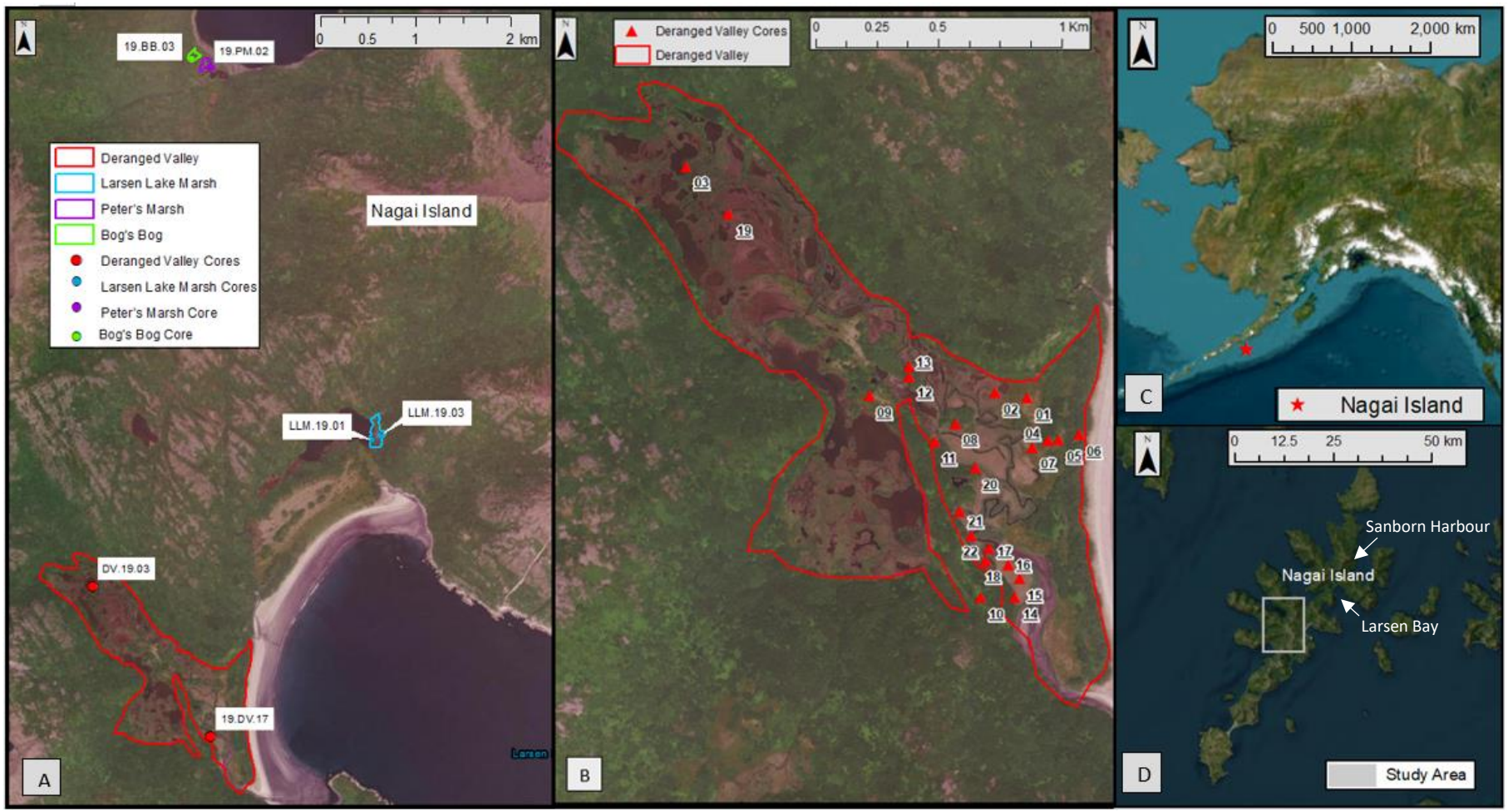

Figure 3.1 Location map. A is the location of the six cores retrieved from the Deranged Valley, Larsen Lake Marsh, Bog's Bog and Peter's Marsh sites on Nagai Island that represent the broader Nagai Island lithostratigraphy. B is the location of the exploratory cores from the Deranged Valley which were used to develop a holistic understanding of the lithostratigraphy of Deranged Valley, which is the focused study site on Nagai Island. C locates Nagai Island within the Alaska-Aleutian arc. D locates the study area on Nagai Island.

3.2 Tectonic Setting and Seismic History of Nagai Island

The Alaska-Aleutian subduction zone is approximately 4000 km long from Kamchatka in the west to south central Alaska to the east and occurs at the convergence of the Pacific and North American plate (Figure 1.1) (Nishenko and Jacob, 1990; Nelson *et al.,* 2015). The Alaska-Aleutian subduction zone is split into twelve sections based on the history of great earthquakes, though defining a rupture area to a confined section is limited as rupture extent varies spatially through time and across defined sections (Lander, 1996; Briggs *et al.,* 2014).

The rate of Pacific plate subduction beneath the North American plate along the Alaska-Aleutian subduction zone ranges from 53 mm to 78 mm a year with a normal convergence direction to the arc and perpendicular radiated tsunami propagation (Figure 1.1) (Reyners and Coles, 1982; Brown *et al.,* 2013; von Huene *et al.,* 2019). The Shumagin section is located between the Unimak section to the west and the Semidi section to the east and exhibits 63 mm of subduction a year (Figure 1.1) (Calver and Plafker, 2008; von Huene *et al.,* 2012; von Huene *et al.,* 2019). Strain accumulation has been measured in the Shumagin section since 1980 using an extensive network of biennial surveys of trilateration (Savage *et al.,* 1986). Three component GPS velocities in the Shumagin section between 1991 and 2005 identify the west of the Shumagin section as 2 % locked, the east of the Shumagin section as 30 % locked, and the adjacent Semidi section to the east of the Shumagin section as 70% locked to a 95 % confidence level (Figure 1.1b) (Fournier and Freymueller, 2007; Cross and Freymueller, 2008). The percentage of plate locking refers to the rate of slip compared to the rate of plate movement, for example, 70 % locked means that the slip is 30 % of the accumulated rate of plate movement (Fournier and Freymeuller, 2007). Therefore, it is concluded that the Shumagin section accommodates plate movement through creeping (freely slipping at rates similar to plate movement) resulting in more frequent smaller magnitude earthquakes rather than long term strain accumulation when the rate of plate movement greatly exceeds the rate of slip which results in more infrequent larger earthquakes (Burgmann *et al*., 2000; Fournier and Freymueller, 2007; Chlieh *et al.,* 2008; Perfettini *et al*., 2010).

The east of the Shumagin section exhibits greater locking (30 %) compared to the west of the Shumagin section so it has the potential to produce moderate to large earthquakes (up to 7.9 M_w) but there is not enough locking in the east of the Shumagin section to generate great earthquakes (Fournier and Freymeuller, 2007). The adjacent Semidi section is 70 % locked so

it accommodates plate movement through long term strain accumulation that is released through earthquakes, resulting in a history of great earthquakes generated in the Semidi section (1938 and 2021) (Figure 1.1). Witter *et al.* (2014) conclude that lithostratigraphic evidence from Simeonof Island suggests long term persistent creep in the Shumagin section over the last ~3400 years.

Despite a relatively short instrumental period for the Shumagin section of the Alaska-Aleutian subduction zone (1980 onwards), the observational record extends to 1784 from Russian outpost documents from Unga Island (approximately 25 km from Nagai Island and 60km from Simeonof Island), though the Russian outpost documents are temporally and spatially fragmented so likely represent an incomplete palaeoseismic record (Davies *et al.,* 1981).

No great earthquakes have ruptured the Shumagin section of the Alaska-Aleutian subduction zone since at least 1917 (Figure 1.1) (Jaing *et al.,* 2022). Davies *et al.* (1981) infer from the Russian outpost documents that three great earthquakes occurred in the Shumagin section in 1788, 1847 and 1903, and an associated tsunami inundation in 1788 of more than 30m occurred on Unga Island in the Shumagin section of the Alaska-Aleutian subduction zone. Though, since the earthquake identifications were based of spatially fragmented observational records, the magnitudes of the 1788, 1847 and 1903 earthquakes in the Shumagin section remain uncertain (Table 3.1) (Estabrook *et al.,* 1994; Witter *et al.,* 2014).

Since 1917 the Shumagin section has exhibited a high density of moderate earthquakes (<6.9 Mw) and five large earthquakes (6.9-7.9 M_w); a 7.4 M_w on May 31st 1917, a 7.2 M_w on May 14th 1948, a 6.9 M_w on May13th 1993, and an earthquake doublet in 2020 with a 7.8 M_w on July 22nd, 2020, and a 7.6 M_w on October 19th 2020 (Table 3.1) (Estabrook and Boyd, 1992; Nelson *et al.,* 2015; Bufe *et al.,* 1994; Crowell and Melgar, 2020; Jaing *et al.,* 2022). No considerable tsunami accompanied the five large earthquakes that occurred since 1917 (Table 3.1) (Lander, 1996; Jaing *et al.,* 2022). A small earthquake and an accompanying six-meter tsunami on Unga Island is reported in 1868, though it is unclear in the report what the six meters refers to in terms of tsunami wave height or the height of the tsunami runup which produce greatly different tsunami magnitudes (Davis, 1912; Lander, 1996).

The seismic history of the Shumagin section differs considerably to the neighbouring 70 % locked Semidi section, which since 1917 has exhibited two great earthquakes, one in 1938 (8.2 M_w) and the other in 2021 (8.2 M_w), as well as additional large earthquakes and much fewer

smaller to moderate earthquakes compared to the Shumagin section (Fournier and Freymueller, 2007).

Teletsunamis originating from other sections of the Alaska-Aleutian subduction zone are recorded four times in the Shumagin section since 1784 including in 1938 (<0.1 m tsunami from the 8.2 M_w great earthquake in the adjacent Semidi section), 1946 (0.8 m tsunami from the 8.6 M_w great earthquake in the adjacent Unimak section), 1986 (<0.1 m tsunami from the 7.7 M_w Andreanof Island earthquake), and in 1996 (<0.1 m tsunami from the 7.9 M_w Adak earthquake), all of which were small tsunami inundations and too small to leave an identifiable geological imprint in the Shumagin Section (Lander, 1996).

Further, since 1784, the Shumagin section has not been greatly impacted by teletsunamis originating from earthquakes outside of the Alaska-Aleutian subduction zone (Lander, 1996). Two teletsunamis are recorded, one in 1985 (<0.1 m tsunami from the 8.0 M_w Algarroba earthquake in Chile) and one in 1995 (0.1 m tsunami from the 8.0 M_w Antofagasta earthquake in Chile), though, again, both were small tsunamis that were too small to leave an identifiable geological imprint in the Shumagin Section (Lander, 1996).

Stratigraphic evidence from Witter *et al.* (2014) suggests that throughout the last ~3400 years no earthquake originating in the Shumagin section has had the capability to produce a potentially destructive teletsunami that could propagate to Hawaii and the Pacific west coast of the USA and Canada.

Table 3.1. Large earthquakes and associated tsunami inundations in the Shumagin section of the Alaska-Aleutian subduction zone since 1784.

Date	Shumagin section earthquake?	Tsunami inundation in Shumagin section?	Location	References
July 21st 1788	Yes → uncertain magnitude	Not on Unga Island in the Shumagin section	Kodiak Island to Unga Island	Lander, 1996 ; Witter *et al.,* 2014
August 6th 1788	Yes → uncertain magnitude	Yes, reported as >30m on Unga Island in the Shumagin section	Unga Island to Sanak Island	Boyd *et al.,* 1988 ; Davies *et al.,* 1981 ; Soloviev, 1990 ; Lander, 1996
1847	Yes → uncertain magnitude	Uncertain	Semidi Island to Unga Island	Boyd *et al.,* 1988 ; Davies *et al.,* 1981
1903	Yes → uncertain magnitude	Uncertain	Uncertain	Savage *et al.,* 1986 ; Davies *et al.,* 1981
May 31st 1917	Yes → 7.4M_w	Minor Tsunami	Shumagin Islands to the western extent of the 1938 great earthquake	Estabrook and Boyd, 1992
May 14th 1948	Yes → 7.2 M_w	Minor Tsunami	King Cove to Shumagin Islands	Estabrook and Boyd, 1992; Lander, 1996
May 13th 1993	Yes → 6.9 M_w	Minor Tsunami	Shumagin Islands to the western extent of the 1938 great earthquake	Bufe *et al.,* 1994 ; Abers *et al.,* 1995
July 22nd 2020	Yes → 7.8 M_w	Minor Tsunami (24 cm)	Shumagin Islands to the western extent of the 1938 great earthquake	ASHSC, 2020; Crowell and Melgar 2020; Jaing et al., 2022; Ye *et al.,* 2021
October 19th 2020	Yes → 7.6 M_w	Minor Tsunami (1.3 m)	Western edge of the July 22nd, 2020, coseismic slip area	Crowell and Melgar 2020; Jaing et al., 2022; Ye *et al.,* 2021

4.0 Methodology

In order to investigate the long-term history of great earthquakes and high tsunamis, the observational and historical records need to be extended through palaeoseismic reconstructions, including lithostratigraphy, diatom, grain size and chronological analysis (Atwater, 1987; Satake and Atwater, 2007).

4.1 Field Site Reconnaissance

During the summer of 2019, a group of Alaskan sea-level researchers conducted a lithostratigraphic exploration through sediment coring, hand dug pits and photography at four study sites on Nagai Island. The study sites included a tidal flat (Deranged Valley), a freshwater marsh forming in a lake (Larsen Lake Marsh), a freshwater marsh (Bog's Bog) and a saltwater marsh (Peter's Marsh) up to a maximum core depth of 330cm (Figure 3.1).

The lithostratigraphic exploration of Nagai Island occurred above the mean tide level up to the reach of high tsunamis and included the analysis of 71 sediment cores and hand dug pits across the four study sites on Nagai Island (Figure 3.1). The samples ranged from 6 m to 21 m above the mean tide level. A high tsunami is defined as reaching greater than the present-day intertidal zone (Grant, 2002). The mean tide level was measured using two water loggers, one at Larsen Bay and the other at Sanborn Harbor (Figure 3.1d). The locations and elevations of the cores were identified using GPS (Janigian, 2018). A one meter long, 10cm diameter Russian sediment corer was used as it is less likely to compact the sediment or result in contamination compared to other coring techniques (Franzén and Ljung, 2009; Zong and Sawai, 2015). The sediment cores were collected with 10 cm overlapping to ensure a full recovery of the cores (Zong and Sawai, 2015), were photographed, and their lithology was described in the field using the semi objective Troels-Smith (1955) classification as standard practice in palaeoseismicity to enable the comparison of data from other research (Tooley, 1978; Dura, 2014). It is important to record the lithostratigraphy in the field prior to transport to the laboratory as the sediment is fresh and undisturbed (Frew, 2014).

In the field, identified sand deposits were analysed in terms of the sharpness of the upper and lower contacts, the lateral extent, the uniformity of the sand thickness between different cores and the landward thinning (Atwater and Hemphill-Haley, 1996; Switzer, 2010; Witter *et al.,* 2016).

The DV.19.03 and 19.DV.17 cores were chosen for detailed laboratory analysis as they were representative of the lithostratigraphy identified in the 71 sediment cores and hand dug pits from the lithostratigraphic exploration of Nagai Island and they both contained three sand bed deposits which could represent tsunami deposits (Figure 3.1). Alongside the two cores from Deranged Valley, two cores from Larsen Lake Marsh (LLM.19.01 and LLM.19.03), one core from Peter's Marsh (19.PM.02) and one core from Bog's Bog (19.BB.03) were identified for further laboratory analysis as these contained long sections of peat suitable for palaeoseismic analysis and were representative of the lithostratigraphy identified in the 71 exploratory cores and hand dug pits (Figure. 3.1). The selected cores were transferred into PVC tubes and wrapped in plastic for protection, labelled and then transported to a laboratory where they are stored at 4 °C to maximize preservation (Kemp *et al.,* 2013; Janigian, 2018). Further, the selected cores were duplicated in case of damage and to ensure enough sediment for a detailed, multifaceted analysis (Dura and Hemphill-Haley, 2020).

4.2 Laboratory Lithostratigraphy

In the laboratory, the sediment cores were cleaned in case of contamination and oxidation during storage (Dura, 2014; Corbett and Walsh, 2015). The cores were cleaned using a scalpel, scraping away the surface layer perpendicular to the depth and wiping the scalpel before each scrape to avoid contamination between different depths of the core (Dura, 2014). The six sediment cores selected from the lithostratigraphic exploration were redescribed in the laboratory due to the potential for error in the field lithostratigraphy from inconsistent light conditions. The six selected cores then had 2-D X-ray images taken using the Geotek ThermoKevex-Variain-2520DX Ethernet camera, except for the LLM.19.01 core due to its storage in another location. The 2-D X-ray images were analysed using ImageJ software in terms of brightness and contrast to enhance the visual features and were used to produce a sampling strategy for the diatom, grain size and chronology analysis (Orzech *et al.,* 2001; Parnell and Gehrels, 2015; Switzer and Pile, 2015; Zong and Sawai, 2015).

4.3 Diatom Analysis

The lithostratigraphic analysis did not identify any obvious evidence for coseismic land level changes throughout any of the cores retrieved from Nagai Island, thus, unlike other palaeoseismic reconstructions using diatoms, a focused sampling strategy around identified land level changes was not possible (Dura, 2014; Janigian, 2018; Prater, 2021). The lithostratigraphy did however identify six sand beds across DV.19.03 and 19.DV.17 which

could be potential tsunami deposits. Therefore, DV.19.03 and 19.DV.17 were selected to focus the laboratory analysis with the DV.19.03 core as the primary focus due to it being longer than 19.DV.17 and containing large sections of peat which is indicative of a low energy depositional environment suitable for palaeoseismic reconstructions (Pilarczyk *et al.,* 2014; Kelsey *et al.,* 2015)

Initially, 22 subsamples from above, within and below the three identified sand beds from DV.19.03 were prepped for diatom and grain size analysis. Care was taken to avoid vertical contamination through smearing and the cross contamination of equipment during subsampling (Chnat and Conett, 1991; Shennan *et al.,* 2014a). At the identified lithological contacts which the lithostratigraphic analysis identified as possible tsunami deposits, high resolution subsamples were taken at 1cm intervals as standard practice for palaeoseismic diatom analysis (Dura and Hemphill-Haley, 2020). A further 13 subsamples at a lower resolution (every 10cm) from DV.19.03 were prepped for diatom and grain size analysis from the surface of the core to 120 cm where no notable lithostratigraphy was identified (Dura, 2014). The modern sample at 0.5 cm is critical to enable comparison with the palaeo subsamples (Zong *et al.,* 2003; Watcham *et al.,* 2013). The first 35 samples were prepped and initially analysed to direct further sampling.

To analyse diatom species abundances, microscope slides were prepared following the standard methods outlined by Dura and Hemphill-Haley (2020). Approximately 0.5 g of wet sediment for each identified sampling location was transferred into a 50ml centrifuge tube and clearly labelled to identify each sample. In a fume cupboard for safety, the organic matter from the samples was digested through dissolution (Charles *et al.,* 2002). Initially 10 ml of 20 % hydrogen peroxide was added to the samples until the reactions were stable to avoid vigorous reactions overtopping the centrifuge tubes resulting in the cross contamination between samples and the subsequent loss of samples (Dura, 2014). Once the reactions were deemed stable, a further 10 ml of 20 % hydrogen peroxide was added to the samples and placed in a water bath for two hours at 60 °C to catalyze the organic matter digestion and covered in foil to prevent the hydrogen peroxide from evaporating (Dura and Hemphill-Haley, 2020). If the organic matter did not fully dissolve in the water bath after two hours, then a further 20 ml of 20 % hydrogen peroxide was added to the centrifuge tubes and they were placed back in the water bath until full organic matter digestion was completed. Once the samples had complete organic matter digestion, the samples were centrifuged at 3700 rpm for five minutes followed by the decanting of the supernatant liquid (Charles *et al.,* 2002). Then the samples were topped up to 20 ml with deionized water

(Charles *et al.,* 2002). The centrifuging, decanting of the supernatant liquid, and the top up to 20 ml with deionized water was repeated four times, where during the last repetition a few drops of deionized water was added back to the sample to enable an appropriate concentration of diatoms to drip onto the microscope slides (Dura and Hemphill-Haley, 2020).

After five rounds of centrifuging, the samples were ready to be mounted onto the microscope slides (Zong and Sawai, 2015). Each sample was first stirred to ensure the settling of the sand and then using a 1ml pipette, ten drops of deionized water was added to a cover slip followed by five drops of the sample (Charles *et al.,* 2002). The cover slip was then placed onto a hot plate using forceps until the deionized water had fully evaporated (Dura and Hemphill- Haley, 2020). Meanwhile, three drops of Naphrax were added to a microscope slide and once the deionized water had evaporated the coverslip was placed onto the microscope slide with the dried sample faced down and returned to the hotplate for three seconds until the Naphrax began to boil (Palmer and Abbott, 1986). Forceps were used to remove any air bubbles and the microscope slide was clearly labelled to identity the sample (Zong *et al.,* 2010; Dura and Hemphill-Haley, 2020). Once all microscope slides had been mounted, the diatoms could be analysed under the microscope.

The diatoms were analysed using a Leica DM500 light microscope and split into two parts following the standard method outlined by Dura and Hemphill-Haley (2020). The first part of the diatom analysis was conducted at 400x magnification (low magnification), where the microscope slide was scanned to gauge a general idea of the diatom assemblage to make sure the detailed count is representative of the entire slide and to ensure a reasonable diatom abundance and spread across the microscope slide (Dura and Hemphill-Haley, 2020). If the diatom concentration was too sparse or too concentrated another microscope slide was produced increasing or decreasing the number of drops of the sample respectively (Janigian, 2018). Under the 400x magnification at least 100 pennate diatom valves larger than 40 µm were counted as either fractured or unfractured to calculate the percentage of fractured diatoms in each sample (Witter *et al.,* 2009).

After the first scan of the microscope slide, diatoms valves were counted for each sample depth at 1000x magnification (high magnification) with oil immersion to improve the clarity (Dura, 2014). For each sample, at least 300 diatom valves were counted and identified to enable a statistically representative count and for a diatom valve to be counted, centric valves had to be at least half intact and pennate valves had to have at least one complete axis and central area intact to ensure a correct identification (Dura and Hemphill-Haley,

2020). The diatoms were counted by first marking the starting point of the count and then following a transect across until 300 diatoms valves were counted and identified (Charles *et al.,* 2002). If the end of the microscope slide was reached before 300 diatoms were counted, then the microscope was moved one field of view downwards and a new transect began (Dura *et al.,* 2017; Dura *et al.,* 2016b). Diatom valves were only included in the count if more than 50 % of the valve was in the field of view (Charles *et al.,* 2002). Each diatom species identified was photographed using the GXMHICHROME-S camera and measured using the measuring tool and a 1 mm eyepiece graticule for calibration to aid the species identification (Dura, 2014; Spaulding, 2022).

After the diatoms in the initial 35 samples from DV.19.03 were counted and identified, a further 15 diatom samples from throughout DV.19.03 were prepared at depths where notable changes in the percentage of marine, brackish and freshwater diatoms occurred. 22 samples were prepped from the 19.DV.17 core from within the three identified sand beds, the over and underlying units and a surface sample. In total 72 diatom samples from DV.19.03 and 19.DV.17 were prepared, and 23688 diatoms were counted and identified.

Diatoms were identified to species level using their shape, size and unique aspects of their valves (Round *et al.,* 2007), with reference to Krammer and Langer-Bertalot (1986, 1991a, b), vos de Wolf (1988,1993), Patrick and Reimer (1966, 1975), Watcham *et al.* (2013), and Spaulding *et al.* (2021).

The diatom species were classified by their salinity preferences (Table 4.1) and substrate (Table 4.2) to qualitatively infer the depositional environment of the lithostratigraphic units (Hamilton *et al.,* 2005; Judd *et al.,* 2017). Species salinity and substrate preferences were identified in reference to Krammer and Langer-Bertalot (1986, 1991), vos de Wolf (1988,1993), Patrick and Reimer (1966, 1975), Watcham *et al.* (2013), and Spaulding *et al.* (2021).

Marine diatoms include species that are polyhalobous, living in salt concentrations greater than 30 practical salinity units (psu), brackish diatoms include species that are mesohalobous which live in salt concentrations between 0.2 and 30 psu and oligohalobous-halophile species which live in salt concentration of 0.2 psu, and freshwater diatoms include species that are oligohalobous-indifferent which live in salt conditions less than 0.2 psu and halophobous species which live in salt concentrations of 0 psu (Table 4.1) (Zong *et al.,* 2003; Dawson, 2019). The percentages of marine, brackish and freshwater diatoms for each sample were calculated (Prater, 2021).

Table 4.1 Diatom halobian classification (Hamilton et al., 2005).

Salinity	Salinity Range (psu)	Environment	Classification
Halophobous	0	Freshwater marsh	Salt-intolerant
Oligohalobous-Indifferent	<0.2	Freshwater-Saltwater Marsh	Freshwater- low salinity tolerated
Oligohalobous-Halophile	0.2	Saltwater Marsh	Brackish-low salinity
Mesohalobous	0.2-30	Brackish-Tidal Flat	Brackish- moderate salinity
Polyhalobous	>30	Marine- Tidal Flat	Marine- high salinity
Euryhaline	N/A	Range of Environments	N/A

Planktonic species float freely in the water column, tychoplanktonic species are predominantly found in the benthos, though can also be found in the plankton; benthic diatoms are diatoms which live at the bottom of a body of water including epipelic diatoms which live attached to mud, epiphytic diatoms live attached to plants, aerophilic diatoms live on wet sediment though can tolerate short term air exposure, periphytic diatoms live attached to underwater plants and epipsammic diatoms live attached to sand grains (Table 4.2) (Palmer and Abbott, 1986; vos de Wolf, 1993; Dura, 2014).

Table 4.2 Diatom substrate classification (Palmer and Abbott, 1986; vos de Wolf, 1993; Dura, 2014).

Substrate Classification	Description
Planktonic	Live in the water column
Tychoplanktonic	Predominantly benthos species but can be found in the plankton
Benthic- Epipelic	Live attached to mud (sediments, clay and silt)
Benthic- Epiphytic	Live attached to plants
Benthic- Aerophilic	Live on wet sediment though can tolerate air exposure
Benthic- Periphytic	Live on underwater plants
Benthic- Epipsammic	Live on sand grains

Diatom species are presented as percentages of the total diatom counts and only species that exceed 1.5 % of the total sample abundance are included in the statistical analysis and ecological summaries to ensure that there is enough balance between representing enough diatom species from the sample whilst minimizing the influence from statistically insignificant diatom species (Birks, 1995; Shennan *et al.,* 1999; Prater, 2021).

4.4 Diatom Statistical Analysis

Stratigraphically constrained cluster analysis by the method of incremental sum of squares (CONISS) using the Tilia 2.6.1 package was used to quantitively define stratigraphic zones

based on diatom assemblages within DV.19.03 and 19.DV.17 (Grimm, 1986). CONISS is a FORTAN 77 program and only merges stratigraphically adjacent samples into clusters (Grimm, 1986). The horizontal axis represents the dissimilarity between the calculated clusters and the vertical axis represent the inputted samples (Dura, 2014). The closer the clusters are in the horizontal axis the more similar their diatom assemblages are (Grimm, 1986). Large dissimilarities between peat-mud couplets or sand deposits and the host peat could indicate coseismic land level change or a tsunami deposit, whereas considerable mixing between potential coseismic land level changes and tsunami deposits identified in the lithostratigraphy suggests non abrupt changes in the biostratigraphy and hence, does not support coseismic land level change or a tsunami deposit (Dura, 2014).

Further, DCA using the multivariate statistical package MVSP 3.22 was used to identify differences between and within identified lithostratigraphic layers in DV.19.03 and 19.DV.17 (Horton and Edwards, 2006; KCS, 2007). Diatom samples that exhibit similar assemblages group together on the DCA biplot whereas diatom samples that exhibit different assemblages plot apart on the biplot (Birks, 1992).

4.5 Grain Size Analysis

Since grain size is a useful tool in identifying palaeotsunami deposits, high resolution grain size samples (every 1 cm) were taken above, within and below the identified sand beds from both the DV.19.03 and 19.DV.17 cores as standard practice (Dura and Hemphill-Haley, 2020). 67 grain size samples across DV.19.03 and 19.DV.17 were taken with 25 high resolution samples obtained from the sand beds and the overlying and underlying lithostratigraphic units from DV.19.03. A further 16 low resolution grain size samples were obtained between 0.5 cm and 120 cm in DV.19.03, where no sand bed deposits were identified. 25 high resolution grain size samples from above, within and below the identified sand beds from 19.DV.17 were sampled with a further sample from the surface of the core for comparison, corresponding to the depths of the diatom samples within 19.DV.17.

The grain size analysis was carried out using standard methods outlined by Dura and Hemphill-Haley (2020). Approximately 1 g of wet sediment was subsampled from each desired sampling depth and placed into a 50 ml centrifuge tube (Shennan, 2015). Initially 0.5 g of wet sediment was subsampled but the obscuration levels were too low to analyse when the samples were added to the laser diffraction analyzer, so the samples were reprepared with a greater mass of sediment. The organic matter was digested in the fume cupboard by adding 20 ml of 20 % hydrogen peroxide to each centrifuge tube (Charles *et*

al., 2002). The hydrogen peroxide was added slowly to ensure a stable reaction to avoid cross contamination between samples (Switzer and Pile, 2015). Once the reactions were stable, the centrifuge tubes were added to a 55 °C hot bath for two hours to catalyze the organic matter digestion and covered in foil to avoid the evaporation of hydrogen peroxide (Dura and Hemphill-Haley 2020). If the samples were cloudy or contained floating material on the surface after the two hours in the water bath, the organic matter digestion was incomplete and further organic matter digestion was required (Dura and Hemphill-Haley, 2020). The samples with incomplete organic matter digestion were centrifuged for 5 minutes at 3700 rpm and the supernatant liquid was decanted before adding 20 % hydrogen peroxide up to 40 ml and placed back into the 55 °C water bath until the completion of organic matter digestion (Dura, 2014). Once organic matter digestion was complete, the samples were centrifuged at 3700 rpm for five minutes and the supernatant liquid was decanted (Charles *et al.,* 2002). The samples were topped up to 40ml with deionized water and the centrifuge and decanting processes were repeated (Dura and Hemphill-Haley, 2020). After two rounds of centrifuging and decanting, 20 ml of deionized water was added to each sample alongside 2ml of sodium hexametaphosphate solution which is an anti-coagulant to prevent particles sticking together and the subsequent inaccurate grain size analysis (Charles *et al.,* 2002).

The samples were then analysed using the Beckman Coulter LS13320 laser diffraction particle size analyzer as laser diffraction is a commonplace technique for grain size analysis in palaeoseismic reconstructions (Horiba, 2010; Dura, 2014; Judd *et al.,* 2017). The laser diffraction determines the angle at which light is scattered which is directly related to the grain size of the particle; larger particles scatter light more narrowly and smaller particles scatter light more widely (Malvern, 2015; Judd *et al.,* 2017). The distribution of the scattered light produces a grain size distribution for each sample depth (Malvern, 2015).

The grain size data was analysed using GRADISTAT which is a statistical software that rapidly calculates statistics for unconsolidated sediments using the methods of moments in Microsoft visual basic programming language including the mean, degree of sorting, skewness, kurtosis, mode, median, D10, D50, D90, D90/D10, D90-D10, D75/D25,D75-D25, and the percentage of gravel, sand and mud within the sample (Blott and Pye, 2001; Blott, 2020). The Folk and Ward geometric method was used to present the sorting, mean grain size and d10 for each sample for easier comparison between different data (Folk and Ward, 1957; Blott and Pye, 2001; Dura *et al.,* 2015; Nelson *et al.,* 2015; Prater, 2021). The d10 is the diameter at which 10 % of the grains are smaller (Janigian, 2018).

4.6 Chronology

Core chronologies were produced using a combination of quantitative methods including accelerator mass spectrometry (AMS) radiocarbon dating and Caesium-137 dating, and qualitative methods including tephra chronology (Atwater and Hemphill-Haley, 1996; Kemp *et al.,* 2013).

DV.19.03 was the priority for the AMS radiocarbon dating as it contains a larger section of peat and thus, better constrains the palaeoseismic history compared to 19.DV.17 (Nelson *et al.,* 2015). Five radiocarbon dating samples from the peat in DV.19.03 were used to constrain the maximum and minimum ages of the identified sand beds and to identify the sedimentation rate in the core to understand the resolution of the diatom and grain size samples (Prater, 2021). A further three radiocarbon dates between 32.5 cm and 119 cm and the ^{137}Cs peak were obtained from DV.19.03 to better constrain the age-depth model for DV.19.03 (Kemp *et al.,* 2013; Witter *et al.,* 2016). Two radiocarbon samples were analysed from the sandy peat within 19.DV.17 to determine the approximate ages of the 19.DV.17 identified sand beds and to compare to the age of the DV.19.03 core. Finally, the *Rally Hawk, Big Chonky Boy* and *Cracker Hawk tephra* deposits are used to correlate the relative ages between the cores.

At the selected desired depth for dating, a 1 cm thick section of the sediment was cut from the core and wet sieved using a 500 µm to remove finer useless material for AMS radiocarbon dating (Kemp *et al.,* 2013). Under a binocular microscope at 40x magnification the most suitable dating materials from the sample were identified and placed in a glass vial with separate plant macrofossil types in separate glass vials (Kemp *et al.,* 2013). The selected samples were dried in an oven at 40°C for 12 hours to remove moisture and potential bacterial growth which would contaminate the radiocarbon sample (Warner, 1998; Kemp *et al.,* 2013). The dried samples were weighed and required at least 1 mg of sample for AMS radiocarbon dating (Dura, 2014; Kemp *et al.,* 2013). There were only a few plant macrofossils in the cores and for each sample only woody debris was present to at least 1mg to be sent for AMS radiocarbon dating. Care was taken to avoid the cross contamination of younger or older material between different sampling depths through thorough cleaning of tools between samples and wearing gloves (Wohlfarth *et al.,* 1998; Kemp *et al.,* 2013). The samples were labelled and sent to the National Ocean Sciences Accelerator Mass Spectrometry (NOSAMS) facility in Massachusetts, USA for acid base pretreatment and AMS radiocarbon dating (Kemp *et al.,* 2013).

Due to an inaccuracy in the balance used to record the weights of the samples, the AMS radiocarbon samples from DV.19.03 at 127 cm, 131 cm, 134 cm, 137 cm and 143 cm did not contain enough material for the acid pretreatment so the AMS radiocarbon dating was run without the acid base pretreatment for these samples. The inaccuracy in the balance used to weigh the samples was noted as the reweighing of the samples upon arrival at NOSAMS identified a lower weight for the samples from DV.19.03 at 127 cm, 131 cm, 134 cm, 137 cm and 143 cm. The other radiocarbon samples sent to NOSAMS were not affected by the same balance inaccuracy.

The radiocarbon dates produced from the AMS radiocarbon analysis were calibrated into calendar years as standard practice for reporting core chronologies (Marshall *et al.,* 2007; Parnell and Gehrels, 2015) The OxCal calibration software which uses the most recent iteration of the IntCal group calibration curve (IntCal 2020) was used to transform the radiocarbon ages into calendar years (OxCal 4.4) (Bronk Ramsey, 2009; Reimer *et al.,* 2013; Reimer *et al.,* 2020). Radiocarbon age calibration produces multiple potential calendar ages for the radiocarbon sample due to fluctuations in the atmospheric radiocarbon concentrations and the limited precision of the data used to produce the calibration curves; hence, the calendar age is presented as a range of calendar years (calBC/ calAD) (Dura, 2014; Reimer *et al.,* 2020).

To identify the ^{137}C peak in the DV.19.03 sediment core, a ^{137}C profile was produced by subsampling 2 cm section of sediment from the surface of DV.19.03 to 38 cm (Drexler *et al.,* 2018). The subsamples were dried at 80 °C and then ground to less than 2 mm before the ^{137}C concentrations were measured using gamma spectrometry (Baskaran and Naidu, 1995). The depth of 1963 is identified as the peak in the ^{137}C profile (Kemp *et al.,* 2013).

Individual tephra deposits were identified through unique sediment characteristics, that were then used to determine the presence of the tephra deposit in other sediment cores. However, since the tephra deposits were not geochemically analysed to determine the tephra deposit's unique geochemical fingerprint which can then be identified in other sediment cores, caution is required (Shennan *et al.,* 2018). Further, since the tephra deposits were not absolutely aged, the tephra deposits act as relative age markers between the sediment cores as opposed to absolute ages (Alloway *et al.,* 2007).

The absolute ages from radiocarbon dating and Caesium-137 dating were used to produce an age-depth model (Padgett *et al.,* 2021). An age-depth model is a probability estimate that

uses known ages at known depths to estimate the unknown age of sediment at different depths (Parnell and Gehrels, 2015; Wright *et al.,* 2017).

OxCal 4.4 was used to produce a Bayesian age-depth model for both the DV.19.03 and 19.DV.17 cores to estimate the age of undated depths of the cores (Bronk Ramsey, 2008; Padgett, 2021). Eight radiocarbon ages and their depths from DV.19.03 and two radiocarbon ages and depths from 19.DV.17 were used to produce the age-depth models. The peak in ^{137}C was used to constrain 1963 in the age-depth model for DV.19.03. The age-depth models were produced using the P_Sequence to enable fluctuation in the deposition rate as uniformed deposition is unrealistic (code is in Figure S1 of the appendix) (Witter *et al.,* 2019). The P_seqeunce uses a Poisson process to mediate the deposition of the sediments and is commonly used in Alaskan palaeoseismic reconstructions (e.g., Witter *et al.,* 2016, 2019).

5.0 Results

5.1 General Lithostratigraphy of Nagai Island

The six cores collected from Nagai Island and transferred to the laboratory for detailed analysis consist of predominantly peat, silt and sandy peat units and do not exhibit peat-mud or mud-peat couplets (Figure 5.1). The six cores were selected for detailed analysis as they were representative of the lithostratigraphy identified in the 71 sediment cores and hand dug pits and contained long sections of peat, suitable for palaeoseismic analysis. Cores 19.DV.17, DV.19.03, LLM.19.01, 19.BB.03 and 19.PM.02 contain sand or silt buried peat (Figure 5.1). DV.19.03 and 19.DV.17 are the only cores retrieved from Nagai Island that display multiple sand-peat couplets (Figure 5.1).

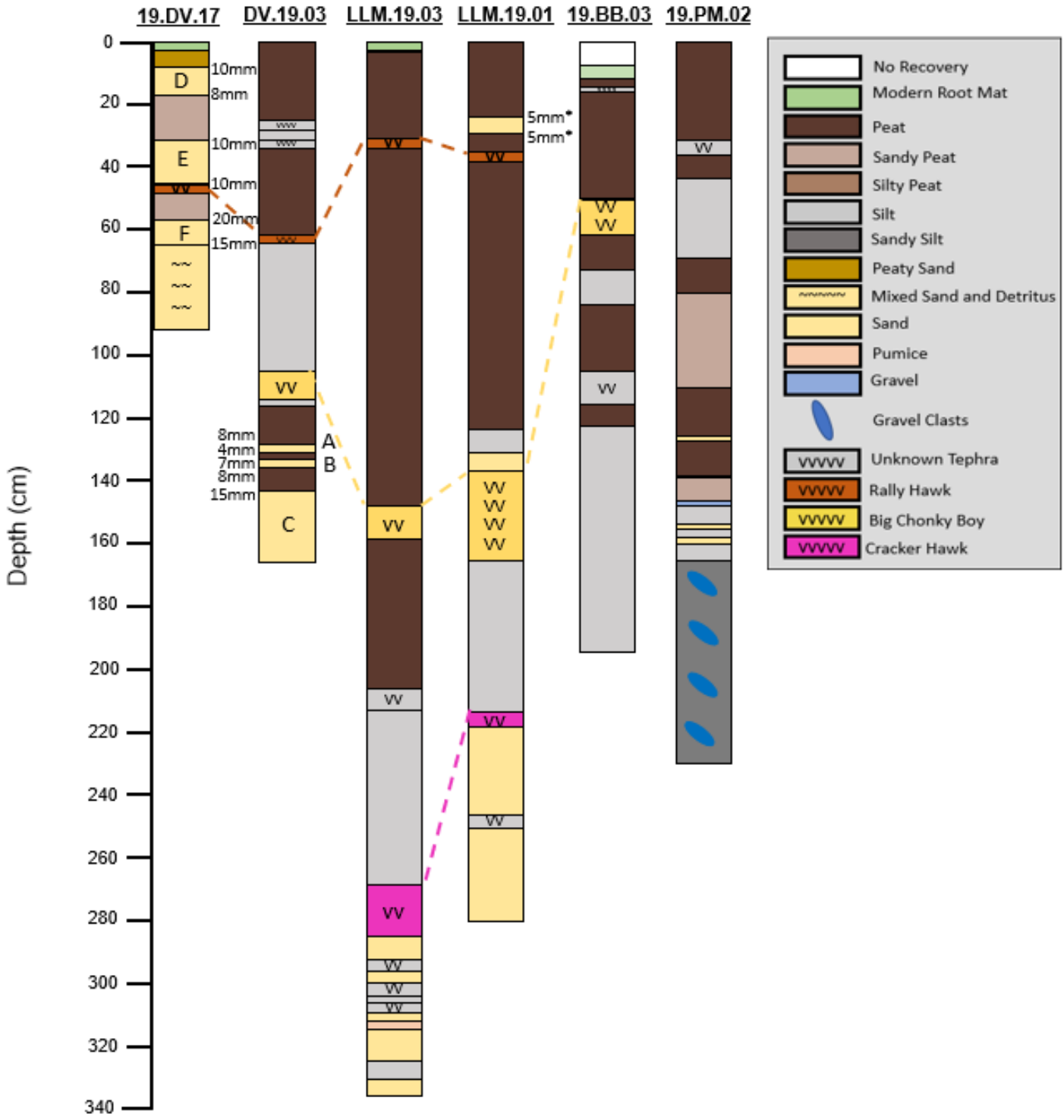

*Figure 5.1. Simplified lithostratigraphy of the six cores collected across the four study sites on Nagai Island. Dashed lines correlate tephra between cores. The abruptness of identified potential tsunami deposits are included (in mm) and are approximate. N.B. * means there is no X-ray image to aid the calculation of contact abruptness. A, B, C, D, E, and F refer to the sand beds.*

5.1.1 Deranged Valley Site Lithostratigraphy

Within DV.19.03, a dark brown peat layer between 117.5 cm and 144 cm embeds two distinct sand layers; sand bed A between 128 cm-131 cm and sand bed B between 135 cm-137 cm (Figures 5.1 and 5.2). The peat between 117.5 cm and 144 cm within DV.19.03 is underlain by a third sand deposit, sand bed C between 144 cm and 166 cm (Figures 5.1 and 5.2). The upper and lower contact of sand bed B as well as the upper contact of sand bed C are diffuse (7-15 mm). Sand bed A exhibits a moderately abrupt lower contact (~4 mm), though a diffuse upper contact (~8 mm) (Figures 5.1 and 5.2). There are no sand layers in the large sections of peat and silt from the surface of DV.19.03 down to 128 cm (Figure 5.2).

The three sand bed deposits identified in DV.19.03 were deposited prior to the deposition of the *Big Chonky Boy* tephra (Figure 5.1). The absence of the DV.19.03's two distinct sand layers in the LLM.19.03, LLM.19.01 and 19.BB.03 cores, which all contain the *Big Chonky Boy* tephra, suggests a spatially limited extent of the identified sand layers in DV.19.03 (Figure 5.1).

Another core from Deranged Valley, 19.DV.17, contains three distinct sand beds within units of sandy peat and peaty sand (Figures 5.1 and 5.3). Sand bed F between 57-64 cm is the smallest (7 cm) and oldest of the three sand bed units in 19.DV.17 and it overlies a unit of mixed sand and detritus (64-90 cm), and underlays a unit of sandy peat (51-57 cm) (Figure 5.3). Sand bed F contains both trace roots and detritus (Figure 5.3). Sand bed E overlays the *Rally Hawk* tephra unit extending 13 cm from 31 cm to 44 cm and contains trace roots and isolated areas of detritus between 33.5 cm-34 cm and 42 cm-43 cm (Figure 5.3). A 12cm sandy peat layer (19 cm-31 cm) overlies sand bed E and underlies sand bed D (Figure 5.3). Within the sandy peat layer, the lithology grades from dark brown sandy peat at 19 cm to peaty sands at the base of the unit (31 cm) (Figure 5.3). Sand bed D extends 12 cm between 7 cm-19 cm, contains some trace roots and is overlain by a 7 cm dark brown decomposed peaty sand layer (Figure 5.3).

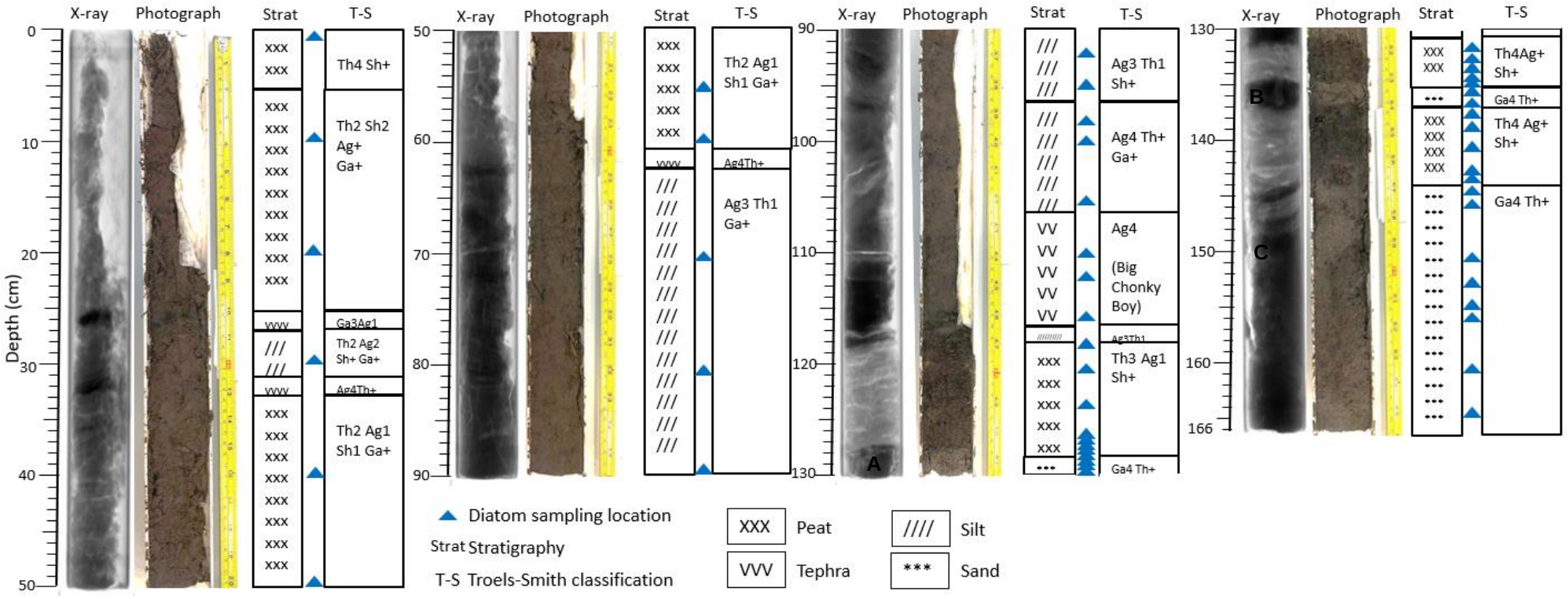

Figure 5.2. X-ray images, photographs, and detailed lithostratigraphy of core DV.19.03 using the Troels-Smith classification (Troels-Smith, 1955; Aaby and Berglung 1986; Long et al., 1999). The denser areas are represented by lighter shades of grey.

19.DV.17

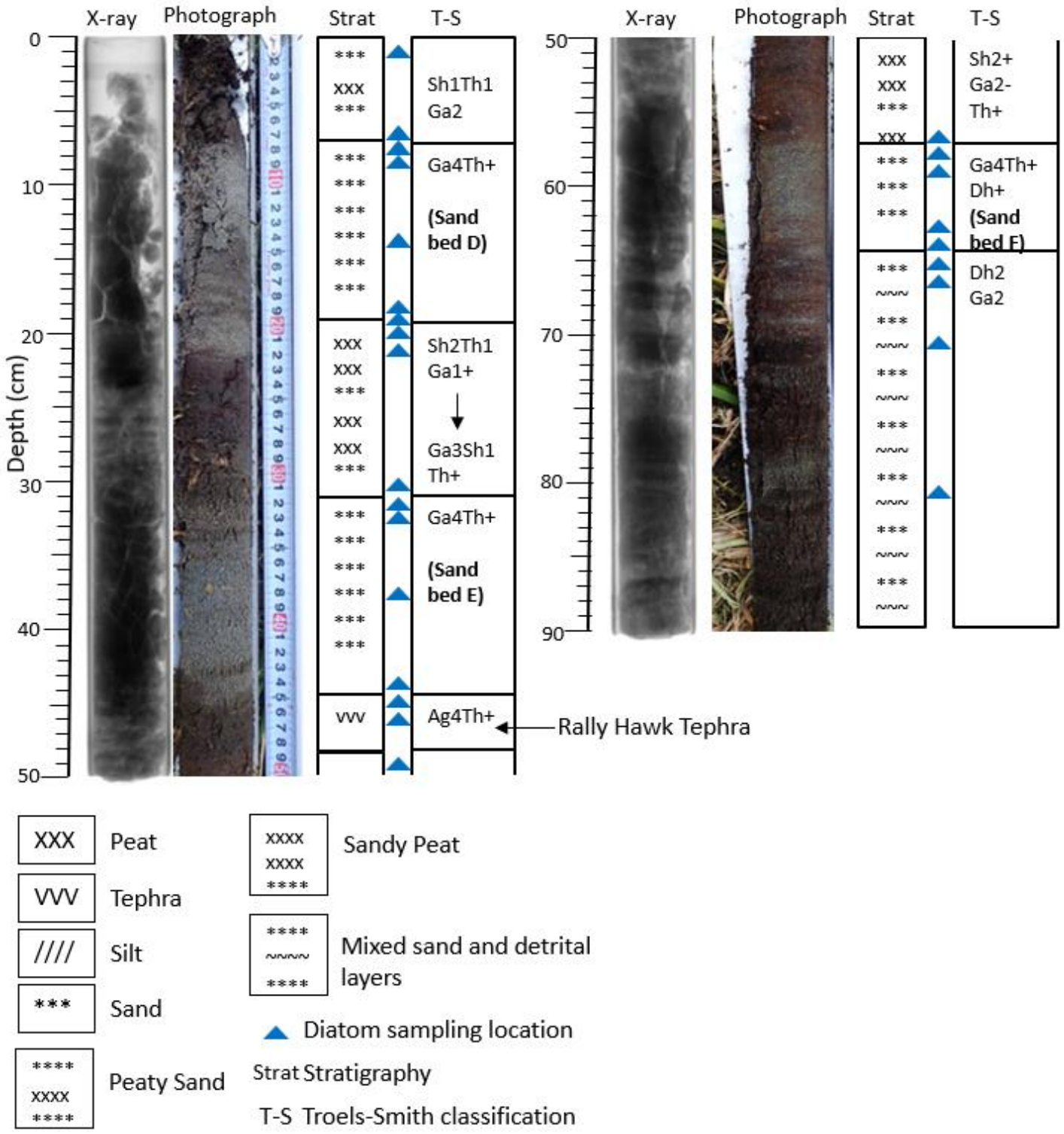

Figure 5.3. X-ray images, photographs, and detailed lithostratigraphy of core 19.DV.17 using the Troels-Smith classification (Troels-Smith, 1995; Aaby and Berglung 1986; Long et al., 1999). The denser areas are represented by lighter shades of grey.

All the upper and lower contacts of sand beds D, E and F within the 19.DV.17 core are diffuse (~8-20 mm) (Figure 5.3). Further, in terms of the spatial extent of the three sand beds identified in 19.DV.17, both sand bed D and sand bed E are younger than the *Rally Hawk* tephra and since the *Rally Hawk* tephra is identified in the DV.19.03, LLM.19.03 and LLM.19.01 cores, it can be used to assess the spatial extent of sand beds D and E (Figures 5.1 and 5.3). There are no sand layers younger than the *Rally Hawk* tephra in the DV.19.03 and LLM.19.03 cores and only one 3 cm sand layer that is younger than the *Rally Hawk* tephra in LLM.19.01 core, suggesting a lack of correlation between sand beds D and E and other cores within Deranged Valley and Larsen Lake Marsh (Figures 5.1 and 5.3). Sand bed F is older than the *Rally Hawk* tephra and is not apparent in any of the other cores from Nagai Island. (Figures 5.1 and 5.3).

The other 20 exploratory cores from Deranged Valley do not contain any peat-mud or mud-peat couplets (Figure 5.4). The sand-peat couplets between 117.5 cm and 166 cm in DV.19.03 can only be correlated with DV.19.09 and DV.19.10 from the Deranged Valley cores as all the other cores do not exhibit the *Big Chonky Boy* or older tephra deposits which are required to correlate the relative depth of the sand-peat couplets to the other cores (Figure 5.4). DV.19.09 and DV.19.10 both contain the *Cracker Hawk tephra* which the LLM.19.03 core determines as older than the *Big Chonky Boy* tephra (Figure 5.1). However, the dominance of sand in both DV.19.09 and DV.19.10 limits the ability to assess the spatial extent of the distinguished sand layers identified in DV.19.03 with the rest of the Deranged Valley cores.

DV.19.02 contains a relatively large section of peat down to 31 cm and, as in the DV.19.03 core, there are no sand deposits younger than the *Rally Hawk* tephra deposition (Figure 5.4). DV.19.04, DV.19.15, DV.19.16, 19.DV.17, DV.19.18, and DV.19.20 all contain sand deposits that are younger than the *Rally Hawk* tephra with the sand layers in DV.19.15, DV.19.16, 19.DV.17, and DV.19.20 burying a unit of peat (Figure 5.4). However, the sand deposits are not deposited in the continuous peat in either of the DV.19.03 or DV.19.02 cores above the *Rally Hawk* tephra, demonstrating a limited spatial extent (Figure 5.4). Further, the lower contacts of the sand layers in DV.19.15, DV.19.16, 19.DV.17, and DV.19.20 that bury a unit of peat are all diffuse (Figure 5.4). As identified with the correlation of 19.DV.17 with the cores from Larsen Lake Marsh, Bog's Bog and Peter's Marsh, there is a lack of spatial correlation between the 19.DV.17 sand buried peats with other cores from Deranged Valley (Figures 5.1 and 5.4).

DV.19.21 contains interfingering of sand and peat which exhibit diffuse upper and lower contacts and are unique to DV.19.21 (Figure 5.4).

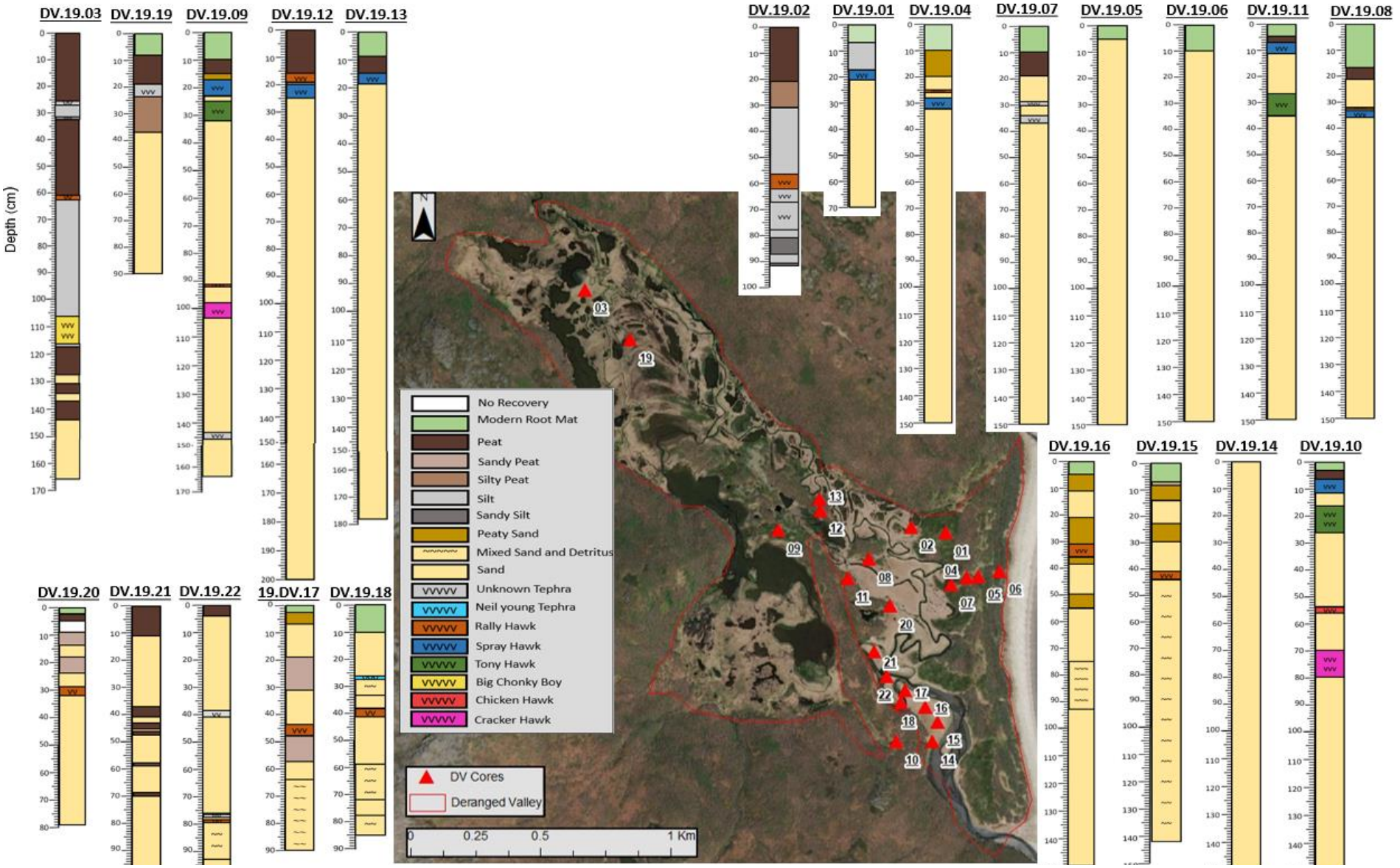

Figure 5.4. Simplified lithostratigraphy of the Deranged Valley cores and soil pits alongside the core locations for spatial context. Note the tephra are listed in the legend in chronological order. N.B. the last two digits of the core title correspond to the core numbers located on the map.

5.1.2 Larsen Lake Marsh Site Lithostratigraphy

The cores retrieved from the Larsen Lake Marsh site contain large sections of peat (up to 205 cm) (Figure 5.1). Within the 205 cm of peat in the LLM.19.01 core, there are no sand deposits identified (Figure 5.1). Interestingly, core LLM.19.01 has a prominent 3 cm layer of sand interbedded within the continuous peat unit between 26-29 cm and exhibits moderately sharp upper and lower contacts (~5 mm) (Figure 5.1). The sand layer identified near the surface of LLM.19.01 is not present in any of the other cores retrieved within the Larsen Lake Marsh site (Figure 5.1). Further, the sand deposit near the surface of LLM.19.01 is younger than the *Rally Hawk* tephra and in the DV.19.03, LLM.19.03 and 19.BB.03 cores, where the *Rally Hawk tephra* is also identified, the sand layer is not present (Figure 5.1). In the 19.DV.17 core, which contains the *Rally Hawk* tephra, sand deposits which are younger than the *Rally Hawk* tephra are present which could correlate to the sand deposition in the LLM.19.01 core (Figure 5.1).

5.1.3 Peter's Marsh Site Lithostratigraphy

The Peter's Marsh cores contains predominantly peat, silt and sandy peat (Figure 5.1). 19.PM.02 exhibits a 1 cm sand lens interbedded by peat (123-124 cm) and two 0.5 cm sand lenses interbedded by silt (153-153.5 cm and 160-160.5 cm), all of which are thin and discontinuous (Figure 5.1). The sand lenses identified are unique to 19.PM.02 (Figure 5.1).

5.1.4 Bog's Bog Site Lithostratigraphy

Like the other study sites on Nagai Island, peat and silt dominate the Bog's Bog sediment. 19.BB.03 contains a thick surface peat down to 73 cm with no interbedded sand layers (Figure 5.1). Between 73 cm and 85 cm a 12 cm layer of silt overlies a layer of peat with a diffuse lower contact (>7 mm). The silt layer cannot be correlated with other cores due to the lack of known tephra units around the depth of the silt deposit.

The six distinguished sand beds in DV.19.03 and 19.DV.17 were chosen for detailed microfossil, grain size and chronological analysis as they appear the most promising tsunami candidates from the lithostratigraphy analysis of the six cores retrieved from Nagai Island.

5.2 Detailed Lithostratigraphy and Grain Sizes of Sand Beds in DV.19.03 and 19.DV.17

5.2.1 Lithostratigraphy and Grain Size of DV.19.03

Sand bed C (144 cm to 164 cm), the basal unit of DV.19.03, is composed of grey poorly sorted, very fine to fine sand with trace roots (Figure 5.2 and Table S1). The average mean

grain size of sand bed C is 129.98 µm (2.96 Φ) and the average d10 is 31.03 µm (1.73 Φ) (Tables 5.1 and S1). Overall, the mean grain size within sand bed C decreases from 149.09 µm at the base (164 cm) to 103.16 µm at 144 cm and the d10 decreases from 45.14 µm at 164 cm to 14.53 µm at 144 cm, though both the mean grain size and d10 fluctuate within sand bed C (Figure 5.5 and Table S1).

Table 5.1. Average d10 and average mean grain size for the identified sand bed units and the over and underlying lithostratigraphic layers in DV.19.03 and 19.DV.17.

Core	Layer	Average d10 (µm/ Φ)	Average Mean Grain Size (µm/ Φ)
DV.19.03	Top 117.5cm	5.70/2.02	43.56/4.66
DV.19.03	Overlying sand bed A	5.31/1.43	39.89/4.69
DV.19.03	Sand bed A	37.94/1.95	133.15/2.91
DV.19.03	Underlying sand bed A/ Overlying sand bed B	7.23/1.77	57.12/4.23
DV.19.03	Sand bed B	46.18/1.96	140.98/2.83
DV.19.03	Underlying sand bed B/ Overlying sand bed C	5.14/1.67	54.47/4.23
DV.19.03	Sand bed C	31.03/1.73	129.98/2.96
19.DV.17	Overlying sand bed D	12.38/0.86	124.36/3.01
19.DV.17	Sand bed D	61.83/1.17	180.69/2.49
19.DV.17	Underlying sand bed D/ Overlying sand bed E	20.45/0.76	136.48/2.89
19.DV.17	Sand bed E	65.46/1.11	177.94/2.57
19.DV.17	Underlying sand bed E	9.26/ 1.18	81.47/3.63
19.DV.17	Overlying sand bed F	36.48/0.86	173.66/2.69
19.DV.17	Sand bed F	55.07/1.16	183.08/2.45
19.DV.17	Underlying sand bed F	37.54/1.11	169.65/2.56

The 7 cm peat layer which overlies sand bed C and underlies sand bed B (137 cm to 144 cm) is composed of very poorly sorted, very fine sand to very coarse silt (Figure 5.2 and Table S1). The average mean grain size of the overlying peat layer is 75.51 μm finer than the average mean grain size of sand bed C (54.47 μm (4.23 Φ)) and the average d10 is 25.89 μm finer than the average d10 of sand bed C (5.14 μm (1.67 Φ)) (Table S1).

Sand bed B, between 135-137 cm, is composed of grey moderately to poorly sorted fine sand with trace roots (Figure 5.2 and Table S1). The average mean grain size of sand bed B is 140.99 μm (2.83 Φ), which is 11.01 μm greater than the average mean grain size of sand bed C. The average d10 is 46.18 μm (1.96 Φ) which is 15.15 μm greater than the average d10 of sand bed C (Tables 5.1 and S1). Unlike sand bed C, within sand bed B, the mean grain size and d10 increase with decreasing depth (Figure 5.5). Between 136 cm to 135 cm the mean grain size increases by 11.17 μm and the d10 increases by 11.92 μm (Figure 5.5).

Sand bed B is underlain by the peat layer which overlies sand bed C (137-144 cm) (Figure 5.2). The average mean grain size of the underlying peat unit is 86.52 μm finer than the average mean grain size of sand bed B and the average d10 of the underlying peat unit is 20.29 μm finer than average d10 of sand bed B (Tables 5.1 and S1).

Sand bed B is overlain by a 4 cm layer of peat (131-135 cm) composed of poorly to very poorly sorted, very find sand to coarse silt (Figure 5.2 and Table S1). The average mean grain size of the peat overlying sand bed B is 83.87 μm finer than the average mean grain size of sand bed B (57.12 μm (4.23 Φ)) and the average d10 is 38.96 μm finer than the average d10 of sand bed C (7.23μm (1.77 Φ)) (Tables 5.1 and S1). Further, compared to the peat underlying sand bed B, the peat overlying sand bed B has a slightly greater average mean grain size and average d10 (2.65 μm and 2.09 μm respectively) (Tables 5.1 and S1).

Sand bed A, between 128-130 cm is composed of grey poorly sorted, fine sand with trace roots (Figure 5.2 and Table S1). The average mean grain size of sand bed A is 133.15 μm (2.91 Φ) which is 7.84 μm less than the average mean grain size of sand bed B and 3.17 μm more than the average mean grain size of sand beds C (Tables 5.1 and S1). The average d10 of sand bed A is 37.94 μm (1.95 Φ) which is 8.23 μm less than the average d10 of sand bed B and 6.92 μm more than the average d10 of sand bed C (Tables 5.1 and S1). Like sand bed C, within sand bed A, the mean grain size and d10 decrease with decreasing depth, though without fluctuations (Figure 5.5). Between 130 cm and 128 cm the mean grain size decreases by 12.64 μm and the d10 decreases by 13.59 μm (Figure 5.2).

Sand bed A is underlain by the peat layer which overlays sand bed B (131-135 cm), and sand bed A is overlain by 10.5 cm of peat (117.5 cm to 128 cm) composed of very poorly sorted, very coarse to coarse silt (Figure 5.1 and Table S1). The average mean grain size of the peat overlying sand bed A is 92.56 μm finer than sand bed A (39.89 μm (4.69 Φ)) and the mean d10 is 32.5 μm finer than sand bed A (5.45 μm (1.43 Φ)) (Tables 5.1 and S1). Compared to the peat underlying sand bed A, the peat overlying sand bed A is on average 17.23 μm finer and has an average d10 1.79 μm finer (Tables 5.1 and S1).

The top 117.5 cm of DV.19.03 does not contain any sand deposits and is composed of 9 lithostratigraphic layers including two peat, three silt and four tephra layers ranging from very poorly sorted to poorly sorted, very coarse silt to very fine sand (Figure 5.2 and Table S1). The average mean grain size of the top 117.5 cm of DV.19.03 is 43.56 μm (4.66 Φ) which is between 86.42 μm and 97.43 μm finer than the average mean grain sizes of sand beds A, B and C and between 31.95 μm finer and 3.66 μm coarser than the average mean grain sizes of the three peat units over and underlying the sand beds A, B and C (Table S1 and Figure 5.6). The average d10 of the top 117.5 cm is 5.70 μm (2.02 Φ), which is between 25.33 μm and 40.48 μm finer than the average d10 of sand beds A, B and C and between 1.53 μm finer and 0.56 μm coarser than the average d10 of the three peat units over and underlying the sand beds A, B and C (Table S1 and Figure 5.6).

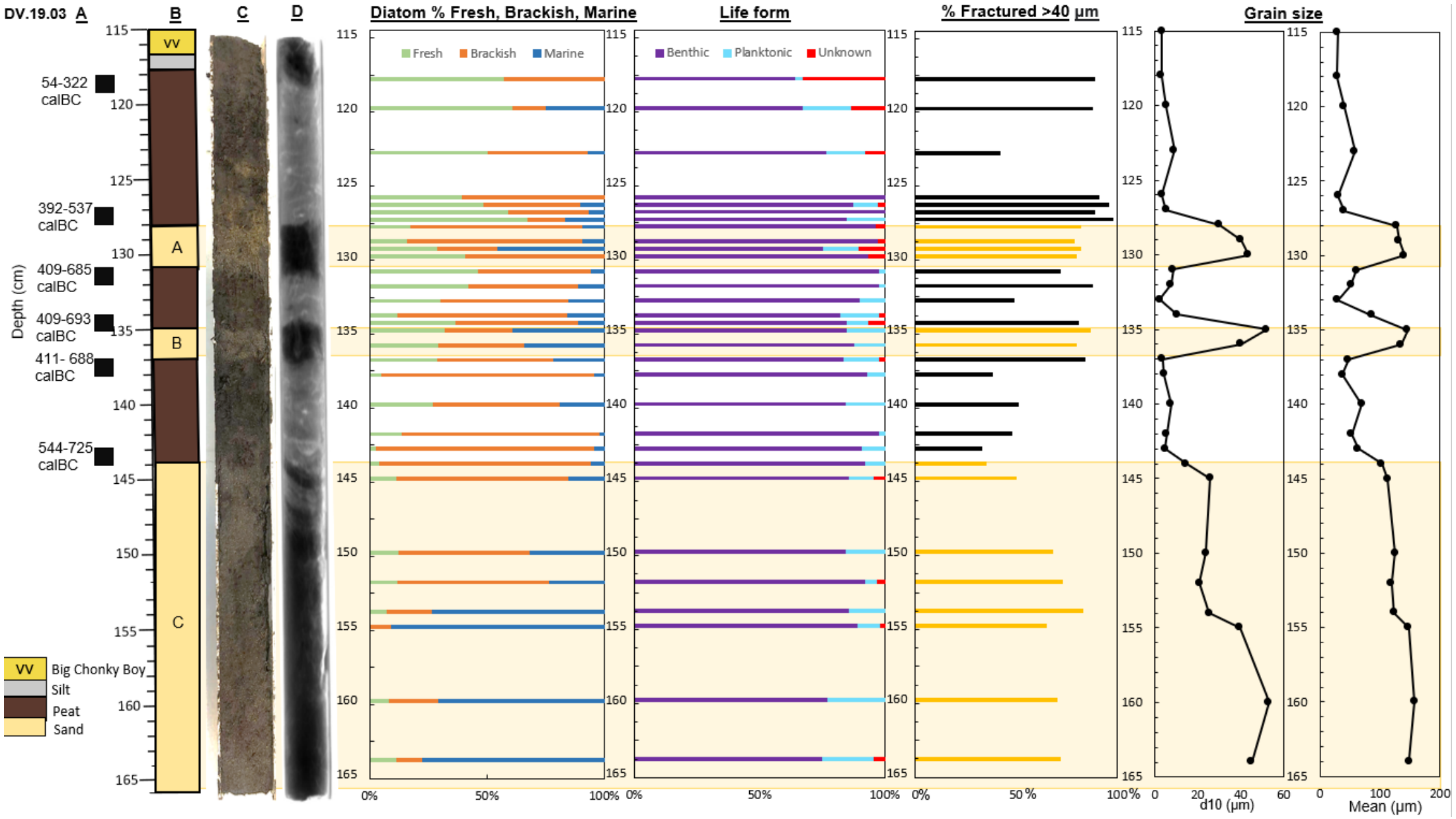

Figure 5.5. Summary of the lithostratigraphy, radiocarbon dating, diatoms, and grain sizes for 115cm- 166cm of DV.19.03. A-Radiocarbon dating. B-Lithostratigraphy. C- Core photograph. D-X-ray image of core. The diatom summary includes the percentage of fresh, brackish and marine diatoms for species exceeding 1.5 % of the total abundance (as standard practice in ecology (Birks, 1995)), the diatom life form and the percentage of fractured diatoms with the sand bed samples in yellow. The grain size summary includes the d10 and mean grain sizes. N.B. The sample at 115cm did not contain any diatoms.

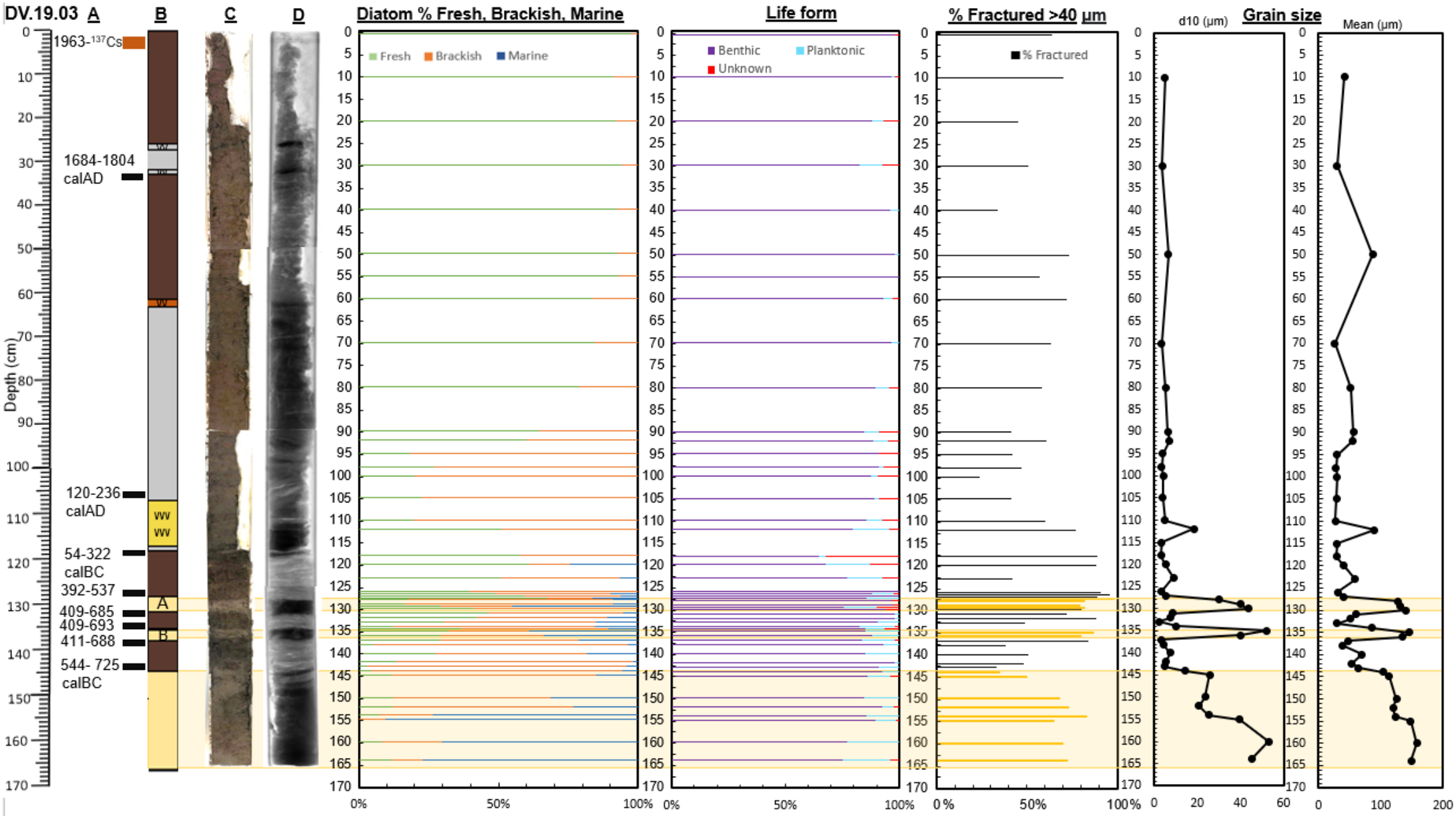

Figure 5.6. *Summary of the lithostratigraphy, radiocarbon dating, diatoms, and grain sizes for the entirety of DV.19.03. A-Chronology. B-Lithostratigraphy. C- Core photograph. D-X-ray image of core. The diatom summary includes the percentage of fresh, brackish and marine diatoms for species exceeding 1.5 % of the total abundance (as standard practice in ecology (Birks, 1995)), the diatom life form and the percentage of fractured diatoms with the sand bed samples in yellow. The grain size summary includes the d10 and mean grain sizes.*

5.2.2 Lithostratigraphy and Grain Size of 19.DV.17

Sand bed F, between 57 cm and 64 cm of 19.DV.17, is composed of grey poorly to moderately sorted fine sand with trace roots and detritus (Figure 5.3 and Table S2). The average mean grain size of sand bed F is 183.08 μm (2.45Φ) and the average d10 is 55.07 μm (1.16 Φ) (Table S2 and Figure 5.7). The mean grain size and the d10 do not decrease from the base to the surface of sand bed F, though they do fluctuate within sand bed F (Figure 5.7).

The 26 cm dark brown and grey mixed sand and detrital layer which underlies sand bed F (64 cm-90 cm) is composed of poorly sorted fine sand (Figure 5.3 and Table S2). The average mean grain size of the underlying mixed sand and detrital layer is 169.65 μm (2.56 Φ), which is on average 13.43 μm finer than sand bed F (Table S2 and Figure 5.7). The average d10 of the underlying mixed sand and detrital layer is 37.54 μm (1.11 Φ), which is on average 17.52 μm finer than sand bed F (Table S2 and Figure 5.7).

The 9 cm dark brown sandy peat layer which overlies sand bed F (48 cm-57 cm) is composed of very poorly to poorly sorted, very fine to fine sand (Figure 5.3 and Table S2). The average mean grain size of the overlying sandy peat layer is similar to sand bed F and the mixed layer underlying sand bed F with an average of 173.66 μm (2.60 Φ), which is on average 9.42 μm finer than sand bed F and 4.02 μm coarser than the mixed sand and detrital layer underlying sand bed F (Tables 5.1 and S2). The average d10 of the overlying sandy peat layer is 36.48 μm (0.86 Φ), which is 18.59 μm finer than sand bed F and 0.97 μm coarser than the mixed layer underlying sand bed F (Table S2 and Figure 5.7).

Sand bed E, between 31 cm and 44 cm, is composed of poorly to moderately sorted, very fine to medium sand with trace roots (Figure 5.3 and Table S2). The average mean grain size of sand bed E is 177.94 μm (2.57 Φ), which is 5.14 μm finer than sand bed F and, like sand bed F, is notably coarser than the average mean grain size of sand beds A, B and C from DV.19.03 which range between 129.98 μm to 140.99 μm (Table S2 and Figure 5.7). The average d10 of sand bed E is 65.46 μm (1.11 Φ), which is 10.39 μm coarser than sand bed F, and like sand bed F, is notably coarser than the average d10 of sand beds A, B, and C from DV.19.03 which range between 31.03 μm and 46.18 μm (Tables S1 and S2). Similar to sand bed F, the mean grain size and the d10 do not decrease with decreasing depth in sand bed E; the two middle samples from sand bed E are considerably coarser than the basal and surface samples which exhibit similar mean grain sizes and d10 (Figure 5.7).

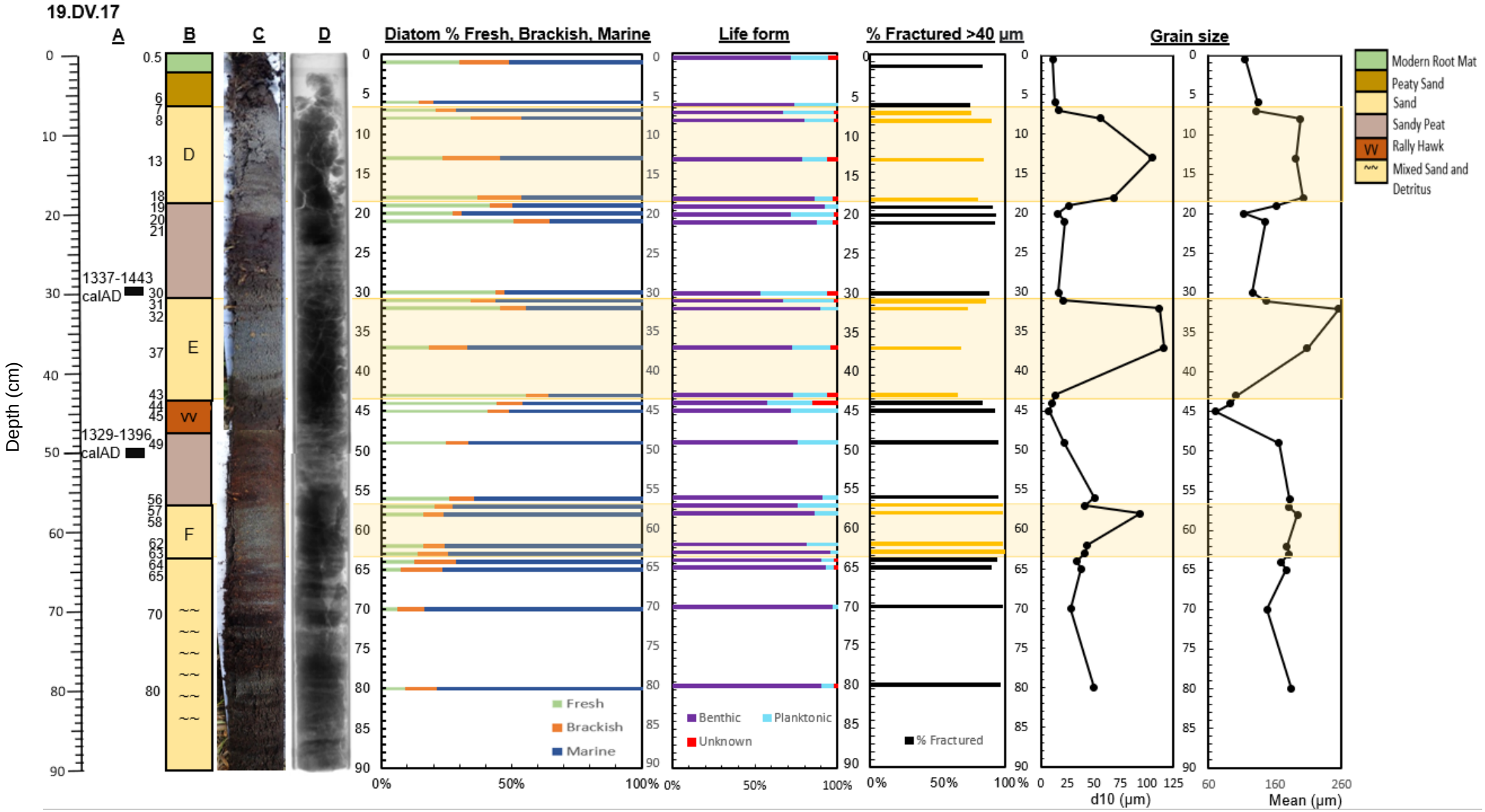

Figure 5.7. Summary of the lithostratigraphy, radiocarbon dating, diatoms, and grain sizes for 19.DV.17. A-Radiocarbon dating. B-Lithostratigraphy. C- Core photograph. D-X-ray image of core. The diatom summary includes the percentage of fresh, brackish and marine diatoms for species exceeding 1.5 % of the total abundance (as standard practice in ecology (Birks, 1995)), the diatom life form and the percentage of fractured diatoms with the sand bed samples in yellow. The grain size summary includes the d10 and mean grain sizes. N.B. The sample at 115 cm did not contain any diatoms.

Sand bed E is underlain by the 4 cm *Rally Hawk* tephra (44cm-48cm) and is composed of very poorly sorted, very fine sand (Figure 5.3 and Table S2). *Rally Hawk* exhibits the finest mean grain size of the entire 19.DV.17 core averaging 81.47 μm (3.63 Φ), which is on average 96.47 μm finer than sand bed E (Table S2 and Figure 5.7). The d10 of the *Rally Hawk* tephra averages 9.26 μm (1.18 Φ) which is on average 56.23 μm finer than sand bed E (Table S2 and Figure 5.7).

Sand bed E is overlain by a 12 cm sandy peat layer (19 cm-31 cm) and is composed of very poorly to poorly sorted, very fine to medium sand (Figure 5.3 and Table S2). The mean grain size of the sandy peat overlying sand bed E averages 136.48 μm (2.89 Φ), which is on average 41.46 μm finer than sand bed E and 55.01 μm coarser than the underlying *Rally Hawk* layer (Tables 5.1 and S2). The average d10 of the overlying peat layer is 20.45 μm (0.76 Φ), which is on average 45.00 μm finer than sand bed E and 11.22 μm coarser than the underlying *Rally Hawk* (Table S2 and Figure 5.7).

Sand bed D between 7 cm and 19 cm is composed of very poorly to moderately sorted fine sand with trace roots (Figure 5.3 and Table S2). The average mean grain size of sand bed D is 180.67 μm (2.49 Φ) which is on average 2.75 μm coarser than sand bed E and 2.41 μm finer than sand bed F (Figure 5.7 and Table S2). The average d10 of sand bed D is 61.83 μm (1.17 Φ), which is on average 3.62 μm finer than sand bed E and 6.76 μm coarser than sand bed F (Figure 5.7 and Table S2). Unlike sand bed E and F, the mean grain size of sand bed D decreases with decreasing depth from 201.99 μm at 18 cm to 131.23 μm at 7 cm, though the mean grain size at 8 cm is slightly greater than at 13 cm (198.31 μm and 191.21μm respectively) (Figure 5.7 and Table S2). Further, the d10 decreases overall within sand bed D from 68.88 μm at 18 cm to 17.24 μm at 7 cm, however, the sample at 13 cm has a considerably larger d10 than any of the samples within sand bed D (104.75 μm compared to the next largest of 68.88 μm) (Figure 5.7).

Sand bed D is underlain by the sandy peat layer between 19 cm and 31 cm which overlies sand bed E as detailed above (Figure 5.3). The average mean grain size of the underlying sandy peat layer is 44.21μm finer than sand bed D and the average d10 is 41.38 μm finer than sand bed D (Table S2 and Figure 5.7).

Sand bed D is overlain by a 6 cm layer of peaty sand (between 0 cm and 6 cm) and is composed of very poorly sorted very fine to fine sand (Figure 5.3 and Table S2). The average mean grain size of the overlying peaty sand layer is 124.36 μm (3.01 Φ) which is 56.33μm finer than sand bed D and 12.12μm finer than the sandy peat layer underlying sand

bed D (Figure 5.7 and Table S2). The average d10 of the overlying peaty sand layer is 12.38 µm (0.86Φ), which is on average 49.45 µm finer than sand bed D and 8.07 µm finer than the sandy peat layer underlying sand bed D (Figure 5.7 and Table S2).

5.3 Core Chronology

5.3.1 Core Chronology of DV.19.03

Eight radiocarbon dates from DV.19.03, between 32.5 cm and 144 cm constrain the ages of the identified sand beds within DV.19.03 (Table 5.2). The peak ^{137}Cs which occurs at 3 cm determines 1963 as this is the year of maximum atmospheric ^{137}Cs (Table 5.3).

Age-depth modelling of core DV.19.03 using the eight radiocarbon dates and the peak ^{137}Cs estimates sand bed C to be aged between 552 BC and 1282 BC (2573 to 3303 years ago) (Figure 5.8 and Table 5.4). Sand bed B is modelled to be deposited between 449 BC and 589 BC (2470 to 2610 years ago) and sand bed A between 388 BC and 492 BC (2409 to 2513 years ago) (Figure 5.8 and Table 5.4). The base of core DV.19.03 is estimated between 1282 BC and 842 BC (3303 and 2863 years ago).

Table 5.2. Summary of the Deranged Valley Radiocarbon ages. Calibrated ages were calculated in OxCal 4.4 using the IntCal20 dataset (Reimer et al., 2020; Bronk-Ramsey, 2021). 95 % probability distribution at 2 σ. Radiocarbon age calculated by the National Ocean Sciences Accelerator Mass Spectrometry Facility in Massachusetts, United States. DV=Deranged Valley. N/A for radiocarbon dating samples that were not targeting specific lithostratigraphic layers instead used to have samples from across a greater range of the core to better constrain the age-depth model.

Core	Calibrated Age cal yr AD 2σ	Calibrated Age cal yr BC 2σ	Radiocarbon Age 1σ	Lab Number	^{13}C (‰)	Depth (cm)	Description of Dated Material	Age Interpretation	Contact	Age-Depth Model Label
DV.19.03	1684- 1804	-	200 +/-15	DV.19.03 RCD 32.5-33.5cm	-27.42	32.5	Wood	N/A	N/A	A
	120-236	-	1870 +/-25	DV.19.03 RCD 105-106cm	-25.08	105	Wood	N/A	N/A	B
	-	54-322	2130 +/- 20	DV.19.03 RCD 118-119cm	-27.18	118	Wood	N/A	N/A	C
	-	392-532	2370 +/- 25	DV.19.03a 127-128cm	-26.81	127	Wood	Minimum	Sand Bed A	D
	-	409-685	2440 +/-25	DV.19.03a 131-132cm	*	131	Wood	Maximum	Sand Bed A	E
	-	409-693	2430 +/- 20	DV.19.03a 134-135cm	-26.61	134	Wood	Minimum	Sand Bed B	F
	-	411-688	2440 +/-20	DV.19.03a 137-138cm	-27.31	137	Wood	Maximum	Sand Bed B	G
	-	544-725	2520+/-30	DV.19.03a 143cm-144cm	-26.23	143	Wood	Minimum	Sand Bed C	H
DV.19.17	1337-1443	-	520 +/- 25	19.DV.17 RCD 29-30cm	-26.41	29	Wood	Minimum	Sand Bed E	A
	1329-1396	-	640 +/-25	19.DV.17 RCD 49.5-50.5cm	-26.46	49.5	Wood	Maximum	Sand Bed E	B

Table 5.3. ^{137}Cs concentrations for DV.19.03 with the peak ^{137}Cs highlighted in yellow and is the inferred depth of 1963.

Depth (cm)	Activity (dpm/g)	Error (+/-)
1	0.09	0.08
3	1.24	0.25
5	0.79	0.27
7	0.25	0.07
9	0.54	0.43
11	0.68	0.36
13	0.01	0.09
15	0.36	0.28
17	0.11	0.05
19	0.04	0.05
25	0.05	0.03
37	0.00	0.00

Table 5.4. Modelled ages for sand beds A, B and C estimated from the Bayesian age-depth model for core DV.19.03 in Deranged Valley, Nagai Island, Alaska. Produced from radiocarbon ages using P-sequence in OxCal 4.4 (Bronk Ramsey, 2008; Padgett et al., 2021). μ, mean; σ, one standard deviation; m, mode. Negative values= cal yr BC and positive values= cal yr AD. Note that the estimated ages for the sand beds are taken from the maximum and minimum ages of the upper and lower contacts of the sand beds.

	From (BC/AD)	To (BC/AD)	%	μ	Σ	*m*
Sand Bed A Base	-492	-408	95.4	-447	22	-444
Sand Bed A Surface	-445	-388	95.4	-408	13	-406
Sand Bed B Base	-589	-457	95.4	-522	32	-520
Sand Bed B Surface	-543	-449	95.4	-496	26	-496
Sand Bed C Base	-1282	-842	95.4	-1051	112	-1041
Sand Bed C Surface	-776	-552	95.4	-639	52	-628
Sand Bed A	-492	-388	N/A	N/A	N/A	N/A
Sand Bed B	-589	-449	N/A	N/A	N/A	N/A
Sand Bed C	-1281	-552	N/A	N/A	N/A	N/A

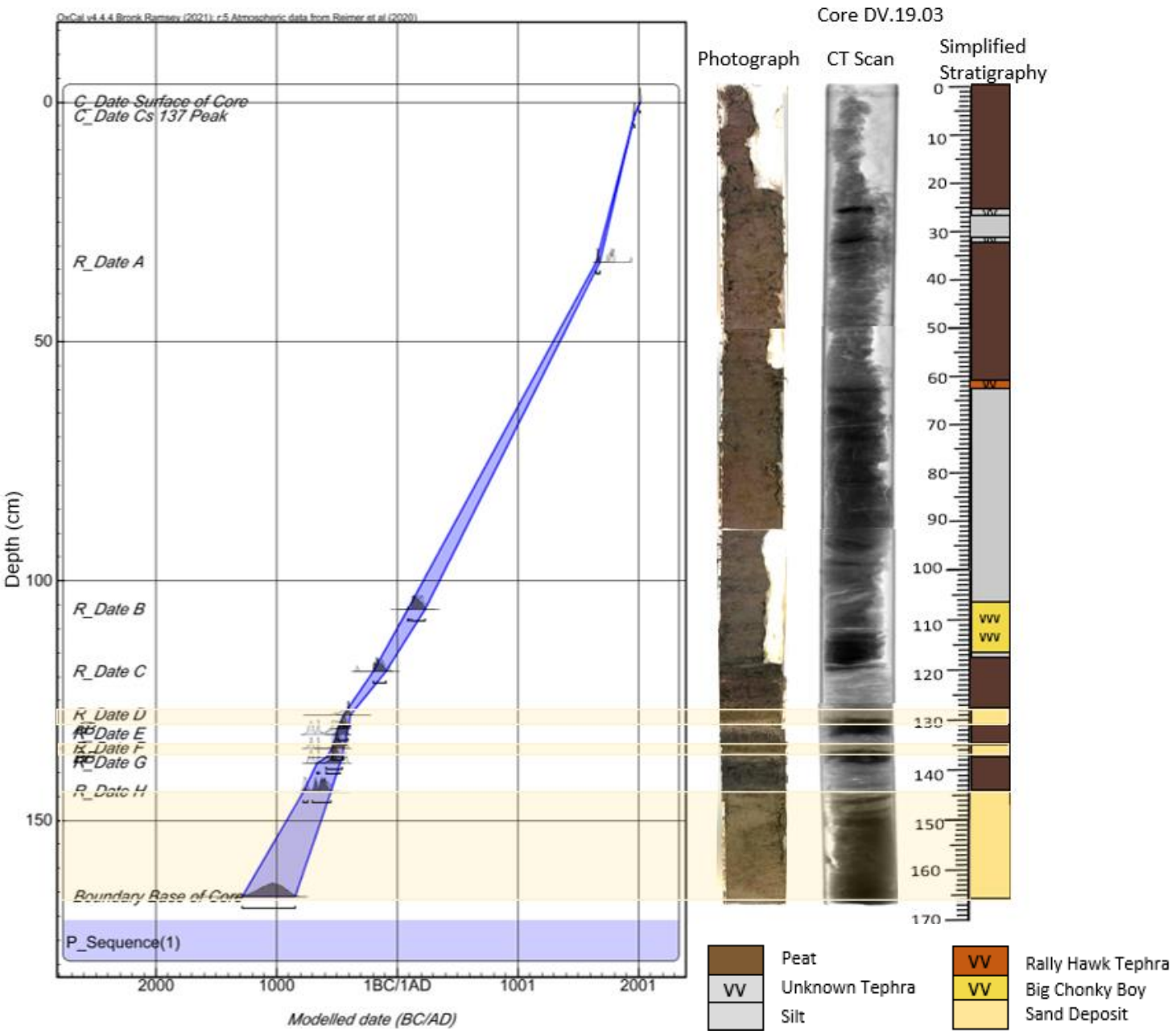

Figure 5.8. Age-Depth Model for DV.19.03 using the P-sequence in OxCal 4.4 (Appendix Figure S1) alongside the core photograph, x-ray image and simplified lithostratigraphy (Bronk-Ramsey, 2021).

5.3.2 Core Chronology of 19.DV.17

Two radiocarbon dates from 19.DV.17, between 29 cm and 50.5 cm constrain the ages of the identified sand beds within 19.DV.17 (Table 5.2). The two radiocarbon dates from 19.DV.17 determines that the sand beds identified in DV.19.03 do not correspond to the sand beds identified in 19.DV.17 as 19.DV.17 is much younger than the deposition of the sand beds in DV.19.03 (Tables 5.2, 5.4 and 5.5).

The age-depth model of core 19.DV.17 using the two radiocarbon dates estimates the deposition of sand bed F between 986 AD and 1276 AD (746 to 1036 years ago), sand bed E between 1311 AD to 1444 AD (578 to 711 years ago) and sand bed D between 1545 AD and 1965 AD (57 to 477 years ago) (Figure 5.9 and Tables 5.2 and 5.5). The base of core 19.DV.17 is estimated between 508 AD and 927 AD (1514 to 1095 years ago) (Figure 5.9 and Tables 5.2 and 5.5).

Table 5.5 Modelled ages for sand beds D, E, and F from a Bayesian Age-Depth model for core 19.DV.17 from Deranged Valley, Nagai Island, Alaska. Produced from radiocarbon ages using P-sequence in OxCal 4.4 (Bronk Ramsey, 2008; Padgett et al., 2021). μ, mean; σ, one standard deviation; m, mode. Negative values= BC and positive values= AD. Note that the estimated ages for the sand beds are taken from the maximum and minimum ages of the upper and lower contacts of the sand beds.

	From (BC/AD)	To (BC/AD)	%	μ	σ	*m*
Sand Bed D Base	1545	1747	95.4	1644	51	1643
Sand Bed D Surface	1788	1965	95.4	1881	45	1885
Sand Bed E Base	1311	1372	95.4	1340	15	1340
Sand Bed E Surface	1400	1444	95.4	1422	11	1423
Sand Bed F Base	986	1212	95.4	1106	58	1112
Sand Bed F Surface	1125	1276	95.4	1206	40	1212
Sand Bed D	1545	1965	N/A	N/A	N/A	N/A
Sand Bed E	1311	1444	N/A	N/A	N/A	N/A
Sand Bed F	986	1276	N/A	N/A	N/A	N/A

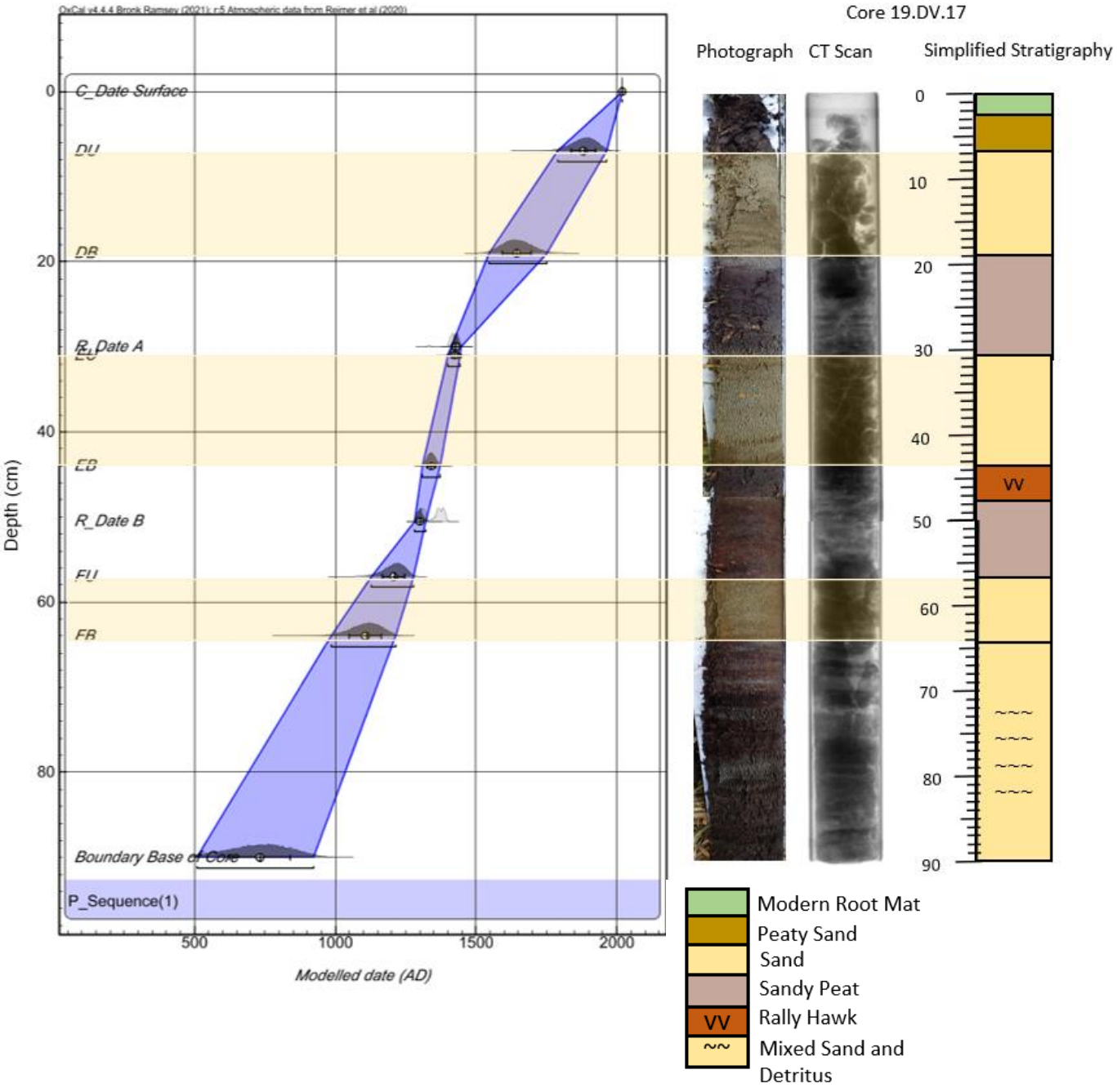

Figure 5.9. Age-Depth Model for 19.DV.17 using the P-sequence in OxCal 4.4 (Appendix Figure S1) alongside the core photograph, x-ray image and simplified lithostratigraphy (Bronk-Ramsey, 2021).

5.4 Diatom Analysis of DV.19.03

DV.19.03 exhibits a diverse range of diatoms with 192 diatom species identified (138 freshwater species, 27 brackish species, 26 marine species and 1 species with unknown salinity preferences). 86 diatom species account for at least 1.5 % of the total diatom count in at least one diatom sample in DV.19.03. DV.19.03 displays overall diatom freshening from the base of the core to the surface (Table 5.6). The base of the core (between 154 cm and 164 cm) contains predominantly marine diatoms (ranging from 70.33 % to 90.66 % marine diatoms), switching to predominantly brackish diatoms between 128-152 cm (ranging from 36.95 % to 90.70 % brackish diatoms), except for at 129.5 cm and 135 cm where marine diatoms dominate (45.22 % and 38.89 % brackish diatoms respectively) (Table 5.6). Between 0.5 cm and 127.5 cm freshwater diatoms dominate ranging between 97.29 % freshwater diatoms at 0.5 cm to 48.93 % freshwater diatoms at 126.5 cm (Table 5.6). Although, the predominantly freshwater samples are intermittently interrupted by periods of brackish species domination between 95 cm and 110 cm (73.29 % to 81.71 % brackish diatoms) and at 126 cm (60.63 % brackish diatoms) (Table 5.6). The abundances of *Tabellaria floculosa* and *Pinnularia lagerstedii* most influence the freshwater diatom compositions in DV.19.03, the abundances of *Stauroforma exiguiformis* and *Diploneis interrupta* most determine the brackish diatom compositions in DV.19.03, and the abundance of *Delphineis surirella* and *Cocconeis Californica* dominate the marine diatom compositions in DV.19.03 (Figures 5.10 and 5.11).

Table 5.6. Percentage of freshwater, brackish and marine diatoms in core DV.19.03 including species greater than 1.5% of the total abundance. Green highlighted samples are where freshwater diatoms contribute the most to the diatom assemblage, orange highlighted samples are where brackish diatoms contribute the most to the diatom assemblage, and blue highlighted samples are where marine diatoms contribute the most to the diatom assemblage.

Depth (cm)	%Fresh/Olig-indifferent	% Brackish/Marine	% Marine
0.5	97.29	2.71	0.00
10	91.41	8.59	0.00
20	92.04	7.96	0.00
30	93.98	6.02	0.00
40	92.46	7.54	0.00
50	92.71	7.29	0.00
55	92.89	7.11	0.00
60	83.73	16.27	0.00
70	84.25	15.75	0.00
80	78.63	21.37	0.00
90	64.41	35.59	0.00
92	60.08	39.92	0.00
95	18.29	81.71	0.00
98	26.71	73.29	0.00
100	19.92	80.08	0.00
105	22.53	77.47	0.00
110	19.54	80.46	0.00
112	51.29	48.71	0.00
118	57.62	42.38	0.00
120	60.95	14.60	24.45
123	50.70	42.61	6.69
126	39.37	60.63	0.00
126.5	48.93	41.28	9.79
127	59.35	34.53	6.12
127.5	67.63	15.83	16.55
128	17.61	73.24	9.15
129	16.40	74.40	9.20
129.5	29.13	25.65	45.22
130	41.16	58.84	0.00
131	46.50	48.25	5.24
132	42.48	46.62	10.90
133	30.63	54.24	15.13
134	12.20	72.44	15.35
134.5	36.64	52.67	10.69
135	32.14	28.97	38.89
136	29.32	36.95	33.73
137	29.01	49.62	21.37
138	5.43	90.70	3.88
140	27.27	54.17	18.56
142	13.73	84.31	1.96
143	3.00	92.88	4.12
144	4.51	89.85	5.64
145	11.79	73.00	15.21
150	12.40	56.20	31.40
152	12.24	64.69	23.08
154	7.52	19.17	73.31
155	0.00	9.34	90.66
160	8.42	21.25	70.33
164	11.84	11.02	77.14

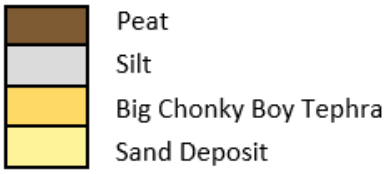

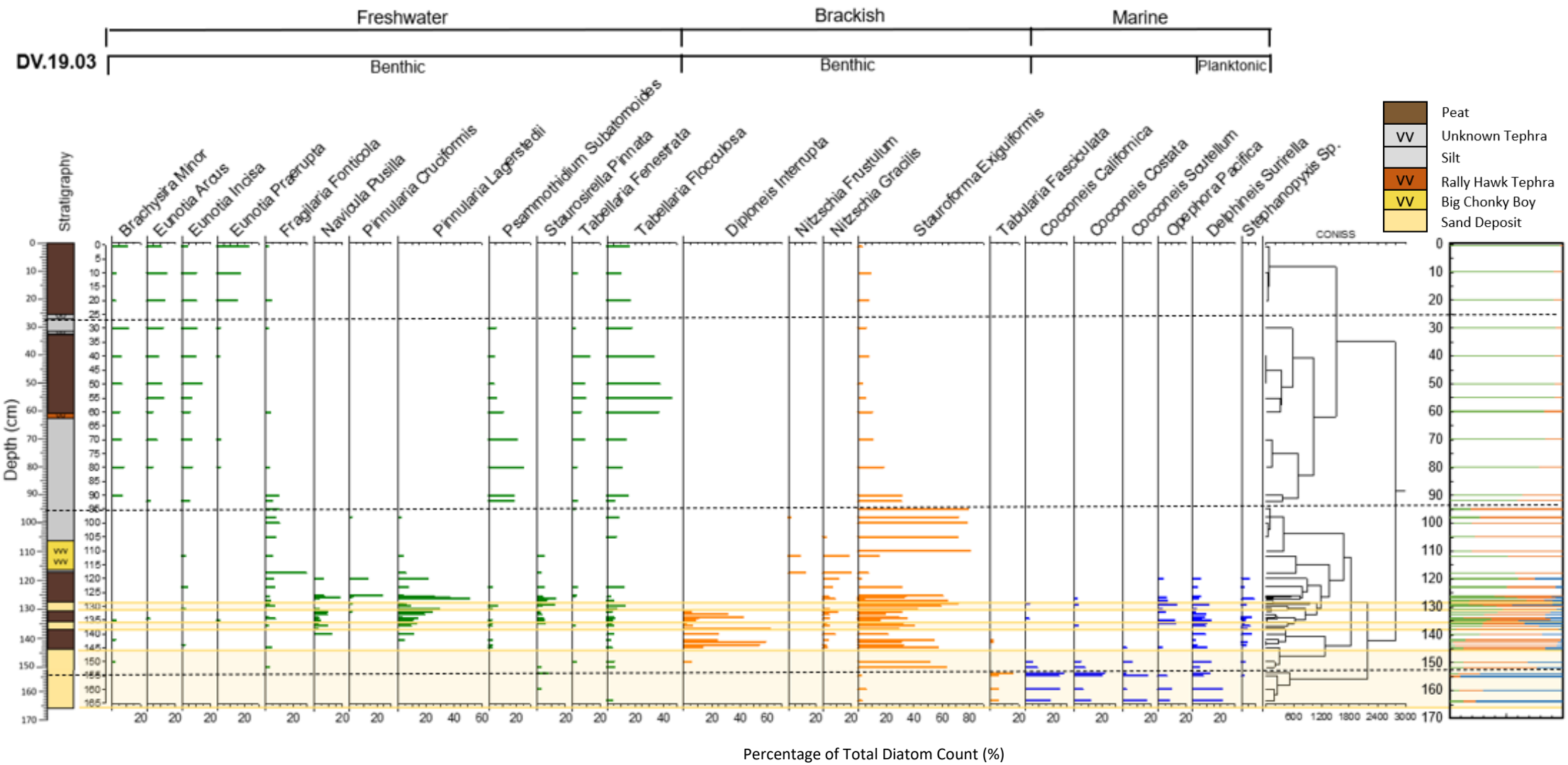

Figure 5.10. Diatom species accounting for more than 5% of the total diatom abundances for the entirety of DV.19.03. The green bars represent freshwater diatom species, the orange bars represent brackish diatoms, and the blue bars represent marine diatoms, and are divided into benthic and planktonic species. CONISS including diatom species accounting for more than 1.5% of total diatom abundance. %FBM is the percentage of freshwater, brackish and marine diatoms for species greater than 1.5% of the total diatom abundances. Dashed lines highlight the dominating clusters.

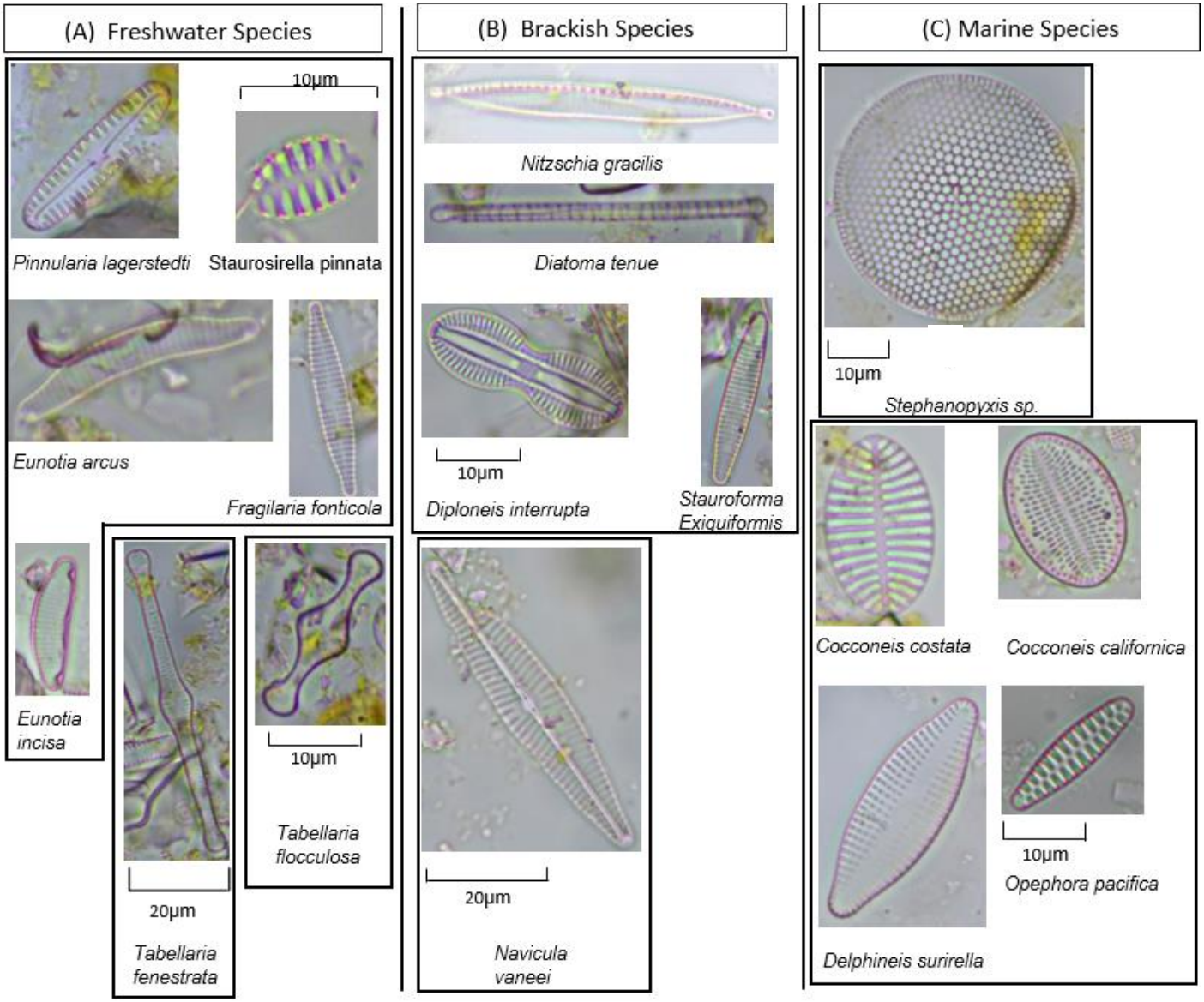

Figure 5.11. Common freshwater, brackish and marine diatoms identified in the Deranged Valley cores, Nagai Island using the GXMHICHROME-S camera and measured using the measuring tool and a 1 mm eyepiece graticule for calibration under 1000x magnification. N.B. the scales refer to all images within the same box.

5.4.1. Sand Bed C and Under and Overlying Units (DV.19.03)

The four samples in sand bed C, between 164 cm and 154 cm, are dominated by marine diatom species ranging from 70.33 to 90.66 % marine diatoms and the most common marine species are *Cocconeis californica, Cocconeis costata, Cocconeis scutellum* and *Delphineis surirella* (Table 5.6 and Figure 5.12). Whereas the four shallower samples in sand bed C, between 144 cm and 152 cm, are dominated by brackish species ranging from 56.20 % to 89.85 % brackish diatoms (Table 5.6 and Figure 5.5). The most notable differences causing the shift from the predominantly marine to predominantly brackish diatom compositions between the basal four samples and the shallower four samples in sand bed C are due to increases in *Stauroforma exiguiformis* from an average of 2.79 % to 55.68 %, increases in *Diploneis interrupta* from an average of 2.79 % to 55.68 %, and decreases in *Cocconeis californica* from an average of 25.83 % to 3.72 % and *Cocconeis costata* from an average of 25.83 % to 3.41 % (Figure 5.12).

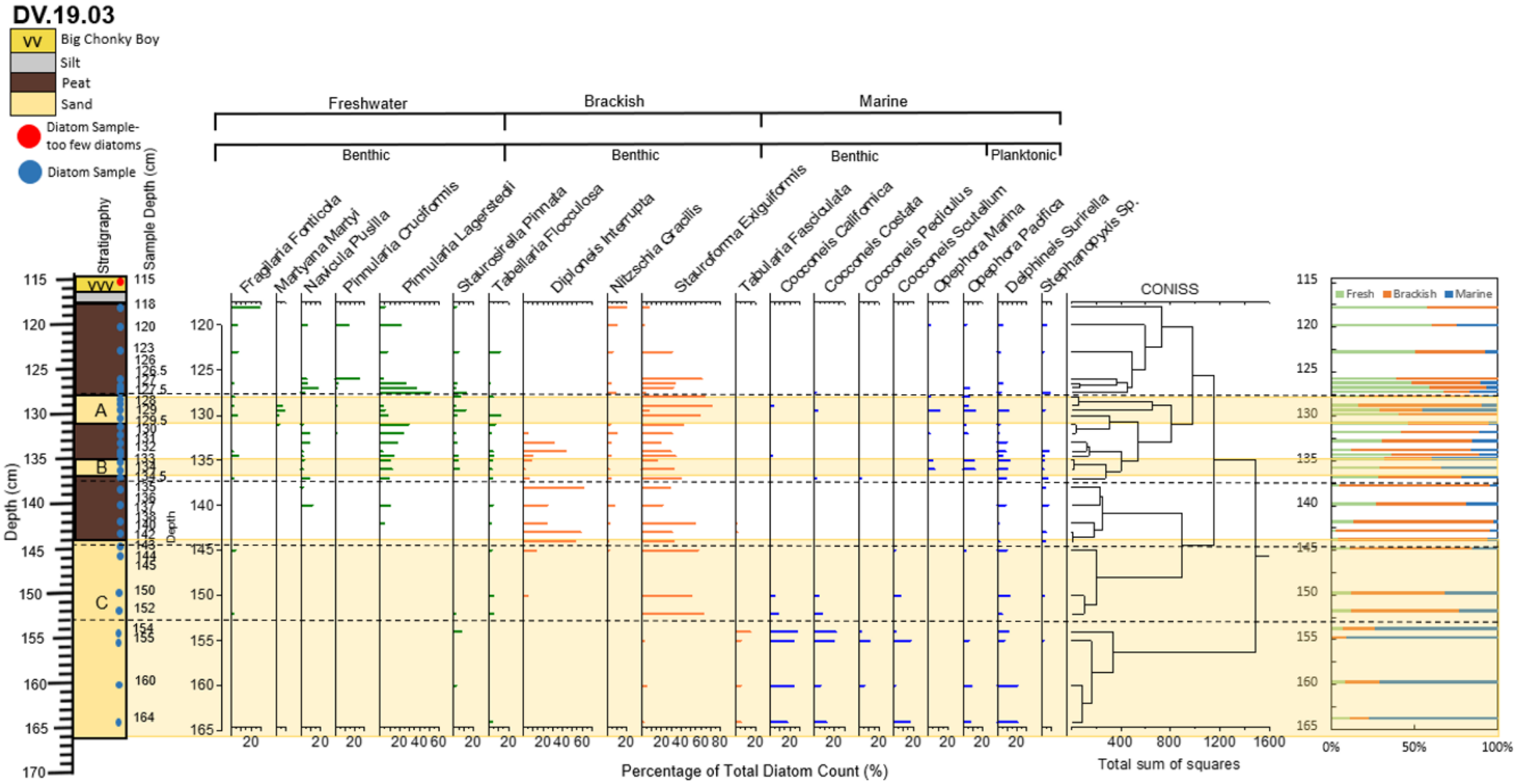

Figure 5.12. Diatom species accounting for more than 5 % of the total diatom abundances for samples between 115 cm-166 cm of DV.19.03. The green bars represent freshwater diatom species, the orange bars represent brackish diatoms, and the blue bars represent marine diatoms and are divided into benthic and planktonic species. CONISS including diatom species accounting for more than 1.5 % of total diatom abundance. % FBM is the percentage of freshwater, brackish and marine diatoms for species greater than 1.5 % of the total diatom abundances. Dashed lines highlight the dominating clusters.

Like the upper section of sand bed C (between 144-152 cm), the peat unit overlying sand bed C contains predominantly brackish diatoms ranging from 49.62 % to 92.88 % brackish diatoms and on average compared to the four shallowest samples in sand bed C, the samples from the overlying peat layer contains 3.4 % more brackish species (Table 5.6 and Figure 5.5). Generally, there are fewer marine diatoms and more freshwater diatoms in the overlying peat layer compared to sand bed C, though there are fluctuations (Table 5.6). For example, at 140 cm in the overlying peat layer there are more marine diatoms than at 144 cm and 145 cm in sand bed C (18.56 %, 5.64 % and 15.21 % respectively) (Table 5.6). *Stephanopyxis sp.* contributes the most to the marine diatoms in the overlying peat layer and contains abundances greater than in sand bed C, followed by *Delphineis surirella* at abundances lower than in sand bed C (Figure 5.12). Like the shallowest four samples in sand bed C, the diatom composition of the overlying peat unit is most influenced by the brackish species *Stauroforma exiguiformis* and *Diploneis interrupta* which account for an average abundance of 34.89 % and 34.81 % respectively (Figure 5.12).

The diatom lifeform composition is similar for both sand bed C and the overlying peat unit; benthic species dominate with average respective abundances of 85.35 % and 90.10 % compared to 13.05 % and 9.52 % average percentages respectively for planktonic species (Figure 5.5). Notably, the two deepest samples in sand bed C (164 cm and 160 cm) exhibit a much lower proportion of benthic species compared to the other samples from sand bed C and the overlying peat unit (77.29 % for 160 cm and 75.10 % for 164 cm), and much greater proportions of planktonic species (22.71 % for 160 cm and 20.81 % for 164 cm) (Figure 5.5).

The percentage of fractured diatoms greater than 40 µm averages 13.7% higher in sand bed C compared to the overlying peat unit (64.5 % and 50.8 % respectively), though both sand bed C and the overlying peat unit exhibit large fluctuations and display similar ranges (35-83 % in sand bed C and 33-84 % in the overlying peat unit) (Figure 5.5). The percentage of fractured diatoms greater than 40 µm does not consistently increase from the base to the surface of sand bed C (Figure 5.5).

5.4.2 Sand Bed B and Under and Overlying Units (DV.19.03)

The diatoms within the sand bed B samples differ from the sand bed C samples (Table 5.6). The diatom distributions in the two samples from sand bed B are similar in terms of the proportions of freshwater, brackish and marine diatom contributions (Table 5.6 and Figure 5.5). The basal sample from sand bed B (136 cm) contains predominantly brackish diatom

species (36.95 %) and the upper sample (135 cm) contains predominantly marine diatom species (38.89 %) (Table 5.6 and Figure 5.5). Notably, both the sand bed B samples have similar percentages of freshwater, brackish and marine diatoms (ranging between 29.32 % and 38.89 %), unlike the sand bed C samples which are either dominated by marine or brackish diatoms (Table 5.6 and Figure 5.5). Sand bed B contains fewer brackish diatoms compared to the four shallower samples in sand bed C (averaging 32.96 % and 70.94 % respectively), fewer marine diatoms compared to the four deeper samples from sand bed C (averaging 36.31 % and 77.86 % respectively), and greater freshwater diatoms compared to all sand bed C samples (averaging 30.73 % and 8.59 % respectively) (Table 5.6 and Figure 5.5).

Key diatom differences between sand bed C and sand bed B are firstly, the contribution from the freshwater species *Pinnularia lagerstedii* and *Navicula pusilla,* which do not account for more than 1.5 % of the total diatom counts in any of the sand bed C samples yet contribute on average 11.71 % and 2.78 % respectively to the sand bed B samples (Figure 5.12). Secondly, there is an absence of the marine diatom species *Cocconeis californica, Cocconeis costata, Cocconeis pediculus* and *Cocconeis scutellum* in sand bed B which dominate the diatom assemblages in sand bed C, especially the four basal samples (up to 27.44 % of the total abundance) (Figure 5.12). Like sand bed C, *Stauroforma exiguiformis* and *Diploneis interrupta* are the greatest contributors to the brackish diatom species in sand bed B (Figure 5.12). However, the percentages of *Stauroforma exiguiformis* and *Diploneis interrupta* differ between sand bed C and sand bed B; the two sand bed B samples (135 cm and 136 cm) contain 15.87 % and 32.14 % *Stauroforma exiguiformis* and 8.33 % and 1.98 % *Diploneis interrupta* respectively which is greater than the basal four samples from sand bed C (averaging 3.38 % for *Stauroforma exiguiformis* and *Diploneis interrupta* was absent) and notably lower than the shallower four samples from sand bed C (averaging 50.66 % for *Stauroforma exiguiformis* and 24.15 % for *Diploneis interrupta*) (Figure 5.12). *Opephora pacifca, Opephora marina, Dimeregramma minor var. nana* and *Delphineis surirella* contribute the greatest to the marine species in sand bed B; *Opephora pacifca* and *Opephora marina* exhibit greater percentages in sand bed B than in sand bed C (averaging 11.90 % and 5.02 % respectively in sand bed B), *Delphineis surirella* has similar abundances within both sand bed B and C (averaging 11.31 % in sand bed B and 11.35 % in sand bed C), and *Dimeregramma minor var. nana* exhibits lower percentages in sand bed B compared to sand bed C (averaging 6.73 % and 3.57 % respectively) (Figure 5.12).

The peat unit underlying sand bed B exhibits greater percentages of brackish species compared to sand bed B (ranging from 49.62 % to 92.88 % in the underlying peat unit and 28.97 % to 36.95 % in sand bed B), and lower percentages of freshwater and marine species compared to sand bed B (Table 5.6). The freshwater diatom percentages range from 3.00 % to 29.01 % in the underlying peat unit and 29.32 % to 32.14 % in sand bed B, and the marine diatom percentages range from 1.96 % to 21.37 % in the underlying peat unit compared to 33.73 % to 38.89 % in sand bed B (Table 5.6). Interestingly, samples 137 cm and 140 cm are distinct from the other samples in the underlying peat layer and contain similar distributions of freshwater, brackish and marine diatoms to sand bed B as well as similar species contributing to the diatom compositions (*Tabellaria floculosa, Pinnularia lagerstedii, Navicula pusilla, Stauroforma exiguiformis, Diploneis interrupta, Delphineis surirella* and *Stephanopyxis sp.* (Table 5.6 and Figure 5.12).

Most notably, compared with the underlying peat layer, sand bed B contains a greater proportion of *Pinnularia lagerstedii* (11.78 % in sand bed B and 4.97 % in the underlying peat layer) accounting for the increase in freshwater diatoms in sand bed B (Figure 5.12). Sand bed B exhibits fewer *Diploneis interrupta* (averaging 34.87 % in the overlying peat compared to 5.17 % in sand bed B), and fewer *Stauroforma exiguiformis* compared to the underlying peat layer (averaging 25.20 % in sand bed B and 35.12 % in the underlying peat) accounting for the decrease in brackish diatoms in sand bed B (Figure 5.12). Further, sand bed B exhibits more *Opephora pacifica* (averaging 11.98 % in sand bed B compared to 0.00 % in the underlaying peat), *more Opephora marina* (averaging 5.02 % in sand bed B compared to 0.00 % in the underlaying peat), and more *Delphineis surirella* compared to the underlying peat layer (averaging 11.37 % in sand bed B compared to 3.89 % in the underlaying peat) accounting for the increase in marine diatoms in sand bed B compared to the underlying peat layer (Figure 5.12).

The peat layer overlying sand bed B exhibits notable intra layer variation both in terms of the percentage of freshwater, brackish and marine diatoms as well as species abundances (Table 5.6 and Figure 5.12). Compared to sand bed B, the peat layer overlying sand bed B exhibits greater percentages of brackish diatoms (on average 54.84 % brackish diatoms), though lower percentages of brackish diatoms compared to the underlying peat layer (on average 74.34 % brackish diatoms) (Table 5.6). The peat layer overlying sand bed B contains slightly greater percentages of freshwater diatoms compared to sand bed B (33.69 % and 30.73 % on average respectively), though the overlying peat layer contains considerably greater freshwater diatoms compared to the peat layer underlying sand bed B

(33.69 % and 15.69 % on average respectively) (Table 5.6). Further, the peat layer overlaying sand bed B is on average 24.85 % less marine than sand bed B, though on average 1.48 % more marine than the peat layer underlying sand bed B (Table 5.6). The ranges within the samples from sand bed B for the percentages of freshwater, brackish and marine diatoms are much less than those exhibited in sand bed C and the peat units overlying and underlying sand bed B (Table 5.6). The ranges are between 2.82 % and 7.98 % in sand bed B compared to between 12.4 % and 85.02 % in sand bed C, between 19.41 % and 43.26 % in the peat layer overlying sand bed C and underlying sand bed B and between 10.11 % and 25.82 % in the peat layer overlying sand bed B (Table 5.6).

The greater percentage of freshwater diatoms in the peat layer overlying sand bed B is primarily due to greater contributions from *Pinnularia lagerstedii* and *Navicula Pusilla* (17.76 % and 5.29 % average total contributions) (Figure 5.12). Though, there is a large range *Pinnularia lagerstedii* and *Navicula Pusilla* abundances within the overlying peat layer (26.27 % range for *Pinnularia lagerstedii* and 6.55 % range for *Navicula pusilla*) (Figure 5.12). The greatest difference in the freshwater diatoms between the peat layer overlying sand bed B and the underlying peat is the greater contribution of *Pinnularia lagerstedii* in the overlying peat (17.76 % and 4.97 % respectively) (Figure 5.12).

The brackish species, *Stauroforma exiguiformis,* accounts for a large percentage of the overall diatom counts in the peat layer overlying sand bed B, though there is considerable intra layer variation, ranging from 19.19 % to 42.66 % of the total diatom count. On average the overlying peat layer contains more *Stauroforma exiguiformis* than in sand bed B and less than the underlying peat layer (on average 31.46 % in the overlying peat, 24.20 % in sand bed B, and 35.12 % in the underlying peat) (Figure 5.12). The brackish species, *Diploneis interrupta,* on average exhibits greater percentages in the overlying peat layer compared to sand bed B (17.89 % and 5.17 % average contribution respectively) (Figure 5.12). Though, the average increase in *Diploneis interrupta* between sand bed B and the overlying peat is dominated by samples at 133 cm and 134 cm which contain 31.37 % and 42.91 % *Diploneis interrupta* respectively, compared to the 0.00 % to 9.92 % for the other samples within the overlying peat unit (Figure 5.12). Further, the percentage of *Diploneis interrupta* in the peat layer overlying sand bed B contributes less on average compared to the peat layer underlying sand bed B (17.89 % and 34.87 % average respective contributions) (Figure 5.12).

*Delphineis surirella i*s the greatest contributor to the marine diatoms in the overlying peat layer, though on average contributes less than exhibited in sand bed B (5.51 % and 11.37

% respective average contributions) (Figure 5.12). There is a notable decrease in the presence of *Opephora pacifica and Opephora marina* in the overlying peat layer compared to sand bed B where the overlying peat averages 1.61 % and 0.38 % respective contributions from *Opephora pacifica and Opephora marina,* compared to sand bed B which exhibits 5.82 % and 4.99 % respective contributions from *Opephora pacifica and Opephora marina* (Figure 5.12).

Benthic diatoms dominate the lifeforms of sand bed B (averaging 86.44 %) compared to an average of 90.84 % benthic species in the peat layer overlying sand bed B and 90.10 % average benthic species in the peat layer underlying sand bed B (Figure 5.5). The average percentage of planktonic species is slightly greater in sand bed B compared to the peat layer over and underlying sand bed B (13.56 % compared to 7.46 % and 9.52 % respectively) (Figure 5.5). The average percentage of benthic and planktonic species in sand bed B are similar to sand bed C, though the range in benthic and planktonic species in sand bed B is much less than the ranges in sand bed C and the peat layers under and overlying sand bed B (Figure 5.5).

The percentages of fractured diatoms greater than 40 µm within sand bed B are similar between samples, ranging from 80.00 % to 87.00 % and are 19.00 % on average more fractured than in sand bed C, 32.7 % on average more fractured than the peat layer underlying sand bed B, and 19.3 % on average more fractured than the peat layer overlying sand bed B (Figure 5.5). However, the samples directly above and below sand bed B display similar fracturing to the samples within sand bed B (81.00 % and 84.00 % respectively compared to 80.00 % and 87.00 % within sand bed B) (Figure 5.5). The percentage of fractured diatoms greater than 40 µm increases from 80.00 % at the base of sand bed B to 87.00 % at the surface of sand bed B (Figure 5.5).

5.4.3 Sand Bed A and Under and Overlying Units (DV.19.03)

Three out of the four samples in sand bed A (128 cm, 129 cm and 130 cm) contain predominantly brackish species, ranging from 58.84 % at 130 cm to 74.40 % at 129 cm, followed by freshwater diatoms ranging from 41.16 % at 130 cm to 16.4 % 129 cm (Table 5.6). The contribution of marine diatoms in 128 cm, 129 cm and 130 cm is small (0.00 to 9.00 %). Interestingly, the diatom composition of sample 129.5 cm is considerably different to the other three samples in sand bed A with 45.22 % marine diatoms, 25.65 % brackish diatoms, and 29.13 % freshwater diatoms (Table 5.6). Samples 128 cm, 129 cm and 130 cm within sand bed A are unique compared to sand beds B and C (Table 5.6). Despite a

similar average abundance of brackish species compared to the shallowest four samples in sand bed C (68.83 % and 70.94 % respectively), 128 cm, 129 cm and 130 cm differ in terms of marine average abundances (6.12 % and 18.83 % respectively) and freshwater average abundances (25.06 % and 10.24 % respectively) (Table 5.6). Sample 129.5 cm is most similar to sample 135 cm in sand bed B (Table 5.6).

Like sand bed B, *Pinnularia lagerstedii* and *Staurosirella pinnata* are key contributors to the freshwater diatoms in sand bed A (averaging 4.48 % and 5.94 % of the total diatom counts in sand bed A) (Figure 5.12). The freshwater species *Martyana martyi* is not present in either sand bed B or C but accounts for 4.40 % of the total diatom counts in sand bed A (Figure 5.12). Sand bed A is dominated by the brackish species *Stauroforma exiguiformis* which averages 50.59 % of the total diatoms and is much greater than the average contributions from sand beds B and C (24.20 % and 26.64 % respectively), although similar to the four shallowest samples in sand bed C (50.78%) (Figure 5.12).

The brackish species, *Diploneis interrupta,* is a key contributor to the diatom abundances in sand beds B and C (averaging 5.17 % and 9.05 % respectively), though it is not present in any of the sand bed A samples (Figure 5.12).

Like sand bed B, *Opephora pacifica and Opephora marina* are key contributors to the marine diatom abundances in sand bed A (averaging 6.43 % and 3.44 % of the total diatom counts respectively) (Figure 5.12). *Cocconeis californica, Cocconeis costata,* and Cocconeis *scutellum* which average 13.25 %, 8.93 % and 5.88 % of the total diatom counts respectively in sand bed C are present in low abundances in sand bed A (averaging between 0.00 % to 0.8 % of the total diatom count) (Figure 5.12). Similarly, *Delphineis surirella* which account on average for 11.37 % and 11.35 % of the total diatoms in sand beds B and C respectively is only present in 129.5 cm in sand bed A (Figure 5.12).

The peat layer overlying sand bed A exhibits much greater percentages of freshwater diatoms (averaging 54.93 % compared to averages between 8.59 %-33.69 % for sand beds A, B, and C, and the two other peat layers analysed) and exhibits a drastic 50.02 % increase between the uppermost sample in sand bed A and the deepest sample in the overlying peat (Table 5.6). The peat layer overlying sand bed A contains predominantly freshwater diatoms (ranging between 48.93 % to 67.63 %), except for 126 cm which contains predominantly brackish diatoms (60.63 %) (Table 5.6). Like the other two peat layers below, the peat overlying sand bed A exhibits notable intra layer variations in terms of the proportions of

freshwater, brackish and marine diatoms and the species abundances (Table 5.6 and Figure 5.12).

The percentage of brackish species in the peat overlying sand bed A is considerably lower than that in sand bed A, especially sample 127.5 cm, which contains 15.83 % brackish diatoms compared to sample 128 cm in sand bed A which contains 73.24 % brackish diatoms (Table 5.6). Further, the percentage of brackish species in the overlying peat unit is notably less on average than the peat which underlies sand bed A (35.98 % compared to 54.84 %) (Table 5.6). The range of brackish species is large within the peat overlying sand bed A (ranging from 15.83 % at 127.5 cm to 60.63 % at 126 cm) (Table 5.6). The percentage of marine diatoms in the overlying peat unit displays notable variation within the layer between 0.00 % at 118 cm and 126 cm to 24.45 % at 120 cm, and like sand bed A and the underlying peat unit, the marine species generally account for the fewest diatoms (Table 5.6).

The considerable increase in freshwater diatoms between sand bed A and the peat which overlies sand bed A is mostly contributed to by an increase in *Pinnularia lagerstedii* in the overlying peat (21.76 % average contribution in the overlying peat compared to 4.48 % average contribution in sand bed A), an increase in *Navicula pusilla* (5.88 % and 0.00 % average respective contributions), and *Pinnularia cruciformis* (5.96 % and 0.60 % average respective contributions) (Figure 5.12). The 21.25 % average increase in freshwater diatoms between the peat layer which underlies sand bed A and the peat which overlies sand bed A is mostly accounted for by increases in *Pinnularia cruciformis* (on average 5.36 % increase), *Pinnularia lagerstedii* (on average 4.00 % increase) and *Fragilaria fonticola* (on average 3.15 % increase) (Figure 5.12). Interestingly, *Navicula pusilla* is a key contributor to freshwater diatoms in both the peat over and underlying sand bed A (5.88 % and 5.29 % respective average contribution) but is not present in any of the samples in sand bed A (Figure 5.12).

The notable decrease in brackish species between sand bed A and the overlying peat unit is accounted for by a considerable decrease in *Stauroforma exiguiformis* (24.68 % average contribution in the overlying peat compared to 50.59 % average contribution in sand bed A), though this is partially offset by a general increase in the brackish species *Nitzschia gracilis* in the overlying peat layer compared to sand bed A (7.01 % and 0.00 % respective contributions) (Figure 5.12). Notably, the peat which underlies sand bed A contains on average 17.89 % *Diploneis interrupta* whereas no samples in the peat which overlies sand bed A contain *Diploneis interrupta* (Figure 5.12). The generally fewer marine diatoms in the overlying peat unit compared to sand bed A is primarily due to a decrease in *Opephora*

pacifica (1.39 % average contribution in the overlying peat compared to 6.43 % average contribution in sand bed A) (Figure 5.12). The anomalously large percentage of marine diatoms at 126 cm in the peat overlying sand bed A is primarily due to the presence of *Delphineis surirella* (5.47 % of total diatoms), *Stephanopyxis sp.* (5.11 % of total diatoms), *Thalaaiosira gracilis* (4.01 % of total diatoms), and *Navicula distans* (3.65 % of total diatoms) (Figure 5.12). Further, the anomalously large percentage of marine diatoms at 127.5 cm in the peat overlying sand bed A is primarily due to the presence of *Stephanopyxis sp.* (8.63 % of total diatoms), *Delphineis surirella* (3.60 % of total diatoms) and *Rhaphoneis amphiceros* (2.52 % of total diatoms) (Figure 5.12).

Benthic diatoms dominate the lifeforms of sand bed A samples averaging 90.98 % which is on average greater than the contribution of benthic diatoms in sand bed B and C (86.44 % and 85.35 % respectively) (Figure 5.5). In sand beds A, B and C the composition of benthic and planktonic diatoms are similar, though sand beds B and C are most similar with only a 1.08 % difference in benthic diatoms and a 0.51 % difference in planktonic diatoms (Figure 5.5). Sand beds A and C have greater intra layer variation in the percentage of benthic and planktonic diatoms compared to sand bed B, where benthic diatoms and planktonic diatoms exhibit 21.95 % and 14.35 % respective ranges in sand bed A, 17.38 % and 17.82 % respective ranges in sand bed C and 3.03 % and 3.03 % respective ranges in sand bed B (Figure 5.5). Notably in sand bed A, only sample 129.5 cm contains planktonic species (14.35 %) (Figure 5.5). Sand bed A contains 7.83 % more benthic diatoms and 5.27 % fewer planktonic diatoms than the overlying peat unit, and 0.14 % more benthic diatoms and 3.88 % fewer planktonic diatoms compared to the underlying peat unit (Figure 5.5).

The percentages of fractured diatoms greater than 40 µm within sand bed A are consistent between samples (ranging from 79-82 %) and are on average 16.25 % more fractured than sand bed C and 2.75 % less fractured than sand bed B (Figure 5.5). Compared to the peat unit underlying sand bed A, sand bed A is on average 16.55 % more fractured, though samples 131 cm and 132 cm directly below sand bed A average only 0.75 % less fractured than sand bed A (Figure 5.5). The peat layer overlying sand bed A is 3.96 % more fractured than sand bed A and 20.51 % more fractured than the peat underlying sand bed A (Figure 5.5). The percentage of fractured diatoms greater than 40 µm does not consistently increase from the base to the surface of sand bed A (Figure 5.5).

5.4.4 Surface Peat and Silt (Top 117.5cm of Core DV.19.03)

The top 117.5 cm of DV.19.03 does not contain any marine diatom species at abundances greater than 1.5 % of the total diatom counts (Table 5.6 and Figure 5.10). The silt between 95 cm and 105 cm and the upper sample of the *Big Chonky Boy Tephra* (110 cm) are dominated by brackish diatoms ranging from 73.29 % to 81.71 % brackish, (Table 5.6). Sample 112 cm from the *Big Chonky Boy* tephra contains 31.75 % fewer brackish diatoms than sample 110 cm (the shallower sample from the *Big Chonky Boy* tephra) and exhibits primarily freshwater diatoms (51.29 %) (Table 5.6). The peat and silt layers between 0.5 cm and 92 cm contain predominately freshwater diatoms and generally the percentage of freshwater diatoms increases with decreasing depth ranging from 60.08 % freshwater diatoms at 92 cm to 97.29 % freshwater diatoms at 0.5 cm (Table 5.6).

The brackish diatoms exhibiting more than 1.5 % of the total diatom counts between 0.5 cm and 117.5 cm are all oligohalobous-halophilous rather than mesohalobous (Figure 5.10). Further, there is a notable absence of *Pinnularia lagerstedii* and *Navicula pusilla* in the top 117.5 cm of DV.19.03, which are key contributors to the freshwater diatoms in the underlying layers (Figure 5.10). Between 95 cm and 110 cm where brackish diatoms prevail, *Stauroforma exiguiformis* completely dominates contributing between 71.15 % and 80.46 % of the total diatom counts, greater than any other part of the core (Figure 5.10). *Fragilaria fonticola* contributes greatest to the freshwater diatom assemblages between 95 cm and 110 cm (averaging 4.43 % of the total diatom count) (Figure 5.10). A large sudden decrease in *Stauroforma exiguiformis* accounts for the change from predominately brackish diatoms between 95 cm and 110 cm to majority freshwater diatoms between 0.5 cm and 92 cm (Figure 5.10). The sample at 95 cm contains 78.99 % *Stauroforma exiguiformis* compared to 30.65 % at 92 cm (Figure 5.10). The percentage of *Stauroforma exiguiformis* decreases with decreasing depth from 30.65 % of the total diatom count at 92 cm to 2.71 % at 0.5 cm (Figure 5.10). *Tabellaria floculosa* (averaging 21.52 % of the total diatom count), *Psammothidium subatomoides* (averaging 9.23 % of the total diatom count), Eunotia arcus (averaging 8.01 % of the total diatom count), Eunotia Incisa (averaging 7.54 % of the total diatom count), and Brachysira minor (averaging 5.56 % of the total diatom count) are the greatest contributors to the freshwater diatom abundances between 0.5 cm and 92 cm in DV.19.03 (Figure 5.10). Between 0.5 cm and 20 cm, there are notably greater abundances of the halophobous species *Eunotia praerupta* (18.37 % average abundance between 0.5 cm and 20 cm), *Eunotia arcus* (12.19 % average abundance between 0.5 cm and 20 cm)

and *Eunotia lunaris* (5.67 % average abundance between 0.5 cm and 20 cm) compared to the underlying samples (Figure 5.10).

There are no considerable changes in the proportion of benthic and planktonic diatoms within the top 117.5 cm of DV.19.03 (ranging from 79.34 % and 100 % and 0.00 % to 16.24 % respectively) (Figure 5.6). The proportions of benthic diatoms between 0.5 cm and 117.5 cm are similar to the underlying layers especially sand bed A, the peat layer underlying sand A and the peat layer overlying sand bed B (averaging 90.75 %, 90.99 %, 90.84 % and 90.10 % respectively) (Figure 5.6). The percentages of planktonic diatoms between 0.5 cm and 117.5 cm are similar to the underlying layers, though exhibit a greater range compared to the benthic species due to differences in unknown lifeforms of species (Figure 5.6).

The percentage of fractured diatoms in the top 117.5 cm of DV.19.03 displays considerable fluctuations ranging between 24.29 % at 100 cm to 77.20 % at 112 cm and a weak correlation between percentage of fracturing and depth (-0.194) (Figure 5.6).

5.4.5 CONISS Cluster Analysis of DV.19.03

Sand bed C displays three clusters in CONISS, classifying statistically distinct diatom assemblages within sand bed C (Figure 5.12). The four basal samples in sand bed C cluster together and are statistically different from the four shallower samples from sand bed C (Figure 5.12). Further, the four basal samples from sand bed C display the second largest cluster dissimilarity from the entirety of DV.19.03 (Figure 5.10). Three of the four samples from the top of the sand bed C cluster together (Figure 5.12). The shallowest sample in sand bed C (144 cm) clusters strongly with four out of the five samples from the overlying peat unit (Figure 5.12). The shallowest sample from the overlying peat layer clusters strongly with the samples from sand bed B as opposed to the other samples from the overlying peat layer (Figure 5.12).

Sand bed B samples cluster closely together followed by a cluster with the shallowest sample from the underlying peat unit and a cluster with the three deepest samples in the overlying peat unit (Figure 5.12). Sand bed B clusters least strongly with the 4 samples from the underlying peat unit (138-143 cm) (Figure 5.12).

The four samples in sand bed A are part of three clusters in CONISS: sample 130 cm clusters most strongly with the two shallowest samples in the underlying peat unit, though with a relatively large horizontal difference (Figure 5.12). Sample 129.5 cm does not cluster closely with any of the samples in sand bed A, though is more similar to samples 128 cm

and 129 cm than sample 130 cm (Figure 5.12). Samples 128 cm and 129 cm cluster closely but are dissimilar to the other samples in sand bed A and even more dissimilar to the sample in the overlying peat layer (Figure 5.12).

The samples between 0.5 cm and 92 cm cluster most strongly away from the underlying samples, though with clear clusters within (Figure 5.10). The three shallowest samples (0.5 cm,10 cm and 20 cm) cluster strongly together with similar horizontal axis as do the samples between 95 cm and 105 cm (Figure 5.10). The top 117.5 cm display smaller horizontal axis compared to the samples between 117.5 cm and 164 cm (Figure 5.10).

5.4.6 DCA of DV.19.03

DCA groups 155 cm, 160 cm and 164 cm from sand bed C together, though the fourth sample (154 cm) that exhibits similar proportions of marine, brackish and freshwater diatom compositions is grouped apart (Figure 5.13). The four shallower samples from sand bed C do not strongly group together (Figure 5.13). Further, the samples from the overlying peat layer display similar axis one values (1.5-2.0) but a larger range for axis two (1.0-2.8), so do not produce a strong grouping (Figure 5.13). The four shallowest samples from sand bed C display a similar grouping to the overlying peat layer samples and are more similar to the overlying peat layer than the four samples from the base of sand bed C (Figure 5.13).

DCA groups the sand bed B samples closely as well as closely to the over and underlying peat layers (Figure 5.13). Both the under and overlying peat layers exhibit small axis one ranges (0.6 and 0.2 respectively) and wider axis two ranges (1.6); with the underlying peat layer plotting slightly higher on axis two than the overlying peat layer (Figure 5.13. Contrastingly sand bed B samples have a greater axis one range (0.8) and a lower axis two range (0.1) (Figure 5.13).

DCA does not group sand bed A samples closely, except for 129 cm and 129.5 cm, nor does it group samples from sand beds A, B and C closely (Figure 5.13). Sample 128 cm groups closely with four of the samples from the overlying peat layer, though sample 130 cm does not group closely with the underlying peat layer (Figure 5.13). Sand bed A samples have a large axis one and axis two range (1.20 and 1.15 respectively) (Figure 5.13). The samples from the peat layer underlying sand bed A group closely in axis one but have a wide axis two range (1.60) (Figure 5.13). The samples from the peat overlying sand bed A have a close grouping for the four deepest samples whereas the three shallowest samples plot similar axis two values to the four deepest samples but much lower axis one values (0.00-1.20 axis one values for the three shallowest samples compared to 1.50-1.65 for the

four deepest samples) (Figure 5.13). Further, the three shallowest samples from the peat unit overlying sand bed A do not plot closely to any samples from any other deeper layers (Figure 5.13).

DCA groups the shallowest 12 samples (between 0.5 cm and 92 cm) from DV.19.03 together and away from the other samples (Figure 5.14). The samples between 0.5cm and 92 cm plot considerably lower on axis one compared to all the other samples from DV.19.03 (0.00-2.20) and have a large axis one range (2.20), though a small axis two range (0.30) (Figure 5.14). Samples 95 cm to 122 cm plot closely together and plot higher axis one values (2.55-2.90), and higher axis two values (2.35 to 2.55) compared to the samples between 0.5 cm and 92 cm (Figure 5.14).

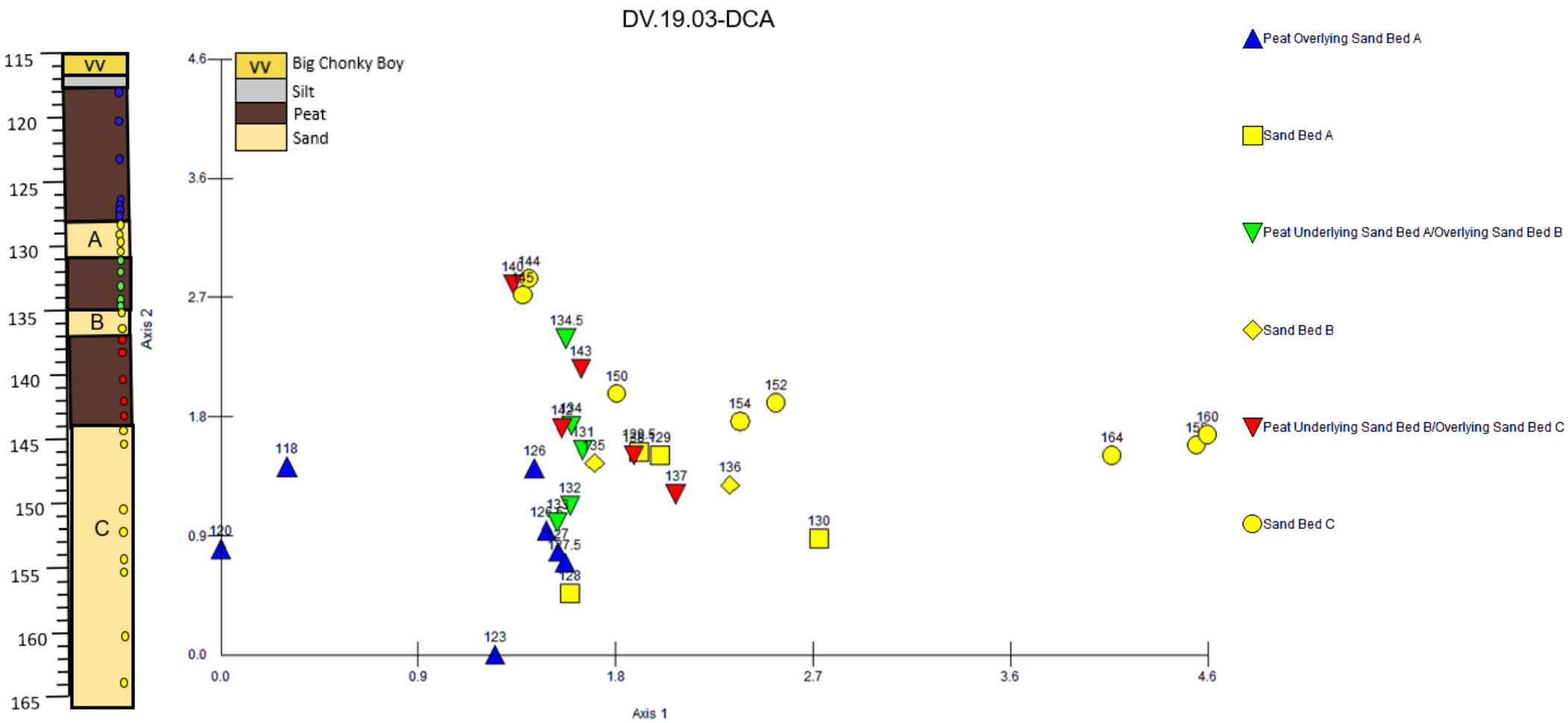

Figure 5.13. DCA biplot for diatom samples between 115 cm-166 cm of DV.19.03. N.B. Only diatom species accounting for more than 1.5 % of the total abundance are included in the analysis.

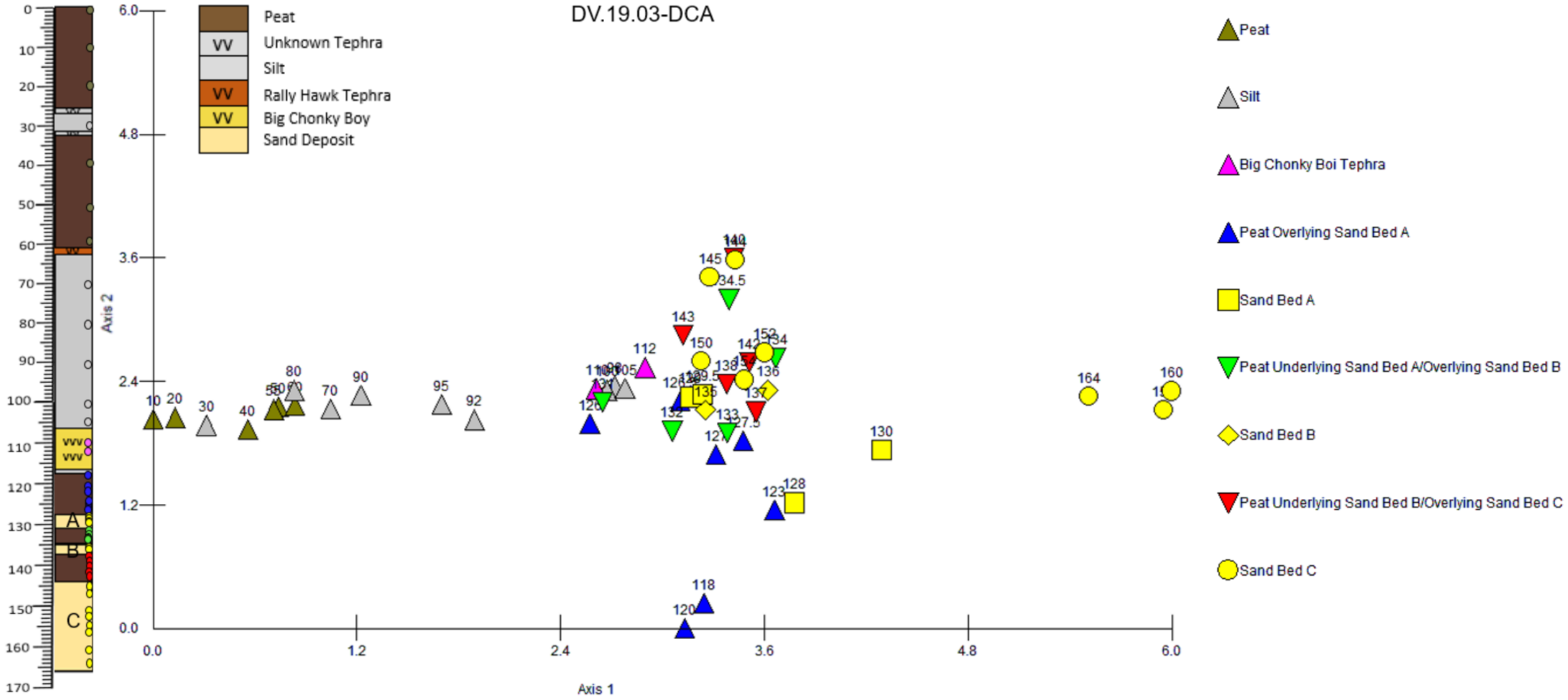

Figure 5.14. DCA biplot for all diatom samples from DV.19.03. N.B. Only diatom species accounting for more than 1.5 % of the total abundance are included in the analysis.

5.5 Diatom Analysis of 19.DV.17

Core 19.DV.17 is a tidal habitat, less diverse than DV.19.03, with 113 diatom species identified (76 freshwater species, 14 brackish species, 20 marine species and 3 species with unknown salinity preferences). 42 diatom species account for at least 1.5 % of the total diatom count in at least one sample in 19.DV.17. All but three samples in 19.DV.17 contain primarily marine diatoms ranging from 45.61 % marine diatoms at 44 cm to 83.09 % at 70cm (Table 5.7). Three isolated samples exhibit primarily freshwater diatoms (50.97 % freshwater diatoms at 21 cm, 45.49 % freshwater diatoms at 32 cm, and 55.77 % freshwater diatoms at 43 cm) (Table 5.7).

Like DV.19.03 there is overall freshening from the base of 19.DV.17 to the surface, though at a much shallower rate and with much greater fluctuation than in DV.19.03 (Tables 5.6 and 5.7). Brackish diatoms account for small percentages of the total diatom counts throughout the entirety of 19.DV.17 with a much lower range than in DV.19.03 (ranging from 3.39 % to 22.08 % in 19.DV.17 compared to 2.71 % and 92.88 % in DV.19.03) (Tables 5.6 and 5.7). For all samples between 0 cm and 63 cm, the proportion of brackish species contribute the least to the overall diatom counts and between 64 cm and 80 cm, the brackish species account for a greater proportion of the diatom assemblages than the freshwater species, though considerably less than the percentage of marine species (Table 5.7). The abundances of *Pinnularia lagerstedii, Staurosirella pinnata,* and *Martyana martyi* most influence the freshwater diatom compositions in 19.DV.17, the abundances of *Stauroforma exiguiformis* and *Tabularia fasciculata* most influence the brackish diatom compositions in 19.DV.17, and *Cocconeis californica, Delphineis surirella, Cocconeis costata*, and *Opephora pacifica* most influence the marine diatom compositions in 19.DV.17 (Figures 5.11 and 5.15). Interestingly, *Diploneis interrupta* was not identified in any sample in 19.DV.17 yet is a large influence on the brackish diatom compositions in DV.19.03 (Figures 5.10 and 5.15).

Table 5.7. Percentage of freshwater, brackish and marine diatoms in core 19.DV.17 including species greater than 1.5 % of the total abundance. Green highlighted samples are where freshwater diatoms contribute the most to the diatom assemblage and blue highlighted samples are where marine diatoms contribute the most to the diatom assemblage.

Depth (cm)	%Fresh/Olig-indifferent	% Brackish	% Marine
0.5	30.32	18.77	50.90
6	14.62	5.53	79.84
7	21.19	7.81	71.00
8	34.57	19.33	46.10
13	23.75	22.08	54.17
18	36.96	17.03	46.01
19	41.79	8.58	49.63
20	27.34	3.75	68.91
21	50.97	13.90	35.14
30	44.07	3.39	52.54
31	34.64	9.15	56.21
32	45.49	10.11	44.40
37	18.63	14.45	66.92
43	55.77	8.46	35.77
44	44.26	10.14	45.61
45	40.97	8.33	50.69
49	24.73	8.73	66.55
56	26.13	9.41	64.46
57	20.77	6.92	72.31
58	16.10	7.87	76.03
62	16.14	8.42	75.44
63	14.18	11.64	74.18
64	12.85	15.97	71.18
65	7.75	15.87	76.38
70	6.47	10.43	83.09
80	9.18	12.24	78.57

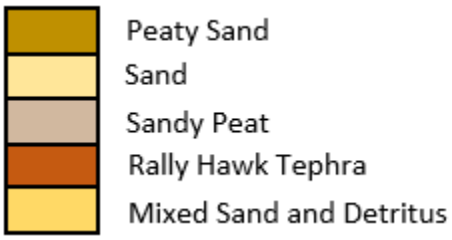

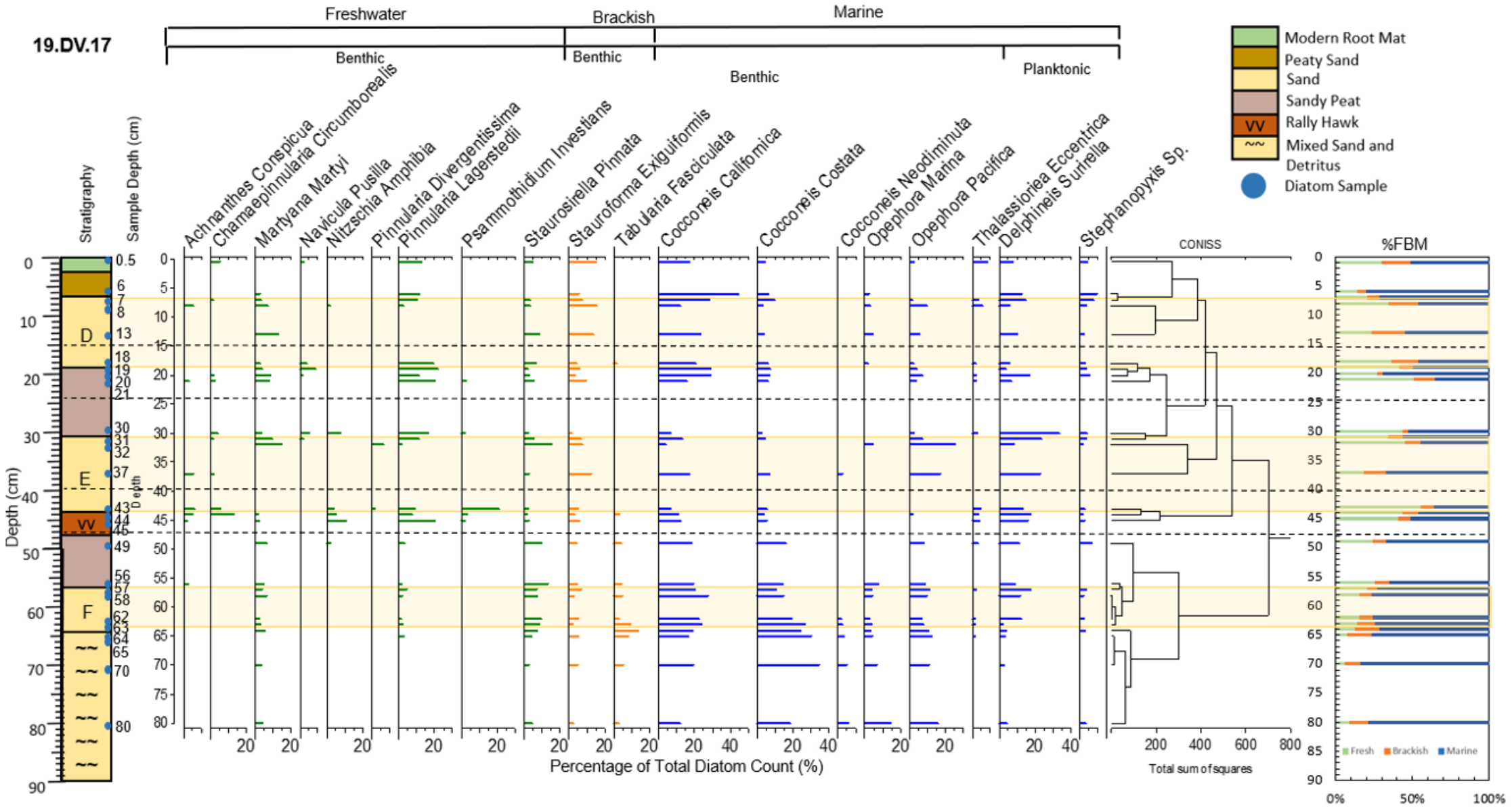

Figure 5.15. Diatom species accounting for more than 5 % of the total diatom abundances for samples in core 19.DV.17. The green bars represent freshwater diatom species, the orange bars represent brackish diatoms, and the blue bars represent marine diatoms and are divided into benthic and planktonic species. CONISS including diatom species accounting for more than 1.5 % of total diatom abundance. % FBM is the percentage of freshwater, brackish and marine diatoms for species greater than 1.5 % of the total diatom abundances. N.B. Dashed lines highlight the dominating clusters.

5.5.1 Sand Bed F and Under and Overlying Units (19.DV.17)

Sand bed F is dominated by marine diatoms ranging from 72.31 % to 76.03 % (Table 5.7). Freshwater diatoms are the next largest contributors, ranging between 14.18 % and 20.77 %, followed by a small contribution from brackish diatoms, ranging between 6.92 % and 11.64 % (Table 5.7). The percentage of marine diatoms remains consistent throughout sand bed F; however, the percentage of brackish diatoms decreases, and the percentage of freshwater diatoms increase with decreasing depth (ranging from 11.64 % brackish at the base to 6.92 % brackish at the surface and 14.18 % freshwater at the base to 20.77 % freshwater at the surface) (Table 5.7).

The most common diatoms in sand bed F are *Cocconeis californica* averaging 23.91 %, *Cocconeis costata* averaging 17.90 %, *Delphineis surirella* averaging 10.94 %, and *Opephora pacifica* averaging 8.98 % (Figure 5.15). There is considerable variation in the proportion of Cocconeis *costata* and *Delphineis surirella* within sand bed F; the percentage of Cocconeis *costata* decreases with decreasing depth ranging from 10.77 % of the total diatom count at 57 cm to 26.91 % at 63 cm and the percentage of *Delphineis surirella* increases with decreasing depth ranging from 2.18 % at 63 cm to 17.69 % at 57 cm (Figure 5.15). The decrease in brackish diatoms with decreasing depth is mostly due to a 9.45% decrease in *Tabularia fasciculata* from the base to the surface of sand bed F, and the increase in freshwater diatoms with decreasing depth is mostly due to the 2.07 % increase in *Pinnularia lagerstedii* from the base to the surface of sand bed F as well as the presence of the freshwater species *Chamaepinnularia gracilistriata* and *Planothidium marginostriatum* at 57 cm (Figure 5.15).

The four samples from the mixed sand and detrital layer underlying sand bed F contain predominately marine diatoms ranging from 71.18 % at 64 cm to 83.09 % at 70 cm (Table 5.7). Brackish species account for the second largest proportion of diatoms in the layer underlying sand bed F, though considerably lower than the marine diatoms (10.43 % at 70 cm to 15.97 % at 64 cm) (Table 5.7). Freshwater species account for a small proportion of the diatom composition in the mixed sand and detrital layer ranging from 6.47 % at 70 cm to 12.85 % at 64 cm (Table 5.7). The mixed sand and detrital layer exhibit similar marine diatoms proportions compared to sand bed F (averaging 77.31 % and 74.49 % respectively), more brackish diatoms compared to sand bed F (averaging 13.63 % and 8.71 % respectively), and fewer freshwater diatoms (averaging 9.06 % and 16.80 % respectively) (Table 5.7). Overall, within the underlying mixed layer, the percentage of marine diatoms

decrease, and the brackish and freshwater species increase, though with fluctuations (Table 5.7).

Like sand bed F, *Cocconeis californica*, *Cocconeis costata*, *Delphineis surirella* and *Opephora pacifica* contribute the most to the marine diatoms in the mixed sand and detrital layer underlying sand bed F (Figure 5.15). However, there are key differences between the marine species in the underlying mixed layer and sand bed F (Figure 5.15). *Cocconeis costata* accounts for the greatest percentage of marine species in the underlying mixed layer and is much greater than in sand bed F (averaging 27.04 % compared to 17.90 % in sand bed F). *Cocconeis californica* averages less in the underlying mixed layer compared to sand bed F where it is the primary marine species (averaging 17.11 % and 23.91 % respectively) (Figure 5.15). The underlying mixed layer contains on average more *Opephora pacifica* (averaging 12.43 % compared to 8.98 % in sand bed F) (Figure 5.15). Interestingly, the percentage of *Delphineis surirella* is on average 7.33 % lower in the underlying mixed layer compared to sand bed F (3.61 % and 10.94 % respectively), though this is most strongly influenced by the upper three samples in sand bed F as the deepest sample in sand bed F exhibits a similar proportion of *Delphineis surirella* to the underlying mixed unit (Figure 5.15). Like sand bed F, there are considerable ranges of the marine species within the underlying mixed layer, though the abundances fluctuate rather than correlate to depth (Figure 5.15).

The greater proportion of brackish species in the underlying mixed layer compared to sand bed F and the increase in the percentage of brackish species with decreasing depth within the underlying mixed layer is mostly due to changes in *Tabularia fasciculata* which is on average 3.34 % greater in the underlying mixed unit than in sand bed F and increases by 10.83 % between 80 cm and 64 cm (Figure 5.15). The greater proportion of freshwater diatoms in sand bed F compared to the underlying mixed unit is most attributed to the 3.32 % greater average of Staurosirella pinnata and 1.96 % greater average of *Pinnularia lagerstedii* (Figure 5.15). Further, the general increase in the freshwater species within the underlying mixed layer is mostly due to the 2.88 % increase in *Staurosirella pinnata* from the base to the surface (Figure 5.15).

Like sand bed F and the mixed layer underlying sand bed F, the sandy peat layer overlying sand bed F contains predominantly marine diatoms ranging from 64.46 % to 66.55 % (Table 5.7). The overlying sandy peat layer is on average 8.99 % less marine than sand bed F and 11.8 % less marine than the mixed layer underlying sand bed F (Table 5.7). The average percentage of brackish species within sand bed F and the overlying sandy peat layer are similar (8.71 % and 9.07 % respectively), though on average 4.56 % lower than the mixed

layer underlying sand bed F (Table 5.7). The sandy peat layer overlying sand bed F contains an average of 8.63 % more freshwater diatoms than sand bed F and on average 16.37 % more freshwater diatoms than the mixed layer underlying sand bed F (Table 5.7).

Cocconeis californica, *Cocconeis costata*, *Delphineis surirella* and *Opephora pacifica* are the most prominent species in the peat layer overlying sand bed F accounting for 19.03 %, 15.32 %, 9.98 % and 8.54 % of the total diatom counts respectively and mirrors the most prominent species in sand bed F (Figure 5.15). The 8.99 % average decrease in marine diatoms between sand bed F and the overlying peat unit is mostly due to the average decrease in *Cocconeis californica* (19.02 % average in the overlying peat and 23.91 % average in sand bed F) and the average decrease in *Cocconeis costata* (15.32 % average in the overlying peat and 17.90 % average in sand bed F) (Figure 5.15). The average percentages of *Opephora pacifica* and *Delphineis surirella* are smaller in the sandy peat overlying sand bed F than in sand bed F but only by 0.44 % and 0.96 % respectively (Figure 5.15). The similar percentages of brackish diatoms in sand bed F and the overlying sandy peat layer are attributed to similar average percentages *of Stauroforma Exiguiformis* (4.34 % and 4.80 % respectively) and *Tabularia fasciculata* (4.26 % and 4.37 % respectively) (Figure 5.15). The 8.63 % average increase in freshwater diatoms in the sandy peat layer overlying sand bed F is predominately due to an average increase in *Staurosirella pinnata* (19.02 % average in the overlying peat and 23.91 % average in sand bed F), an average increase in *Martyana martyi* (5.71 % average in the overlying peat and 3.89 % average in sand bed F) and an average increase in *Planothidium marginostriatum* (3.20% average in the overlying peat and 1.38 % average in sand bed F) (Figure 5.15).

The most notable differences between the sandy peat overlying sand bed F and the mixed layer underlying sand bed F are that on average the overlying sandy peat layer contains 11.73 % fewer *Cocconeis costata,* 3.90 % fewer *Opephora pacifica,* and 3.59 % fewer *Opephora marina* (Figure 5.15). Despite an overall decrease in the proportion of marine species, the sandy peat layer overlying sand bed F contains on average 6.37 % more *Delphineis surirella* compared to the mixed layer underlying sand bed F (Figure 5.15). The decrease in the proportion of brackish species between the sandy peat layer overlying sand bed F and the underlying mixed layer is mostly attributed to an average decrease in *Tabularia fasciculata* (4.26 % average in the overlying peat and 8.13 % average in the underlying peat) (Figure 5.15). The increase in the proportion of freshwater diatoms in the overlying sandy peat layer compared to the underlying mixed layer is mostly due to the average increase *in Staurosirella pinnata* (11.53 % average in the overlying sandy peat and

5.21 % average in the underlying peat), the average increase in *Planothidium marginostriatum* (3.19 % average in the overlying sandy peat and 0.00 % average in the underlying peat), and the average increase in *Martyana martyi* (5.71 % average in the overlying sandy peat and 3.5 % average in the underlying peat) (Figure 5.15).

Sand bed F and the overlying sandy peat unit exhibit similar percentages of benthic diatoms (averaging 84.92 % and 83.65 % respectively) and similar percentages of planktonic diatoms (averaging 15.07 % and 16.34 % respectively) (Figure 5.7). The mixed layer underlying sand bed F exhibits much larger percentages of benthic diatoms (averaging 92.89 %) and much lower percentages of planktonic diatoms (averaging 5.70 %) compared to sand bed F and the overlying sandy peat layer (Figure 5.7). The differences in the percentage of benthic and planktonic diatoms between the mixed layer underlying sand bed F, sand bed F and the overlying sandy peat layer are mostly due to the changes in the planktonic species *Delphineis surirella* (Figure 5.15).

The percentage of fractured diatoms greater than 40 µm is high in sand bed F (averaging 99.00 %), though is only 4 % higher than the averaging fracturing in the overlying sandy peat layer and the underlying mixed layer (both averaging 95.00 %) (Figure 5.7). The percentage of fractured diatoms greater than 40 µm does not consistently increase from the base to the surface of sand bed F (Figure 5.7).

5.5.2 Sand Bed E and Under and Overlying Units (19.DV.17)

Sand bed E exhibits drastic ranges in the proportion of freshwater, brackish and marine diatoms and is notably different from all the other sand beds identified (Tables 5.6 and 5.7). The samples at 31 cm and 37 cm exhibit primarily marine diatoms (56.21 % and 66.92 % respectively) followed by freshwater diatoms (34.64 % and 18.63 % respectively), whereas freshwater diatoms contribute the most to the samples at 32 cm and 43 cm (45.49 % and 55.77 % respectively), followed by marine diatoms (44.40 % and 35.77 % respectively) (Table 5.7). Brackish diatoms account for similar proportions in all four samples ranging from 8.46 % to 14.45 % (Table 5.7).

Delphineis surirella followed by *Cocconeis californica, Opephora pacifica, and Cocconeis costata* contribute the greatest to both the diatom counts at 31 cm and 37 cm (Figure 5.15). However, the species abundances of *Opephora pacifica,* Cocconeis *californica,* and *Cocconeis costata* vary considerably between the two samples (9.92 %, 3.71 % and 2.65 % difference respectively) whereas *Delphineis surirella* exhibits similar abundances (23.53 % and 22.81 % respectively) (Figure 5.15). *Stauroforma exiguiformis* contributes greatest to

the brackish diatom abundances in all four sand bed E samples ranging from 5.77 % to 12.54 % (Figure 5.15). The freshwater diatoms in 31 cm and 37 cm differ; *Pinnularia lagerstedii, Martyana martyi* and Staurosirella *pinnata* contribute the most to the freshwater diatoms at 31 cm (11.44 %, 9.48 % and 5.56 % respectively) and *Achnanthes conspicua, Planothidium marginostriatum, Staurosirella pinnata* and *Pinnularia intermedia* contribute the most to the freshwater diatoms at 37 cm (5.70 %, 3.04 %, 2.69 % and 2.69 % respectively) (Figure 5.15).

The two samples within sand bed E that are freshwater diatom dominated (32 cm and 43 cm) exhibit considerably smaller percentages of *Delphineis surirella* and *Cocconeis californica* compared to samples 31 cm and 37 cm (averaging 10.88 % and 5.45 % respectively) (Figure 5.15). Interestingly, 32 cm contains 25.63 % *Opephora pacifica* compared to 0.00 % at 43 cm and is 18.44 % and 8.52 % greater than samples 31 cm and 37 cm respectively which are marine diatom dominated (Figure 5.13). Despite, 32 cm and 43 cm containing predominately freshwater diatoms, the contributing species vary between the two samples with Staurosirella *pinnata,* Martyana *martyi* and *Pinnularia divergentissima* contributing the most to the diatom assemblage at 32 cm (15.52 %, 14.80 % and 6.86 % respectively) compared *to Psammothidium investians, Pinnularia lagerstedii, Achnanthes conspicua,* and *Chamaepinnularia circumborealis* contributing the most to the diatom assemblages at 43 cm (21.15 %, 9.23 %, 6.15 % and 5.77 % respectively) (Figure 5.15).

Sand bed E exhibits greater intra sand bed diatom variation compared to sand bed F (Table 5.7 and Figure 5.15). The predominant marine diatom species in sand bed E are the same as in sand bed F, though in smaller quantities, except for *Opephora pacifica* which is greater in samples 32 cm and 37 cm and *Delphineis surirella* which is considerably greater in the two marine dominated samples in sand bed E (31 cm and 37 cm) compared to the sand bed F samples (Figure 5.15). Unlike sand bed F, there is no *Tabularia fasciculata* in sand bed E and on average more *Stauroforma exiguiformis* in sand bed E compared to sand bed F (8.19 % and 4.34 % respectively) (Figure 5.15). *Pinnularia lagerstedii, Staurosirella pinnata* and *Martyana martyi* are key contributors to the freshwater diatoms in both sand beds E and F, though additional freshwater species are major contributors to sand bed E that are not in sand bed F (e.g., *Pinnularia divergentissima, Psammothidium investians, Achnanthes conspicua,* and *Chamaepinnularia circumborealis*) (Figure 5.15).

The *Rally Hawk* tephra layer underlaying sand bed E contains predominantly marine diatoms (45.81 % to 50.69 %), followed by similar proportions of freshwater diatoms (40.97 % to 44.26 %) and small contributions from brackish diatoms (8.33 % to 10.14 %) (Table

5.7). The two samples from the *Rally Hawk* tephra contain fewer marine diatoms than the two marine dominated samples from sand bed E (31 cm and 37 cm) and fewer freshwater diatoms compared to the two sand bed E freshwater dominated samples (32 cm and 43 cm) (Figure 5.15). Like the samples from sand bed E (31 cm and 37 cm), *Delphineis surirella, Cocconeis californica,* and *Cocconeis costata* contribute the most to the marine species in the Rally Hawk tephra (averaging 16.9 %, 11.99 % and 4.64 % of the total diatom counts) (Figure 5.15). *Pinnularia lagerstedii* (14.13 % average), *Nitzschia amphibia* (7.92 % average) and *Chamaepinnularia circumborealis* (6.59 % average) contribute the most to the freshwater diatoms in the *Rally Hawk* tephra layer and are major contributors to at least one sample in sand bed E (Figure 5.15).

Three of the four samples from the sandy peat layer overlying sand bed E (19 cm, 20 cm and 30 cm) exhibit predominately marine diatoms ranging from 49.63 % to 68.91 % followed by freshwater diatoms ranging from 27.34 % to 44.07 % (Table 5.7). However, the sample at 21 cm contains predominately freshwater diatoms (50.97 %) followed by marine diatoms (35.14 %) (Table 5.7). The samples at 19 cm, 20 cm and 30 cm display similar but smaller percentages of marine diatoms compared to the marine dominated samples at 31 cm and 37 cm in sand bed E (averaging 57.03 % and 61.57 % respectively), and greater proportions of freshwater diatoms (averaging 37.73 % and 26.63 % respectively) (Table 5.7).

Like sand bed E, *Cocconeis californica, Delphineis surirella, Cocconeis costata* and *Opephora pacifica* contribute the greatest to the marine diatom composition in the peat layer overlying sand bed E (averaging 21.81 %, 15.36 %, 5.77 % and 4.36 % respectively) (Figure 5.15). Further, as in sand bed E, there is considerable intra layer variation within the overlying peat layer, especially *Delphineis surirella* which ranges from 33.56 % at 30 cm to 3.73 % at 19 cm and *Cocconeis californica* which increases from 7.12 % at 30 cm to 29.21 % at 20 cm (Figure 5.15). *Stauroforma exiguiformis* contributes the greatest to the brackish composition of the overlying peat layer (averaging 5.27 % abundance) (Figure 5.15). *Pinnularia lagerstedii* dominates the freshwater diatoms in the overlying peat layer averaging 17.67 % of the total diatom counts but does not account for the greater proportion of freshwater diatoms at 21 cm (Figure 5.15). The presence of *Planothidium renei* (4.24 % of the total diatom count) and *Achnanthes conspicua* (3.09 % of the total diatom count), and the greater abundances from *Staurosirella pinnata* (5.41 % and 2.54 % respectively) and *Martyana martyi* (8.11 % and 5.48 % respectively) are the greatest contributors to the increased proportion of freshwater diatoms at 21 cm compared to the rest of the sandy peat layer overlying sand bed E (Figure 5.15). Interestingly, the three samples within 19.DV.17

that contain predominantly freshwater diatoms (21 cm, 32 cm and 43 cm) are most influenced by different freshwater and marine diatom species (Figure 5.15).

Sand bed E exhibits on average 9.00 % fewer benthic diatoms compared to sand bed F and 6.10% more planktonic diatoms (75.69 % and 84.92 % respectively) (Figure 5.7). Sand bed E contains similar average proportions of benthic and planktonic diatoms compared to the overlying sandy peat layer (75.92 % and 76.69 % benthic diatoms respectively and 21.18 % and 20.63 % planktonic diatoms respectively) (Figure 5.7). The *Rally Hawk* tephra underlying sand bed E exhibits considerably fewer benthic diatoms compared to sand bed E (64.82 % and 75.92 % respectively) and more planktonic diatoms on average (27.58 % and 21.18 % respectively) (Figure 5.7).

The percentage of fractured diatoms greater than 40 µm in sand bed E averages 72.44 % which is 26.56 % lower on average than sand bed F (99.00 % average fracturing), 15.01 % lower than the *Rally Hawk* tephra layer underlying sand bed E (87.45 % average fracturing), and 18.78 % lower than the sandy peat layer overlying sand bed E (91.22 % average fracturing) (Figure 5.7). The percentage of fractured diatoms greater than 40 µm consistently increases from 65.00 % to 86.16 % between the base and the surface of sand bed E (Figure 5.7).

5.5.3 Sand Bed D and Under and Overlying Units (19.DV.17)

Like sand bed F, all samples within sand bed D are dominated by marine diatoms (ranging from 46.01 % to 71 %), followed by freshwater diatoms (ranging from 21.19 % to 36.96 %) (Table 5.7). However, the contribution of marine diatoms in sand bed D is much lower than in sand bed F (averaging 54.32 % and 74.49 % respectively), the proportion of freshwater diatoms is notably greater (averaging 29.12 % and 16.80 % respectively), and the percentage of brackish species is on average 7.85 % more (16.56 % and 8.71 % respectively) (Table 5.7). Like sand beds E and F, there are no notable patterns of diatoms within sand bed D (Table 5.7).

As seen in sand beds E and F, *Cocconeis californica, Delphineis surirella, Cocconeis costata,* and *Opephora pacifica* contribute the most to the marine diatoms in sand bed D (averaging 21.31 %, 9.35 %, 5.82 % and 4.78 % respectively) and exhibit considerable intra sand bed ranges (16.35 %, 9.44 %, 6.69 % and 7.70 % ranges respectively) (Figure 5.15). *Stauroforma exiguiformis* is the greatest contributor to the brackish diatoms in sand bed D, like in sand beds E and F (27.25 %, 22.50 % and 11.75 % respective abundances) (Figure 5.15). *Pinnularia lagerstedii* followed by *Martyana martyi* and *Staurosirella pinnata*

contribute the most to the freshwater assemblages in sand bed D (averaging 8.14 %, 6.47 %, and 5.58 % respectively) which are also key contributors of the freshwater diatoms in sand beds E and F (Figure 5.15).

The sandy peat layer underlying sand bed D contains on average 2.77 % fewer marine diatoms (51.55 % average), 9.16 % fewer brackish diatoms (7.40 % average) and 11.93 % more freshwater diatoms (41.04 %) compared to sand bed D (Table 5.7). The marine diatom assemblages are similar between sand bed D and the underlying sandy peat layer, though notably, the contribution from *Delphineis surirella* is on average 6.01 % less in sand bed D compared to the underlying sandy peat unit (9.35 % and 15.37 % respective average abundances) (Figure 5.15). Like sand bed D, the underlying peat unit displays considerable intra layer variation in the percentages of the marine diatom species, especially *Delphineis surirella* and *Cocconeis californica* (Figure 5.15). Stauroforma exiguiformis dominate the brackish diatom assemblages in both sand bed D and the underlying sandy peat layer and the variance in the proportion of brackish diatoms between sand bed D and the underlying peat layer is mostly due to changes in the abundance *of Stauroforma exiguiformis* (Figure 5.15). *Pinnularia lagerstedii, Staurosirella pinnata* and *Martyana martyi* contribute the most to the freshwater diatoms in both sand bed D and the underlying peat unit, and the generally greater proportion of freshwater diatoms in the sandy peat underlying sand bed D compared to sand bed D is mostly attributed to the average 9.53 % more *Pinnularia lagerstedii* in the underlying peat layer (17.67 % and 8.14 % respective average abundances) (Figure 5.15).

Like sand bed D, the peaty sand layer overlying sand bed D is dominated by marine diatoms ranging from 50.90 % to 79.84 %, followed by freshwater diatoms ranging from 14.62 % to 30.32 %, and brackish diatoms ranging from 5.53 % to 18.77 % (Table 5.7). On average the peaty sand layer overlying sand bed D contains 11.05 % more marine diatoms, 6.65 % fewer freshwater diatoms and 4.41 % fewer brackish diatoms compared to sand bed D (Table 5.7). Compared to the sandy peat layer underlying sand bed D, on average the peaty sand layer overlying sand bed D contains 18.57 % fewer freshwater diatoms, 4.75 % more brackish diatoms and 13.82 % more marine diatoms (Table 5.7). However, like sand bed D and the sandy peat layer underlying sand bed D, there is notable intra layer variations in the proportions of marine, brackish and freshwater diatoms in the peaty sand layer overlying sand bed D, especially the proportion of marine diatoms which has a 28.94 % range from 50.9 % at 0.5 cm to 79.84 % at 6 cm (Table 5.7).

The peaty sand layer overlying sand bed D contains similar marine diatoms to sand bed D and the sandy peat layer underlying sand bed D with *Cocconeis californica*, *Delphineis*

surirella, Cocconeis costata, and *Stephanopyxis Sp.* contributing the most to the diatom assemblages in the peaty sand layer (Figure 5.15). The greater average proportion of marine diatoms in the overlying peaty sand layer is mostly due to greater contributions from *Cocconeis californica,* averaging 31.00 % in the overlying peaty sand compared to an average of 21.31 % in sand bed D (Figure 5.15). Interestingly, *Opephora pacifica* averages 1.44 % in the overlying peaty sand compared to 4.77 % and 4.36 % in sand bed D and the underlying sandy peat layer respectively (Figure 5.15). Like sand bed D and the underlying sandy peat, *Stauroforma exiguiformis* dominates the brackish diatoms in the peaty sand overlying sand bed D (averaging 10.52 % abundance) (Figure 5.15). *Pinnularia lagerstedii* is the greatest contributor to the freshwater diatoms in the overlying peaty sand layer (averaging 12.43 % abundance) and *Staurosirella pinnata* and *Chamaepinnularia circumborealis* are further important freshwater species at 6 cm (Figure 5.15). As in sand bed D and the underlying sandy peat, the overlying peaty sand exhibits large intra layer ranges in diatom species abundances (Figure 5.15).

Sand bed D contains on average 1.65 % more benthic species than the underlying sandy peat layer (78.34 % and 76.69 % respectively) and 5.46 % more benthic diatoms than the overlying peaty sand layer (78.34 % and 72.88 % respectively) (Figure 5.7). On average, sand bed D contains 2.08 % fewer planktonic diatoms than the underlying sandy peat layer (18.55 % and 20.63 % respectively) and 5.87% fewer planktonic diatoms than the overlying peaty sand layer (18.55 % and 24.42 % respectively) (Figure 5.7). However, like sand beds E and F, sand bed D exhibits large ranges in the percentages of benthic and planktonic diatom species (ranges of 18.57 % and 19.61 % respectively) (Figure 5.7).

The percentage of fractured diatoms greater than 40 µm in sand bed D averages 82.00 % which is on average 8.94 % more than the underlying sandy peat layer and 3.89 % more than the overlying peaty sand layer (Figure 5.7). Sand bed D averages 9.84 % more fractured than sand bed E and 16.21 % less fractured than send bed F for diatoms greater than 40 µm (Figure 5.7). The percentage of fractured diatoms greater than 40 µm does not consistently increase from the base to the surface of sand bed D (Figure 5.7).

5.5.4 CONISS Cluster Analysis of 19.DV.17

The four samples from sand bed F display small cluster dissimilarity, with the middle two samples clustering most strongly followed by the addition of the basal samples then the surface sample (Figure 5.15). Sand bed F exhibits a small cluster dissimilarity with the deepest sample from the overlying sandy peat layer (56 cm) and is more similar to the

overlying sandy peat layer than the mixed sand and detritus layer underlying sand bed F (Figure 5.15). The four samples from the underlying mixed layer produce a small cluster dissimilarity (Figure 5.15).

The shallowest and deepest samples from sand bed E (31 cm and 43 cm) both cluster most strongly with the samples from the over and underlying layers respectively, and cluster strongly with the other samples within sand bed E (Figure 5.15). All the samples within sand bed E cluster more strongly to sand bed D samples than sand bed F samples (Figure 5.15).

Like sand bed E, the shallowest and deepest sample from sand bed D cluster most strongly with the nearest sample from the under and overlying layer (Figure 5.15). The two central samples from sand bed D cluster most closely to the samples from the overlying peaty sand layer rather than the other samples from sand bed D (Figure 5.15). The sample at 18 cm in sand bed D clusters more strongly with the underlying sandy peat unit, whereas the other three sand bed D samples at 7 cm, 8 cm and 13 cm cluster more strongly with the overlying peaty sand layer than the sample at 18 cm in sand bed D (Figure 5.15).

5.5.5 DCA of 19.DV.17

DCA groups the deepest three sand bed F samples closely with relatively high axis one values (1.80 to 1.95) and axis two values (1.25 to 1.55) (Figure 5.16). The shallowest sample from sand bed F does not plot closely to the other samples in sand bed F with much lower axis one and axis two values (1.48 and 0.90 respectively) (Figure 5.16). DCA plots three of the four samples from the mixed layer underlying sand bed F closely with similar axis two ranges to sand bed F (1.45-1.70), though higher and narrower axis one ranges compared to sand bed F (2.00-2.10) (Figure 5.16). The fourth sample from the mixed layer underlying sand bed F plots in isolation with a much lower axis one value (1.45), though similar axis two value (1.40) (Figure 5.16). The two samples from the overlying sandy peat layer do not plot closely, though the sample at 56 cm plots close to three of the sand bed F samples and the sample at 49 cm in the overlying sandy peat plots closely to the sand bed F sample at 57 cm (Figure 5.16).

DCA does not group any of the samples from sand bed E closely, exhibiting the largest axis one range of any of the layers (0.00-2.25) (Figure 5.16). Further, samples 32 cm, 37 cm and 43 cm do not plot closely to any of the samples from the underlying *Rally Hawk* tephra or the overlying sandy peat layer (Figure 5.16). Sample 31 cm plots closely to sample 20 cm from the overlying sandy peat layer (Figure 5.16). Apart from samples 31 cm and 57 cm, DCA does not plot sand bed E and sand bed F samples closely (Figure 5.16).

As seen with the sand bed E samples, DCA does not plot the sand bed D samples closely, ranging from 0.80 to 2.40 on axis one and from 0.00 to 1.55 in axis two (Figure 5.16). DCA plots 7 cm and 18 cm from sand bed D closely to the samples from the underlying sandy peat layer, whereas samples 8 cm and 13 cm from sand bed D plot in isolation (Figure 5.16).

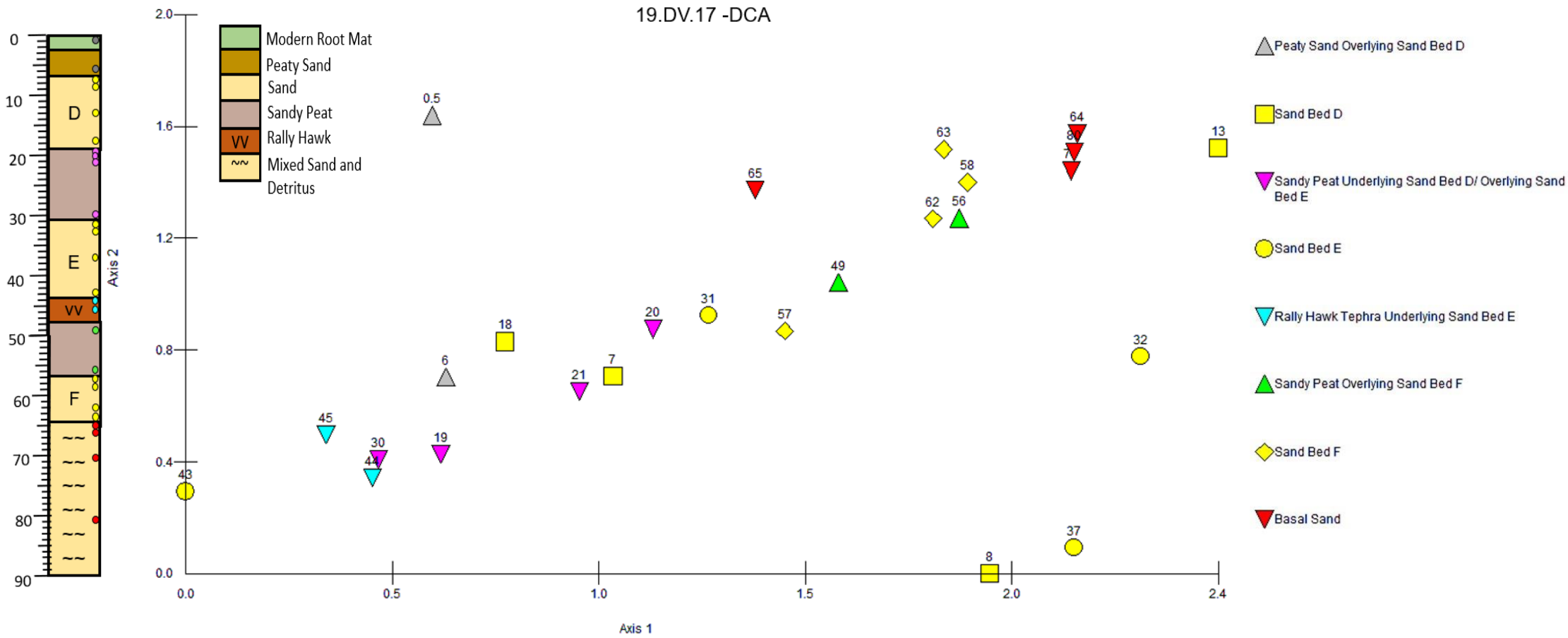

Figure 5.16. DCA biplot for all diatom samples from 19.DV.17. N.B. Only diatom species accounting for more than 1.5 % of the total abundance are included in the analysis.

6.0 Discussion

6.1 Summary

Overall, the lithostratigraphic, grain size and diatom evidence from Nagai Island supports a lack of identifiable land level change or sand beds conclusively linked to high tsunamis, thus, suggesting limited evidence for great earthquakes and high tsunamis on Nagai Island throughout the last ~2900 years. A high tsunami is defined as reaching greater than the present-day intertidal zone (Grant, 2002). The palaeoseismic reconstruction of Nagai Island supports Witter's *et al.* (2014) suggestion of long-term persistent creep to accommodate plate convergence in the Shumagin section of the Alaska-Aleutian subduction zone. The absence of geological evidence for identifiable land level change on both Nagai Island and Simeonof Island implies that the Shumagin section has neither generated a great earthquake nor coseismically weakened through the propagation of a great earthquake from the adjacent Semidi and Unimak sections throughout at least the last ~2900 years (Noda and Lapustra, 2013; Witter *et al.,* 2014). Further, the limited evidence for high tsunami inundation in the geological record on Nagai Island alongside Simeonof Island suggests that the Shumagin section has neither generated a large tsunami, nor exhibited deposition of high tsunamis sourced from teletsunamis generated elsewhere along the AASZ or other subduction zones, over at least the last ~2900 years (Witter *et al.,* 2014). Therefore, it does not appear that large tsunamis generated within the Shumagin section have propagated to far field communities in Hawaii and along the Pacific West coast of the USA and Canada throughout the late Holocene (Ryan *et al.,* 2012; Witter *et al.,* 2014).

The lack of geological evidence for a great earthquake and high tsunami inundation in 1788 on both Nagai and Simeonof Islands does not support Davies' *et al.* (1981) interpretation and inferences of the Russian outpost documents from Unga Island for a great earthquake and high tsunami in 1788 in the Shumagin section of the Alaska-Aleutian subduction zone. Therefore, it is unlikely that in 1788, a great earthquake and high tsunami inundation generated within the Shumagin section or propagated from adjacent sections of the Alaska-Aleutian subduction zone. The disparity between the Russian outpost documents implying a great earthquake and high tsunami in the Shumagin section of the Alaska-Aleutian subduction zone in 1788 and the lack of evidence for a great earthquake and high tsunami inundation in the geological evidence from both Nagai and Simeonof Islands could be due to several reasons including firstly, the possibility of a small, locked section of the Alaska-Aleutian subduction zone near Unga Island

which ruptured to produce a great earthquake and tsunami in 1788 (Freymueller and Beavan, 1999). Secondly, the overinterpretation of the magnitude and tsunami reported in the Russian outpost documents where instead of a great earthquake, a large earthquake and low-level tsunami could have occurred in the Shumagin section in 1788 that would result in too little vertical displacement and tsunami inundation to leave a geological imprint (Witter *et al.,* 2014). Thirdly, the possibility of foul play by Russian settlers towards the indigenous Aleuts leading to an exaggeration of the magnitude of the earthquake and tsunami in the Russian outpost documents to cover up a genocide of the indigenous Aleuts on Unga Island (Engelhart *et al.,* 2018). Finally, the possibility for missing or eroded geological evidence. The potential reasons for the disparity between the Russian outpost documents and the geological evidence from Nagai and Simeonof Island are discussed in more detail in section 6.4.

The absence of identifiable coseismic land level change on both Nagai and Simeonof Islands over at least the last ~2900 and ~3400 years respectively implies a low hazard for great earthquakes generated in the Shumagin section of the Alaska-Aleutian subduction zone as well as a low hazard for the propagation of great earthquakes into the Shumagin section from the adjacent Semidi and Unimak sections of the Alaska-Aleutian subduction zone (Witter *et al.,* 2014). Further, the absence of sand beds conclusively linked to high tsunamis on both Nagai and Simeonof Islands over at least the last ~2900 and ~3400 years respectively suggests that there is a low hazard for a high tsunami generating or propagating into the Shumagin section of the Alaska-Aleutian subduction zone as well as a low hazard for a large tsunami generated in the Shumagin section propagating towards Hawaii and the Pacific West coast of the USA and Canada (Ryan *et al.,* 2012; Witter *et al.,* 2014).

However, great earthquakes and high tsunamis generating or propagating into the Shumagin section cannot be ruled out in the future due to the potential for missing evidence for coseismic land level change and tsunami inundation in the geological records on Nagai and Simeonof Islands, the geological records do not encapsulate the entire history of the Shumagin section so the recurrence intervals of great earthquakes and high tsunamis in the Shumagin section could be longer than the geological record, and the dynamics of the plate interface can vary through time as evident at Sedanka Island where it is currently creeping, but the geological evidence exhibits a history of plate interface locking (Kelsey *et al.,* 2015; Shennan *et al.,* 2016; Witter *et al.,*2016; Witter *et al.,* 2019). The lack of modern tsunami deposits in the Shumagin section to compare potential palaeotsunami deposits to, and the absence of palaeoseismic

reconstructions in the western Semidi section and Unimak section which limits the understanding of teletsunamis, further demonstrates the inability to rule out high tsunamis generating or propagating into the Shumagin section of the Alaska-Aleutian subduction zone in the future (Kelsey *et al.,* 2015; Nelson *et al.,* 2015; Witter *et al.,* 2016; Witter *et al.,* 2019). Therefore, despite the apparent low hazard for great earthquakes and high tsunamis generating or propagating into the Shumagin section, great earthquakes and high tsunamis cannot be completely ruled out of the Shumagin section seismic hazard assessments nor in tsunami hazard assessments in communities vulnerable to Shumagin sourced tsunamis in Hawaii and along the Pacific west coasts of the USA and Canada.

6.2 Late Holocene Evolution of DV.19.03 and 19.DV.17.

The lithostratigraphy, diatom assemblages and statistical analyses of DV.19.03 and 19.DV.17 identify a general freshening and reduction in marine influence throughout the late Holocene. The transition in DV.19.03 from predominately marine diatoms in the base of the core to predominately brackish diatoms between 152 cm and 128 cm, followed by predominately freshwater diatoms between 127.5 cm to 0.5 cm implies a transition from a tidal flat to a saltwater marsh to a freshwater marsh over the last ~2900 years (Hamilton *et al.,* 2005; Dura, 2014). On nearby Simeonof Island, Witter *et al.* (2014) suggest relative sea-level stability over approximately the last 3400 years, identifying evidence of slow relative sea-level rise (<0.2 m/ka) from the analysis of deposits in cores and bluff exposures. Therefore, the general freshening throughout the late Holocene in DV.19.03 suggests that there is likely additional protection of Deranged Valley through time which may limit marine inundation. This has important implications on identifying coseismic land level changes and high tsunami inundation using DV.19.03 as in the top 92 cm of DV.19.03, where freshwater diatoms dominate, coseismic land level changes may not be clearly recorded in the sediment and diatom evidence because the elevation of the site may be too high that coseismic land level change may not produce an identifiable signal in the sediment and diatom evidence. However, even if DV.19.03 became too dominated by freshwater diatoms within the top 92cm, a tsunami deposit generated from a great earthquake could still be possible despite the potential limitations of identifying coseismic land level change in predominantly freshwater assemblages.

19.DV.17 exhibits predominately marine diatoms throughout, though there is a general decrease in marine diatoms and an increase in freshwater diatoms towards the surface of

19.DV.17, suggesting a transition from a tidal flat to saltwater marsh throughout the late Holocene (Hamilton *et al.,* 2005; Dura, 2014). The general decrease in marine influence and the increase in freshwater diatoms from the base to the surface of 19.DV.17, despite the identification of likely slow relative sea-level rise throughout the late Holocene from nearby Simeonof Island, again supports the additional protection and isolation from marine inundation in the Deranged Valley site over the last ~1700 years (Witter *et al.,* 2014). However, since the diatom freshening throughout the late Holocene in 19.DV.17 is less drastic than in DV.19.03 it is likely that despite some freshening over time, a land level change signal would be recorded at 19.DV.17 as the diatom assemblages are mixed throughout the entirety of 19.DV.17 as opposed to completely dominated by freshwater species.

6.3 Coseismic Land Level Change and Tsunami Inundation on Nagai Island Throughout the Late Holocene

6.3.1 Is there Sediment and Microfossil Evidence for Coseismic Land Level Change on Nagai Island Throughout the Late Holocene?

The absence of peat-mud or mud-peat couplets and the lack of anomalous diatom assemblages in all six of the cores retrieved from across Nagai Island as well as the exploratory cores analysed during the fieldwork suggests that at least over the last ~2900 years, a great earthquake (M_w >8.0) has not ruptured the east of the Shumagin section of the Alaska-Aleutian subduction zone (Nelson *et al.,* 1996b; Witter *et al.,* 2003; Shennan *et al.,* 2016). However, great earthquakes in the Shumagin section of the Alaska-Aleutian subduction zone throughout the late Holocene cannot be completely ruled out due to the potential for missing evidence associated with the identified general freshening of the Deranged Valley site over time, as discussed in the previous section. The general freshening of Deranged Valley throughout the late Holocene results in the possibility of missing evidence because if the diatom assemblage is too fresh a land level change may not result in a considerable change in the sediment or diatom evidence and thus, produce an unidentifiable land level change. Further, it is important to note that the geological evidence for coseismic land level change is only able to reconstruct the occurrence of great earthquakes (M_W > 8.0) because smaller earthquakes do not leave an identifiable imprint in the geology, thus, the palaeoseismic history of large earthquakes and smaller in the Shumagin section cannot be determined from the geological record (Witter *et al.,* 2014). Therefore, the occurrence of large earthquakes throughout the late Holocene cannot be ruled out (Witter *et al.,* 2014).

The lack of evidence for coseismic land level change throughout the late Holocene suggests that the Shumagin section of the Alaska-Aleutian subduction zone has exhibited long term persistent creep and that great earthquakes from the adjacent highly locked Semidi or Unimak sections have not propagated through coseismic weakening into the Shumagin section to produce a multi section rupture as seen in the 1999 Chi-Chi and the 2011 Tohoku-Oki earthquakes as well as in the Kenai section of the Alaska-Aleutian subduction zone during the 1964 Alaskan earthquake (Noda and Lapustra, 2013; Shennan et al., 2016). However, palaeoseismic reconstructions in the west of the Semidi section is critical to confirm that the Shumagin section is a long-term barrier to great earthquakes from the Semidi section as there is only one palaeoseismic reconstruction in the Semidi section, in the east approximately 200km from the western Semidi section boundary (Nelson *et al.,*2015). Without a palaeoseismic reconstruction in the west of the Semidi section of the Alaska-Aleutian subduction zone, it is not known how many great earthquakes have occurred in the west of the Semidi section and hence, it is not known the number of times that the Shumagin section has resisted the propagation of a great earthquake (Nelson *et al.,* 2015). Ideally, a palaeoseismic reconstruction within the Semidi section, just west of the 1938 and 2021 great earthquake rupture areas and within the Semidi section in the western boundary of the rupture area of the 1938 great earthquake would enable a better understanding of the history of great earthquakes in the western Semidi section of the Alaska-Aleutian subduction zone and the persistence of the apparent barrier to great earthquake propagation into the Shumagin section of the Alaska-Aleutian subduction zone.

The absence of coseismic land level change on Nagai Island throughout the Late Holocene supports Witter *et al.* (2014), who did not find geological evidence for coseismic land level change on Simeonof Island, also in the Shumagin section of the Alaska-Aleutian subduction zone over at least the last ~3400 years. Further, the geological evidence from Nagai Island supports and extends the findings of Fournier and Freymeuller (2007) who conclude that since 1991 the Shumagin section has accommodated strain accumulation through more frequent moderate to large earthquakes as opposed to more infrequent great earthquakes.

Interestingly, the palaeoseismic behavior of the Shumagin section throughout the late Holocene differs to other sections of the Alaska-Aleutian subduction zone which are currently creeping (Witter *et al.,* 2016, 2019). For example, Sedanka Island, which is currently creeping, exhibits geological evidence for past great earthquakes and high tsunamis on average every 300-340

years due to the changes in the locking of the plate interface throughout the late Holocene (Nicolsky *et al.,* 2016; Witter *et al.,* 2016, 2019). Whereas the evidence from Nagai Island and Simeonof Island (Witter *et al.,* 2014) suggests persistent creep over at least the last ~2900 years and ~3400 years respectively, demonstrating the spatial uniqueness of plate dynamics along the Alaska-Aleutian subduction zone and the inability to spatially transplant palaeoseismic history based on modern plate dynamics. The Shumagin section differs from the other areas of the Alaska-Aleutian subduction zone where palaeoseismic reconstructions have identified great earthquakes throughout the late Holocene including the Prince William Sound section (e.g., Hamilton *et al.,* 2005; Hamilton and Shennan (2005a), the Kenai section (e.g., Zong *et al.,* 2003; Hamilton and Shennan 2006a) , the Kodiak section (e.g. Shennan *et al.,* 2014c; Shennan *et al.,* 2018; Prater, 2021), the Semidi section (e.g., Nelson *et al.,* 2015), and the adjacent Yakutat microplate (Shennan *et al.,* 2009).

Although there is a lack of evidence for a great earthquake on Nagai Island over at least the last ~2900 years, it is possible that a great earthquake was not recorded in the geology due to erosion, missing evidence and the location of the hingeline which can result in too little vertical deformation to be recorded in the geology (Coe, 2003; Witter *et al.,* 2014; Kelsey *et al.,* 2015; Shennan *et al.,* 2016). Though, since the dune system is stabilized in Deranged Valley it suggests a lack of erosion and since Simeonof Island also does not exhibit geological evidence for coseismic land level change, it increases the confidence in determining a lack of coseismic land level change throughout the late Holocene in the Shumagin section of the Alaska-Aleutian subduction zone (Witter *et al.,* 2014). Even if the hingeline location resulted in too little vertical deformation on one of Nagai or Simeonof Islands, it would produce a geological imprint at the other and since this is not identified in the geological record it further supports the lack of coseismic land level change throughout the late Holocene in the Shumagin section of the Alaska-Aleutian subduction zone (Witter *et al.,* 2014; Kelsey *et al.,* 2015).

6.3.2 Is there Sediment and Microfossil Evidence for Tsunami Inundation on Nagai Island Throughout the Late Holocene?

The absence of coseismic land level change coinciding with the six identified potential tsunami sand bed deposits in DV.19.03 and 19.DV.17 complicates the determination of the source of the sand bed deposits because coseismic land level change provides convincing additional evidence for a tsunami sourced sand bed whereas isolated sand beds have several potential sources with similar lithostratigraphic and microfossil imprints (Nelson *et al.,* 1996a; Nelson *et*

al., 2015; Engel and Brückner, 2011; Dura, 2014). The following sections discuss the evidence for tsunami inundation on Nagai Island throughout the late Holocene and suggests possible sources for the six identified sand beds from DV.19.03 and 19.DV.17.

6.3.3 Is there Sediment Evidence for Tsunami Inundation on Nagai Island Throughout the Late Holocene?

Sand beds B and C from DV.19.03 and sand beds D, E and F from 19.DV.17 do not exhibit the typical lithostratigraphic imprint of a tsunami deposit in terms of abrupt upper and lower contacts and spatially extensive deposits that thin landward (Table 6.1) (Atwater and Hemphill-Haley, 1996; Switzer, 2010; Witter *et al*., 2016). The 7-20 mm contacts identified for sand beds B-F on Nagai Island are notably greater than observed contacts for identified tsunami deposits globally (e.g., Dura *et al.,* 2015; Janigian, 2018). Along the central Chilean subduction zone, six tsunami deposits identified by Dura *et al.* (2015) exhibited upper and lower contacts between 1 mm and 3 mm, two tsunami deposits identified by Janigian (2018) on Kodiak Island along the Alaska-Aleutian subduction zone exhibited upper and lower contacts between 2-3 mm, and Nelson *et al.* (2015) identified lower contacts of 1mm or less and upper contacts of 3 mm or less on Chirikof Island along the Alaska-Aleutian subduction zone. Thus, the 7-20 mm contacts exhibited for sand beds B-F on Nagai Island are much more diffuse than identified tsunami deposits along the Alaska-Aleutian subduction zone and other subduction zones globally, suggesting limited lithostratigraphic support for a tsunami source for sand beds B-F.

Table 6.1. Summary of sand bed's A-F characteristics compared to identified tsunami deposit characteristics. Ticks indicate the deposit met the criteria, crosses indicate the deposit does not meet the criteria and a tick and a cross shows partial fulfillment of tsunami deposit criteria.

Sand bed	Abrupt upper and lower contact	Spatially extensive	Relatively coarse grained	Upward fining of grain size	Anomalous diatom assemblage	Anomalous fracturing of diatom valves	Anomalous life forms	Coseismic land level change
C	×	×	✓	x/✓	×	x	x	×
B	×	×	✓	×	×	×/✓	×	×
A	×/✓	×	✓	✓	×	×	×	×
F	×	×	×	×	×	×	×	×
E	×	×	✓	×	×	×	×	×
D	×	×	✓	×/✓	×	×	×	×

The moderately abrupt lower contact from sand bed A could be synonymous to a tsunami deposit as it is similar to identified tsunami contacts identified by Dura *et al.* (2015) and Janigian (2018) (4 mm compared to a maximum of 3 mm). The diffuse upper contact of sand bed A (8mm) differs from the six tsunami deposits identified along the central Chilean subduction zone and the two tsunami deposits identified on Kodiak Island along the Alaska-Aleutian subduction zone (Dura *et al.,* 2015; Janigian, 2018). However, Sawai *et al.* (2009) identified abrupt lower (<2mm) and diffuse upper contacts (>5mm) for the 2004 Indian Ocean tsunami deposits on Phra Thong Island, Thailand due to the slowing of the current as the tsunami progresses resulting in the less abrupt deposition at the surface of the tsunami deposit and the possibility of bioturbation at the surface of the tsunami deposit producing a diffuse upper contact (Spiske *et al.,* 2013).

Despite the similarity of sand bed A's contact sharpness to identified tsunami deposits from the 2004 Indian Ocean tsunami (Sawai *et al.,* 2009), the absence of the sand beds A- F in the other cores across the Deranged Valley and Larsen Lake Marsh sites suggests a local depositional process as opposed to widespread tsunami inundation (Nelson *et al.,* 1996b; Switzer, 2010; Witter *et al.,* 2016). Additionally, the absence of sand beds A-F in the Bog's Bog and Peter's Marsh cores could further support a limited spatial extent of the sand beds and thus a non-tsunami deposit. However, since the Bog's Bog and Peter's Marsh sites are non-trench facing, they may not record a tsunami inundation, so they are not as suitable as the Larsen Lake Marsh cores in assessing the spatial congruity of the identified sand beds (Witter et al., 2019).

Unlike the sand beds identified on Nagai Island, tsunami deposits identified along the Alaska-Aleutian subduction zone (e.g., Shennan *et al.,* 2014c; Witter *et al.,* 2016; Witter *et al.,* 2019) and other subduction zones globally (e.g., Sawai, 2002; Dura, 2014) exhibit large spatial extents and the landward thinning. For example, at Stardust Bay along the west of the Alaska-Aleutian subduction zone, Witter *et al.* (2016) were able to trace six tsunami deposits across 45 sites spanning 800 m inland and complimentary research by Witter *et al.* (2019) identified the landward thinning of tsunami deposits from Stardust Bay and nearby Driftwood Bay from 2-11.5 cm near the beach to 0.5-1.5 cm inland. Further, on Kodiak Island along the eastern Alaska-Aleutian subduction zone, Shennan *et al.* (2014c) traced four tsunami deposits between two sites approximately 100m apart. On the Kuril–Kamchatka subduction zone, Japan, Sawai (2002) traced two tsunami deposits approximately 500m inland across three sediment cores, both of which thin landward by approximately 1cm. Finally, six tsunami deposits from the central

Chilean subduction zone were traced approximately 300 m inland and exhibited landward thinning (Dura *et al.,* 2015).

The locally constrained sand bed deposits and the lack of landward thinning exhibited by sand beds A-F from Nagai Island is not consistent with the lithostratigraphy of identified tsunami deposits both along the Alaska-Aleutian subduction zone and at other subduction zones globally supporting a non-tsunami sourced deposition for sand beds A-F. The dominance of sand in the other Deranged Valley cores limits the assessment of the spatial extent of the sand beds A-F across Deranged Valley as sand beds A-F identified in DV.19.03 and 19.DV.17 could be masked within the other sand dominated cores from Deranged Valley. Thus, low level tsunamis for sand beds A-F cannot be ruled out based on sediment evidence. However, since sand beds A-F are not present in the Larsen Lake Marsh cores, the Bog's Bog cores, or the Peter's Marsh cores, sand beds A-F are unlikely to represent high tsunami inundation (Shennan *et al*., 2014; Witter *et al.,* 2014). Further, there is uncertainty in the assessment of the spatial extent of sand beds A, B and C due to the lack of tephra or radiocarbon dating in a Larsen Lake Marsh core to constrain the maximum relative depth of sand beds A, B and C in the Larsen Lake Marsh cores. Therefore, there is an inability to definitively conclude the absence of sand beds A, B and C in the Larsen Lake Marsh cores as there is uncertainty if the peat within the Larsen Lake Marsh cores encapsulates the depositional period of sand beds A, B and C.

The uncertainty in the assessment of the spatial extent for sand beds A-F is offset for sand beds B-F as the non-characteristic tsunami deposit contact sharpness suggests limited lithostratigraphic evidence for tsunami deposits, though additional grain size and diatom evidence would strengthen the determination of non-tsunami deposits for sand beds B-F. However, since sand bed A exhibits similarity in the contact sharpness of tsunami deposits identified on Phra Thong Island, Thailand, and the additional uncertainty in assessing the spatial extent of sand bed A, further grain size and diatom evidence is required to more confidently rule out a tsunami source for sand bed A (Sawai *et al.,* 2009).

The sediment evidence from the Larsen Lake Marsh cores does not exhibit evidence for tsunami inundation (Switzer, 2010; Witter *et al.,* 2014). The sand bed interbedded by peat between 26 cm and 29 cm in LLM.19.01 with moderately sharp upper and lower contacts is synonymous to a tsunami deposit (Nelson *et al.,* 1996; Dura, 2014). However, since the sand bed from LLM.19.01 is not deposited in LLM.19.03, 19.DV.17 or DV.19.03, it likely indicates a

localised extent of the sand bed and hence, does not support a tsunami source for the sand deposit identified in LLM.19.01 (Switzer, 2010; Shennan *et al.,* 2016; Witter *et al.,* 2016). The sand bed identified in LLM.19.01 could be an overbank fluvial deposit, though the non-tsunami source cannot be determined without grain size and diatom analysis (Nelson *et al.,* 2015; Dura and Hemphill-Haley, 2020). Since the Larsen Lake Marsh cores contain large sections of peat and are trench facing, the absence of sand bed deposits supports a lack of high tsunami inundation on Nagai Island throughout the Late Holocene (Witter *et al.,* 2019). Radiocarbon dating of the Larsen Lake Marsh cores would be useful to constrain the age of the base of the core to determine the timeframe where there is no evidence for high tsunami inundation and to compare the ages determined from DV.19.03 to confirm the lack of sand beds A, B and C at the Larsen Lake site (Atwater and Hemphill-Haley, 1996; Kemp *et al.,* 2013).

The sediment evidence within the cores from Bog's Bog and Peter's Marsh (19.BB.03 and 19.PM.02) further support the lack of high tsunami inundation on Nagai Island due to the absence of distinct sand bed deposits (Witter *et al.,* 2014; Nelson *et al.,* 2015). Both Bog's Bog and Peter's Marsh sites are not trench facing, thus, a tsunami originating elsewhere along the Alaska-Aleutian subduction zone may not deposit evidence or exhibit smaller inundation at Bog's Bog and Peter's Marsh (Witter *et al.,* 2019). However, since there is no evidence for tsunami inundation in both Deranged Valley and Larsen Lake Marsh which are trench facing, the non-trench facing Bog's Bog and Peter's Marsh sites does not limited the ability to determine the tsunami history on Nagai Island and the east of the Shumagin section of the Alaska-Aleutian subduction zone.

The 12 cm layer of silt interbedded by peat between 73 cm and 85 cm in 19.BB.03 could indicate a tsunami deposit but the diffuse lower contact and the lack of spatial correlation suggests that the silt buried peat in 19.BB.03 is unlikely a tsunami deposit (Witter *et al.,* 2016; Shennan *et al.,* 2016). Further, Peter's Marsh does exhibit 0.5 cm to 1 cm sand deposits but they are thin, discontinuous and not evident in the adjacent Bog's Bog cores suggesting that they are not a result of tsunami inundation (Switzer, 2010; Witter *et al.,* 2014). The lens of gravel clasts between 147 and 148 cm within 19.PM.02 between the sand lenses as well as in the other cores in the Peter's Marsh site supports the presence of channel margin peat with intermittent flood deposits of sand, gravel clasts and silt as opposed to tsunami inundation (Nelson *et al.,* 2015). However, like the sand deposit identified in LLM.19.01, without grain size and diatoms analysis, the exact source of the sand lenses in 19.PM.02 cannot be identified, but since they

are spatially limited, thin and discontinuous, the evidence for a tsunami source is limited (Atwater and Hemphill-Haley, 1996; Sawai *et al.,* 2015; Witter *et al.,* 2016).

Overall, the sediment evidence from Nagai Island suggests a lack of high tsunami inundation over at least the last ~2900 years, though additional grain size and diatom evidence is required to confidently rule out high tsunami inundation, especially for sand bed A, where the contact sharpness exhibits similarities with tsunami deposits from the 2004 Indian Ocean tsunami (Sawai *et al.,* 2009) and the uncertainty in the spatial extent assessments which limits the confidence of ruling out high tsunami inundation.

6.3.4 Grain Size Evidence for Tsunami Inundation on Nagai Island Throughout the Late Holocene?

Sand bed F from DV.19.03 does not exhibit the typical grain size characteristics of a tsunami deposit in terms of relatively coarse-grained deposits and upward fining (Table 6.1) (Switzer, 2010; Sawai *et al.,* 2015). The mean grain size and d10 within sand beds A-E from DV.19.03 and 19.DV.17 are notably coarser than their respective over and underlying layers which is synonymous to tsunami deposits elsewhere along the Alaska-Aleutian subduction zone (e.g., Nelson et al., 2015; Janigian, 2018; Witter et al., 2019; Prater, 2021). However, only sand beds A, C and D exhibit upward fining of the mean grain size and d10 suggesting that despite relatively coarser deposits for sand beds B and E, the lack of upward fining does not support a tsunami (Table 6.1) (Switzer, 2010; Sawai *et al.,* 2015). Further, only the mean grain size and d10 of sand bed A consistently fine upwards as the overall fining of the mean grain size and d10 within sand beds C and D fluctuates considerably throughout the sand beds, suggesting that the grain size characteristics of sand beds C and D are not diagnostic with tsunami deposits from elsewhere along the Alaska-Aleutian subduction zone (e.g., Nelson et al., 2015; Witter et al., 2019; Prater, 2021). Two tsunami deposits identified by Janigian (2018) on Central Kodiak Island along the Alaska-Aleutian subduction zone displayed multiple upward fining sequences within the sand beds which could explain the fluctuations in the overall fining identified in sand beds C and D. However, the upward fining sequences determined in the two tsunami deposits from Central Kodiak Island differ from the fluctuations in the mean grain size and d10 from sand beds C and D as there are no consistent sub sections of fining within sands bed C and D, instead the grain sizes change erratically within the overall fining (Janigian, 2018). Thus, despite the overall fining within sand beds C and D, the erratic fluctuations suggest non-characteristic tsunami deposits (Sawai *et al.,* 2015; Janigian, 2018).

Combined with the lithostratigraphic evidence, the grain size evidence for sand beds B-F appear inconsistent with tsunami deposits (Table 6.1) (Switzer, 2010; Sawai *et al.,* 2015). Since the grain size characteristics of sand bed A from DV.19.03 are synonymous to identified tsunami deposits elsewhere along the Alaska-Aleutian subduction zone (e.g., Nelson et al., 2015; Janigian, 2018; Witter et al., 2019; Prater, 2021), biostratigraphic analysis is required to overcome the uncertainty in the sediment evidence, discussed in the previous section, in terms of assessing the spatial extent of sand bed A which limits the confidence of ruling out high tsunami inundation for sand bed A.

6.3.5 Diatom Evidence for Tsunami Inundation on Nagai Island Throughout the Late Holocene?

None of sands beds A-F identified in DV.19.03 exhibit anomalous diatom assemblages compared to the overlying and underlying layers, supporting non-tsunami deposits for all of sand beds A-F from Nagai Island (Sawai *et al.,* 2009; Sawai et al., 2012; Nelson *et al.,* 2015) (Table 6.1). Therefore, despite sand bed A's grain size characteristics aligning with palaeotsunami deposits, its moderately abrupt lower contact, and the uncertainty in assessing the spatial extent of sand bed A, the non-anomalous diatom assemblages of sand bed A is more suggestive of a non-tsunami source for sand bed A (Sawai *et al.,* 2009; Nelson et al., 2015; Witter et al., 2019; Prater, 2021). The strong clustering in CONISS between the two basal samples from sand bed A and the underlying peat layer as opposed to a strong independent cluster within sand bed A, and the lack of grouping of the sand bed A samples together or independently from the overlying and underlying layers in DCA is critical evidence to suggest that sand bed A is not an anomalous deposit, implying a non-tsunami source (Pilarczyk *et al.,* 2014). The additional lack of a considerable increase in the diatom fracturing between sand bed A compared to the overlying and underlying peat layers and the absence of notable change in the percentage of planktonic and benthic diatoms between sand bed A and the over and underlying peat layers provides further support for a non-tsunami deposition for sand bed A (Witter *et al.,* 2016; Dura and Hemphill-Haley, 2020).

Since the lithostratigraphy and grain size characteristics of sand beds B-F suggest a non-tsunami deposit, the absence of anomalous diatom assemblages within sand beds B-F further supports the suggestion of non-tsunami sources for sand beds B-F (Table 6.1) (Goff *et al.,* 2001; Goff *et al.,* 2004; Grand Pre *et al.,* 2012; Dura, 2014).

Although, the diatom assemblages of palaeotsunami deposits from elsewhere along the Alaska-Aleutian subduction zone and other subduction zones globally exhibit varying characteristics in terms of the prevailing salinity type and diatom species, the established line of evidence to identify tsunamis deposition is the divergence in the diatom assemblages between the sand beds and the under and overlying layers (Szczicinski *et al.,* 2012; Dura, 2014; Nelson *et al.,* 2015; Janigian, 2018). For example, Nelson *et al.* (2015) identified predominately freshwater diatoms with very few brackish and no marine diatoms in 13 probable tsunami deposits on Chirikof Island. However, they determined that the presence of the brackish coastal diatoms *T. debilis* and *S. brebissonii* which were not identified in the rest of the core were indicative of a tsunami deposition as the former lower lake did not rise high enough to source the brackish coastal diatoms and thus, they must have been transported from the lower shallower lake during tsunami inundation (Nelson *et al.,* 2015). Further, the dominance of freshwater diatoms in the tsunami deposits is likely due to the entrainment of freshwater species as the tsunami waves traverse over freshwater environments (Szczicinski *et al.,* 2012; Nelson *et al.,* 2015). Contrastingly, Janigian (2018) and Prater (2021) identified mixed diatom assemblages for two palaeotsunami deposits from Central Kodiak Island, Alaska and three palaeotsunami deposits on Sitkadilik Island, Alaska respectively which were anomalous to the over and underlying layers which contained predominately freshwater and brackish diatoms. Therefore, since there are no considerable changes or anomalous species between the diatom assemblages from the over and underlying layers and sand beds A-F on Nagai Island, it appears that the diatom assemblages from sand beds A-F are not consistent with tsunami deposition.

The primary clustering of the diatom assemblages from sand beds D, E and F with their respective over and underlying layers, and the close clustering of the sand bed B samples to the over and underlying layers suggests that the diatom assemblages from sand beds B, D, E and F are not considerably different to the over and underlying layers, thus, limiting the support for a tsunami deposit (Grimm, 1986; Dura, 2014; Witter *et al.,* 2016; Janigian, 2018; Prater, 2021).

The close grouping of sand beds A, B, C, D, and F to their under and overlying layers in the DCA and the lack of independent grouping in sand bed E demonstrates that the sand bed diatom assemblages are not consistently different to their over and underlying layers and hence provides additional diatom evidence for non-tsunami depositions for sand beds A-F (Birks,

1992; Dura, 2014). Diatom samples from two palaeotsunami deposits from Central Kodiak Island, Alaska plotted together and independently from the rest of the samples in a DCA biplot (Janigian, 2018) and three palaeotsunamis from central Chile displayed distinct shifts in the DCA biplot between sand beds and their over and underlying layers (Dura *et al.,* 2015) suggesting that sand beds A-F are not distinctly different from their over and underlying layers as they do not plot together and independently further supporting non tsunami disposition (Birks, 1992; Dura, 2014).

It is possible that the transition from predominantly marine diatoms in the basal 10cm of sand bed C to predominantly brackish diatoms in the surface 10cm of sand bed C is due to the fallout of heavier marine diatoms first, followed by lighter brackish diatoms during a tsunami or storm deposit (Tanigawa *et al.,* 2018). However, as identified in sand beds B, D and F, the preferred clustering in CONISS and the similar grouping in DCA for the four surface samples from sand bed C with the overlying peat samples as opposed to the four surface samples from sand bed C clustering and grouping with the four basal samples from sand bed C suggests the gradual transition from a tidal channel to a saltwater marsh environment due to additional protection from tidal inundation at DV.19.03as opposed to an anomalous tsunami deposit responsible for the deposition of sand bed C (Hemphill-Haley, 1996; Switzer and Jones, 2008; Dura, 2014). Further, if sand bed C is a tsunami deposit, it would likely represent the deposition of multiple waves since it is 20 cm thick as evidence by Janigian (2018) in tsunami deposits up to 12 cm thick. Therefore, despite the possibility that the transition from predominantly marine to predominantly brackish species in sand bed C is a result of the fallout of heavier marine diatoms first, followed by lighter brackish diatoms, the similarity between the four surface samples of sand bed C and the overlying peat samples, and the lack of evidence for multiple waves within sand C, it suggests that the diatom assemblages for sand bed C supports a non-tsunami deposition.

The mixed diatom assemblages and the fluctuation between predominantly freshwater diatoms and predominately marine diatoms between the samples within sand bed E is interesting as it differs from the three sand beds identified in DV.19.03 and sand beds D and F from 19.DV.17. Nelson *et al.* (2015) determined that mixed assemblages can be indicative of a tsunami deposit due to the entrainment of freshwater and brackish diatoms during the transportation inland. However, since the layer underlying sand bed E contains predominately marine diatoms and there is a limited contribution of brackish diatoms, it suggests that it is unlikely that freshwater

diatoms were entrained during a tsunami inundation as the host material is not a freshwater marsh (Tanaka *et al.,* 2012; Pilarczyk *et al.,* 2014; Nelson *et al.,* 2015). Further, the fluctuation between predominately marine and predominately freshwater diatoms evident in the layer overlying sand bed E implies that the diatom assemblages of sand bed E is not anomalous (Pilarczyk *et al.,* 2014). Therefore, the mixed diatom assemblages identified within sand bed E and the fluctuation in the dominance between freshwater and marine diatoms could be due to a mixture of tidal inundation and overbank fluvial deposits, especially as sand is found within the fluvial channel system, rather than from a tsunami inundation (Hemphill-Haley, 1996; Pilarczyk *et al.,* 2014; Nelson *et al.,* 2015; Dura and Hemphill-Haley, 2020).

Additional diatom evidence to suggest non-tsunami deposits for sand beds A-F include the lack of considerable changes in the percentage of fractured diatoms between the sand beds and their over and underlying layers (Table 6.1) (Dominey-Howes *et al.,* 2006; Kortekaas and Dawson, 2007; Pilarczyk *et al.,* 2014; Dura and Hemphill-Haley, 2020). Although sand bed B exhibits a notably higher average of fractured diatoms compared to the underlying layer, which could be argued as anomalous, one sample from the underlying layer exhibits a similar percentage of fractured diatoms as the sand bed B samples and the layer overlying sand bed B exhibits similar diatom fracturing to sand bed B suggesting that, like the other sand beds, the fracturing within sand bed B is not anomalous, thus, further supporting the lack of diatom evidence in favour of tsunami disposition for sand beds A-F (Dominey-Howes *et al.,* 2006; Dura and Hemphill-Haley, 2020).

Compared to palaeotsunami deposits elsewhere along the Alaska-Aleutian subduction zone and along other subduction zones globally, the percentage of fractured diatom within sand beds A-F is high (Kortekaas and Dawson, 2007; Chagué-Goff *et al.,* 2011; Nelson *et al.,* 2015; Janigian, 2018). For example, on Chirikof Island, Alaska, Nelson *et al.* (2015) determined diatom fracturing in 13 probable tsunami deposits between 65-88 % and for two palaeotsunamis from Central Kodiak Island, Alaska, Janigian (2018) identified diatom fracturing between 63-65 %, whereas sand beds A-F exhibited 35-100% fractured diatoms. Despite the relatively higher diatom fracturing in sand beds A-F compared to palaeotsunami deposits, a key difference between sand beds A-F and the identified palaeotsunamis is the lack of considerable change between the percentage of fractured diatoms in the sand beds and the percentage of fractured diatoms in the over and underlying layers. The stratigraphic layers over and underlying the 13 probable palaeotsunamis on Chirikof Island, Alaska exhibited considerably lower diatom

fracturing compared to the 13 probable tsunami deposits (30-50 % compared to 65-88 %) (Nelson *et al.,* 2015) which is similar to the two palaeotsunamis on Central Kodiak Island, Alaska (58 % compared to 63-65 %) (Janigian, 2018). Therefore, the diatom fracturing in sand beds A-F is not synonymous to tsunami deposits as there is minimal change in the percentage of fractured valves between the sand beds and the over and underlying layers, further supporting the lack of diatom evidence for tsunami deposition for sand beds A-F.

Finally, the lack of notable changes in the diatom life forms between sand beds A-F and their over and underlying layers supports non-tsunami depositions for sand beds A-F (Table 6.1) (Dura and Hemphill-Haley, 2020). For example, Janigian (2018) identified large increases in the percentage of benthic diatoms like *Planothidium Delicatulum* in identified tsunami deposits (approximately 40-50 % increases within tsunami deposits) suggesting that the absence of considerable changes in the percentage of planktonic and benthic species between the sand bed A-F deposits and their over and underlying layers alongside the lack of anomalous diatoms assemblages and diatom fracturing within sand beds A-F further limits the diatom evidence for tsunami deposition.

6.3.6 Collectively Does the Lithostratigraphy, Grain Size and Diatom Evidence Support Tsunami Inundation on Nagai Island Throughout the Late Holocene?

Overall, the absence of abrupt upper and lower contacts, a limited spatial extent, non-upward fining deposits, and the lack of anomalous diatom assemblages, anomalous fracturing or anomalous changes in diatom life forms for sand beds B-F suggests a non-tsunami source (Switzer, 2010) (Table 6.1).

Despite sand bed A exhibiting some characteristics synonymous to palaeotsunami deposits from elsewhere along the Alaska-Aleutian subduction zone and other subduction zones globally in terms of the contact sharpness and the upward fining of grain size, and the uncertainty in assessing the spatial extent of sand bed A, the lack of anomalous diatom assemblages, anomalous fracturing and anomalous life forms in sand bed A provides limited support for a tsunami deposition (Table 6.1) (Switzer, 2010; Sawai *et al.,* 2015).

The additional lithostratigraphic evidence from the cores at Larsen Lake Marsh, Bog's Bog and Peter's Marsh to the detailed lithostratigraphic, grain size and diatoms analysis of DV.19.03 and 19.DV.17 from Deranged Valley further support a lack of high tsunami inundation on Nagai Island throughout the Late Holocene. The absence of tsunami evidence on Nagai Island agrees

with the findings of Witter *et al.* (2014) who found no evidence of high tsunami inundation on nearby Simeonof Island over the last ~3400 years. Although, Bécel *et al.* (2017) and von Huene *et al.* (2019) determined that the geological features of the Shumagin section are favourable to large tsunamis in terms of heterogenous plate interfaces, a small wedge of deformed sediment in the frontal prism and splay faults, it appears that throughout the late Holocene (~2900 years) no large tsunami has neither originated within the Shumagin section nor propagated into the Shumagin section from a great earthquake generated elsewhere along the Alaska-Aleutian subduction zone or generated from another subduction zone globally.

The lithostratigraphic, grain size and diatom evidence for sand beds A-C in DV.19.03 is more consistent with three periods of tidal channel deposition during salt marsh establishment, especially due to the overall freshening of the DV.19.03 from the base to the surface which suggests increased protection from tidal inundation throughout the Late Holocene as opposed to changes associated with coseismic land level change and tsunami inundation (Dura and Hemphill-Haley, 2020). The radiocarbon dating confirms that sand beds D-F in 19.DV.17 are younger than sand beds A-C in DV.19.03, thus, they do not relate to the same depositional events. However, sand beds D-F also likely represent three separate periods of tidal inundation during salt marsh establishment with the additional input from intermittent fluvial overbank channel deposits for sand bed E.

However, as discussed for the coseismic land level change on Nagai Island, high tsunami inundation on Nagai Island throughout the late Holocene cannot be completely ruled out due to the potential of missing evidence in terms of erosion, the masking of a tsunami deposit within a sand dominated system, and the lack of known modern tsunami deposits in the Shumagin section to compare potential palaeotsunami deposits to (Dura, 2014; Kelsey *et al.,* 2015; Nelson *et al.,* 2015). Modern known tsunami deposits are important as tsunami diatom characteristics are spatially unique (Szczicinski *et al.,* 2012; Nelson *et al.,* 2015). For example, Nelson *et al.* (2015) found no marine diatoms in tsunami deposits on Chirikof Island due to the entrainment of freshwater and brackish diatoms from beaches and dunes, whereas Witter *et al.* (2019) identified marine diatoms in the palaeotsunami deposits on Sedanka and Umnak Island, demonstrating the importance of a site-specific modern tsunami analogue for interpreting potential palaeotsunami deposits. Nelson *et al.* (2015), Janigian (2018), Witter *et al.* (2019), and Prater (2021) all compared potential sand bed deposits identified to known modern tsunami deposits from historical great earthquakes and high tsunami inundation to determine similarities

and differences and to aid the interpretation of the potential palaeotsunami deposits. Therefore, the lack of a modern tsunami deposit in Deranged Valley increases the uncertainty in the determination of the sources of the six identified sand beds, hence high tsunami inundation on Nagai Island throughout the late Holocene cannot be completely ruled out (Sawai *et al.,* 2009; Zong and Sawai, 2015).

The apparent lack of high tsunami inundation on Nagai Island throughout at least the last ~2900 years suggests a persistence of small magnitude and or the locally constrained extent of tsunamis associated with great earthquakes in the Semidi and Unimak sections of the Alaska-Aleutian subduction zone as evidenced by the lack of tsunami inundation on Nagai Island from the 1938 Semidi section great earthquake and the 1946 Unimak section great earthquake (Lander, 1996). Though, without palaeoseismic reconstructions in the western Semidi and the Unimak sections of the Alaska-Aleutian subduction zone, the absence of high tsunami inundation coinciding with palaeo great earthquakes from the adjacent Semidi and Unimak sections of the Alaska-Aleutian subduction zone cannot be determined, as it is not known how many great earthquakes and associated tsunamis in the adjacent sections have occurred throughout the late Holocene (von Huene *et al.,* 2019).

The absence of evidence for high tsunami inundation on Nagai Island differs from other sections of the Alaska-Aleutian subduction zone. For example, the Prince William sound section has exhibited two high tsunami inundations since A.D. 1020-1150 (Shennan *et al.,* 2014c), the Kodiak section has geological evidence for four high tsunami inundations since A.D. 1020-1150 (Shennan *et al.,* 2014c), on Sitkinak Island on the boundary between the Kodiak and Semidi section, six high tsunamis occurred over the last 3000 years, Nelson *et al.* (2015) determined a probable 180 yr recurrence interval for 5 m tsunamis over the last ~3400 years in the eastern Semidi section, and Witter *et al.* (2019) determined a recurrence interval between 164 and 257 years for large tsunamis between Driftwood Bay and Sedanka Island compared to Nagai Island and Simeonof Island in the Shumagin section of the Alaska-Aleutian subduction zone which do not appear to exhibit high tsunami inundation over at least the last ~2900 years and ~3400 years respectively (Witter *et al.,* 2014).

6.4 Does the Late Holocene Lithostratigraphic and Microfossil Data from Nagai Island Support Davies' *et al.* (1981) Interpretation of the Russian Outpost Documents for a Great Earthquake in the Shumagin Section of the Alaska-Aleutian Subduction Zone in 1788?

The geological evidence from Nagai Island does not identify coseismic land level change or high tsunami inundation associated with the report of strong ground shaking and high tsunami inundation in 1788 recorded in Russian outpost documents on Unga Island (Davies *et al.,* 1981; Lander, 1996). The lack of evidence to suggest a great earthquake and high tsunami inundation on Nagai Island in 1788 supports the findings of Witter *et al.* (2014) who did not find evidence for coseismic land level change or tsunami inundation in 1788 on Simeonof Island. Thus, it is unlikely that in 1788, a great earthquake and high tsunami inundation generated within the Shumagin section or propagated from adjacent sections of the Alaska-Aleutian subduction zone as determined by Davies' *et al.* (1981) interpretation of the Russian outpost documents and by Bécel's *et al.* (2017) analysis of the geological features within the Shumagin section that suggested that the Shumagin section could have ruptured coseismically from the propagation of a great earthquake from the Semidi section in 1788.

Since the Russian outpost documents reporting the strong ground shaking and tsunami inundation are from Unga Island, located approximately 55 km from Nagai Island, Freymueller and Beavan (1999) suggest that it is possible that there was a small, locked section of the Alaska-Aleutian subduction zone near Unga Island which could have generated a great earthquake and tsunami in 1788. However, if a great earthquake was generated in a small, locked section of the Shumagin section near Unga Island, tsunami evidence would be expected on Nagai Island and Simeonof Island and since it is not, the argument for a spatially isolated locked section of the Shumagin section appears unlikely (Freymeuller and Beavan, 1999). Further, the Russian outpost documents report the height of the tsunami as more than 30m which under a scenario where a small, locked section of the Alaska-Aleutian subduction zone near Unga Island generated a great earthquake in 1788, a tsunami greater than 30 m would be unlikely (Soloviev, 1986; Lander, 1996). A palaeoseismic reconstruction of Unga Island would confirm if a great earthquake and coinciding tsunami occurred on Unga Island in 1788.

The lack of evidence for coseismic land level change on Nagai Island associated with the 1788 reported earthquake and tsunami inundation provides evidence to test Witter's *et al.* (2014) suggestion that the absence of evidence for a great earthquake and high tsunami inundation on Simeonof Island in 1788 could be due to the location of the hingeline near Simeonof Island.

Witter *et al.* (2014) used an elastic model to generate different scenarios of earthquake ruptures underneath Simeonof Island where the produced maximum estimates of slip of the megathrust correspond to small (<0.3 m) vertical displacement on Simeonof Island. The 0.3 m of vertical displacement was chosen by Witter *et al.* (2014) as it would unlikely record identifiable sediment and microfossil signals. Scenarios where megathrust slip extended from the trench to depths between 20-35 km depths require 1.8-5 m of slip elsewhere along the megathrust to produce less than 0.3 m of vertical displacement on Simeonof Island, for scenarios where slip stopped short of the trench between 15-25 km required 2-4 m of slip elsewhere along the megathrust, and a final scenario where rupture between 40 km depth and the trench required 15 m of slip on the megathrust which would result in at least a 9 M_W earthquake elsewhere in the Shumagin section and a large seafloor displacement producing high tsunami inundation on Simeonof Island and elsewhere in the Shumagin section. Therefore, the lack of evidence for coseismic land level change between 1.8 m and 15 m and high tsunami inundation on Nagai Island suggests that the scenarios modelled by Witter *et al.* (2014) to possibly reconcile the disparity between the Russian outpost documents and the geological evidence from Nagai and Simeonof Islands seem unlikely.

The apparent disconnect between the Russian outpost documents and the geological evidence from Nagai Island and Simeonof Island could be because of the overinterpretation of the magnitude of the earthquake and tsunami reported in 1788, especially as it is not clear what the Russian outpost documents are referring to in their recording of the magnitude of the tsunami inundation (Tarr and Martin, 1912; Lander, 1996; Witter *et al.,* 2014). Instead of a great earthquake either generated within the Shumagin section as interpreted by Davies *et al.* (1981) or a multi section great earthquake propagated from the adjacent Semidi section as suggested by Bécel *et al.* (2017), a large earthquake and low-level tsunami could have occurred in the Shumagin section in 1788, as too little vertical displacement associated with large earthquakes would result in the absence of coseismic land level change and tsunami inundation evidence in the geological record in the Shumagin section, as identified on Nagai Island and Simeonof Island (Witter *et al.,* 2014). However, since large earthquakes and low-level tsunamis are not identifiable in the geological record due to the lack of a distinguishable geological imprint, the magnitude of the 1788 reported earthquake and tsunami cannot be determined, though it can be concluded that the absence of geological evidence for coseismic land level change and high tsunami inundation on both Nagai Island and Simeonof Island opposes Davies *et al.* (1981)

interpretation of a great earthquake and high tsunami inundation in the Shumagin section of the Alaska-Aleutian subduction zone in 1788 (Witter *et al.,* 2014). A palaeoseismic reconstruction of the western Semidi section would be useful to determine if there is evidence for a great earthquake and high tsunami inundation east of the Shumagin section in 1788 because if there is no geological evidence for coseismic land level change and high tsunami inundation it would support a spatially constrained large earthquake generated in the Shumagin section in 1788 coincidently at a similar time to the great earthquake which ruptured the Kodiak section in 1788 as opposed to a second great earthquake either originating in the Shumagin section or propagating from the adjacent Semidi section (Davies *et al.,* 1981; Bécel *et al.,* 2017).

The absence of identifiable geological evidence on Nagai Island for the 1917 and 1948 large earthquakes and low-level tsunami inundations in the Shumagin section further supports the possibility that the 1788 reported earthquake and tsunami in the Shumagin section of the Alaska-Aleutian subduction zone was a large earthquake as opposed to a great earthquake as interpreted by Davies *et al.* (1981) (Estabrook and Boyd, 1992; Lander, 1996). The 1917 and 1948 large earthquakes in the Shumagin section demonstrate that historical large earthquakes and associated tsunamis in the Shumagin section did not leave identifiable geological evidence thus, since there is no geological evidence for coseismic land level change or tsunami inundation for the reported 1788 earthquake and tsunami on either Nagai or Simeonof Island, it suggests that the reported 1788 earthquake and tsunami could have been a large earthquake and associated tsunami as that would have likely not have left a geological imprint as identified on both Nagai and Simeonof Islands.

It has been proposed that foul play by the Russian settlers towards the indigenous Aleuts may have led to an exaggeration in their recording of the magnitude of the 1788 earthquake and tsunami in the Shumagin section (Engelhart *et al.,* 2018). A previous massacre of 300 to 3000 Koniag Alutiiq people occurred in 1784 on Sitkadilik Island demonstrating the conflict between the Russian settlers and the indigenous Aleuts (Engelhart *et al.,* 2018). The Russian outpost documents suggests that the 1788 tsunami on Unga Island disproportionately impacted the Aleuts, translated from Veniaminov by Black and Geoghegan (1984), as “there was a terrible inundation on Unga Island in which many Aleuts perished but God spared the Russians”. Thus, the magnitude of the earthquake and tsunami reported on Unga Island in 1788 may have been exaggerated in the Russian outpost documents to cover up a genocide of the indigenous Aleuts on Unga Island as violence against Aleuts was prohibited and only Aleuts died (Engelhart *et*

al., 2018). The possibility that the earthquake and tsunami magnitudes were exaggerated in the Russian outpost documents further supports the suggestion that a large earthquake and low-level tsunami occurred in the Shumagin section in 1788 as opposed to a great earthquake and high tsunami inundation proposed by Davies *et al.* (1981), though as discussed above, the occurrence of a large earthquake and a low-level tsunami in the Shumagin section of the Alaska-Aleutian subduction zone in 1788 cannot be determined due to the lack of a geological imprint associated with large earthquakes (Witter *et al.,* 2014).

Since the top 92 cm of the DV.19.03 core, where the 1788 earthquake would likely be recorded, is dominated by freshwater diatoms, it is possible that even if coseismic land level change occurred in 1788 it may not have imprinted an identifiable signal in the diatom assemblages of DV.19.03. However, despite the potential for missing geological evidence for coseismic land level change in DV.19.03, the lack of coseismic land level change evidence in the diatom analysis of 19.DV.17, where freshwater diatoms generally do not dominate the diatom assemblages, the absence of tsunami evidence across Nagai Island, and the lack of coseismic land level change and tsunami inundation on Simeonof Island suggests that it is unlikely (Witter *et al.,* 2014).

Further, the poor preservation of the geological evidence could result in the erosion of geological evidence for a great earthquake and high tsunami inundation associated with the reported 1788 earthquake and tsunami on Unga Island (Coe and Church, 2003; Dura, 2014; Kelsey *et al.,* 2015). Further, since there is an absence of geological evidence for coseismic land level change and tsunami inundation on Nagai and Simeonof Islands, it is unlikely that both islands exhibit poor preservation of the geological record, especially as the relative sea level has gradually risen throughout the Late Holocene on Simeonof Island enabling good preservation of geological evidence due to accommodation space availability and the stabilised dune system on Nagai Island suggests minimal erosion throughout the late Holocene on Nagai Island (Witter *et al.,* 2014; Kelsey *et al.,* 2015). Therefore, the poor preservation of geological evidence limiting the identification of a great earthquake and high tsunami inundation in the Shumagin section in 1788 seems unlikely.

The potential misinterpretation or inaccurate recording of the 1788 earthquake and tsunami on Unga Island highlights the limitations of using the Russian outpost documents for inferring seismic hazard along the Alaska-Aleutian subduction zone, especially as the Russian outpost

documents predate the historical documents from Hawaii, where a large tsunami generated from a great earthquake in the Semidi or Shumagin section would likely propagate towards (Lander, 1996).

Overall, the geological evidence from Nagai Island alongside the additional geological evidence from Simeonof Island (Witter *et al.,* 2014) does not support Davies' *et al.* (1981) interpretation of the Russian outpost documents from Unga Island that a great earthquake and high tsunami inundation occurred in 1788. Instead, a large earthquake and low-level tsunami in the Shumagin section in 1788 is more aligned with the geological evidence from the Shumagin section throughout the Late Holocene. However, since the vertical displacement of a large earthquake is too small to leave a geological imprint, the occurrence of a large earthquake and low-level tsunami in 1788 in the Shumagin section cannot be definitively concluded (Witter *et al.,* 2014).

6.5 What are the Implications of the Nagai Island Palaeoseismic Reconstruction for the Seismic and Tsunamigenic Potential of the Shumagin section of the AASZ?

The absence of geological evidence for coseismic land level change on Nagai Island combined with Simeonof Island (Witter *et al.,* 2014) suggests that over at least the last ~2900 years there has been an absence of great earthquakes generated in the Shumagin section of the Alaska-Aleutian subduction zone. Therefore, it appears that the current creeping of the Shumagin section to accommodate plate convergence has persisted throughout the late Holocene, which contrasts Witter's *et al.* (2016) research on Sedanka Island where the current creeping has not persisted throughout the late Holocene. The geological evidence from both Nagai Island and Simeonof Island suggests that unlike at Sedanka Island, large earthquakes in the Shumagin section, such as in 2020 have been sufficient to release any strain accumulation in the Shumagin section over at least the last ~2900 years and thus, the hazard of a great earthquake generating in the Shumagin section is low (Estabrook and Boyd, 2002; Fournier and Freymueller, 2007; Jiang *et al.,* 2021). The hazard of a great earthquake in the Shumagin section is lower compared to other sections of the Alaska-Aleutian subduction zone despite previous conclusions that the Shumagin section has the equally highest probability for a great earthquake along the Alaska-Aleutian subduction zone (Jacob, 1984). Large earthquakes and associated tsunamis appear to be the greatest hazard, hence hazard assessments and preparation should focus on large earthquakes in the Shumagin section, though, without ruling out the possibility of a great earthquake.

Further, over the last ~3400 years the Shumagin section has not coseismically weakened from the propagation of a great earthquake from the adjacent sections of the Alaska-Aleutian subduction zone, implying that the Shumagin section has been a persistent barrier to great earthquake rupture over the late Holocene (Noda and Lapustra, 2013). Although, without palaeoseismic reconstructions of the western Semidi section and Unimak section of the Alaska-Aleutian subduction zone, it is not known how many times over the last ~3400 years that the Shumagin section has resisted the propagation of a great earthquake generated in the adjacent Semidi and Unimak sections.

The geological evidence from Nagai Island implies that there is a low hazard for a great earthquake generating or propagating into the Shumagin section, contrasting Davies *et al.* (1981) suggestion that a great earthquake would likely occur in the Shumagin section in the following two decades. However, despite the geological evidence suggesting a low hazard for a great earthquake in the Shumagin section, a great earthquake cannot be completely ruled out (Dura *et al.,* 2017). The geological evidence is relatively short term; therefore, it is possible that before ~3400 years ago there were periods of a locked plate interface in the Shumagin section and that great earthquakes occurred as evident on Sedanka Island as the locking at the plate interface can change through time (Witter *et al.,* 2019). Thus, a great earthquake generated in the Shumagin section cannot be ruled out in the future if the dynamics of the plate interface change from creeping to locked (Fournier and Freymueller, 2007).

Further, it is possible that despite the apparent lack of propagation of a great earthquake into the Shumagin section, a great earthquake propagating from the adjacent Semidi or Unimak section cannot be completely ruled out as rupture areas are not spatially consistent through time (e.g., Briggs *et al.,* 2014) and even in areas of a persistent barrier to rupture such as the Arauca Peninsula along the Chilean subduction zone, great earthquakes have propagated into but not entirely throughout (Dura *et al.,* 2017). Thus, suggesting that the Shumagin section could partially rupture in a great earthquake in the future, especially as it is unknown how many times the Shumagin section has impeded rupture from the adjacent Semidi and Unimak sections due to the lack of palaeoseismic reconstructions in the adjacent sections and it is unknown why the Shumagin section has acted as a persistent resistor to slip throughout the late Holocene (McKay *et al.,* 1997; Bécel *et al.,* 2017; Dura *et al.,* 2017; von Huene *et al.,* 2019).

The potential for the erosion of the geological record and uncertainties associated with palaeoseismic reconstructions prohibits the definitive conclusion for the absence of great earthquakes and therefore cannot be certain that there is a low hazard for a great earthquake in the Shumagin section in the future (Kelsey *et al., 2015;* Shennan *et al.,* 2016).

The lack of high tsunami inundation on Nagai Island as well as Simeonof Island over at least the last ~2900 and ~3400 years respectively suggests that there is a low hazard for high tsunamis generated from a great earthquake within the Shumagin section (Witter *et al.,* 2014). Further, the absence of high tsunami inundation on Nagai and Simeonof Islands propagated from a great earthquake in the adjacent Semidi and Unimak sections of the Alaska-Aleutian subduction zone over at least the last ~2900 and ~3400 years respectively implies that the Shumagin section has a low hazard for teletsunami inundation from tsunamis generated from earthquakes elsewhere along the Alaska-Aleutian subduction zone and other subduction zones (Witter *et al.,* 2014). Overall, there appears to be a low hazard for high tsunamis generated locally within the Shumagin section, a low hazard for communities in Hawaii and along the Pacific west coast of the USA and Canada that would be vulnerable to a tsunami generated from a great earthquake in the Shumagin section of the Alaska-Aleutian subduction zone, and a low hazard for teletsunamis propagating into the Shumagin section from earthquakes elsewhere along the Alaska-Aleutian subduction zone and from other subduction zones (Ryan *et al.,* 2012).

However, high tsunami generation in the Shumagin section cannot be ruled out in the future as it is possible that the plate interface in Shumagin section can change from creeping to locked thus, posing a hazard for great earthquake and high tsunami inundation (Freymueller and Beavan, 1999; Witter *et al.,* 2019). Further, since Bécel *et al.* (2017) and von Huene *et al.* (2019) determined that the geology of the Shumagin section is favorable to generating widespread large tsunamis a change in the locking of the plate interface in the Shumagin section would considerably increase the hazard of a large tsunami in the Shumagin section and for far field communities in Hawaii and along the Pacific West coast of the USA.

In addition, the potential for missing evidence for high tsunami inundation on Nagai Island in terms of the erosion of tsunami deposits, a tsunami deposit masked within a sand dominated system, and the uncertainties in assessing the spatial congruity of tsunami deposits further limited by the absence of a modern tsunami deposit in the Shumagin section to compare

potential tsunami deposits to limits the confidence in concluding a lack of high tsunami inundation in the Shumagin section throughout the late Holocene (Spiske *et al.,* 2013; Kelsey *et al.,* 2015; Nelson *et al.,* 2015). Therefore, despite the apparent low hazard of high tsunami generation and propagation in the Shumagin section, the potential for missing high tsunami evidence cannot be ruled out.

Without palaeoseismic reconstructions of the western Semidi section and the Unimak section of the Alaska-Aleutian subduction zone, it is not known how many great earthquakes have occurred with too little tsunami inundation to leave a geological imprint in the Shumagin section. Thus, the persistence of limited tsunami hazard in the Shumagin section and trans Pacifically, associated with great earthquakes from the adjacent Semidi and Unimak sections, cannot be fully assessed without palaeoseismic reconstructions of the western Semidi section and the Unimak section.

Overall, the hazard of a great earthquake and high tsunami inundation, both generated and propagated into the Shumagin section is low, although they cannot be ruled out in the future. Thus, it is important to acknowledge the potential but low hazard of great earthquakes and high tsunamis in seismic hazard assessments of the Shumagin section of the Alaska-Aleutian subduction zone as well as far field communities in Hawaii and along the Pacific west coasts of the USA and Canada that would be vulnerable to tsunamis generated in the Shumagin section and adjacent Semidi and Unimak sections of the Alaska-Aleutian subduction zone. Further, just because the hazard of great earthquakes generated and propagated into the Shumagin section appears low, the hazard of large earthquakes and accompanying tsunamis, as evident by the 2020 large earthquake doublet, need to be considered and prepared for in seismic hazard assessments (Jiang *et al.,* 2021).

A key implication of the geological evidence from Nagai Island combined with the geological evidence from Simeonof Island is the limitation of using historical records to assess seismic hazard (Engelhart *et al.,* 2018). The conclusions drawn by Davies *et al.* (1981) based on the Russian outpost documents produced vastly different conclusions to the geological evidence, demonstrating the need to be aware of the potential inaccuracies of historical data and that palaeoseismic reconstructions are critical to best constrain seismic hazard. The geological evidence also identified the unique palaeoseismic behavior of the Shumagin section compared to the other areas of the Alaska-Aleutian subduction zone that have undergone palaeoseismic

reconstructions despite similar current plate interface dynamics (e.g., Witter *et al.,* 2019). Thus, demonstrating the importance of wide scale palaeoseismic reconstructions to produce a holistic understanding of seismic hazard along the Alaska-Aleutian subduction zone rather than assuming similarities between areas of similar modern plate interface dynamics (e.g., Witter *et al.,* 2019).

6.6 Future Recommendations

Palaeoseismic reconstructions in the western Semidi section is a critical future recommendation to identify the number of great earthquakes that have occurred in the western Semidi section to determine the number of times that the Shumagin section has resisted the propagation of a great earthquakes from the adjacent Semidi section throughout the late Holocene. Ideally, a palaeoseismic reconstruction within the Semidi section, just west of the 1938 and 2021 great earthquake rupture areas and in the Semidi section within the western boundary of the rupture area of the 1938 great earthquake would enable a better understanding of the history of great earthquakes in the western Semidi section of the Alaska-Aleutian subduction zone and if there is a persistent barrier to great earthquake propagation into the Shumagin section of the Alaska-Aleutian subduction zone (Figure 1.1).

Palaeoseismic reconstructions of the eastern Unimak section alongside the western Shumagin section is an additional recommendation as it would determine if the west of the Shumagin section is susceptible to the propagation of great earthquakes from the adjacent Unimak section and identify the spatial extent of the long-term persistent creep identified in the eastern Shumagin section. The eastern Unimak Island for the Unimak section and Sanak Island for the western Shumagin section would be suitable locations for the palaeoseismic reconstructions.

The palaeoseismic reconstructions of the adjacent Semidi and Unimak sections suggested are important to better understand the hazard of teletsunamis in the Shumagin section from tsunamis generated in the adjacent Semidi and Unimak sections of the Alaska-Aleutian subduction zone as well as the hazard of teletsunamis to far field locations in Hawaii and along the Pacific west coast of the USA and Canada.

A further palaeoseismic reconstruction of Unga Island, where the Russian outpost documents are from, would complement the geological evidence from Nagai Island and Simeonof Island in terms of ruling out a locally constrained locking of the plate interface near Unga Island

suggested by Freymueller and Beavan (1999) and hence rule out a great earthquake for the 1788 reported ground shaking and tsunami in the Russian outpost documents (Dura *et al.,* 2017; von Huene *et al.,* 2019).

Research into the structural features of the Shumagin section that enable the repeated resistance to slip propagating from adjacent sections identified in the geological evidence from Nagai Island and Simeonof Island is important to understand why the Shumagin section of the Alaska-Aleutian subduction zone has unique seismic behaviour over the late Holocene compared to other areas of the Alaska-Aleutian subduction zone (e.g., Becel *et al.,* 2017; von Huene *et al.,* 2019). Understanding the mechanisms that have enabled long term creep of the Shumagin section could complement the palaeoseismic reconstruction to give further insight in the future hazard of great earthquakes in the Shumagin section (Becel *et al.,* 2017; von Huene *et al.,* 2019).

Modern diatom samples across the elevational range from the intertidal to the freshwater marsh would enable a quantitative reconstruction of the depositional environments as opposed to a qualitive reconstruction of the depositional environments on Nagai Island. Further, modern diatom samples across the elevational range would enable a comparison of the sand bed diatom compositions to modern environments to better determine the sources of the sand bed deposits (Dura, 2014).

Finally, radiocarbon dating of the base of the LLM.19.01 or the LLM.19.03 core would be useful to compare to the age of the DV.19.03 core to confidently conclude if the three sand beds identified in the DV.19.03 core are absent from the Larsen Lake Marsh cores.

Overall, palaeoseismic reconstructions in the west of the Semidi section, the west of the Shumagin section, the Unimak section and on Unga Island are the most important recommendations for future research to improve the understanding of the spatial extent of the persistent creep identified in the eastern Shumagin section of the Alaska-Aleutian subduction zone and to constrain the history of great earthquakes and accompanying tsunamis in the immediately adjacent sections of the Alaska-Aleutian subduction zone. The palaeoseismic reconstructions will enable a more holistic understanding of the seismic history to best constrain the seismic hazard along the Alaska-Aleutian subduction zone.

7.0 Conclusion

To conclude, the lithostratigraphic, grain size, diatom and chronological evidence from Nagai Island identifies a lack of land level change and sand bed deposits conclusively linked to high tsunamis suggesting an absence of great earthquakes and high tsunamis in the Shumagin section of the Alaska-Aleutian subduction zone over at least the last ~2900 years. The geological evidence from Nagai Island supports Witter's *et al.* (2014) suggestion of long-term persistent creep to accommodate plate convergence in the Shumagin section of the Alaska-Aleutian subduction zone.

The lack of geological evidence for coseismic land level change on both Nagai Island and Simeonof Island suggests that the Shumagin section has neither generated a great earthquake nor coseismically weakened through the propagation of a great earthquake from the adjacent Semidi or Unimak sections throughout the late Holocene (at least ~2900 years for Nagai Island and at least ~3400 years for Simeonof Island).

Further, the absence of geological evidence for high tsunami inundation on both Nagai Island and Simeonof Island implies that the Shumagin section of the Alaska-Aleutian subduction zone has not generated a large tsunami over at least the last ~2900 and ~3400 years respectively. Further, the absence of high tsunami inundation on both Nagai Island and Simeonof Island throughout the late Holocene suggests that teletsunamis generated from both great earthquakes elsewhere along the Alaska-Aleutian subduction zone and other subduction zones have not resulted in the propagation of high tsunamis into the Shumagin section of the Alaska-Aleutian subduction zone. Thus, it does not appear that a large tsunami generated within the Shumagin section have propelled to far field communities along the Pacific West coast of the USA and Canada or to Hawaii over at least the last ~2900 years.

Davies' *et al.* (1981) interpretation and inferences of the Unga Island Russian outpost documents for a great earthquake and high tsunami in 1788 in the Shumagin section is not supported by the geological evidence from Nagai Island and Simeonof Island, suggesting that the Russian outpost documents were misinterpreted by Davies *et al.* (1981). The geological evidence from Nagai Island and Simeonof Island is more aligned with a localised large earthquake and low-level tsunami in 1788 as opposed to a Shumagin section wide or multi section great earthquake and high tsunami as interpreted by Davies *et al.* (1981).

The absence of identifiable coseismic land level change on both Nagai and Simeonof Islands over at least the last ~2900 and ~3400 years respectively implies a low hazard for great earthquakes generated in the Shumagin section of the Alaska-Aleutian subduction zone as well as a low hazard for the propagation of great earthquakes into the Shumagin section from the adjacent Semidi and Unimak sections of the Alaska-Aleutian subduction zone (Witter *et al.,* 2014). Further, the absence of sand beds conclusively linked to high tsunamis on both Nagai and Simeonof Islands over at least the last ~2900 and ~3400 years respectively suggests that there is a low hazard for a high tsunami generating or propagating into the Shumagin section of the Alaska-Aleutian subduction zone as well as a low hazard for a large tsunami generated in the Shumagin section propagating towards Hawaii and the Pacific West coast of the USA and Canada (Ryan *et al.,* 2012; Witter *et al.,* 2014).

However, great earthquakes and high tsunamis generating or propagating into the Shumagin section cannot be ruled out in the future due to the potential for missing evidence for coseismic land level change and tsunami inundation in the geological records on Nagai and Simeonof Islands, the geological records do not encapsulate the entire history of the Shumagin section so the recurrence intervals of great earthquakes and high tsunamis in the Shumagin section could be longer than the geological record, and the dynamics of the plate interface can vary through time as evident at Sedanka Island where it is currently creeping but the geological evidence exhibits a history of plate interface locking (Kelsey *et al.,* 2015; Shennan *et al.,* 2016; Witter *et al.,*2016; Witter *et al.,* 2019). The lack of modern tsunami deposits in the Shumagin section to compare potential palaeotsunami deposits to, and the absence of palaeoseismic reconstructions in the western Semidi section and Unimak section which limits the understanding of teletsunamis, further demonstrates the inability to rule out high tsunamis generating or propagating into the Shumagin section of the Alaska-Aleutian subduction zone (Kelsey *et al.,* 2015; Nelson *et al.,* 2015; Witter *et al.,* 2016; Witter *et al.,* 2019). Therefore, despite the apparent low hazard for great earthquakes and high tsunamis generating or propagating into the Shumagin section, great earthquakes and high tsunamis cannot be completely ruled out of the Shumagin section seismic hazard assessments nor in tsunami hazard assessments in communities vulnerable to Shumagin sourced tsunamis in Hawaii and along the Pacific west coasts of the USA and Canada.

The greatest recommendations for future research include palaeoseismic reconstructions in the western Semidi section, the eastern Unimak section and the western Shumagin section of the

Alaska-Aleutian subduction zone. Palaeoseismic reconstructions in the western Semidi section is critical to identify the number of times the Shumagin section has resisted the propagation of great earthquakes from the Semidi section, and palaeoseismic reconstructions of the eastern Unimak section and the western Shumagin section is important to identify the spatial extent of the long term persistent creep identified in the eastern Shumagin section and would determine if the west of the Shumagin section is susceptible to the propagation of great earthquakes from the adjacent Unimak section. Further, palaeoseismic reconstructions of the western Semidi, the Unimak and the western Shumagin sections are important to better understand the hazard of teletsunamis in the Shumagin section from tsunamis generated in the adjacent Semidi and Unimak sections of the Alaska-Aleutian subduction zone as well as the hazard of teletsunamis to far field locations in Hawaii and along the Pacific west coast of the USA and Canada.

Appendix

Figure S1. Code used in OxCal 4.4 to produce the Bayesian age-depth models for DV.19.03 and 19.DV.17.

DV.19.03

```
 P_Sequence(1)
 {
  Boundary("Base of Core")
  {
   z=166;
  };
  R_Date("H",2520,30)
  {
   z=144;
  };
  R_Date("G",2440,20)
  {
   z=138;
  };
   Date("BB")
   {
    z=137;
};
  R_Date("F",2430,20)
  {
   z=135;
  };
  R_Date("E",2440,25)
  {
   z=132;
  };
   Date("AB")
   {
    z=131;
 };
  R_Date("D",2370,25)
  {
   z=128;
  };
  R_Date("C",2130,20)
  {
   z=119;
  };
  R_Date("B",1870,25)
  {
   z=106;
  };
```

```
  R_Date("A",200,15)
  {
   z=33.5;
  };
  C_Date("Cs 137 Peak", 1963)
  {
   z=3;
  };
  C_Date("Surface of Core", 2019)
  {
   z=0;
};
  Boundary();
 };
```

19.DV.17

```
P_Sequence(1)
 {
  Boundary("Base of Core")
  {
   z=90;
};
Date("FB")
  {
   z=64;
  };
Date("FU")
  {
   z=57;
   };
  R_Date("B",640,25)
  {
   z=50.5;
};
Date("EB")
  {
   z=44;
};
Date("EU")
  {
   z=31;
  };
  R_Date("A",520,25)
  {
   z=30;
};
Date("DB")
```

```
  {
   z=19;
};
Date("DU")
  {
   z=7;
    };
  C_Date("Surface", 2019)
  {
   z=0;
};
  Boundary("Surface of Core");
 };
```

Table S1. Summary of the Gradistat output for DV.19.03 using the Folk and ward geometric method for grain size analysis. The sand bed samples are highlighted in yellow.

Depth (cm)	d10 (µm)	Mean grain size (µm)	Mean Desc.	Sorting (µm)	Sorting Desc.	Skewness (µm)	Skewness Desc.	Kurtosis (µm)	Kurtosis Desc.	% Gravel	% Sand	%Mud
10	4.98	41.45	Very Coarse Silt	5.65	Very Poorly Sorted	0.09	Symmetrical	1.08	Mesokurtic	0.0%	37.6%	62.4%
30	3.68	29.56	Coarse Silt	5.40	Very Poorly Sorted	0.04	Symmetrical	1.25	Leptokurtic	0.0%	28.4%	71.6%
50	6.54	87.09	Very Fine Sand	7.22	Very Poorly Sorted	-0.01	Symmetrical	0.82	Platykurtic	0.0%	53.8%	46.2%
70	3.41	25.92	Coarse Silt	5.03	Very Poorly Sorted	0.00	Symmetrical	1.12	Leptokurtic	0.0%	28.1%	71.9%
80	5.33	51.47	Very Coarse Silt	5.00	Very Poorly Sorted	-0.30	Very Fine Skewed	1.16	Leptokurtic	0.0%	55.4%	44.6%
90	6.34	56.43	Very Coarse Silt	4.53	Very Poorly Sorted	-0.32	Very Fine Skewed	1.04	Mesokurtic	0.0%	55.3%	44.7%
92	7.11	53.97	Very Coarse Silt	4.06	Very Poorly Sorted	-0.31	Very Fine Skewed	1.11	Mesokurtic	0.0%	54.1%	45.9%
95	3.92	29.98	Coarse Silt	5.12	Very Poorly Sorted	0.01	Symmetrical	1.08	Mesokurtic	0.0%	31.4%	68.6%
98	3.54	28.16	Coarse Silt	5.01	Very Poorly Sorted	-0.04	Symmetrical	1.07	Mesokurtic	0.0%	30.4%	69.6%
100	4.37	29.90	Coarse Silt	4.60	Very Poorly Sorted	-0.01	Symmetrical	1.09	Mesokurtic	0.0%	30.3%	69.7%
105	3.95	28.92	Coarse Silt	4.60	Very Poorly Sorted	-0.05	Symmetrical	1.03	Mesokurtic	0.0%	30.7%	69.3%

110	4.93	26.66	Coarse Silt	3.86	Poorly Sorted	0.04	Symmetrical	1.03	Mesokurtic	0.0%	26.8%	73.2%
112	18.34	90.20	Very Fine Sand	2.82	Poorly Sorted	-0.42	Very Fine Skewed	1.18	Leptokurtic	0.0%	70.0%	30.0%
115	3.38	30.10	Coarse Silt	4.15	Very Poorly Sorted	-0.31	Very Fine Skewed	1.13	Leptokurtic	0.0%	33.6%	66.4%
118	3.22	28.77	Coarse Silt	4.01	Very Poorly Sorted	-0.32	Very Fine Skewed	1.14	Leptokurtic	0.0%	31.0%	69.0%
120	5.39	40.75	Very Coarse Silt	5.01	Very Poorly Sorted	0.03	Symmetrical	1.07	Mesokurtic	0.0%	39.3%	60.7%
123	9.08	58.63	Very Coarse Silt	4.26	Very Poorly Sorted	-0.01	Symmetrical	1.05	Mesokurtic	0.0%	48.2%	51.8%
126	3.40	30.73	Coarse Silt	4.57	Very Poorly Sorted	-0.22	Fine Skewed	1.14	Leptokurtic	0.0%	33.3%	66.7%
127	5.45	40.59	Very Coarse Silt	5.14	Very Poorly Sorted	0.07	Symmetrical	1.05	Mesokurtic	0.0%	37.9%	62.1%
128	30.11	127.69	Fine Sand	2.35	Poorly Sorted	-0.55	Very Fine Skewed	1.73	Very Leptokurtic	0.0%	82.4%	17.6%
129	40.03	131.43	Fine Sand	2.16	Poorly Sorted	-0.45	Very Fine Skewed	1.77	Very Leptokurtic	0.0%	84.6%	15.4%
130	43.70	140.33	Fine Sand	2.08	Poorly Sorted	-0.45	Very Fine Skewed	1.78	Very Leptokurtic	0.0%	86.0%	14.0%
131	8.61	60.92	Very Coarse Silt	4.29	Very Poorly Sorted	-0.15	Fine Skewed	1.02	Mesokurtic	0.0%	52.6%	47.4%
132	7.71	51.77	Very Coarse Silt	4.59	Very Poorly Sorted	0.04	Symmetrical	1.09	Mesokurtic	0.0%	43.4%	56.6%

133	2.24	29.51	Coarse Silt	5.57	Very Poorly Sorted	-0.26	Fine Skewed	1.02	Mesokurtic	0.0%	37.1%	62.9%
134	10.34	86.28	Very Fine Sand	3.94	Poorly Sorted	-0.46	Very Fine Skewed	1.28	Leptokurtic	0.0%	69.0%	31.0%
135	52.14	146.57	Fine Sand	1.94	Moderately Sorted	-0.37	Very Fine Skewed	1.89	Very Leptokurtic	0.0%	88.1%	11.9%
136	40.22	135.40	Fine Sand	2.12	Poorly Sorted	-0.47	Very Fine Skewed	1.97	Very Leptokurtic	0.0%	85.5%	14.5%
137	3.49	47.76	Very Coarse Silt	5.16	Very Poorly Sorted	-0.45	Very Fine Skewed	1.00	Mesokurtic	0.0%	52.1%	47.9%
138	4.25	37.54	Very Coarse Silt	5.19	Very Poorly Sorted	-0.05	Symmetrical	0.97	Mesokurtic	0.0%	39.1%	60.9%
140	7.50	70.10	Very Fine Sand	5.57	Very Poorly Sorted	-0.02	Symmetrical	1.00	Mesokurtic	0.0%	51.8%	48.2%
142	5.70	53.01	Very Coarse Silt	4.78	Very Poorly Sorted	-0.24	Fine Skewed	0.99	Mesokurtic	0.0%	51.4%	48.6%
143	4.77	63.93	Very Fine Sand	5.23	Very Poorly Sorted	-0.50	Very Fine Skewed	1.12	Leptokurtic	0.0%	60.4%	39.6%
144	14.53	103.16	Very Fine Sand	3.31	Poorly Sorted	-0.53	Very Fine Skewed	1.43	Leptokurtic	0.0%	74.7%	25.3%
145	25.85	113.06	Very Fine Sand	2.61	Poorly Sorted	-0.43	Very Fine Skewed	1.49	Leptokurtic	0.0%	78.3%	21.7%
150	23.79	125.66	Fine Sand	2.69	Poorly Sorted	-0.50	Very Fine Skewed	2.02	Very Leptokurtic	0.0%	81.7%	18.3%

152	20.84	119.49	Very Fine Sand	2.84	Poorly Sorted	-0.50	Very Skewed	Fine	1.81	Very Leptokurtic	0.0%	79.9%	20.1%
154	25.32	123.56	Very Fine Sand	2.68	Poorly Sorted	-0.44	Very Skewed	Fine	1.58	Very Leptokurtic	0.0%	80.2%	19.8%
155	39.62	148.14	Fine Sand	2.35	Poorly Sorted	-0.37	Very Skewed	Fine	1.78	Very Leptokurtic	0.0%	85.7%	14.3%
160	53.13	157.71	Fine Sand	2.07	Poorly Sorted	-0.30	Fine Skewed		1.71	Very Leptokurtic	0.0%	88.3%	11.7%
164	45.14	149.09	Fine Sand	2.14	Poorly Sorted	-0.36	Very Skewed	Fine	1.76	Very Leptokurtic	0.0%	86.6%	13.4%

Table S2. Summary of the Gradistat output for DV.19.03 using the Folk and ward geometric method for grain size analysis. The sand bed samples are highlighted in yellow.

Depth (cm)	d10 (µm)	Mean Grain Size (µm)	Mean Desc.	Sorting (µm)	Sorting Desc.	Skewness (µm)	Skewness Desc.	Kurtosis (µm)	Kurtosis Desc.	% Gravel	% Sand	%Mud
0.50	11.52	114.64	Very Fine Sand	4.42	Very Poorly Sorted	-0.39	Very Fine Skewed	1.26	Leptokurtic	0.0%	72.5%	27.5%
6.00	13.25	134.08	Fine Sand	4.22	Very Poorly Sorted	-0.41	Very Fine Skewed	1.54	Very Leptokurtic	0.0%	77.5%	22.5%
7.00	17.24	131.23	Fine Sand	4.01	Very Poorly Sorted	-0.33	Very Fine Skewed	1.29	Leptokurtic	0.0%	75.1%	24.9%
8.00	56.46	198.31	Fine Sand	2.37	Poorly Sorted	-0.13	Fine Skewed	2.19	Very Leptokurtic	0.0%	89.4%	10.6%
13.00	104.75	191.21	Fine Sand	1.69	Moderately Sorted	-0.08	Symmetrical	1.79	Very Leptokurtic	0.0%	94.4%	5.6%
18.00	68.88	201.99	Fine Sand	2.11	Poorly Sorted	-0.22	Fine Skewed	2.15	Very Leptokurtic	0.0%	90.5%	9.5%
19.00	26.24	161.99	Fine Sand	3.33	Poorly Sorted	-0.28	Fine Skewed	1.88	Very Leptokurtic	0.0%	82.3%	17.7%
20.00	16.27	113.27	Very Fine Sand	4.05	Very Poorly Sorted	-0.23	Fine Skewed	1.04	Mesokurtic	0.0%	68.0%	32.0%
21.00	22.57	145.07	Fine Sand	3.43	Poorly Sorted	-0.35	Very Fine Skewed	1.39	Leptokurtic	0.0%	78.7%	21.3%
30.00	16.74	125.58	Fine Sand	4.28	Very Poorly Sorted	-0.21	Fine Skewed	0.98	Mesokurtic	0.0%	68.8%	31.2%
31.00	21.03	146.46	Fine Sand	3.77	Poorly Sorted	-0.36	Very Fine Skewed	1.19	Leptokurtic	0.0%	76.2%	23.8%
32.00	111.37	255.96	Medium Sand	2.05	Poorly Sorted	-0.11	Fine Skewed	1.47	Leptokurtic	0.0%	93.7%	6.3%
37.00	115.99	207.68	Fine Sand	1.71	Moderately Sorted	-0.04	Symmetrical	1.70	Very Leptokurtic	0.0%	94.8%	5.2%
43.00	13.43	101.67	Very Fine Sand	3.81	Poorly Sorted	-0.36	Very Fine Skewed	1.34	Leptokurtic	0.0%	71.5%	28.5%
44.00	10.68	92.58	Very Fine Sand	4.22	Very Poorly Sorted	-0.39	Very Fine Skewed	1.06	Mesokurtic	0.0%	66.4%	33.6%
45.00	7.85	70.36	Very Fine Sand	5.09	Very Poorly Sorted	-0.13	Fine Skewed	1.06	Mesokurtic	0.0%	55.7%	44.3%
49.00	22.19	165.51	Fine Sand	3.60	Poorly Sorted	-0.29	Fine Skewed	1.88	Very Leptokurtic	0.0%	82.3%	17.7%
56.00	50.78	181.81	Fine Sand	2.34	Poorly Sorted	-0.24	Fine Skewed	2.14	Very Leptokurtic	0.0%	88.4%	11.6%
57.00	41.55	179.81	Fine Sand	2.65	Poorly Sorted	-0.21	Fine Skewed	2.23	Very Leptokurtic	0.0%	86.9%	13.1%
58.00	93.76	193.85	Fine Sand	1.82	Moderately Sorted	-0.14	Fine Skewed	1.98	Very Leptokurtic	0.0%	92.9%	7.1%
62.00	43.60	177.40	Fine Sand	2.51	Poorly Sorted	-0.24	Fine Skewed	2.09	Very Leptokurtic	0.0%	87.2%	12.8%
63.00	41.36	181.26	Fine Sand	2.74	Poorly Sorted	-0.18	Fine Skewed	2.20	Very Leptokurtic	0.0%	86.8%	13.2%
64.00	33.92	169.37	Fine Sand	2.82	Poorly Sorted	-0.29	Fine Skewed	2.11	Very Leptokurtic	0.0%	85.3%	14.7%
65.00	37.85	176.55	Fine Sand	2.78	Poorly Sorted	-0.23	Fine Skewed	2.09	Very Leptokurtic	0.0%	86.0%	14.0%
70.00	28.23	148.16	Fine Sand	2.88	Poorly Sorted	-0.38	Very Fine Skewed	1.70	Very Leptokurtic	0.0%	82.5%	17.5%

Bibliography

Aaby, B and Berglund, B.E., 1986. Characterisation of peat and lake sediments. In: Berglund, B.J., (ed), *Handbook of Holocene Palaeoecology and Palaeohydrology,* 231-246. John Wiley and Sons, Chichester.

Abers, G., Beavan, J., Horton, S., Jaumé, S. and Triep, E., 1995. Large accelerations and tectonic setting of the May 1993 Shumagin Islands earthquake sequence. *Bulletin of the Seismological Society of America*, 85(6), pp.1730-1738.

Alloway B.V., Larsen G., Lowe D.J., Shane P.A.R., Westgate J.A. (2007). "Tephrochronology", *Encyclopedia of Quaternary Science*, pp.2869–2869.

ASHSC, 2020. *The M7.8 July 21, 2020 Simeonof Island Earthquake*. [online] Fairbanks, Ak: Alaska Seismic Hazards Safety Commission, pp.1-2. Available at: <https://seismic.alaska.gov/download/ashsc_meetings_minutes/sig_eq_2020_Simeonof_July 21.pdf> [Accessed 3 September 2022].

Atwater, B., 1987. Evidence for Great Holocene Earthquakes Along the Outer Coast of Washington State. *Science*, 236(4804), pp.942-944.

Atwater, B., 1992. Geologic evidence for earthquakes during the past 2000 years along the Copalis River, southern coastal Washington. *Journal of Geophysical Research: Solid Earth*, 97(B2), pp.1901-1919.

Atwater, B.F., and Hemphill-Haley, E., 1996, Recurrence intervals for great earthquakes of the past 3,500 years at northeastern Willapa Bay, Washington: U.S. Geological Survey Professional Paper 1576, pp.1-108.

Bartsch-Winkler, S., Schmoll, H., 1993. Evidence for late Holocene relative sea-level fall from reconnaissance stratigraphical studies in an area of earthquake-subsided intertidal deposits, Isla Chiloe, southern Chile. In: Frostwick, L. E., Steel, R. J. (eds.) Tectonic controls and signatures in sedimentary successions. *International Association of Seismologists.* pp. 91- 108.

Bartsch-Winkler, S., Schmoll, H.R., 1987. Earthquake-caused sedimentary couplets in the upper Cook Inlet region. U.S. Geological Survey, Circular 998, pp. 92-95.

Baskaran, M. and Naidu, A., 1995. 210Pb-derived chronology and the fluxes of 210Pb and 137Cs isotopes into continental shelf sediments, East Chukchi Sea, Alaskan Arctic. *Geochimica et Cosmochimica Acta*, 59(21), pp.4435-4448.

Beavan, J., 2013. *Scaling relations of seismic moment, rupture area, average slip, and asperity size for M ~9 subduction-zone earthquakes*. Reston, VA: US Geological Survey, pp.195-205.

Bécel, A., Shillington, D., Delescluse, M., Nedimović, M., Abers, G., Saffer, D., Webb, S., Keranen, K., Roche, P., Li, J. and Kuehn, H., 2017. Tsunamigenic structures in a creeping section of the Alaska subduction zone. *Nature Geoscience*, 10(8), pp.609-613.

Birks, H. J. B., 1992. *Some reflections on the application of numerical methods in Quaternary palaeoecology.* University of Joensuu, Publication Karelian Institute, 102, pp.7-20.

Birks, H.J.B., 1995. Quantitative palaeoenvironmental reconstructions. In: Maddy, D., Brew, J.S. (Eds.), *Statistical Modelling of Quaternary Science Data*. Quaternary Research Association, Cambridge, pp. 161e254.

Blott, S. and Pye, K., 2001. GRADISTAT: a grain size distribution and statistics package for the analysis of unconsolidated sediments. *Earth Surface Processes and Landforms*, 26(11), pp.1237-1248.

Blott, S., 2020. *GRADISTAT VERSION 9.1: A Grain Size Distribution and Statistics Package for the Analysis of Unconsolidated Sediments by Sieving or Laser Granulometer*. Wokingham: Kenneth Pye Associates Ltd.

Boyd, T., Taber, J., Lerner-Lam, A. and Beavan, J., 1988. Seismic rupture and arc segmentation within the Shumagin Islands Seismic Gap, Alaska. *Geophysical Research Letters*, 15(3), pp.201-204.

Boyd, T., Taber, J., Lerner-Lam, A. and Beavan, J., 1988. Seismic rupture and arc segmentation within the Shumagin Islands Seismic Gap, Alaska. *Geophysical Research Letters*, 15(3), pp.201-204.

Briggs, R., Engelhart, S., Nelson, A., Dura, T., Kemp, A., Haeussler, P., Corbett, D., Angster, S. and Bradley, L., 2014. Uplift and subsidence reveal a nonpersistent megathrust rupture boundary (Sitkinak Island, Alaska). *Geophysical Research Letters*, 41(7), pp.2289-2296.

Brill, D., Jankaew, K., Neubauer, N. -P., Kelletat, D., Scheffers, A., Voett, A. and Brueckner, H., 2014. *Holocene coastal evolution of southwest Thailand - implications for the site-specific preservation of palaeotsunami deposits.* Z. *Geomorphology*, 58 (3), pp. 273 - 304.

Bronk Ramsey, C., 2008, Deposition models for chronological records. *Quaternary Science Reviews*, 27, pp. 42– 60.

Bronk Ramsey, C., 2009. Bayesian Analysis of Radiocarbon Dates. *Radiocarbon*, 51(1), pp.337-360.

Bronk Ramsey, C., 2021. *OxCal*. Oxford: University of Oxford.

Brown, J., Prejean, S., Beroza, G., Gomberg, J. and Haeussler, P., 2013. Deep low-frequency earthquakes in tectonic tremor along the Alaska-Aleutian subduction zone. *Journal of Geophysical Research: Solid Earth*, 118(3), pp.1079-1090.

Bufe, C., Nishenko, S. and Varnes, D., 1994. Seismicity trends and potential for large earthquakes in the Alaska-Aleutian region. *Pure and Applied Geophysics PAGEOPH*, 142(1), pp.83-99.

Bürgmann, R., Schmidt, D., Nadeau, R., d'Alessio, M., Fielding, E., Manaker, D., McEvilly, T. and Murray, M., 2000. Earthquake Potential Along the Northern Hayward Fault, California. *Science*, 289(5482), pp.1178-1182.

Butler, R., Burney, D. and Walsh, D., 2014. Palaeotsunami evidence on Kaua‘i and numerical modelling of a great Aleutian tsunami. *Geophysical Research Letters*, 41(19), pp.6795-6802.

Carver, G. and Plafker, G., 2008. Palaeoseismicity and Neotectonics of The Aleutian Subduction Zone—An Overview. *Geophysical Monograph*, 179, pp.43-62.

Chagué-Goff, C., Schneider, J., Goff, J., Dominey-Howes, D. and Strotz, L., 2011. Expanding the proxy toolkit to help identify past events — Lessons from the 2004 Indian Ocean Tsunami and the 2009 South Pacific Tsunami. *Earth-Science Reviews*, 107(1-2), pp.107-122.

Chant, L. and Cornett, R., 1991. Smearing of gravity core profiles in soft sediments. *Limnology and Oceanography*, 36(7), pp.1492-1498.

Charles, D., Knowles, C. and Davis, R., 2002. *Protocols for the analysis of algal samples collected as part of the U.S. Geological Survey National Water-Quality Assessment Program*. Philadelphia, PA: The Academy of Natural Sciences Philadelphia, pp.1-124.

Chileh, M., Awouac, J., Sieh, K., Natawidjaja, D. and Galetzia, J., 2008. Heterogeneous coupling of the Sumatran megathrust constrained by geodetic and palaeogeodetic measurements. *Geophysics Research*, 113(B05305), pp.1-31.

Cochran, U., Berryman, K., Zachariasen, J., Mildenhall, D., Hayward, B., Southall, K., Hollis, C., Barker, P., Wallace, L., Alloway, B. and Wilson, K., 2006. Palaeoecological insights into subduction zone earthquake occurrence, eastern North Island, New Zealand. *Geological Society of America Bulletin*, 118(9-10), pp.1051-1074.

Coe, A. and Church, K., 2003. Sequence Stratigraphy. In: A. Coe, ed., *The sedimentary record of sea level change*. Cambridge: Cambridge University Press, pp.57-98.

Coe, A., 2003. The sedimentary record of sea level change. *Geoscience Canada*, 31(2), pp.93-94.

Cohen, S. and Freymueller, J., 2004. Crustal deformation in the southcentral Alaska subduction zone. *Advanced Geophysics*, 47, pp.1-63.

Combellick, R.A., 1991. Palaeoseismicity of the Cook Inlet region, Alaska: Evidence from peat stratigraphy in Turnagain and Knik Arms. Alaska Division of Geological and Geophysical Surveys Professional Report, Fairbanks, 52 pp.

Corbett, R. and Walsh, J., 2015. ^{210}Lead and ^{137}Cesium establishing a chronology for the last century. In: I. Shennan, A. Long and B. Horton, ed., *Handbook of Sea Level Research*. Hoboken, New Jersey: John Wiley & Sons, Ltd., pp.361-373.

Cross, R. and Freymueller, J., 2008. Evidence for and implications of a Bering plate based on geodetic measurements from the Aleutians and western Alaska. *Journal of Geophysical Research*, 113(B7).

Crowell, B. and Melgar, D., 2020. Slipping the Shumagin Gap: A Kinematic Coseismic and Early Afterslip Model of the Mw 7.8 Simeonof Island, Alaska, Earthquake. *Geophysical Research Letters*, 47(19).

Davies, J., Sykes, L., House, L. and Jacob, K., 1981. Shumagin Seismic Gap, Alaska Peninsula: History of great earthquakes, tectonic setting, and evidence for high seismic potential. *Journal of Geophysical Research*, 86(B5), p.3821.

Davis, E., 1912. The Earthquakes at Yakutat Bay, Alaska, in September 1899. *Bulletin of the Seismological Society of America*, 2(4), pp.254-255.

Dawson, A., 2019. *Introducing sea level change*. London: Academic Press.

Dawson, A., Shi, S., Dawson, S., Takahashi, T. and Shuto, N., 1996. Coastal sedimentation associated with the June 2nd and 3rd, 1994 tsunami in Rajegwesi, Java. *Quaternary Science Reviews*, 15(8-9), pp.901-912.

Dawson, S., 2007. Diatom biostratigraphy of tsunami deposits: examples from the 1998 Papua New Guinea tsunami. *Sedimentary Geology,* 200, pp. 328–335.

Dawson, S., Smith, D., Ruffman, A. and Shi, S., 1996. The diatom biostratigraphy of tsunami sediments: Examples from recent and middle holocene events. *Physics and Chemistry of the Earth*, 21(1-2), pp.87-92.

Dawson, S., Smith, D.E., 2000. The sedimentology of mid-Holocene tsunami facies in northern Scotland. *Marine Geology*, 170, pp.69–79.

Dominey-Howes, D., Humphreys, G. and Hesse, P., 2006. Tsunami and palaeotsunami depositional signatures and their potential value in understanding the late-Holocene tsunami record. *The Holocene*, 16(8), pp.1095-1107.

Dominey-Howes, Dale T.M., Geoff S. Humphreys, and Hesse, P.P., 2006. Tsunami and palaeotsunami depositional signatures and their potential value in understanding the late Holocene tsunami record. *The Holocene*, 16 (8), pp. 1095-1107.

Drexler, J., Fuller, C. and Archfield, S., 2018. The approaching obsolescence of 137Cs dating of wetland soils in North America. *Quaternary Science Reviews*, 199, pp.83-96.

Dura, C., 2014. *Diatom Based reconstructions of megathrust earthquake deformation and tsunami inundation on central and south central Chile*. PhD. University of Pennsylvania.

Dura, T. and Hemphill-Haley, E., 2020. Diatoms in Tsunami Deposits. In: M. Engel, J. Pilarcyzyk, S. May, D. Brill and E. Garrett, ed., *Geological Records of Tsunamis and Other Extreme Waves*. Amsterdam: Elsevier, pp.291-333.

Dura, T., Cisternas, M., Horton, B., Ely, L., Nelson, A., Wesson, R. and Pilarczyk, J., 2015. Coastal evidence for Holocene subduction-zone earthquakes and tsunamis in central Chile. *Quaternary Science Reviews*, 113, pp.93-111.

Dura, T., Engelhart, S., Vacchi, M., Horton, B., Kopp, R., Peltier, W. and Bradley, S., 2016b. The Role of Holocene Relative Sea-Level Change in Preserving Records of Subduction Zone Earthquakes. *Current Climate Change Reports*, 2(3), pp.86-100.

Dura, T., Garner, A., Weiss, R., Kopp, R., Engelhart, S., Witter, R., Briggs, R., Mueller, C., Nelson, A. and Horton, B., 2021. Changing impacts of Alaska-Aleutian subduction zone tsunamis in California under future sea-level rise. *Nature Communications*, 12(1), pp.1-9.

Dura, T., Hemphill-Haley, E., Sawai, Y. and Horton, B., 2016a. The application of diatoms to reconstruct the history of subduction zone earthquakes and tsunamis. *Earth-Science Reviews*, 152, pp.181-197.

Dura, T., Horton, B., Cisternas, M., Ely, L., Hong, I., Nelson, A., Wesson, R., Pilarczyk, J., Parnell, A. and Nikitina, D., 2017. Subduction zone slip variability during the last millennium, south-central Chile. *Quaternary Science Reviews*, 175, pp.112-137.

Engel, M. and Brückner, H., 2011. *The identification of palaeo-tsunami deposits – a major challenge in coastal sedimentary research*. Cologne: Coastline Reports 17, pp.65-80.

Engelhart, S., Horton, B., Nelson, A., Hawkes, A., Witter, R., Wang, K., Wang, P. and Vane, C., 2013. Testing the use of microfossils to reconstruct great earthquakes at Cascadia. *Geology*, 41(10), pp.1067-1070.

Engelhart, S., Witter, R., Briggs, R., Dura, T., Koehler, R., Vane, C., Nelson, A., Gelfenbaum, G. and Haeussler, P., 2018. Historical and stratigraphic evidence for two ruptures of the Alaska-Aleutian megathrust in 1788. In: *EGU General Assembly 2018*.

Estabrook, C. and Boyd, T., 1992. The Shumagin Islands, Alaska, Earthquake of 31 May 1917. *Bulletin of the Seismological Society of America*, 82(2), pp.755-773.

Estabrook, C. H., and T. M. Boyd., 1992. The Shumagin Islands, Alaska, earthquake of 31 May 1917, Bull. *Seismological Society of America*., 82(2), pp.755–773.

Estabrook, C., Jacob, K. and Sykes, L., 1994. Body wave and surface wave analysis of large and great earthquakes along the Eastern Aleutian Arc, 1923-1993: Implications for future events. *Journal of Geophysical Research: Solid Earth*, 99(B6), pp.11643-11662.

Fedotov, S. A., 1965. Regularities of the distribution of strong earthquakes in Kamchatka, the Kurile Islands and northeastern Japan (in Russian), Tr. Inst. Fiz. Zemli Akad. Nauk SSSR, 36, 66-93.

Folk, R. and Ward, W., 1957. Brazos River bar [Texas]; a study in the significance of grain size parameters. *Journal of Sedimentary Research*, 27(1), pp.3-26.

Fournier, T. and Freymueller, J., 2007. Transition from locked to creeping subduction in the Shumagin region, Alaska. *Geophysical Research Letters*, 34(6).

Franzén L, Ljung T. 2009. A carbon fibre composite (CFC) Byelorussian peat corer. *Mires and Peat*, 5, pp. 1-9.

Frew, C., 2014. Coring Methods. In: A. Goudie, M. Anderson, T. Burt, J. Lewin, K. Richards, B. Whalley and P. Worsely, ed., *Geomorphological Techniques*. London: British Society for Geomorphology, pp.1-10.

Freymueller, J. and Beavan, J., 1999. Absence of strain accumulation in the Western Shumagin Segment of the Alaska Subduction Zone. *Geophysical Research Letters*, 26(21), pp.3233-3236.

Freymueller, J., Suleimani, E. and Nicolsky, D. (2021). Constraints on the Slip Distribution of the 1938 M W 8.3 Alaska Peninsula Earthquake From Tsunami Modeling. Geophysical Research Letters, 48(9).

Freymueller, J., Woodward, H., Cohen, S., Cross, R., Elliot, J., Larsen, C., Hreinsdóttir, S. and Zweck, C., 2008. Active Deformation Processes in Alaska, Based on 15 Years of GPS Measurements. In: J. Freymueller, P. Haeuussler, R. Wesson and G. Ekström, ed., *Active Tectonics and Seismic Potential of Alaska*. Washington D.C.: American Geophysical Union, pp.1-42.

Fujino, S., Naruse, H., Fujita, K., Suphawajruksakul, A., Jarupongsakul, T., 2006. Tsunami sedimentation: an example from Indian Ocean Tsunami in southwestern Thailand. Proceedings of International Symposium on Fluvial and Coastal Disasters (CD-ROM).

Gelfenbaum, G. & B.E. Jaffe., 2003. Erosion and sedimentation from the 17 July, 1998 Papua New Guinea Tsunami. *Pure and Applied Geophysics,* 160, pp. 1969–1999.

Gelfenbaum, G. and Jaffe, B., 2003. Erosion and Sedimentation from the 17 July, 1998 Papua New Guinea Tsunami. *Pure and Applied Geophysics*, 160(10-11), pp.1969-1999.

Geller, R., 2011. Shake-up time for Japanese seismology. *Nature*, 472(7344), pp.407-409.
Givens, L., McConnell, V., Pollock, A., Smith, R. and Madin, I., 2013. *Tsunami Inundation Map for Arch Cape - Falcon Cove, Tillamook County, Oregon*. Warner Valley, Lake County, Oregon: State of Oregon Department of Geology and Mineral Industries, p.1.

Goff, J., Chague´-Goff, C. and Nichol, S., 2001. Palaeotsunami deposits: a New Zealand perspective. *Sedimentary Geology,* 143, pp.1-6.

Goff, J., Lui, P., Higman, B., Morton, R., Jaffe, B., Fernando, H. and Fernando, S., 2006. Sri Lanka field survey after the December 2004 Indian Ocean tsunami. *Earthquake Spectra*, 22(S3), pp.155-172.

Goff, J., McFadgen, B. and Chagué-Goff, C., 2004. Sedimentary differences between the 2002 Easter storm and the 15th-century Okoropunga tsunami, southeastern North Island, New Zealand. *Marine Geology*, 204(1-2), pp.235-250.

Govers, R., Furlong, K., van de Wiel, L., Herman, M. and Broerse, T., 2018. The Geodetic Signature of the Earthquake Cycle at Subduction Zones: Model Constraints on the Deep Processes. *Reviews of Geophysics*, 56(1), pp.6-49.

Grand Pre, C., Horton, B., Kelsey, H., Rubin, C., Hawkes, A., Daryono, M., Rosenberg, G. and Culver, S., 2012. Stratigraphic evidence for an early Holocene earthquake in Aceh, Indonesia. *Quaternary Science Reviews*, 54, pp.142-151.

Grant, L., 2002. Palaeoseismology. In: W. Lee, H. Kanamori, P. Jennings and C. Kisslinger, ed., *International Handbook of Earthquake and Engineering Seismology, Part A*. Cambridge, Ma: Academic Press, pp.475-480.

Grimm, E., 1987. CONISS: a FORTRAN 77 program for stratigraphically constrained cluster analysis by the method of incremental sum of squares. *Computers & Geosciences*, 13(1), pp.13-35.

Hamilton, S. and Shennan, I., 2005a. Late Holocene relative sea-level changes and the earthquake deformation cycle around upper Cook Inlet, Alaska. *Quaternary Science Reviews*, 24(12-13), pp.1479-1498.

Hamilton, S. and Shennan, I., 2005b. Late Holocene great earthquakes and relative sea-level change at Kenai, southern Alaska. *Journal of Quaternary Science*, 20(2), pp.95-111.

Hamilton, S., Shennan, I., Combellick, R., Mulholland, J. and Noble, C., 2005. Evidence for two great earthquakes at Anchorage, Alaska and implications for multiple great earthquakes through the Holocene. *Quaternary Science Reviews*, 24(18-19), pp.2050-2068.

Hardy, E., 1968. *Fallout Program. Quarterly Summary Report.* New York: New York Operations Office (AEC), N. Y. Health and Safety Lab., p.255.

Hawkes, A., Horton, B., Nelson, A., Vane, C. and Sawai, Y., 2011. Coastal subsidence in Oregon, USA, during the giant Cascadia earthquake of AD 1700. *Quaternary Science Reviews*, 30(3-4), pp.364-376.

Hawkes, A., Scott, D., Lipps, J. and Combellick, R., 2005. Evidence for possible precursor events of megathrust earthquakes on the west coast of North America. *Geological Society of America Bulletin*, 117(7), p.996.

Heki, K., 2011. A Tale of Two Earthquakes. *Science*, 332(6036), pp.1390-1391.

Hemphill-Haley, E., 1993. *Taxonomy of recent and fossil (Holocene) diatoms (Bacillariophyta) from northern Willapa Bay, Washington*. Menio Park, CA: U.S. Department of The Interior and U.S. Geological Survey, pp.1-151.

Hemphill-Haley, E., 1995a. Intertidal diatoms from Willipa bay Washington application to studies of small scale sea level changes. *Northwest Science*, 69(1), pp.29-45.

Hemphill-Haley, E., 1995b. Diatom evidence for earthquake-induced subsidence and tsunami 300 yr ago in southern coastal Washington. *GSA Bulletin*, 107(3), pp.367-378.

Hemphill-Haley, E., 1996. Diatoms as an aid in identifying late-Holocene tsunami deposits. *The Holocene*, 6(4), pp.439-448.

Heyworth, A., Kidson, C. & P. Wilks., 1985. Late-Glacial and Holocene sediments at Clarach Bay, near Aberystwyth. *Ecology*. 73, pp. 459–480.

Horiba, 2010. "*A Guidebook To Particle Size Analysis*", PSA_Guidebook.pdf (ats-scientific.com). Accessed 5 September 2022.

Horton, B. and Sawai, Y., 2010. Diatoms as indicators of former sea levels, earthquakes, tsunamis, and hurricanes. In: J. Smol and E. Stoermer, ed., *The Diatoms: Applications for the Environmental and Earth Sciences*. Cambridge, UK: Cambridge University Press, pp.357-372.

Horton, B. P., Zong, Y., Hillier, C., & Engelhart, S., 2007. Diatoms from Indonesian mangroves and their suitability as sea-level indicators for tropical environments. *Marine Micropalaeontology,* 63(3), pp.155-168.

Horton, B.P., Edwards, B.P., 2006. Quantifying Holocene Sea-Level Change using Intertidal Foraminifera: Lessons from the British Isles. *Cushman Foundation for Foraminiferal Research*, Special Publication, 40, pp.1-97.

House, L., Sykes, L., Davies, J. and Jacob, K., 1981. Identification of a Possible Seismic Gap Near Unalaska Island, Eastern Aleutians, Alaska. *Earthquake Prediction: An International Review*, 4, pp.81-92.

Hutchinson, I. and Crowell, A., 2007. Recurrence and Extent of Great Earthquakes in Southern Alaska During the Late Holocene from an Analysis of the Radiocarbon Record of Land Level Change and Village Abandonment. *Radiocarbon*, 49(3), pp.1323-1385.

Jacob, K., 1984. Estimates of long term probabilities for future great earthquakes in the Aleutians. *Geophysical Research Letters*, 11(4), pp.295-298.

Janigian, G., 2018. *A stratigraphic and microfossil record of coseismic land level A stratigraphic and microfossil record of coseismic land level changes and tsunami deposits from Old Harbor, Central Kodiak changes and tsunami deposits from Old Harbor, Central Kodiak Island, Alaska*. Master of Science. University of Rhode Island.

Jankaew, K., Atwater, B., Sawai, Y., Choowong, M., Charoentitirat, T., Martin, M. and Prendergast, A., 2008. Medieval forewarning of the 2004 Indian Ocean tsunami in Thailand. *Nature*, 455(7217), pp.1228-1231.

Jiang, Y., González, P. and Bürgmann, R., 2022. Subduction earthquakes controlled by incoming plate geometry: The 2020 M > 7.5 Shumagin, Alaska, earthquake doublet. *Earth and Planetary Science Letters*, 584, p.117447.

Jiang, Y., González, P. and Bürgmann, R., 2022. Subduction earthquakes controlled by incoming plate geometry: The 2020 M > 7.5 Shumagin, Alaska, earthquake doublet. *Earth and Planetary Science Letters*, 584, p.117447.

Johnson, J., Tanioka, Y., Ruff, L., Satake, K., Kanamori, H. and Sykes, L., 1994. The 1957 great Aleutian earthquake. *Pure and Applied Geophysics PAGEOPH*, 142(1), pp.3-28.

Jones, V.J., 2007. Diatom Introduction, in: Elias, S., (Ed.) Encyclopaedia of Quaternary Science. Elsevier, Oxford, pp. 476 – 484.

Jordan, J., Lander, J. and Black, R., 1965. Aftershocks of the 4 February 1965 Rat Island Earthquake. *Science*, 148(3675), pp.1323-1325.

Judd, K., Chagué-Goff, C., Goff, J., Gadd, P., Zawadzki, A. and Fierro, D., 2017. Multi-proxy evidence for small historical tsunamis leaving little or no sedimentary record. *Marine Geology*, 385, pp.204-215.

Kagan, Y. and Jackson, D., 1991. Seismic Gap Hypothesis: Ten years after. *Journal of Geophysical Research: Solid Earth*, 96(B13), pp.21419-21431.

Karlstrom, T.N.V., 1964. *Quaternary geology of the Kenai lowland and the glacial history of Cook Inlet region, Alaska.* US Geological Survey Professional Paper 443, 1–69.

Kelsey, H., Engelhart, S., Pilarczyk, J., Horton, B., Rubin, C., Daryono, M., Ismail, N., Hawkes, A., Bernhardt, C. and Cahill, N., 2015. Accommodation space, relative sea level, and the archiving of palaeo-earthquakes along subduction zones. *Geology*, 43(8), pp.675-678.

Kemp, A., Nelson, A. and Horton, B., 2013. Radiocarbon dating of plant macrofossils from tidal-marsh sediments. In: J. Shroder, A. Switzer and A. Kennedy, ed., Treatise on Geomorphology. San Diego: Academic Press, vol 14, *Methods in Geomorphology*, pp.370-388.

Kemp, A., Nelson, A. and Horton, B., 2013. Radiocarbon dating of plant macrofossils from tidal-marsh sediments. In: J. Shroder, A. Switzer and A. Kennedy, ed., Treatise on Geomorphology. San Diego: Academic Press, vol 14*, Methods in Geomorphology*, pp.370-388.

Kirwan, M.L., Guntenspergen, G.R., D'Alpaos, A., Morris, J.T., Mudd, S.M., Temmerman, S., 2010. Limits on the adaptability of coastal marshes to rising sea level. *Geophysics Research Letters*, 37 (23), pp. 1-5.

Kirwan, M.L.., Megonigal, J.P., 2013. Tidal wetland stability in the face of human impacts and sea-level rise. *Nature*, 504(7478), pp,53–60.

Kortekaas, S. and Dawson, A., 2007. Distinguishing tsunami and storm deposits: An example from Martinhal, SW Portugal. *Sedimentary Geology*, 200(3-4), pp.208-221.

Kovach Computing Services (KCS), 2007. "*Multi-Variate Statistical Package Version 3.1 Users*' *Manual*", MVSP3ManA5 (kovcomp.co.uk). Accessed 5 September 2022.

Krammer, K. and H. Lange-Bertalot., 1988. Bacillariophyceae. 2. Teil: Bacillariaceae, Epithemiaceae, Surirellaceae. In: Ettl, H., Gerloff, J., Heynig, H. and Mollenhauer, D. (eds) *Süsswasserflora von Mitteleuropa*, Band 2/2. VEB Gustav Fischer Verlag: Jena. pp,596.

Krammer, K., Lange-Bertalot, H., 1991a. Bacillarophyceae 2/3. Centrales, Fragilariaceae, Eunotiaceae. In: Ettl, H., Gerloff, J., Heynig, H., Mollenhauser (Eds.), *Süsswasserflora von Mitteleuropa*. Gustav Fischer Verlag, Stuttgart, pp. 1–600.

Krammer, K., Lange-Bertalot, H., 1991b. Bacillarophyceae 2/4. Achnanthaceae, Kritische Erganzungen zu Navicula (Lineolatae) und Gomphonema. In: Ettl, H. (Ed.), *Pascher's Süsswasserflora von Mitteleuropa*, 2(4). Gustav Fischer Verlag, Stuttgart, pp. 1–437.

Lander, J., 1996. *Tsunamis Affecting Alaska 1737-1996*. NGDC Key to Geophysical Research Documentation No. 31. Boulder, Colorado: U.S. Department of Commerce, pp.1-195.

Libby, W., 1958. Radioactive fallout. *Proceedings of the National Academy of Sciences of the United States of America*, 44(8), pp.800-820.

Long, A., Innes, J., Shennan, I. and Tooley, M., 1999. Coastal stratigraphy: A case study from Johns River, Washington, U.S.A. In: A. Jones, M. Tucker and J. Hart, ed., *The description & analysis of quaternary stratigraphic field sections*. London: Quaternary Research Association, pp.267-286.

Long, A., Innes, J., Shennan, I. and Tooley, M., 1999. Coastal stratigraphy: A case study from Johns River, Washington, U.S.A. In: A. Jones, M. Tucker and J. Hart, ed., *The description & analysis of quaternary stratigraphic field sections.* London: Quaternary Research Association, pp.267-286.

Long, A.J., Shennan, I., 1994. Sea-level changes in Washington and Oregon and the ‘‘Earthquake deformation cycle’’. *Journal of Coastal Research* 10, pp. 825–838.

López, A. and Okal, E., 2006. A seismological reassessment of the source of the 1946 Aleutian ‘tsunami’ earthquake. *Geophysical Journal International*, 165(3), pp.835-849.

Loveless, J. and Meade, B., 2010. Geodetic imaging of plate motions, slip rates, and partitioning of deformation in Japan. *Journal of Geophysical Research*, 115(B2).
Ma, K., Brodsky, E., Mori, J., Ji, C., Song, T. and Kanamori, H., 2003. Evidence for fault lubrication during the 1999 Chi-Chi, Taiwan, earthquake (Mw7.6). *Geophysical Research Letters*, 30(5).

Liu, C., Lay, T. and Xiong, X. (2022) “The 29 July 2021 M_w 8.2 Chignik, Alaska Peninsula earthquake rupture inferred from seismic and geodetic observations: Re-rupture of the western 2/3 of the 1938 rupture zone,” Geophysical Research Letters, 49(4).

Ma, K., Song, T., Lee, S. and Wu, H., 2000. Spatial slip distribution of the September 20, 1999, Chi-Chi, Taiwan, Earthquake (MW7.6) -Inverted from teleseismic data. *Geophysical Research Letters*, 27(20), pp.3417-3420.

Mackey, K., Fujita, K., Gunbina, L., Kovalev, V., Imaev, V., Koz'min, B. and Imaeva, L., 1997. Seismicity of the Bering Strait region: Evidence for a Bering block. *Geology*, 25(11), p.979.

Malvern, 2015. “*A basic guide to particle characterization*”, Particle Characterization Guide.pdf (iastate.edu). Accessed 5 September 2022.

Mamo, B., Strotz, L. and Dominey-Howes, D., 2009. Tsunami sediments and their foraminiferal assemblages. *Earth-Science Reviews*, 96(4), pp.263-278.

Marshall, W., Gehrels, W., Garnett, M., Freeman, S., Maden, C. and Xu, S., 2007. The use of ‘bomb spike’ calibration and high-precision AMS 14C analyses to date salt-marsh sediments deposited during the past three centuries. *Quaternary Research*, 68(3), pp.325-337.

Matsumoto, D., Naruse, H., Fujino, S., Surphawajruksakul, A., Jarupongsakul, T., Sakakura, N. and Murayama, M., 2008. Truncated flame structures within a deposit of the Indian Ocean Tsunami: evidence of syn-sedimentary deformation. *Sedimentology*, 55(6), pp.1559-1570.

McCalpin, J. (2009) *Palaeoseismology*. Burlington (Mass.): Academic Press.

McCann, W., Nishenko, S., Sykes, L. and Krause, J., 1979. Seismic gaps and plate tectonics: Seismic potential for major boundaries. *Pure and Applied Geophysics PAGEOPH*, 117(6), pp.1082-1147.

Minoura, K. and Nakaya, S., 1991. Traces of Tsunami Preserved in Inter-Tidal Lacustrine and Marsh Deposits: Some Examples from Northeast Japan. *The Journal of Geology*, 99(2), pp.265-287.

Mogi, K.,1968. Development of Aftershock Areas of Great Earthquakes. *Bulletin of the Earthquake Research Institute*, University of Tokyo, 46, 175-203.

Murotani, S., Satake, K. and Fujii, Y., 2013. Scaling relations of seismic moment, rupture area, average slip, and asperity size for M ~9 subduction-zone earthquakes. *Geophysical Research Letters*, 40(19), pp.5070-5074.

Nelson, A., 1992. Discordant 14C Ages from Buried Tidal-Marsh Soils in the Cascadia Subduction Zone, Southern Oregon Coast. *Quaternary Research*, 38(1), pp.74-90.

Nelson, A., 1992. Discordant 14C Ages from Buried Tidal-Marsh Soils in the Cascadia Subduction Zone, Southern Oregon Coast. *Quaternary Research*, 38(1), pp.74-90.

Nelson, A., Briggs, R., Dura, T., Engelhart, S., Gelfenbaum, G., Bradley, L., Forman, S., Vane, C. and Kelley, K., 2015. Tsunami recurrence in the eastern Alaska-Aleutian arc: A Holocene stratigraphic record from Chirikof Island, Alaska. *Geosphere*, 11(4), pp.1172-1203.

Nelson, A., Jennings, A. and Kashima, K., 1996. An earthquake history derived from stratigraphic and microfossil evidence of relative sea-level change at Coos Bay, southern coastal Oregon. *Geological Society of America Bulletin*, 108(2), pp.141-154.

Nelson, A., Sawai, Y., Jennings, A., Bradley, L., Gerson, L., Sherrod, B., Sabean, J. and Horton, B., 2008. Great-earthquake palaeogeodesy and tsunamis of the past 2000 years at Alsea Bay, central Oregon coast, USA. *Quaternary Science Reviews*, 27(7-8), pp.747-768.

Nelson, A., Shennan, I. and Long, A., 1996a. Identifying coseismic subsidence in tidal-wetland stratigraphic sequences at the Cascadia subduction zone of western North America. *Journal of Geophysical Research: Solid Earth*, 101(B3), pp.6115-6135.

Nicolsky, D., Freymueller, J., Witter, R., Suleimani, E. and Koehler, R., 2016. Evidence for shallow megathrust slip across the Unalaska seismic gap during the great 1957 Andreanof Islands earthquake, eastern Aleutian Islands, Alaska. *Geophysical Research Letters*, 43(19).

Nilsson, M., Klarqvist, M., Bohlin, E., Possnert, G.R., 2001. Variation in 14C age of macrofossils and different fractions of minute peat samples dated by AMS. *Holocene,* 11, pp.579–586.

Nishenko, S. and Jacob, K., 1990. Seismic potential of the Queen Charlotte-Alaska-Aleutian Seismic Zone. *Journal of Geophysical Research*, 95(B3), p.2511.

Nishimura, Y. and Miyaji, N., 1995. Tsunami deposits from the 1993 Southwest Hokkaido earthquake and the 1640 Hokkaido Komagatake eruption, northern Japan. *Pure and Applied Geophysics PAGEOPH*, 144(3-4), pp.719-733.

Noda, H. and Lapusta, N., 2010. Three-dimensional earthquake sequence simulations with evolving temperature and pore pressure due to shear heating: Effect of heterogeneous hydraulic diffusivity. *Journal of Geophysical Research*, 115(B12).

Noda, H. and Lapusta, N., 2013. Stable creeping fault segments can become destructive as a result of dynamic weakening. *Nature*, 493(7433), pp.518-521.
Orzech, K., Dahl, W. and Edwards, B., 2001. *Core Descriptions, Core Photographs, Physical Property Logs and Surface Textural Data of Sediment Cores Recovered from the Continental Shelf of the Monterey Bay National Marine Sanctuary During the Research Cruises M-1-95-MB, P-2-95-MB and P-1-97-MB.* Reston, VA: U.S. Geological Survey, pp.1-21.

Padgett, J.S and Engelhart, S.E and Kelsey, H.M and Witter, R.C and Cahill, N and Hemphill-Haley, E., 2021.'Timing and amount of southern Cascadia earthquake subsidence over the past 1700 years at northern Humboldt Bay, California, USA.', *Geological Society of America Bulletin*, 133 (9-10). pp. 2137-2156.

Palmer, A. and Abbott, W., 1986. Diatoms as indicators of sea-level change. In: O. van de Plassche, ed., *Sea level research: a manual for the collection and evaluation of data.* Norwich, UK: Geo Books, pp.457-489.

Parnell, A. and Gehrels, R., 2015. Using chronological models in late Holocene sea-level reconstructions from saltmarsh sediments. In: I. Shennan, A. Long and B. Horton, ed., *Handbook of Sea-Level Research.* Chichester, UK: John Wiley and Sons, Ltd, pp.500-514.

Patrick, R. M., and Reimer, C. W., 1966. *The diatoms of the United States exclusive of Alaska and Hawaii*, Volume 1: Monographs of the Academy of Natural Sciences of Philadelphia, 688.

Patrick, R. M., and Reimer, C. W., 1966. *The diatoms of the United States exclusive of Alaska and Hawaii*, Volume 1: Monographs of the Academy of Natural Sciences of Philadelphia, 688.

Patrick, R. M., and Reimer, C. W., 1975, The diatoms of the United States exclusive of Alaska and Hawaii, Volume 2: Monographs of the Academy of Natural Sciences of Philadelphia, 213.

Patterson RT, Hutchinson I, Guilbault JP, *et al*. 2000. A comparison of the vertical zonation of diatom, foraminifera, and macrophyte assemblages in a coastal marsh: implications for greater palaeo-sea level resolution. *Micropalaeontology* **46**, pp. 229– 244.

Pennington, W., Tutin, T., Cambray, R. and Fisher, E., 1973. Observations on Lake Sediments using Fallout 137Cs as a Tracer. *Nature*, 242(5396), pp.324-326.

Perfettini, H., Avouac, J., Tavera, H., Kositsky, A., Nocquet, J., Bondoux, F., Chlieh, M., Sladen, A., Audin, L., Farber, D. and Soler, P., 2010. Seismic and aseismic slip on the Central Peru megathrust. *Nature*, 465(7294), pp.78-81.

Pilarczyk, J., Dura, T., Horton, B., Engelhart, S., Kemp, A. and Sawai, Y., 2014. Microfossils from coastal environments as indicators of palaeo-earthquakes, tsunamis and storms. *Palaeogeography, Palaeoclimatology, Palaeoecology*, 413, pp.144-157.
Prater, A., 2021. *Stratigraphic and Microfossil Evidence of Repeated Late Holocene Tsunami Inundation at Sitkalidak Island, Alaska*. Master of Science. Virginia Polytechnic Institute.

Reddy, C., Arora, S., Sunil, P. and Prajapati, S., 2011. Earthquake Related Deformation Cycle: Perspectives from 2004 Sumatra and 2010 Chile Mega-Earthquakes. *Disaster Advances*, 4(2), pp.13-21.

Reimer, P., Austin, W., Bard, E., Bayliss, A., Blackwell, P., Bronk Ramsey, C., Butzin, M., Cheng, H., Edwards, R., Friedrich, M., Grootes, P., Guilderson, T., Hajdas, I., Heaton, T., Hogg, A., Hughen, K., Kromer, B., Manning, S., Muscheler, R., Palmer, J., Pearson, C., van der Plicht, J., Reimer, R., Richards, D., Scott, E., Southon, J., Turney, C., Wacker, L., Adolphi, F., Büntgen, U., Capano, M., Fahrni, S., Fogtmann-Schulz, A., Friedrich, R., Köhler, P., Kudsk, S., Miyake, F., Olsen, J., Reinig, F., Sakamoto, M., Sookdeo, A. and Talamo, S., 2020. The IntCal20 Northern Hemisphere Radiocarbon Age Calibration Curve (0–55 cal kBP). *Radiocarbon*, 62(4), pp.725-757.

Reimer, P., Bard, E., Bayliss, A., Beck, J., Blackwell, P., Ramsey, C., Buck, C., Cheng, H., Edwards, R., Friedrich, M., Grootes, P., Guilderson, T., Haflidason, H., Hajdas, I., Hatté, C., Heaton, T., Hoffmann, D., Hogg, A., Hughen, K., Kaiser, K., Kromer, B., Manning, S., Niu, M., Reimer, R., Richards, D., Scott, E., Southon, J., Staff, R., Turney, C. and van der Plicht, J., 2013. IntCal13 and Marine13 Radiocarbon Age Calibration Curves 0–50,000 Years cal BP. *Radiocarbon,* 55(4), pp.1869-1887.

Reyners, M. and Coles, K., 1982. Fine structure of the dipping seismic zone and subduction mechanics in the Shumagin Islands, Alaska. *Journal of Geophysical Research: Solid Earth*, 87(B1), pp.356-366.

Rhodes, B., Tuttle, M., Horton, B., Doner, L., Kelsey, H., Nelson, A. and Cisternas, M., 2006. Palaeotsunami research. *Eos, Transactions American Geophysical Union*, 87(21), p.205.
Rice, J., 2006. Heating and weakening of faults during earthquake slip. *Journal of Geophysical Research: Solid Earth*, 111(B5).

Roe, C., Davidson, C., Garver, J., DeLuca, M. and Short, A., 2013. *Provenance and thermal history of the Upper Cretaceous Shumagin Formation, Nagai Island, southern Alaska*. p.51.

Ross, S., Jones, L., Miller, K., Porter, K., Wein, A., Wilson, R., Bahng, B., Barberopoulou, A., Borrero, J., Brosnan, D., Bwarie, J., Geist, E., Johnson, L., Kirby, W., Long, K., Lynett, P., Mortensen, C., Nicolsky, D., Perry, S., Plumlee, G., Real, C., Ryan, K., Suleimani, E., Thio, H., Titov, V., Whitmore, P. and Wood, N., 2013. *The SAFRR (Science Application for Risk Reduction) Tsunami Scenario—Executive Summary and Introduction*. Open-File Report 2013–1170–A California Geological Survey Special Report 229. Virginia: U.S. Geological Survey, pp.1-17.

Round, F.E., Crawford, R.M., and Mann, D.G. (2007) *The Diatoms: Biology and Morphology of the Genera*. Cambridge University Press, Cambridge, UK.

Ryan, H., von Heune, R., Wells, R., Scholl, D., Kirby, S. and Draut, A., 2012. *History of Earthquakes and Tsunamis Along the Eastern Aleutian-Alaska Megathrust, with Implications for Tsunami Hazards in the California Continental Borderland*. Studies by the U.S. Geological Survey in Alaska, Virginia, U.S. Geological Survey, pp.1-31.

Satake, K. and Atwater, B., 2007. Long term Perspectives on Giant Earthquakes and Tsunamis at Subduction Zones. *Annual Review of Earth and Planetary Sciences*, 35(1), pp.349-374.

Savage, J. and Lisowski, M., 1986. Strain accumulation in the Shumagin Seismic Gap, Alaska. *Journal of Geophysical Research: Solid Earth*, 91(B7), pp.7447-7454.

Savage, J., Lisowski, M. and Prescott, W., 1986. Strain Accumulation in the Shumagin and Yakataga Seismic Gaps, Alaska. *Science*, 231(4738), pp.585-587.

Sawai, Y., 2002. Evidence for 17th century tsunamis generated on the Kuril–Kamchatka subduction zone, Lake Tokotan, Hokkaido, Japan. Journal of Asian Earth Science 20, 903–911.

Sawai, Y., Fujii, Y., Fujiwara, O., Kamataki, T., Komatsubara, J., Okamura, Y., Satake, K. and Shishikura, M., 2008. Marine incursions of the past 1500 years and evidence of tsunamis at Suijin-numa, a coastal lake facing the Japan Trench. *The Holocene*, 18(4), pp.517-528.

Sawai, Y., Jankaew, K., Martin, M., Prendergast, A., Choowong, M. and Charoentitirat, T., 2009. Diatom assemblages in tsunami deposits associated with the 2004 Indian Ocean tsunami at Phra Thong Island, Thailand. *Marine Micropalaeontology*, 73(1-2), pp.70-79.

Sawai, Y., Namegaya, Y., Okamura, Y., Satake, K. and Shishikura, M., 2012. Challenges of anticipating the 2011 Tohoku earthquake and tsunami using coastal geology. *Geophysical Research Letters*, 39(21), pp. 1-6.

Sawai, Y., Satake, K., Kamataki, T., Nasu, H., Shishikura, M., Atwater, B., Horton, B., Kelsey, H., Nagumo, T. and Yamaguchi, M., 2004. Transient Uplift After a 17th-Century Earthquake Along the Kuril Subduction Zone. *Science*, 306(5703), pp.1918-1920.

Scott, E., 2003. The fourth international radiocarbon inter-comparison. *Radiocarbon,* 45, pp.135-408.

Shennan, I. and Barlow, N., 2008. Palaeoseismological Records of Multiple Great Earthquakes in Southcentral Alaska: A 4000-Year Record at Girdwood. *Geophysical Monograph Series*, 179, pp.185-200.

Shennan, I. and Hamilton, S., 2006. Coseismic and pre-seismic subsidence associated with great earthquakes in Alaska. *Quaternary Science Reviews*, 25(1-2), pp.1-8.

Shennan, I., Barlow, N., Carver, G., Davies, F., Garrett, E. and Hocking, E., 2014c. Great tsunamigenic earthquakes during the past 1000 yr on the Alaska megathrust. *Geology*, 42(8), pp.687-690.

Shennan, I., Barlow, N., Combellick, R., Pierre, K. And Stuart-Taylor, O., 2014b. Late Holocene Palaeoseismology of A Site In The Region of Maximum Subsidence During The 1964 Mw 9.2 Alaska Earthquake. *Journal Of Quaternary Science*, 29(4), Pp.343-350.

Shennan, I., Brader, M., Barlow, N., Davies, F., Longley, C. and Tunstall, N., 2018. Late Holocene palaeoseismology of Shuyak Island, Alaska. *Quaternary Science Reviews*, 201, pp.380-395.

Shennan, I., Bruhn, R., Barlow, N., Good, K. and Hocking, E., 2014a. Late Holocene great earthquakes in the eastern part of the Aleutian megathrust. *Quaternary Science Reviews*, 84, pp.86-97.

Shennan, I., Garrett, E. and Barlow, N., 2016. Detection limits of tidal-wetland sequences to identify variable rupture modes of megathrust earthquakes. *Quaternary Science Reviews*, 150, pp.1-30.

Shennan, I., Long, A., Rutherford, M., Green, F., Innes, J., Lloyd, J., Zong, Y. and Walker, K., 1996. Tidal marsh stratigraphy, sea-level change and large earthquakes, i: a 5000 year record in Washington, U.S.A. *Quaternary Science Reviews*, 15(10), pp.1023-1059.

Shennan, I., Long, A., Rutherford, M., Innes, J., Green, F. And Walker, K., 1998. Tidal Marsh Stratigraphy, Sea-Level Change And Large Earthquakes—Ii: Submergence Events During The Last 3500 Years At Netarts Bay, Oregon, USA. *Quaternary Science Reviews*, 17(4-5), Pp.365-393.

Shennan, I., Scott, D., Rutherford, M. and Zong, Y., 1999. Microfossil analysis of sediments representing the 1964 earthquake, exposed at Girdwood Flats, Alaska, USA. *Quaternary International*, 60(1), pp.55-73.

Shimazaki, K. and Nakata, T., 1980. Time-predictable recurrence model for large earthquakes. *Geophysical Research Letters*, 7(4), pp.279-282.

Simons, M., Minson, S., Sladen, A., Ortega, F., Jiang, J., Owen, S., Meng, L., Ampuero, J., Wei, S., Chu, R., Helmberger, D., Kanamori, H., Hetland, E., Moore, A. and Webb, F., 2011. The 2011 Magnitude 9.0 Tohoku-Oki Earthquake: Mosaicking the Megathrust from Seconds to Centuries. *Science*, 332(6036), pp.1421-1425.

Soloviev, S.L., 1968. The Sanak Kodiak Tsunami of 1788, The Tsunami Problem, Moscow, Nauka, p. 232-237. Translated in Science of Tsunami Hazards, Vol. 8, No. 1, 1990, p. 34-38.

Spaulding, S., 2022. *How to measure the length, width, and stria density of diatoms | Resources for Practitioners - Diatoms of North America*. [online] Diatoms.org. Available at: <https://diatoms.org/practitioners/how-to-measure-striae> [Accessed 5 September 2022].

Spaulding, S., Potapova, M., Bishop, I., Lee, S., Gasperak, T., Jovanoska, E., Furey, P. and Edlund, M., 2021. Diatoms.org: supporting taxonomists, connecting communities. *Diatom Research*, 36(4), pp.291-304.

Spiske, M., Piepenbreier, J., Benavente, C., Kunz, A., Bahlburg, H. and Steffahn, J., 2013. Historical tsunami deposits in Peru: Sedimentology, inverse modeling and optically stimulated luminescence dating. *Quaternary International*, 305, pp.31-44.

Srisutam, C. and Wagner, J., 2010. Tsunami Sediment Characteristics at the Thai Andaman Coast. *Pure and Applied Geophysics*, 167(3), pp.215-232.

Switzer, A. and Pile, J., 2015. Grain Size Analysis. In: I. Shennan, A. Long and B. Horton, ed., *Handbook of Sea Level Research*. Chichester: John Wiley and Sons Ltd., pp.331-349.

Switzer, A., 2010. Distinguishing between storm and tsunami in the geological record; progress, perturbations and potential. In: *2010 Fall Meeting, AGU*. San Francisco, p.1.

Switzer, A.D., and Jones, B.G., 2008. Setup, deposition, and sedimentary characteristics of two storm overwash deposits, Abrahams Bosom Beach, southeastern Australia, *Journal of Coastal Research*, 24, pp. 189–200.

Sykes, L.R.,1971. Aftershock zones of great earthquakes, seismicity gaps, and earthquake prediction for Alaska and the Aleutians. Journal of Geophysical Research, 76(32), pp.8021–8041.

Szczuciński, W., Kokociński, M., Rzeszewski, M., Chagué-Goff, C., Cachão, M., Goto, K. and Sugawara, D., 2012. Sediment sources and sedimentation processes of 2011 Tohoku-oki tsunami deposits on the Sendai Plain, Japan — Insights from diatoms, nannoliths and grain size distribution. *Sedimentary Geology*, 282, pp.40-56.

Tanaka, G., Naruse, H., Yamashita, S. and Arai, K., 2012. Ostracodes reveal the sea-bed origin of tsunami deposits. *Geophysical Research Letters*, 39(5), pp. 1-4.

Tanigawa, K., Sawai, Y. and Namegaya, Y., 2018. Diatom assemblages within tsunami deposit from the 2011 Tohoku-oki earthquake along the Misawa coast, Aomori Prefecture, northern Japan. *Marine Geology*, 396, pp.6-15.

Tanioka, Y., Satake, K., Ruff, L. and González, F., 1994. Fault parameters and tsunami excitation of the May 13, 1993, Shumagin Islands earthquake. *Geophysical Research Letters*, 21(11), pp.967-970.

Tooley, M., 1978. *Sea-level changes: northwest England during the Flandrian Stage.*. Oxford: Clarendon Press, p.230-232.

Törnqvist, T., Rosenheim, B., Hu, P. and Fernandez, A., 2015. Radiocarbon dating and callibration. In: I. Shennan, A. Long and B. Horton, ed., *Handbook of Sea-Level Research.* Chichester, UK: John Wiley and Sons, Ltd, pp.349-360.

Troels-Smith, J., 1955. Characterization of unconsolidated sediments. *Danmarks geologiske undersøgelse*, 3, pp.38-73.

Tsuru, T., Park, J., Takahashi, N., Kodaira, S., Kido, Y., Kaneda, Y. and Kono, Y., 2000. Tectonic features of the Japan Trench convergent margin off Sanriku, northeastern Japan, revealed by multichannel seismic reflection data. *Journal of Geophysical Research: Solid Earth*, 105(B7), pp.16403-16413.

Van de Plassche, O., 1986. *Sea Level Research: A Manual for the Collection and Evaluation of Data.* Geobooks, Norwich, UK.

van Hengstum, P., Scott, D., Gröcke, D. and Charette, M., 2011. Sea level controls sedimentation and environments in coastal caves and sinkholes. *Marine Geology*, 286(1-4), pp.35-50.

Veniaminov, I,, 1984. *Notes on the Islands of the Utialaska District, Translated by Lydia Black and R.H. Geoghegan, edited by Richard A. Pierce.* Published jointly by the Elmer E. Rasniuson Library translation program, University of Alaska and The Limestone Press, Kingston, Ontario, Canada, pp. 512.

von Huene, R., Miller, J. and Krabbenhoeft, A., 2019. The Shumagin seismic gap structure and associated tsunami hazards, Alaska convergent margin. *Geosphere*, 15(2), pp.324-341.

von Huene, R., Miller, J.J. and Weinrebe, W., 2012. Subducting plate geology in three great earthquake ruptures of the western Alaska margin, Kodiak to Unimak. Geosphere, 8(3), pp.628–644.

Vos, P. and de Wolf, H., 1993. Diatoms as a tool for reconstructing sedimentary environments in coastal wetlands; methodological aspects*. Hydrobiologia*, 269-270(1), pp.285–296.

Vos, P. C., and H. de Wolf., 1988. Methodological aspects of palaeo-ecological diatom research in coastal areas of the Netherlands, Neth. J. *Geosci./Geol. Mijnb*, 67, pp. 31–40.

Watcham, E., Shennan, I. and Barlow, N., 2013. Scale considerations in using diatoms as indicators of sea-level change: lessons from Alaska. *Journal of Quaternary Science*, 28(2), pp.165-179.

Wei, S., Graves, R., Helmberger, D., Avouac, J. and Jiang, J., 2012. Sources of shaking and flooding during the Tohoku-Oki earthquake: A mixture of rupture styles. *Earth and Planetary Science Letters*, 333-334, pp.91-100.

Wilson, F.H., Detterman, R.L., Miller, J. W., and Case, J.E., 1995, Geologic map of the Port Moller, Stepovak Bay, and Simeonof Island quadrangles, Alaska: U.S. Geological Survey Miscellaneous Investigation Series Map I-2272, 1 sheet, scale 1:250,000.

Wise, J.L., Comiskey, A.L., and Becker, R., Jr., 1981. *Storm Surge Climatology and Forecasting in Alaska*, Anchorage, Alaska, USA, University of Alaska, Arctic Environmental Information and Data Center, 26.

Witter, R. C., Kelsey, H.M., and Hemphill-Haley, E., 2003. Great Cascadia earthquakes and tsunamis of the past 6700 years, Coquille River estuary, southern coastal Oregon. Geological Society of America Bulletin 115, no. 10, pp. 1289-1306.

Witter, R., Briggs, R., Engelhart, S., Gelfenbaum, G., Koehler, R., Nelson, A., Selle, S., Corbett, R. and Wallace, K., 2019. Evidence for frequent, large tsunamis spanning locked and creeping parts of the Aleutian megathrust. *GSA Bulletin*, 131(5-6), pp.707-729.

Witter, R., Briggs, R., Engelhart, S., Gelfenbaum, G., Koehler, R. and Barnhart, W., 2014. Little late Holocene strain accumulation and release on the Aleutian megathrust below the Shumagin Islands, Alaska. *Geophysical Research Letters*, 41(7), pp.2359-2367.

Witter, R., Carver, G., Briggs, R., Gelfenbaum, G., Koehler, R., La Selle, S., Bender, A., Engelhart, S., Hemphill-Haley, E. and Hill, T., 2016. Unusually large tsunamis frequent a currently creeping part of the Aleutian megathrust. *Geophysical Research Letters*, 43(1), pp.76-84.

Witter, R., Hemphill-Haley, E., Hart, R. and Gay, L., 2009. *Tracking Prehistoric Cascadia Tsunami Deposits At Nestucca Bay, Oregon*. Newport, Oregon: Oregon Department of Geology and Mineral Industries, pp.1-34.

Witter, R., Zhang, Y., Wang, K., Priest, G., Goldfinger, C., Stimely, L., English, J. and Ferro, P., 2011. *Simulating Tsunami Inundation at Bandon, Coos County, Oregon, Using Hypothetical Cascadia and Alaska Earthquake Scenarios*. Oregon Department of Geology and Mineral Industries, pp.1-57.

Wohlfarth, B., Skog, G., Possnert, G., Holmquist, B., 1998. Pitfalls in the AMS radiocarbon-dating of terrestrial macrofossils. *Journal of Quaternary Science,* 13, pp.137–145.

Wood, K., Stern, L., Furlong, K., Benz, H., Briggs, R., Herman, M. and Goldberg, D., 2021. *2020-2021 Alaska Peninsula Earthquake Sequence*. [online] Earthquake.usgs.gov. Available at: <https://earthquake.usgs.gov/storymap/index-ak2020-21.html> [Accessed 3 September 2022].

Ye, L., Lay, T., Kanamori, H., Yamazaki, Y. and Cheung, K., 2021. The 22 July 2020 M 7.8 Shumagin seismic gap earthquake: Partial rupture of a weakly coupled megathrust. *Earth and Planetary Science Letters*, 562, p.116879.

Zong, Y. and Sawai, Y., 2015. Diatoms. In: I. Shennan, A. Long and B. Horton, ed., *Handbook of sea-level research*. Chichester, UK: John Wiley &Sons Ltd, pp.233-249.

Zong, Y., Kemp, A.C., Yu, F., Lloyd, J.M., Huang, G., and Yim, W.W-S., 2010. Diatoms from the Pearl River estuary, China and their suitability as water salinity indicators for coastal environments. *Marine Micropalaeontology*, 75, pp. 38–49.

Zong, Y., Shennan, I., Combellick, R., Hamilton, S. and Rutherford, M., 2003. Microfossil evidence for land movements associated with the AD 1964 Alaska earthquake. *The Holocene*, 13(1), pp.7-20.

Zweck, C., Freymueller, J. and Cohen, S., 2002. The 1964 great Alaska earthquake: present day and cumulative postseismic deformation in the western Kenai Peninsula. *Physics of the Earth and Planetary Interiors*, 132(1-3), pp.5-20.